Electrokinetic Phenomena of Electrically Induced Janus Droplets and Their Applications

By

Mengqi Li

A thesis
presented to the University of Waterloo
in fulfilment of the
thesis requirement for the degree of
Doctor of Philosophy
in
Mechanical Engineering

Waterloo, Ontario, Canada, 2018

EXAMINING COMMITTEE MEMBERSHIP

The following served on the Examining Committee for this thesis. The decision of the Examining Committee is made by majority vote.

External Examiner

NAME	Alidad Amirfazli
Title	Professor

Supervisor(s)

NAME	Dongqing Li
Title	Professor

Internal Member

NAME	Fue-Sang Lien
Title	Professor

Internal Member

NAME	John Wen
Title	Associate Professor

Internal-external Member

NAME	Boxin Zhao
Title	Associate Professor

AUTHOR'S DECLARATION

I hereby declare that I am the sole author of this thesis. This is a true copy of the thesis, including any required final revisions, as accepted by my examiners.

I understand that my thesis may be made electronically available to the public.

Abstract

Janus droplets refer to droplets comprised of two hemispheres with different properties. Among the Janus droplets, electrically anisotropic Janus droplets with two sides carrying opposite signs of surface charges are unique. Due to their specific properties, electrokinetic phenomena of the electrically anisotropic Janus droplets are quite different from homogeneous ones and are not covered by the classical electrokinetic theory. The electrically heterogeneous Janus droplets have great potential in many fields, such as biotechnology, materials science, pharmaceutical science, food analysis as well as chemistry. Although various techniques have been developed to form the Janus droplets with different anisotropic properties, the techniques for generating the electrically anisotropic Janus droplets are seldom reported. Restricted by the fabrication methods, the studies of electrokinetic phenomena of electrically anisotropic Janus droplets and the applications are limited.

This thesis systematically studies the electrokinetic phenomena of electrically induced Janus droplets (EIJDs), as well as their corresponding applications in microfluidic systems. The initial stage of the thesis is focused on developing simple and controllable methods for generating EIJDs and droplets with multiple heterogeneous surface strips with nanoparticles. Both sessile and suspended EIJDs are formed by partially covering the oil droplets with Al_2O_3 nanoparticles under an electric field. Because the Al_2O_3 nanoparticles and the oil-water interface carrying surface charges with opposite signs, the EIJDs are electrically anisotropic. The nanoparticle coverage of the EIJDs is controllable using the concentration of the nanoparticle suspension and the electric field strength. The droplets with multiple heterogeneous surface strips are prepared in a microfluidic chip under an electric field. By controlling the delivery of nanoparticles in the microfluidic chip, different nanoparticles, Al_2O_3, MgO and ZnO, accumulate on the surfaces of the oil droplets to form desired strips.

In fundamental part, the studies of the electrokinetic phenomena of the EIJDs are conducted, including electroosmosis, electrokinetic motion and wall-induced dielectrophoresis. Electroosmotic flow fields around sessile EIJDs are visualized with the particle tracing method. Because two sides of the Janus droplets carry opposite surface charges, vortices can be generated around the dipoles under electric field. To understand the evolution of these vortices, the effects

of the electric field strength and nanoparticle coverage of the EIJDs on the vortices are studied. The comparisons between the experimental results and the numerical results indicate good agreement. The Electrokinetic motions of the suspended EIJDs in a straight microchannel under both a relatively weak electric field and a relatively high electric field are investigated, respectively. In this study of the electrokinetic motion, the effects of the electric field strength, the nanoparticle coverage of the EIJDs, the droplet size and the electrolyte concentration on the electrokinetic velocity of the EIJDs are studied systematically. The results indicate that, under weak electric field, nonlinear electrokinetic motion of the EIJDs is observed due to the variation of the nanoparticle coverage with electric field. Finally, the wall-induced dielectrophoretic lateral migration of the EIJDs in a microchannel is studied theoretically and experimentally. The lateral migration of the EIJDs is compared with that of the oil droplets, and it is shown that separation of target EIJDs is accomplishable with wall-induced dielectrophoresis.

Two applications of the Janus droplets are introduced in this thesis: microvalve and micromotor. The EIJD-based microvalve is controllable using electric field. By testing the performance of the microvalve systematically, the capability of such an EIJD-based microvalve in sealing, switching time and flow rate control is confirmed. The micromotor moves spontaneously in an alkaline solution through the propulsion of gas bubbles generated on the particle-coated side of the Janus droplet. The factors affecting the motion of the microvalve include: time, pH value of the buffer solution, particle coverage and surfactant. The experimental results verify that the directional motion of the micromotor can be accomplished using an externally applied electric field.

This thesis develops simple methods for fabricating EIJDs and droplets with multiple heterogeneous surface strips. The fundamental research in this thesis extends the understanding in the electrokinetic phenomena. The microvalve and the micromotor fabricated from the Janus droplets offer great potential in various microfluidic devices and applications.

Acknowledgements

I would like to thank my supervisor, Prof. Dongqing Li, for his support and guidance. It's my great fortune to work under the supervision of him. His enthusiasm in work set an example for me to do research like him. I would like to thank him for his time, efforts and confidence on me. I really appreciate his encouragement when I meet with difficulties in my research. I would also like to thank my committee members, Professor Alidad Amirfazli, Professor Fue-Sang Lien, Professor John Wen and Professor Boxin Zhao. Their comments and suggestions are very helpful.

I would like to thank my lab mates and friends. With the company of them, the life in Waterloo becomes joyful. I will never forget the cheerful moments we spent together.

I would like to thank my parents for their love. Thank you for your support and encouragement in the past years. I would also like to thank my wife, Ya Sun, for her understanding and love. She always comforts me when I feel sad. With her thoughtfulness and encouragement, I overcame the obstacles in my PhD study.

Table of Contents

List of Figures

List of Tables

List of Abbreviations

AC	Alternating current
CCD	Charge-coupled device
CM	Clausius-Mossotti
CMC	Critical micelle concentration
CTAB	Cetyltrimethylammonium bromide
DAQ	Data-acquisition
DC	Direct current
DEP	Dielectrophoresis
DLVO	Derjaguin-Landau-Verwey-Overbeek
EDL	Electric double layer
EHD	Electrohydrodynamic
EIJD	Electrically induced Janus droplet
EK	Electrokinetics
EP	Electrophoresis
FEM	Finite element method
HDDA	Hexanediol diacrylate
ICEK	Induced-charge electrokinetics
ICEO	Induced-charge electroosmosis
MFDG	Microfluidic droplet generator
MST	Maxwell-stress tensor
PDA	Polydopamine
PDMS	Polydimethylsiloxane
PE	Polyethylene
PS	Polystyrene
SDS	Sodium dodecyl sulfate
TPGDA	Tetradecane-tripropylene glycol diacrylate
UV	Ultraviolet

List of Symbols

A	Cross sectional area of the channel	a	Radius of the droplet or particle
C	Concentration of the nanoparticle suspension	d	Diameter of the particle or droplet
D	Diameter of the channel	e	Elementary charge
E	Strength of the electric field	$\vec{E}$	Electric field
E_r	Relative electric field strength	$\vec{E}_o$	Local electric field
E_∞	Electric field strength far from the droplet or particle	$\vec{F}_{DEP}$	DEP force
E_i , E_A , E_B	Electric field strength in the microchannel	$\vec{F}_{vdW}$	Van der Waals (vdW) force
$\vec{F}_f$	Friction force	$\vec{F}_{EDL}$	EDL interaction force
$\vec{F}_{total}$	Summation of F_{vdW} and F_{EDL}	F_{wDEP}	Wall-induced DEP force
$\vec{F}_e$	Electrostatic force	$\vec{F}_{e,J}$	Electrostatic force acting on the EIJD
$\vec{F}_{e,J}^{+}$ ($\vec{F}_{e,J}^{-}$)	Electrostatic force acting on the positive (negative) side of the EIJD	$\vec{F}_h$	Hydrodynamic force
$\vec{F}_{hin}$	Hydrodynamic force generated by the fluid flow inside of EDL	$\vec{F}_{net}$	Net force acting on the droplet or particle
$\vec{F}_{ho}$	Hydrodynamic force generated by the fluid flow outside of EDL	f	Frequency of the electrical field
ΔF	Variation of free energy	L	Length of the channel
f_{CM}	Clausius-Mossotti (CM) factor	$\vec{n}$	Unit vector normal to the boundary
n_∞	Ionic concentration of the aqueous solution	O	Original point of the coordinate system
P	Pressure	Q^+ (Q^-)	Total number of surface charges on the positive (negative) side of the EIJD
r	Size ratio	S	Surface area of the particle or droplet
S^+ (S^-)	Surface area of the positive (negative) side of the EIJD	T	Absolute tempera
t	Time	$\vec{U}_{ek}$	EK velocity
U_{ref}	Reference velocity	$\vec{U}_{ep}$	EP velocity
$\vec{U}_{eof}$	EOF velocity	U_{ek}^*	Dimensionless electrokinetic velocity
U_{ep}^*	Dimensionless electrophoretic velocity	$\vec{u}_w$	Velocity of the aqueous liquid
U_{wDEP}	Wall-induced dielectrophoretic lateral migration velocity	W	Width of the channel
$\vec{u}_o$	Velocity of the oil phase	V_{eof}	Electroosmotic volume flow rate

y_d	Position of the center of the droplet in y-direction	z	Absolute value of the ionic valence
x_d	Position of the center of the droplet in x-direction	β	Angle of the nanoparticle film on EIJD
γ	Nanoparticle coverage	γ_A , γ_B , γ_{ow}, γ_{AB}	Interfacial tension
ε_w	Permittivity of the aqueous liquid	γ_r	Relative coverage
$\tilde{\varepsilon}_w$	Complex permittivity of the aqueous liquid	ε_0	Permittivity of vacuum
ζ	Zeta potential	$\tilde{\varepsilon}_p$	Complex permittivity of particle
ζ_p	Zeta potential of particle	$\bar{\zeta}$	Average zeta potential
ζ_{ow}	Zeta potential of the oil-water interface	ζ_w	Zeta potential of channel wall
ζ_r	Zeta potential ratio	ζ_0	Local zeta potential
η_o	Viscosity of oil	ζ_{nano}	Zeta potential of the nanoparticle film
η_w	Viscosity of the aqueous liquid	η_r	Viscosity ratio
θ_w	Contact angle of the particle in water	θ	Angle between two edge lines of the nanoparticle film on EIJD
k_b	Boltzmann constant	θ_A , θ_B, θ_w	Contact angle
μ_{ep}	Electrophoretic mobility	κ	Debye-Hückel parameter
μ_{ek}	Electrokinetic mobility	λ_D	Debye length
ρ_e	Net charge density in EDL	μ_{eof}	Electroosmotic mobility
ρ_o	Density of oil	ρ_w	Density of the aqueous liquid
σ_s	Surface charge density	ρ_{al}	Density of the particle coated side of the Janus droplet
σ_s^+ (σ_s^-)	Local surface charge density of the positive (negative) side of the EIJD	$\sigma_{c,p}$ ($\sigma_{c,w}$)	Electrical conductivity of particle (aqueous liquid)
ϕ	Electric potential of the applied electric field	τ	Ratio between radius of the droplet and y_d
ψ	Electrical potential in EDL	ϕ_{sample}, ϕ_{sheath}, ϕ_A, ϕ_B, ϕ_C, ϕ_d, ϕ_i	Voltage applying to the reservoir of the microfluidic chip
$\bar{\bar{I}}$	Intensity tensor	ω	Angular frequency of the electrical field

CHAPTER 1 Introduction

1.1 Problem Statement

Janus is a Roman god with two faces towards opposite directions. Janus droplets named after this god, refer to droplets with two sides carrying different properties. Recently, Janus droplets have attracted great interest due to their unique anisotropic properties, which make them suitable in many fields such as biotechnology, materials science, pharmaceutical science, food analysis as well as chemistry. For example, Janus droplets can be solidified to Janus particles with color [1], electrical [2], magnetic [3, 4] or amphiphilic [5] anisotropy, which are useful in stabilizing emulsion [6], fabricating twisting-ball electronic paper [7], detecting cellular components [8, 9] and so on.

A series of fabrication techniques have been developed for synthesizing Janus droplets. The major fabrication techniques include high energy mixing method, microfluidic method and electrohydrodynamic method. Each of these fabrication techniques has its known strengths and weaknesses, and various Janus droplets with different anisotropic properties have been produced with these methods. However, the generation of electrically anisotropic Janus droplets with the existing methods is seldom reported. Since Janus droplets with electrical anisotropy are electrically responsive, they can find application in sensor and actuator-based microfluidic devices. Therefore, a simple, reliable, productive and cost-effective technique for the generation of electrically anisotropic Janus droplets is highly required.

Manipulation of droplets/particles plays a very important role in microsystems, and the electrokinetic technique has been proved to be effective in operating the droplets/particles precisely. The electrokinetic phenomena of homogenous rigid particles and droplets have been investigated extensively. However, for heterogeneous Janus materials, most of the studies have focused on the electrokinetic phenomena of solid Janus particles, and research on Janus droplets has been limited. Understanding of the electrokinetic phenomena of Janus droplets is in demand. First, due to the heterogeneous structure, the electrokinetic phenomena of the Janus droplets are complicated and quite different from that of the homogeneous droplets, especially for electrically anisotropic Janus droplets. The systematic studies of the electrokinetic phenomena of Janus droplets can extend the classic electrokinetic theory. Second, more detailed knowledge of the

electrokinetic properties of the Janus droplets is critical to the operation of them, which is helpful in fabricating Janus droplet-based microfluidic devices for micro-mixing, separation and sorting, as well as programmable cargo delivery.

Due to restrictions of fabrication techniques and understanding of the electrokinetic phenomena, the development and demonstration of the potential of the Janus droplet were seldom reported. The studies of the applications of Janus materials focus on solid Janus particles. For example, the electrokinetic motion of the metallic-dielectric Janus particles in a microchannel were studied, and the applications of the Janus particles in fabricating microvalve and micromotor were proved, respectively. In comparison with solid Janus particles, the Janus droplets have their own advantages. For instance, Janus droplets are more suitable in programmable cargo delivery, offering the advantages of large capacity and high flexibility. For these reasons, development of applications of Janus droplets is highly desirable, and will be useful in many areas of science and technology.

1.2 Research Objectives

Electrically anisotropic Janus droplets are investigated in this thesis; the droplets are fabricated with nanoparticles under an externally applied electric field. Therefore, we would like to name the Janus droplets fabricated with this method as electrically induced Janus droplets (EIJDs). This thesis is aimed at presenting a comprehensive study of the electrically anisotropic Janus droplets in the field of fabrication, electrokinetic properties and applications. The detailed objectives include:

1) Develop simple and cost-effective techniques in fabricating sessile and suspended EIJDs.

2) Analyze the influence factors of the topology of the EIJDs.

3) Characterize the electrokinetic properties of the EIJDs, including electroosmosis, electrokinetic motion and wall-induced dielectrophoresis.

4) Develop a microvalve based on the electrokinetic motion of EIJD.

5) Fabricate self-propelled micromotors with particle-coated Janus droplets in alkaline solution.

1.3 Thesis Outline

The layout of the thesis is shown in Figure 1-1.

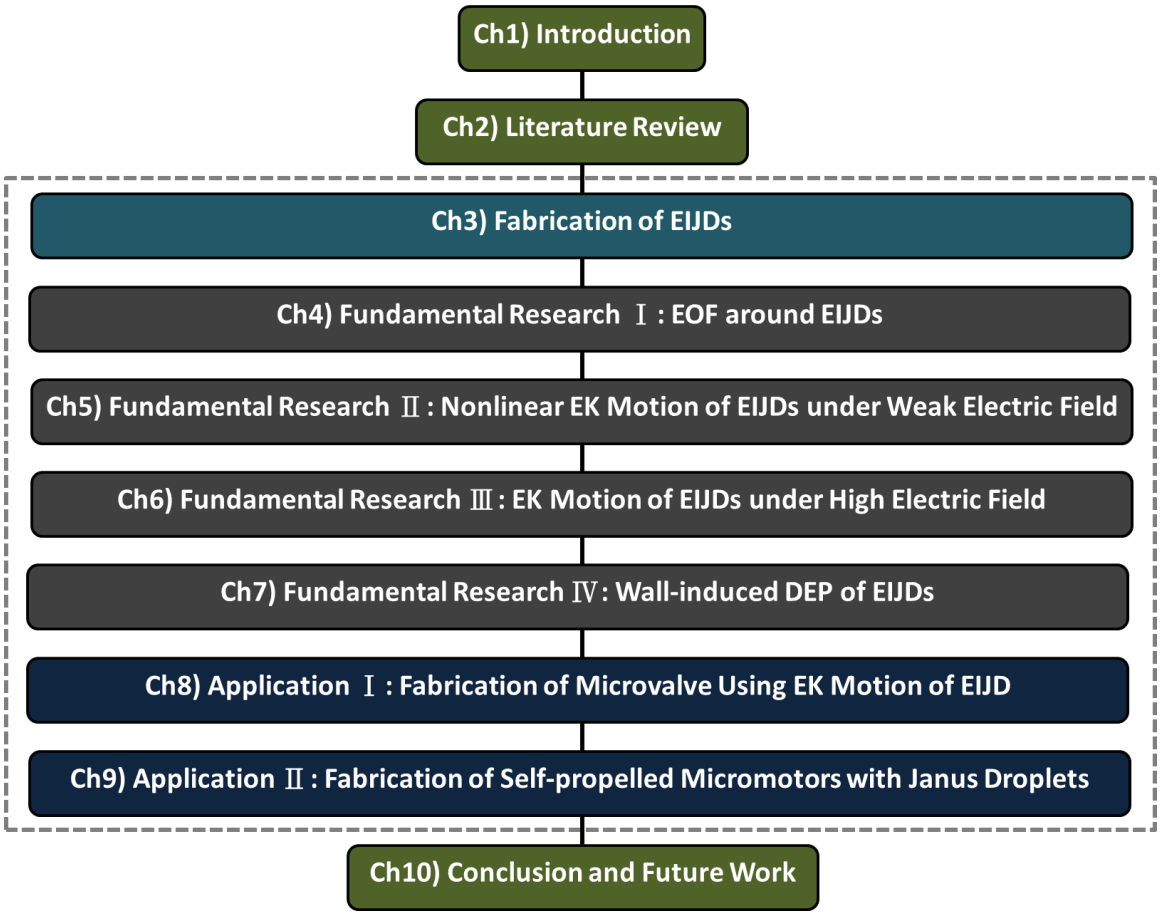

Figure 1-1 Thesis layout.

The thesis includes ten chapters. Chapter 1 presents an overview of this research, including the motivations and the objectives.

In Chapter 2, the literature review is provided. The Janus droplets fabrication techniques, the classic electrokinetic phenomena, as well as the electrokinetic properties of solid Janus particles are reviewed. A brief summary and comparison of the Janus droplets fabrication techniques is

made. Chapter 2 aims to provide a fundamental background of the Janus droplet research and point out the areas for additional investigation.

Chapter 3 presents the novel methods for preparing the EIJDs with nanoparticles under electric field. The methods for generating both sessile and suspended Janus droplets are demonstrated experimentally. The effects of different factors, including electric field strength and concentration of nanoparticle suspension on the topology of the Janus droplets are investigated. The fabrication of droplets with multiple heterogeneous surface strips under electric field in a microchannel is also presented in this chapter.

Chapters 4, 5, 6 and 7 systematically investigate the electrokinetic phenomena of the EIJDs. Chapter 4 studies the electroosmotic flow fields around sessile EIJDs. A multi-physics model is set up to simulate the EOF fields around the EIJDs under DC electric field. The influence factors of the strength of the electric field and the nanoparticle coverage of the EIJDs on the flow fields are explored. The experimental visualization of the flow fields around the EIJDs are also conducted with the tracing particle method. The comparison between the experimental results and the numerical results confirms the numerical predictions.

Chapter 5 studies the nonlinear electrokinetic motion of the EIJDs in microchannels under relative weak electric field experimentally. The lag of the variation of nanoparticle coverage of the EIJDs behind the change of electric field is characterized by measuring the evolution time of the nanoparticle film under different electric field strengths and by comparing the variations of nanoparticle coverage under different time-varying electric fields. The electrokinetic motions of the EIJDs under different electric field strengths and different time-varying electric fields are measured, respectively. Results show that under weak electric field the nanoparticle coverage of the EIJDs is electric-responsive, hence the electrokinetic velocity of the EIJDs increases nonlinearly with the electric field strength. Furthermore, due to the lag effect of the nanoparticle coverage, the electrokinetic velocities of the EIJDs are different under different time-varying electric field.

In Chapter 6, the electrokinetic motion of the EIJDs under relative high electric field (constant nanoparticle coverage) was studied both numerically and experimentally. Numerically, a theoretical model is constructed to calculate the electrokinetic velocity of the Janus droplet by

considering the force balance on the surface of the Janus droplet at steady state. In the model, the effects of the electric double layer and surface charges on the motion at the oil-water interface are considered. The effects of five parameters on the electrokinetic motion of the Janus droplets are studied: the strength of the electric field, the ratio of the zeta potential of the positively charged side of the Janus droplet to that of the negatively charged side, the ratio of the viscosity of the oil phase to that of the water phase, the nanoparticle coverage of the Janus droplet, and the ratio of the diameter of the Janus droplet to that of the cylindrical microchannel. To confirm the numerical findings, the electrokinetic motion of the EIJDs in a microchannel under electric field larger than 50 V/cm is studied, and the numerical results and the experimental results are compared.

Chapter 7 presents the study of the wall-induced dielectrophoresis (DEP) of EIJDs in microchannels. The lateral migrations of homogeneous oil droplets and EIJDs in a straight microchannel under different conditions are experimentally measured first, and the experimental results are compared with the theoretical predications. Based on the wall-induced dielectrophoresis, the oil droplets with different sizes, the Janus droplets with different sizes, and the oil droplets and Janus droplets with the same size are separated respectively in a microchannel. The study in this chapter demonstrates the feasibility of the wall-induced DEP method, for the first time to our knowledge, in separating oil droplets and EIJDs.

The applications of the Janus droplets in fabricating microvalve and micromotor are shown in Chapters 8 and 9, respectively. In Chapter 8, the application of EIJDs in fabricating an electrically responsive microvalve is demonstrated. The electrokinetic motion of the EIJD in a circular microchamber under switching electric field is examined first. Then, the microvalve is fabricated by injecting an EIJD into a three dimensional (3D) microchannel, and the performance of the microvalve, including switching time, flow rate and leakage, is analyzed. In addition, the EIJD is compared with an isotropic oil droplet, and the sealing performance of the oil droplet-based microvalve is tested. The EIJD-based microvalve shown in this chapter offers great potential in fabricating integrated microfluidic devices.

In Chapter 9, the self-propelled micromotor fabricated with particle-coated Janus droplets is developed. The self-propulsion of the micromotor in an alkaline solution is demonstrated experimentally. The factors influencing the motion of the micromotor, including time, pH value

of the surrounding solution, particle coverage of the Janus droplet and surfactant, are investigated systematically. The directionally controlled transportation of the micromotor is accomplished by using an electric field.

The last chapter of the thesis concludes the major findings on the fabrication, electrokinetic properties and applications of the EIJDs. Based on the findings shown in this thesis, suggestions for future research are also briefly introduced.

CHAPTER 2 Literature Background

The main objectives of this thesis are to develop novel methods to fabricate electrically anisotropic Janus droplets and perform a systematically study of the electrokinetic properties of the Janus droplets. In this chapter, the fabrication techniques of Janus droplets and the classic electrokinetic phenomena are reviewed. In the fabrication techniques part, the high energy mixing method, microfluidic method and electrohydrodynamic method are introduced. The theories of electric double layer (EDL), electroosmotic flow (EOF), electrophoresis (EP) as well as dielectrophoresis (DEP) are presented in the part of classic electrokinetic phenomena. The electrokinetic phenomena of solid Janus particles are also included. The chapter provides a fundament background of this thesis.

2.1 Janus Droplet Fabrication Techniques

2.1.1 High Energy Mixing Method

The high energy mixing method (also called one-step bulk vortex mixing method) can be used to prepare Janus emulsions simply and quickly, which includes the following two steps: (a) add two immiscible dispersed phases, usually oils, into a continuous phase, usually aqueous solution; (b) vibrate the mixture using a shear mixer or a vortexer until the emulsion appears homogeneous [10–20]. With this method, the Janus droplets comprised of two immiscible dispersed phases can be formed in the continuous phase, for example, silicone oil-vegetable oil Janus droplets in Tween 80 aqueous solution [11,13] [16], tripropyleneglycol diacrylate (TP)-silicon oil Janus droplets in Tween 80 aqueous solution [17], as well as hexane-perfluorohexane Janus droplets in Zonyl and sodium dodecyl sulfate (SDS) aqueous solution [18]. The equilibrium topology of the Janus droplet is dependent on both the interfacial tensions in the contact line between the two dispersed phases and the continuous phase and the volume ratio of the dispersed phases.

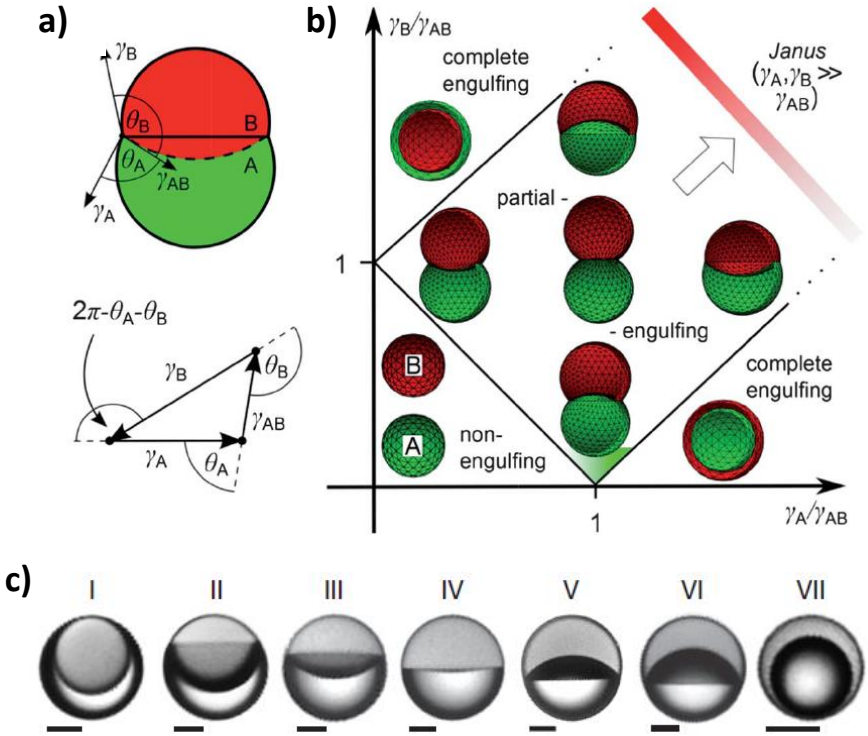

Figure 2-1 (a) Schematic diagram of a Janus droplet comprised of two immiscible fluids, A and B, with indicated interfacial tensions and contact angles. Reproduced with permission [14]. Copyright 2012 The Royal Society of Chemistry (RSC). (b) Transition of the topology of the Janus droplet in terms of the interfacial tension ratios, γ_A/γ_{AB} and γ_B/γ_{AB}. Reproduced with permission [14]. Copyright 2012 The Royal Society of Chemistry (RSC). (c) Optical images of the hexane-perfluorohexane droplets in solutions with different concentration of surfactant, SDS. From Ⅰ to Ⅶ, the concentration of SDS increases gradually from 0 to 0.1%. Reproduced with permission [18]. Copyright 2015 Nature Publishing Group.

The interfacial tensions affect the topology of the Janus droplet by characterizing the curvature of the inner interface between the two immiscible phases. Consider a Janus droplet comprised of two immiscible fluids, A and B, with the same volume, immersed in the continuous phase. As shown in Figure 2-1(a), the three-phase contact line forms between the three phases. At equilibrium state, the relationship between the contact angles and the interfacial tension on the three-phase contact line can be expressed as (known as Neumann triangle) [14]:

$$\gamma_{AB}cos\theta_B + \gamma_B + \gamma_A \cos(\theta_A + \theta_B) = 0 \quad (2\text{-}1)$$

$$\gamma_{AB}cos\theta_A + \gamma_A + \gamma_B \cos(\theta_A + \theta_B) = 0 \quad (2\text{-}2)$$

where γ_A is the interfacial tension between A and the continuous phase, γ_B is the interfacial tension between B and the continuous phase, and γ_{AB} is the interfacial tension between A and B. θ_A and θ_B are the contact angles.

As shown in Eq. (2-1) and (2-2), the contact angles change with the variation of interfacial tension; hence, the topology of the Janus droplet. The transition of the topology of the Janus droplet in terms of the interfacial tension ratio is shown in Figure 2-1(b). It can be clearly seen from this diagram that the partial engulfing Janus droplet can be generated only under the condition of $\gamma_A, \gamma_B \gg \gamma_{AB}$ and the topology of the Janus droplet changes with the interfacial tension ratios, γ_A/γ_{AB} and γ_B/γ_{AB}. Generally, the three interfacial tensions can be adjusted by changing the concentration of surfactant in the continuous phase. Janus droplets with different heterogeneities can be generated by changing the surfactant concentration in the continuous phase. Zarzar et al. [18] experimentally proved this by generating hexane-perfluorohexane droplets with different topologies. As shown in Figure 2-1(c), the topology of the hexane-perfluorohexane droplet changes with the concentration of surfactant, SDS.

The effect of volume ratio between two dispersed phases on the topology can be understood easily. With the variation of the volume ratio, the sizes of the two sides of the Janus droplets change, and the topology of the Janus droplets is different. Hasinovic et al. [20] studied the effect of volume ratio on the topology of the Janus droplet. As shown in Figure 2-2(a), the volume of O1 changes, while O2 remains constant. The numbers at the bottom of each droplet represent the volume ratio. It can be seen that the contact line moves downwards in relative to the whole droplet with the increase of the volume ratio, and Janus droplets with different topologies form. Ge et al. [17] experimentally studied the effect of volume ratio. By injecting silicone oil and tripropyleneglycol diacrylate with different volume fractions into aqueous solution, Janus droplets with different topologies were generated successfully, as shown in Figure 2-2(b).

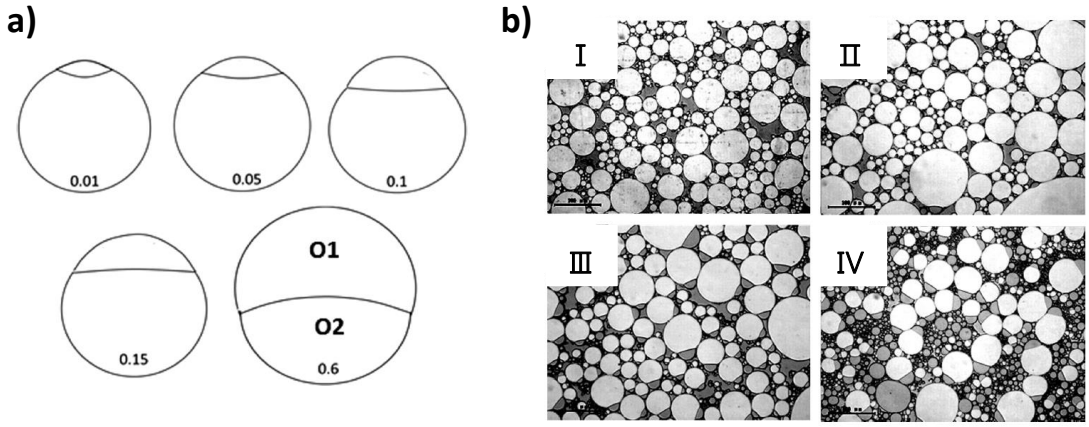

Figure 2-2 (a) Numerical result of the variation of the Janus droplet topology with volume ratio. The volume of O1 change, while O2 remains constant. The number represents the volume ratio of O1/O2. Reproduced with permission [20]. Copyright 2013 Taylor & Francis. (b) Microscopy images of the Janus droplets generated by dispersing different volume fractions of silicone oil and tripropyleneglycol diacrylate into Tween 80 aqueous solutions. From Ⅰ to Ⅳ, the fraction of tripropyleneglycol diacrylate increases gradually. Reproduced with permission [17]. Copyright 2014 Elsevier.

In comparison with other methods, the high energy mixing method has the advantage of being able to prepare a large number of Janus droplets within limited time. However, the size and the topology of the Janus droplets fabricated with this method are hard to control. The size varies from several microns to several hundred microns, and the topology of the Janus droplets is different from each other due to different volume ratio between them.

2.1.2 Microfluidic Method

Recently, the droplet microfluidic system has been developed and widely used for generating and manipulating droplets [21–23], which provides a potential way to form Janus droplets. Based on the formation mechanism, the microfluidic method can be divided into three groups: breakup formation [7,8,24–28], evolution from core-shell emulsion [29–36] and phase separation [37–39].

2.1.2.1 Breakup Formation

The first mechanism, breakup formation, is the most popular one. With this mechanism, Janus droplets can be produced one by one through forcing parallel streams of two immiscible phases to break up into droplets in a microfluidic chip [24,25,40]. Generally, two immiscible dispersed phases flow in the central channels of a microfluidic chip, and the continuous phase flows in the side channels. When the thin stream of the two dispersed phases is forced to flow through a narrow orifice, the shear force generated by the continuous phase breaks up the thin stream and Janus droplets form. The schematic diagrams of the general Janus droplets generators are shown in Figure 2-3 (a) and (b). Maeda et al. [26] extended this method by developing a centrifuge Janus droplet generator to synthesis magnetic anisotropic Janus droplets. The synthesis system comprises two parts: a droplet generator device with built-in capillaries for holding the two immiscible monomers and forming sessile Janus droplets on the capillary orifices, a tabletop centrifuge which is used to provide centrifugal force to drag the sessile Janus droplets away and forms mobile Janus droplets (Figure 2-3 (c)). Furthermore, to increase the volume throughput of the microfluidic method, a lot of attempts have been taken, for example, parallelization devices were utilized to generate multiple Janus droplets at the same time [41–46].

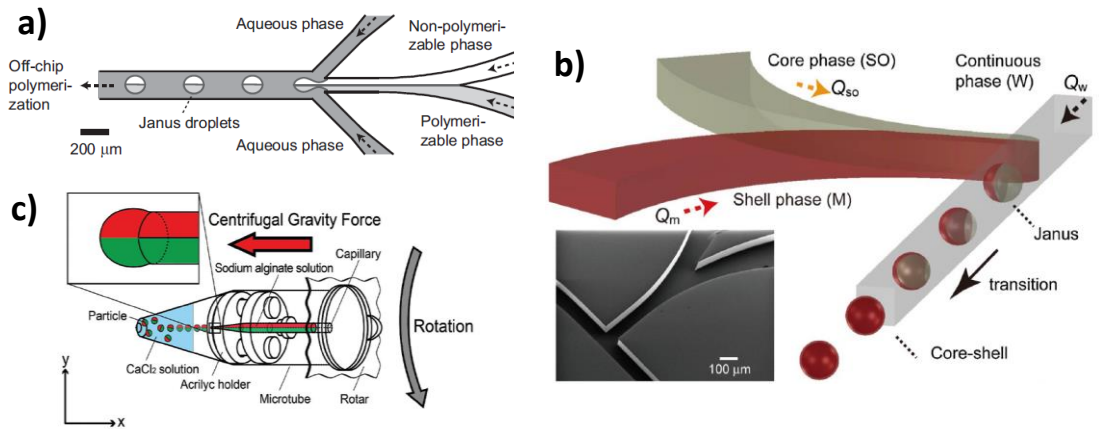

Figure 2-3 Schematic diagrams of the Janus droplets generators. (a) A Y-shaped microfluidic droplet generator (MFDG). Reproduced with permission [24]. Copyright 2007 John Wiley and Sons. (b) A T-shaped MFDG. Reproduced with permission [40]. Copyright 2016 Elsevier. (c) Centrifuge-based Janus droplets generator. Reproduced with permission [26]. Copyright 2012 John Wiley and Sons.

With this mechanism, the topology and size of the Janus droplets can be controlled easily. The proportion of different monomers in the droplets can be changed by adjusting the volume flow rates of the two immiscible dispersed phases, and the size of the droplets can be controlled by regulating the volume flow rates of the dispersed phases and the continuous phase [47]. The properties of different sides of the Janus droplets are dependent on the properties of the two immiscible monomers. With the break up mechanism, a variety of Janus droplets has been fabricated, for example, acrylate monomer-silicon oil Janus droplets [24] (Figure 2-4 (a)), 1,6-hexanediol diacrylate (HDDA)-silicone oil Janus droplets [25] (Figure 2-4 (b)) and soybean oil-deionic water Janus droplets [28].

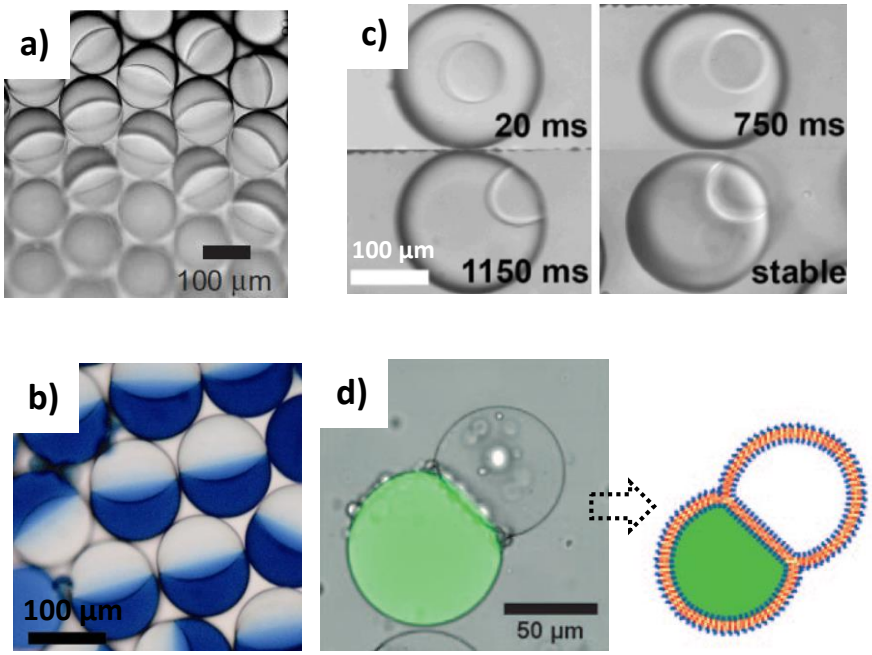

Figure 2-4 Optical images of the Janus droplets. (a) Acrylate monomer-silicon oil Janus droplets developed from breakup mechanism. Reproduced with permission [24]. Copyright 2007 John Wiley and Sons. (b) 1,6-hexanediol diacrylate (HDDA)-silicone oil Janus droplets developed from breakup mechanism. Reproduced with permission [25]. Copyright 2009 Springer Nature. (c) Tetradecane-tripropylene glycol diacrylate (TPGDA) Janus droplet transferred from O/O/W droplet. Reproduced with permission [33]. Copyright 2008 American Physical Society. (d) Janus liposome prepared from W/O/W droplet through solvent evaporation and dewetting. Reproduced with permission [34]. Copyright 2011 John Wiley and Sons.

2.1.2.2 Evolution from Core-shell Emulsion

The Janus droplets can also be produced through the evolution of core-shell emulsion droplets. The core-shell emulsion is consisted with three immiscible phases, i.e., two dispersed immiscible phases and one continuous phase. The core-shell droplets are formed by encapsulating the droplets of one dispersed phase with the other dispersed phase in MFDGs. For oil-in-oil-in-water (O/O/W) droplets, the topology of the core-shell droplets is changeable. With the minimization of the interfacial energy of the droplets, the core-shell droplets transform into Janus droplets. Pannacci et al. [33] introduced three fluids into a microfluidic system to produce double droplets. The core-shell droplets are generated in the upstream of the microchannel. As the translation of the droplets, the complete engulfing droplets transform into Janus droplets in the downstream spontaneously with the minimization of the interfacial energy, as shown in Figure 2-4 (c). The core-shell droplets and the Janus droplets are inter-convertible by using stimuli-responsive surfactants to tune the interfacial tensions. For example, the effectiveness of the stimuli-responsive surfactants changes in response to pH, temperature or light, which further affects the interfacial tensions, and then the topology of the droplets. The Janus droplets can also be fabricated from the water-in-oil-in-water (W/O/W) droplets with the dewetting and evaporation of solvent. The droplets with Janus geometry comprising an aqueous lobe and a solvent lobe show up transiently during the solvent evaporation of W/O/W droplets [36]. Recently, Shum et al. [34] reported a novel method to prepare stable Janus droplet through dewetting. They prepared W/O/W emulsion droplets with two aqueous cores in MFDG. As the evaporation of the middle phase, the amphiphilic diblock copolymers dissolved out and got assembled at the interfaces to form membranes. As a result, the aqueous cores covered with copolymers adhered to each other and a Janus vesicle formed (Figure 2-4 (d)).

2.1.2.3 Phase Separation

The phase separation is another mechanism for generating Janus droplets from single-phase emulsion droplets. In this mechanism, the dispersed phase containing multiple solvents is emulsified into a continuous phase in a MFDG. With the dissolving and evaporation of the co-solvent into the continuous phase, the solvents in the droplet separate out and Janus droplet forms. For example, Zhang et al. [39] injected the ternary mixture (ethanol, water and octanol) and

fluorinated oil (FC-40) into a T-shape microchannel with the ternary mixture as the dispersed phase and the FC-40 as the continuous phase. The homogeneous ternary mixture droplets were generated in the microchannel. As the FC-40 has high permeability for vapor, the volatile solvent in the ternary mixture droplets, ethanol, entered into the continuous phase and evaporated into the air. Finally, the remaining two solvents, water and octanol, in the droplets separated out to form Janus droplets.

2.1.3 Electrohydrodynamic Method

For a dielectric droplet immersed in dielectric bulk liquid, under externally applied electrical field, charges can be induced at the liquid-liquid surface. With the interaction between the electric field and the induced charges, fluids flow can be generated both inside and outside of the droplet. The electrically induced fluids flow is called electrohydrodynamic (EHD) flow [48–51]. For the droplets covered with particles, after applying electric field, the particles at the interfaces are brought to the droplets "electric equator" by EHD flow, and "ribbon-like" structures form on the droplets [52–54]. At the meantime, under the both effects of EHD flow and electrostatic forces, the droplets are attracted and get coalesced. With the electro-coalesce of two droplets carrying different particles, a larger droplet coated with Janus shell can be fabricated. The fabrication process of the Janus capsule with EHD method is shown in Figure 2-5(a). Rozynek et al. [55] first presented and demonstrated this method in 2014. Based on this method, they fabricated variety of Janus capsules, for example, amphiphilic Janus capsule (Figure 2-5(b)), color anisotropic Janus capsule (Figure 2-5(c)), asymmetric Janus capsule (Figure 2-5(d)) and patchy capsule (Figure 2-5(e)).

2.1.4 Other Methods

Apart from the methods shown above, some other methods were also developed to fabricate Janus droplets. Bormashenko et al. [56] inserted two droplets coated with different powders, carbon black, and polytetrafluoroethylene, into a dish. The color anisotropic Janus droplet was formed by vibrating the dish to make the two droplets merge with each other. Xu et al. [57] found that the hydroxide ions (OH^-) and the polydopamine (PDA) particles occupy separate areas on the droplets. Under this mechanism, they generated Janus droplets which were partially covered with PDA particles in water. The coverage of PDA particles of the Janus droplet can be adjusted with the

variation of the pH value of the solution. Subramaniam et al. [58] fabricated Janus capsules by accumulating different colloidal particles to the two hemispheres of oil droplets with hydrodynamic force in a microfluidic system. To introduce the colloidal particles to the oil-water interface, high kinetic energy is essential for overcoming the energy barrier between colloidal particles and oil droplet.

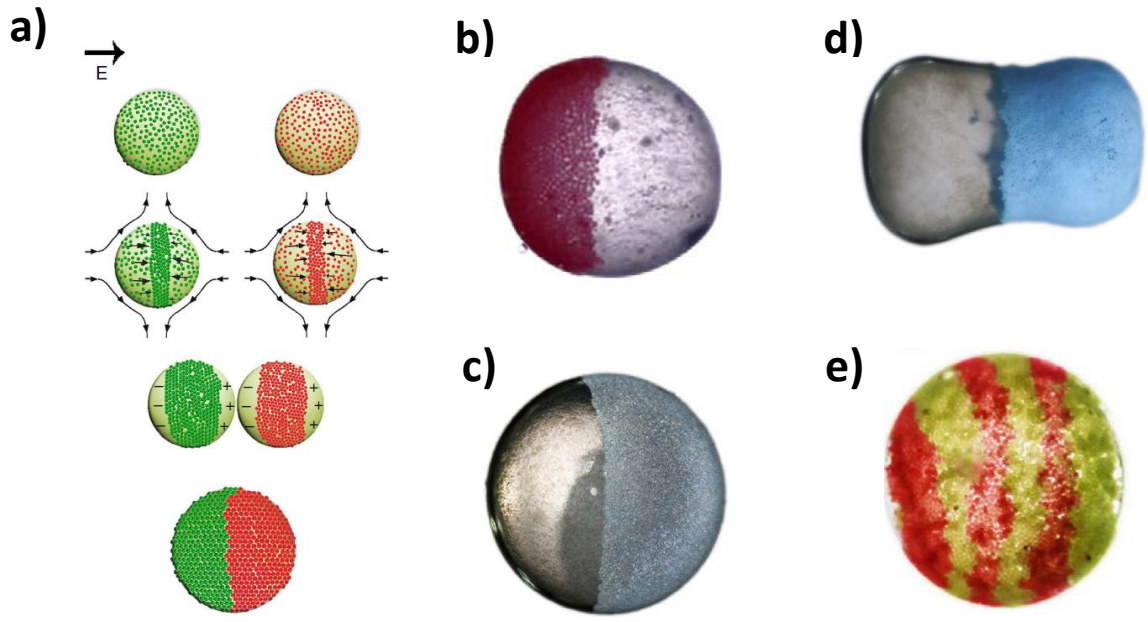

Figure 2-5 (a) Schematic diagram of the fabrication process of the Janus capsule with EHD method. (b) Amphiphilic Janus capsule fabricated with hydrophobic polyethylene (PE) particles (red) and hydrophilic clay particles (white). (c) Color anisotropic Janus capsule fabricated with polystyrene (PS) particles and glass particles. (d) Asymmetric Janus capsule fabricated with glass and polyethylene (PE) particles. (e) Patchy capsule fabricated with red and green PE particles. Reproduced with permission [55]. Copyright 2014 Springer Nature.

2.1.5 Summary

As reviewed in the above sections, a variety of Janus droplet fabrication methods has developed and demonstrated in the last decades. Each method has its own advantages and disadvantages. With the comparison of these methods, the following conclusions can be obtained:

(a) The high energy mixing method can generate Janus droplets fast and enormously. The topology of the Janus droplets generated with this method is adjustable by changing the concentration of surfactant and the volume ratio of the dispersed phases. However, it is difficult to control the size and topology of the Janus droplets precisely. As a result, the high energy mixing method is a large-scale, less precise Janus droplet fabrication technique.

(b) The microfluidic method generated Janus droplets in MFDGs. It includes three mechanisms: breakup formation, evolution from core-shell emulsion and phase separation. Based on these mechanisms, various Janus droplets have been produced. The Janus droplets fabricated by this method have more precise size and topology. However, the generation efficiency of this method is very low compared with the high energy mixing method, even with parallelized microfluidic devices. Therefore, the microfluidic method is a small-scale, precise fabrication technique.

(c) The electrohydrodynamic method fabricates Janus capsules based on the EHD flow in vicinity of droplets and the electro-coalesce between droplets. The fabrication is controlled with electric field. However, as both the dispersed phase and continuous phase are dielectric materials, extremely high electric field is essential in generating EHD flow. Compared with the other methods, the preliminary preparation of this method is complex that droplets should be coated by different particles and placed in appropriate places before applying electric field. Furthermore, due to the uncertainly electro-coalesce between droplets, the fabrication of large amount of Janus droplets at the same time is difficult.

(d) Some unique Janus droplets have also been fabricated with the other methods shown above. However, the shortcomings of these methods are also obvious, for example, low efficiency, complex fabrication process and poor control of droplet size and topology. These shortcomings restrict their applications.

Overall, each of the fabrication methods has its own area, and it is impossible to find a "one-fit-all" fabrication method for generating Janus droplets. The fabrications of color anisotropic Janus droplets and amphiphilic Janus droplets with these methods have been reported. However, for the generating of electrically anisotropic Janus droplets, limited fabrication methods are applicable. Considering the potentials of electrically anisotropic Janus droplets, it is desirable to develop a simple and controllable method for generating electrically anisotropic Janus droplets.

2.2 Electrokinetic phenomena

Electrokinetics includes electroosmosis, electrophoresis and dielectrophoresis, which can be used to drive fluid movement and manipulate the particles/droplets. Most of surfaces carry surface charges when contacting with aqueous electrolyte solution. The charged surfaces attract counter-ions from the surrounding liquid and electric double layer (EDL) forms. Under externally applied electric field, the counter-ions inside EDL are driven to move, which further induces the liquid motion due to the viscosity of the liquid. The liquid motion near a charged surface/interface is called electroosmosis. Reversely, electrophoresis is the motion of charged surfaces, for example, charged particle/droplet immersed in bulk liquid moves under electric field. Recently, with the development of microfluidics, electrokinetics has been applied to this area, which provides efficient techniques for manipulation in micro-scale. Numerous applications of electrokinetics in microfluidics have been developed, for example, drug delivery [59,60], cell separation [61–63], and particle/droplet manipulation [64–66].

2.2.1 Electric Double Layer

The electric double layer (EDL) theory is the fundamental of electrokinetics. For a solid surface immersed in electrolyte solution, it carries surface charges by adsorbing specific ions, hydrolyzing surface groups or breaking crystals. The surface charges on the surface attract counter-ions from the electrolyte solution and expel the co-ions, and then the EDL forms in vicinity of the surface, as shown in Figure 2-6. The EDL comprises the compact layer and the diffuse layer. The compact layer stays next to the charged surface that the counter-ions in this layer are immobile. The diffuse layer is located between the compact layer and the electrically neutral bulk liquid. With the effect of the charged surface, the counter-ions and co-ions in the diffuse layer distribute non-uniformly; therefore, the net charge density in this layer is not zero. Different from the compact layer, the ions

in the diffuse layer are mobile. The boundary between the compact layer and the diffuse layer is called the shear plane. The electrical potential on this plane is measurable, which is called zeta potential (ζ) [67].

The electrical potential distribution in the diffuse layer ψ for symmetric electrolyte solution can be obtained by calculating the well-known Poisson-Boltzmann equation:

$$\nabla^2\psi = \frac{2n_\infty ze}{\varepsilon_0\varepsilon_w} sinh(\frac{ze\psi}{k_bT}) \tag{2-3}$$

where n_∞ is the ionic concentration of the aqueous solution, z is the absolute value of the ionic valence, e is the elementary charge, k_b is the Boltzmann constant, T is the absolute temperature, ε_0 and ε_w are the permittivity of vacuum and the solution, respectively.

Inside of the EDL region, due to the difference between the concentration of the counter-ions and that of the co-ions, the net charge density (ρ_e) is not zero, which is related to the local electrical potential:

$$\rho_e = -2n_\infty zesinh(\frac{ze\psi}{k_bT}) \tag{2-4}$$

The diffuse layer is very thin, generally, the Debye length (λ_D) is regarded as the length scale of the diffuse layer, which can be obtained:

$$\lambda_D = \kappa^{-1} = \sqrt{\frac{\varepsilon_w\varepsilon_0K_bT}{2n_\infty(ze)^2}} \tag{2-5}$$

where κ is the Debye-Hückel parameter. It is clearly shown in Equation (2-5) that the thickness of the EDL decreases when the ionic concentration of the bulk liquid (n_∞) increases. This can be understood like this. When n_∞ increases, more counter-ions in the bulk liquid are attracted to get close to the charged surface to neutralize the surface charges; therefore, the EDL get compressed at equilibrium state.

The surface charge density on the charged surface can be calculated by considering the balance between the surface charges and the charges in the EDL. For a flat surface, the surface charge density σ_s in terms of the zeta potential ζ is:

$$\sigma_s = \frac{4n_\infty ze}{\kappa} sinh(\frac{ze\zeta}{2K_bT}) \quad (2\text{-}6)$$

Using the Debye-Hückle linear approximation, the above equation can be reduced to [68]:

$$\sigma_s = \frac{2n_\infty (ze)^2}{\kappa K_bT} \zeta \quad (2\text{-}7)$$

For a sphere that its size is much larger than the thickness of EDL, the curved surface can be approximated as a flat surface. Therefore, the Equation (2-7) is also suitable for evaluating the surface charge density on a curved surface.

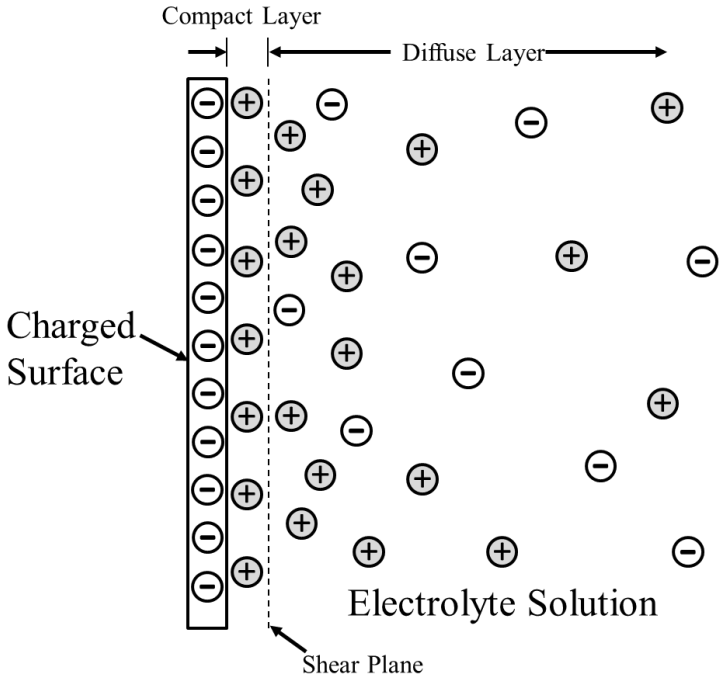

Figure 2-6. Schematic diagram of the charge distribution in electric double layer (EDL) near a flat charged surface.

2.2.2 Electroosmosis

Electroosmosis is the motion of the liquid near a charged surface in response to the externally applied electrical field. As illustrated above, when a surface is immersed into a bulk electrolyte solution, EDL forms in vicinity of it. Due to the effect of the surface charges on the surface, the counter-ions and co-ions distribute non-uniformly in the diffuse layer and the local ionic

concentration of the counter-ions is larger than that of the co-ions. Let's assume the surface carry negative charges. The number of positive ions should be larger than that of negative ions in EDL region. Under externally applied electric field, the excess positive ions in the diffuse layer moves from the anode to the cathode. Due to the viscosity of the liquid, the fluid flow can be generated with the motion of the ions.

Electroosmosis is a very important technique to drive the motion of liquid in microchannels. When the aqueous solution is injected into a microchannel, EDL forms on the channel walls. Therefore, under electrical field, the electroosmotic flow can be generated. As the thickness of EDL is very thin, the electroosmotic flow inside of a microchannel exhibits a plug-like velocity profile (as shown in Figure 2-7). For incompressible electrolyte solution, the electroosmotic flow field can be described with the Navier-Stokes equation and the continuity equation:

$$\rho_w \left[\frac{\partial \vec{u}_w}{\partial t} + \vec{u}_w \cdot \nabla \vec{u}_w\right] = -\nabla P + \eta_w \nabla^2 \vec{u}_w + \vec{F}_e \tag{2-8}$$

$$\nabla \cdot \vec{u}_w = 0 \tag{2-9}$$

where ρ_w and η_w are the density and viscosity of the liquid, respectively. ∇P is the pressure gradient, and $\vec{F}_e$ is the body force which is cause by the interaction between the electric field and the net charges in the liquid:

$$\vec{F}_e = \vec{E}_o \rho_e \tag{2-10}$$

$\vec{E}_o$ is the local electrical field. ρ_e is the local net charge density in the aqueous electrolyte solution, which is equal to zero in the outside EDL region .

As the thickness of the EDL very thin comparing with the width of the microchannel, the fluid flow inside EDL is always neglected when calculating the electroosmotic flow inside of a microchannel. Therefore, the body force term $\vec{F}_e$ in Equation (2-8) is deleted, and a slip boundary condition is given to the channel wall. The slip velocity on the channel wall can be calculated with the Helmholtz-Smoluchowski Equation:

$$\vec{U}_{eof} = -\frac{\varepsilon_w \varepsilon_0 \zeta_w}{\eta_w} \vec{E} \tag{2-11}$$

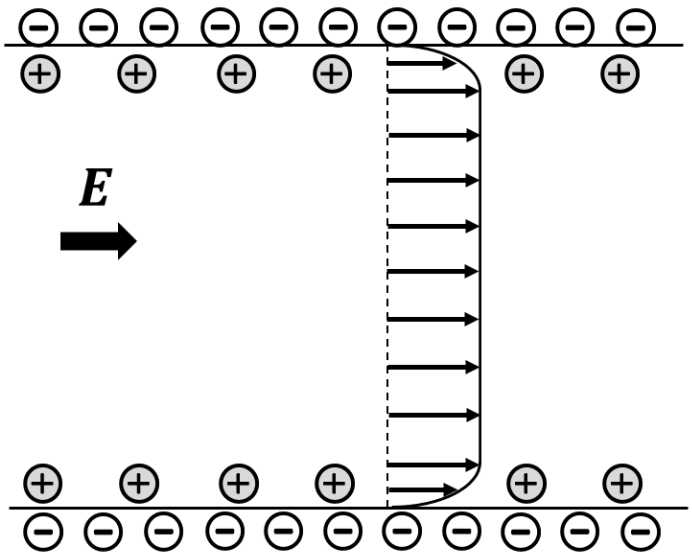

Figure 2-7. Schematic of the electroosmotic flow.

2.2.3 Electrophoresis

The motion of the charged particle in bulk stationary liquid under electric field is called electrophoresis. The moving direction of the particle is determined by the sign of the surface charges on it. Generally, for a negatively charged particle, it moves towards the anode of the electric field. The electrophoretic velocity of a solid particle can be calculated by balancing the electrostatic force ($\vec{F}_e$) acting on the particle and the flow friction force ($\vec{F}_f$). As shown in Figure 2-8(a), for a charged particle with the radius of a, under the condition of thin EDL ($\kappa a \to \infty$), the electrophoretic velocity is obtained:

$$\vec{U}_{ep} = \frac{\varepsilon_w \varepsilon_0 \zeta_p}{\eta_w} \vec{E} \tag{2-12}$$

ζ_p is the zeta potential of the particle, η_w is the viscosity of the surround liquid. As shown in Equation (2-12), the electrophoretic velocity of the charged particle is linear proportional to the strength of the externally applied electrical field.

For the particle in the limit of thick EDL ($\kappa a \to 0$), the electrophoretic retardation effect is non-negligible. The Hückel's equation is applicable for calculating the electrophoretic velocity:

$$\vec{U}_{ep} = \frac{2}{3}\frac{\varepsilon_w \varepsilon_0 \zeta_p}{\eta_w}\vec{E} \tag{2-13}$$

Compared with Equation (2-12), the constant factor of $2/3$ was added into the Hückel's equation to reflect the retardation effect.

A more general equation for calculating the electrophoretic velocity of particles with arbitrary EDL thickness is known as Henry's equation:

$$\vec{U}_{ep} = \frac{\varepsilon_w \varepsilon_0 \zeta_p}{\eta_w}\vec{E} f(\kappa a) \tag{2-14}$$

where $f(\kappa a)$ is the Henry's factor. The specific expression of the Henry's factor is complicated and hard to implement. Therefore, for simplicity, Ohshima [69] derived an approximate expression for this factor:

$$f(\kappa a) = \frac{2}{3} + \frac{1}{3[1+\frac{2.55}{\kappa a(1+\exp(-\kappa a))}]^3} \tag{2-15}$$

Reviewing Equation (2-15), for $\kappa a \to 0$ (thick EDL), $f(\kappa a) = 2/3$, and the Henry's equation becomes Hückel's equation. For $\kappa a \to \infty$ (thin EDL), $f(\kappa a) = 1$, then Henry's equation trends to the Helmholtz-Smoluchowski Equation.

Under externally applied electric field, the motion of a charged particle in a microchannel occurs. (see Figure 2-8(b)). The electrokinetic motion of the particles results from both the EOF of the liquid in the microchannel and the EP of the particle. For small particle with a size negligible compared with the microchannel moving in the center line of the microchannel, the electrokinetic velocity of it is expressed as:

$$\vec{U}_{ek} = -\frac{\varepsilon_w \varepsilon_0 (\zeta_w - \zeta_p)}{\eta_w}\vec{E} \tag{2-16}$$

where ζ_w and ζ_p are the zeta potentials of the microchannel wall and the particle, respectively. As shown in this equation, the electrokinetic velocity of the particle depends on the zeta potentials of

the microchannel wall and the particle. The expression is derived under thin EDL assumption and by neglecting the retardation effect and particle polarization.

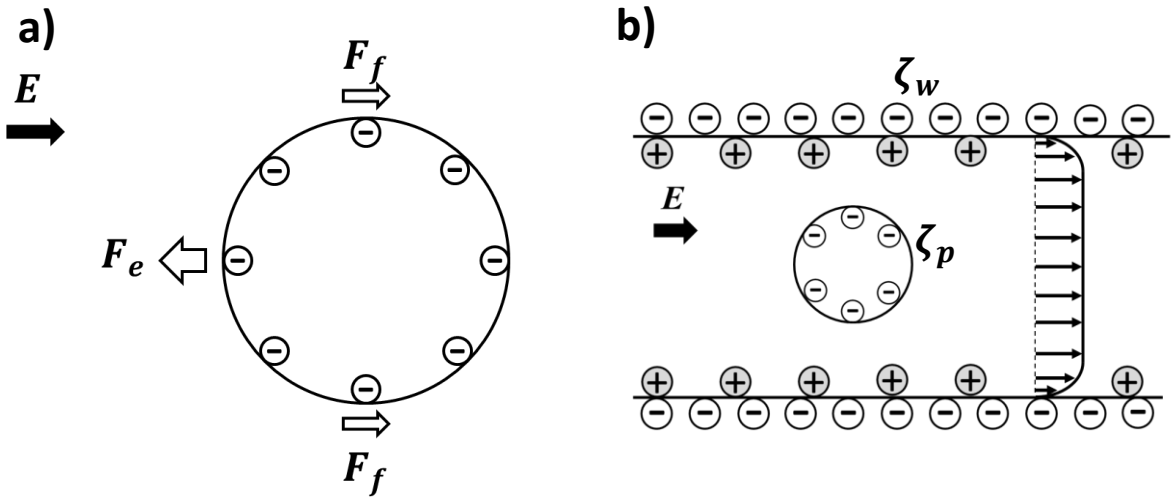

Figure 2-8. Schematics of the electrophoresis of a charged particle in a bulk liquid (a) and the electrokinetic motion of a charged particle in a microchannel (b).

For a particle with size comparable to the channel or a particle moving close to the microchannel wall, the electric field gets distorted with the presence of the particle, which in turn affects the electrokinetic motion of it. In this case, the electrokinetic motion of the particle is very complicated due to the combined hydrodynamic and electrokinetic effects [66]. The electrokinetic velocity is affected by the size of the microchannel and the particle, the zeta potentials of the microchannel wall and the particle, and the separation distance between the particle and the microchannel wall. Generally, with the reduction of the separation distance between particle and channel wall, the viscous retardation becomes significant; hence, the electrokinetic mobility (the ratio between the electrokinetic velocity and the electric field strength) decrease. However, with the further decrease of the separation distance, the electric field in the small gap between microchannel and particle becomes stronger, and the electric force is dominated compared with the viscous retardation. As a result, the electrokinetic velocity increases with the decrease of the separation distance [70–78].

2.2.4 Dielectrophoresis

Dielectrophoresis (DEP) is the motion of a dielectric particle under non-uniform electric field. For a polarizable particle under electric field, surface charges with opposite signs are induced and accumulate to two ends of the particle, respectively. The orientation of the electric field induced dipole is dependent on the relative polarizability of the medium and the particle, which can be characterized with the Clausius-Mossotti (CM) factor. Generally, the charges trend to accumulate to the side with high polarizability. Since the electric field applied to the dipole is non-uniform, the electric forces acting on its two poles are different, which drive the particle to move. The DEP force acting on a sphere ($\vec{F}_{DEP}$) can be derived with the point-dipole method [79] and the Maxwell-stress tensor (MST) formulation [80], the expression of which is obtained as:

$$\vec{F}_{DEP} = 2\pi\varepsilon_w\varepsilon_0 f_{CM} a^3 \nabla\left|\vec{E}\right|^2 \tag{2-17}$$

where ε_0 and ε_w are the dielectric permittivity of vacuum and the electrolyte solution, respectively. a is the radius of the sphere and E is the electrical field. f_{CM} is the Clausius-Mossotti (CM) factor:

$$f_{CM} = \frac{\tilde{\varepsilon}_p - \tilde{\varepsilon}_w}{\tilde{\varepsilon}_p + 2\tilde{\varepsilon}_w} \tag{2-18}$$

where $\tilde{\varepsilon}_p$ and $\tilde{\varepsilon}_w$ are the complex permittivity of the sphere and the surrounding liquid, which are defined as:

$$\tilde{\varepsilon}_p = \varepsilon_p\varepsilon_0 - i\left(\frac{\sigma_{c,p}}{\omega}\right) \tag{2-19}$$

$$\tilde{\varepsilon}_w = \varepsilon_w\varepsilon_0 - i\left(\frac{\sigma_{c,w}}{\omega}\right) \tag{2-20}$$

where ε_p is the dielectric permittivity of the sphere, $i = \sqrt{-1}$, $\sigma_{c,p}$ and $\sigma_{c,w}$ are the electrical conductivities of the sphere and the medium, respectively. ω is the angular frequency of the electric field with $\omega = 2\pi f$ (f is the frequency of the electrical field). If the CM factor is positive, the polarizability of the particle is larger than that of the medium, the particle moves towards the direction of the electric gradient, the DEP is positive-DEP. Reversely, if the CM factor is negative, the polarization of the medium is dominated and negative-DEP is induced that the particle moves in the opposite direction of the electric field gradient (see Figure 2-9).

Under DC electric field, the expression of CM factor is reduced to [81,82]:

$$f_{CM} = \frac{\sigma_{c,p} - \sigma_{c,w}}{\sigma_{c,p} + 2\sigma_{c,w}} \tag{2-21}$$

For the case of $\sigma_{c,p} \ll \sigma_{c,w}$ (dielectric particle in electrolyte), the CM factor is approaching to $(-1/2)$; therefore, the expression of DEP force can be simplified [83,84]:

$$\vec{F}_{DEP} = -\pi \varepsilon_w \varepsilon_0 a^3 \nabla \left|\vec{E}\right|^2 \tag{2-22}$$

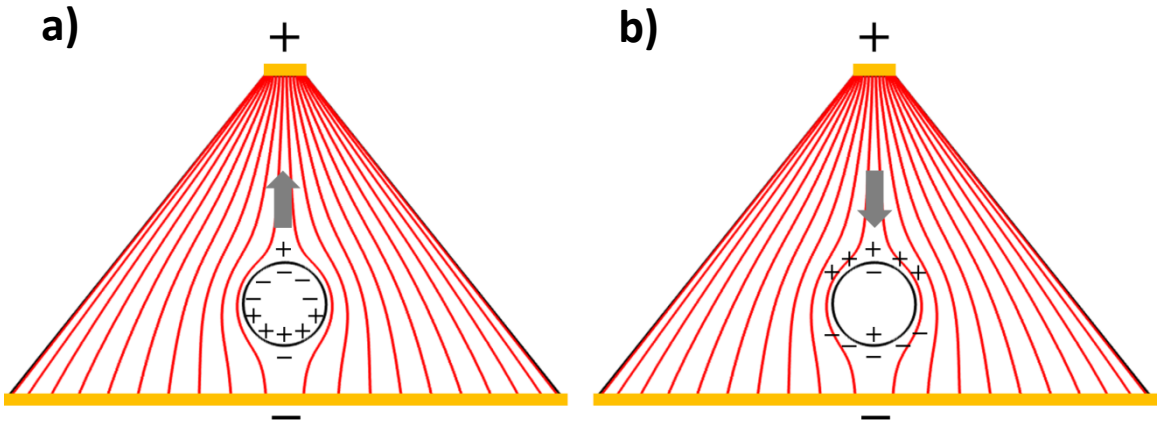

Figure 2-9. Schematic diagrams of the positive-DEP (a) and the negative-DEP (b).

2.2.5 Electrokinetic Phenomena of Janus Particles

As the development of the fabrication techniques, Janus particle with two sides possessing different properties has shown up. The electrokinetic phenomena of these heterogeneous particles are quite different from the homogeneous ones, which extend the classical electrokinetic theory. The electrokinetic motion of Janus particles in bulk liquid and microchannel has been studied theoretically and experimentally, respectively.

Due to the limitation of the fabrication method, most studies of the electrokinetic phenomena of non-conducting Janus particles with non-uniform surface charge distribution limit in theoretical analysis [85–90]. For example, Anderson [85] theoretically studied the electrophoresis of a Janus

particle with non-uniform surface charge distribution under the assumption of thin EDL. By considering the force and torque balance, the analytical expressions of the translational and rotational velocities of the Janus particle was derived. Based on Anderson's theory, the electrophoretic mobility is determined by the particle's area-average zeta potential. Furthermore, as the surface charge of the Janus particle is nonuniformly distributed, a dipole moment exert on the Janus particle under externally applied electric field which leads to the rotation of the particle toward alignment with the electric field. The electrophoresis of non-spherical ellipsoidal Janus particles was studied by Fair and Anderson [86]. General formulas were derived to calculate the translational and rotational velocities of the ellipsoidal Janus particle. Hsieh and Keh [87,88] studied the boundary effect on the electrophoretic motions of spherical and cylindrical Janus particles. An analytical solution was obtained by them for the calculation of the transverse electrophoretic velocity of a circular cylinder next to a plane wall. The results indicate that the lengths of the cylindrical Janus particles have no effect on their electrophoretic velocities. The study of electrophoresis of a Janus spherical particle in a spherical cavity indicates that, with the presence of the cavity wall, the electrophoretic velocity is influenced by the following three factors: (a) the variation of the local electric field around the Janus particle; (b) the viscous retardation of the particle; (c) the complex EOF in vicinity of the particle. With numerical method, Hsu et al. [89] studied the electrophoresis of Janus particles with arbitrary double layer thickness. For the Janus particles with thick EDL, the double-layer polarization (DLP) effect becomes significant, which leads to the reduction of electrophoresis of the Janus particles. Qian et al. [90] studied the electrokinetic motion of a Janus nanoparticle in a nanotube numerically. A multi-ion mass transport model was built up to take account of the EDL distortion and the EDL polarization effects. The results indicated that electrokinetic motion of the Janus particle is highly dependent on its surface charge distribution.

In addition to non-conducting solid Janus particles, the electrophoresis of metal-dielectric Janus particles were also analyzed [91–97]. Squires et al. [94] theoretically studied the electrophoresis of a metal-dielectric Janus particle in bulk liquid under alternating current (AC). They found that under the effect of the induced-charge electroosmotic flow on the metal side, the Janus particle always moves towards its dielectric end. Later, Gangwal et al. [93] fabricated the metal-dielectric Janus particle with convective assembly method by depositing gold nanoparticles on one side of the dielectric particles. Through observing the electrophoretic motion of the Janus particle under

electric field, Squires' prediction [94], the metal-dielectric Janus particle always moves towards its dielectric end under AC electric field, was proved. Daghighi et al. [97] studied the electrophoresis of the metal-dielectric Janus particles under DC electric field. They found that the Janus particles move towards alignment with the electric field, and the interface between two distinct hemispheres is perpendicular to the direction of the electric field. The directions of electrophoresis of the Janus particles are forward or backward to the electric field, which are dependent on the orientation of the particles. As shown in Figure 2-10(a), after applying a rightward electric field, induced-charge electroosmosis (ICEO) can be generated on the metallic side and vortices show up around the Janus particle. Under the propulsion of the ICEO, the Janus particles with their conducting side facing the electric field moves toward the downstream, while the Janus particle aligned in the opposite direction moves toward the upstream. In a microchannel, the induced vortices around the Janus particle perform as "engines"; therefore, the electrophoretic velocity of Janus particle is larger than the other homogeneous particles (Figure 2-10(b)) [95–97]. Daghighi et al. [97] measured the electrokinetic velocity of nickel-polystyrene Janus particles under different electric field strengths in a microchannel and compared the velocity of the Janus particles with homogeneous dielectric particles. Due to the polarization limit of the conducting hemisphere of the Janus particle, the measured electrophoretic velocity of the particle changes nonlinearly with the electric field (Figure 2-10(c)).

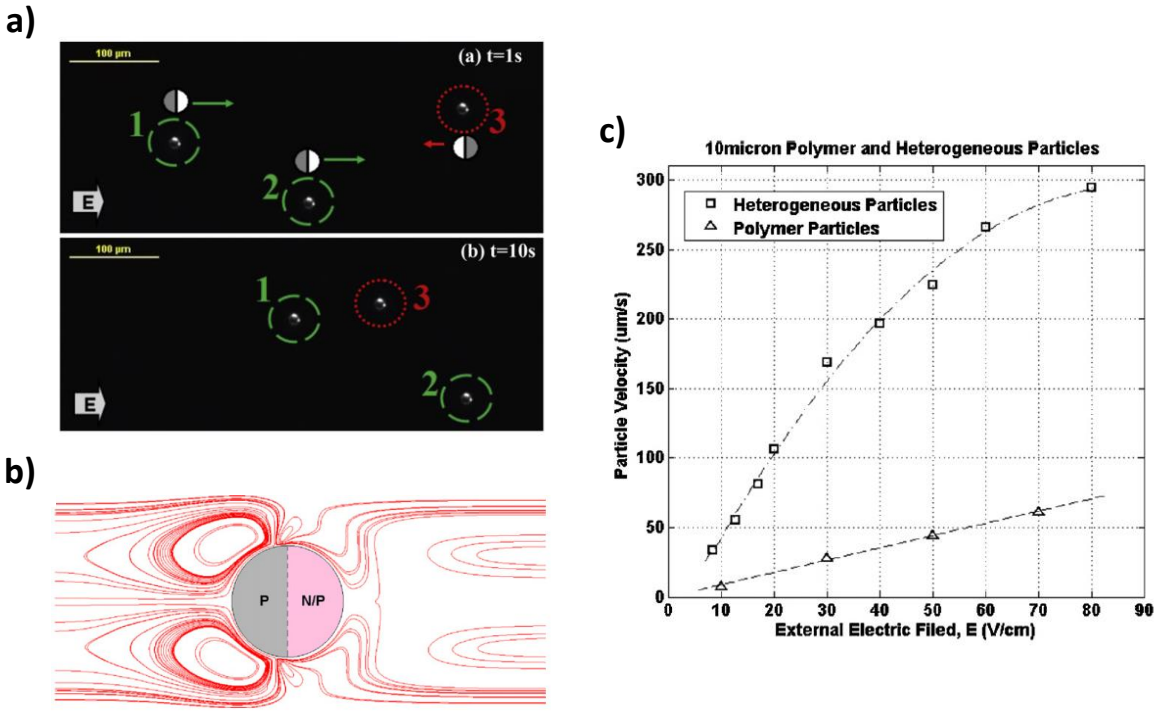

Figure 2-10. (a) Electrophoretic motion of the metallic-dielectric Janus particles under DC electric field. The strength of the electric field is 10 V/cm. The diameter of the Janus particles is 10 μm. Reproduced with permission [97]. Copyright 2012 Elsevier. (b) EOF field around the Janus particle. Reproduced with permission [95]. Copyright 2011 Elsevier. (c) The variation of the electrokinetic velocities of metallic-dielectric Janus particles and polymer particles with electric field. The diameter of the Janus particles and polymer particles is 10 μm. The dimension of the microchannel is 1.5 mm × 200 μm × 20 μm (Length × Width × Depth). Reproduced with permission [97]. Copyright 2012 Elsevier.

CHAPTER 3 Methods: Fabrication of Electrically Anisotropic Janus Droplets*

3.1 Introduction

Janus droplets and droplets with heterogeneous surface properties have potentials in many fields. For example, in material science, Janus droplets and heterogeneous capsules can be used to synthesize Janus and patchy particles [3,4,98,99], which have potentials in building up complex architectures through self-assembling [100–102], modifying liquid-liquid interface properties [6,103,104], detecting cells and molecules [105,106], and fabricating electronic paper [2,107]. In life sciences, Janus droplets and heterogeneous capsules can be used to generate self-propelled micro-motors to pick up, transport and drop-off cargoes (for example, drugs) [108–111]. However, as reviewed in section 2.1, the existing Janus droplets and droplets with heterogeneous surface fabrication techniques, such as high energy mixing method and microfluidic method, do have their limitations in fabricating electrically anisotropic Janus droplets.

In this chapter, we perform novel methods for preparing electrically induced sessile Janus droplets, suspended Janus droplets and droplets with multiple heterogeneous surface strips. The sessile Janus droplets were formed by partially covering the droplets with positively charged aluminum oxide nanoparticles under electric field. The effects of the concentration of nanoparticle suspension and the strength of the electric field on the nanoparticle coverage of the sessile Janus droplets were studied. The fabrication method of suspended Janus droplets includes two main steps. To begin, oil droplets were coated uniformly with positively charged nanoparticles by immersing emulsion droplets into aluminum oxide nanoparticle suspension. The suspended Janus droplets can be

---

* A similar version of this chapter was submitted or published as:

(a) Li, M.; Li, D. Redistribution of Charged Aluminum Nanoparticles on Oil Droplets in Water in Response to Applied Electric Field. *J. Nanopart. Res.* **2016**, 18, 120. https://link.springer.com/article/10.1007/s11051-016-3390-5

(b) Li, M.; Li, D. Fabrication and Electrokinetic Motion of Electrically Anisotropic Janus Droplets in Microchannels. *Electrophoresis* **2017**, 28, 287-295. https://onlinelibrary.wiley.com/doi/abs/10.1002/elps.201600310

(c) Li, M.; Li, D. Janus Droplets and Droplets with Multiple Heterogeneous Surface Strips Generated with Nanoparticles under Applied Electric Field. *J. Phys. Chem.* **2018**, 122, 8461-8472. https://pubs.acs.org/doi/abs/10.1021/acs.jpcc.8b01920

formed when the nanoparticles accumulated to one side of the Janus droplets in response to externally applied DC electric field. The variation of the nanoparticle coverage of the Janus droplets in terms of the nanoparticle suspension and the electric field strength were studied, respectively. In the fabrication of droplets with multiple heterogeneous surface strips, different nanoparticles were delivered to the oil droplets in turn. To control the delivery of nanoparticles to the oil droplets, a microfluidic chip was introduced in the fabrication process. By controlling the delivery of nanoparticles in the microfluidic chip under electric field, different nanoparticles accumulated on the droplet surface and the desired Janus droplets and droplets with heterogeneous strips were formed.

3.2 Materials and Methods

3.2.1 Fabrication of Sessile Electrically Induced Janus Droplets

Aluminum oxide nanoparticles (US Research Nanomaterials, Inc., Houston, TX, USA) with an average diameter of 5 nm were used. The zeta potential of these particles is positive from pH 2.5 to pH 8 [112], which means that these particles carry positive charges when contacting with deionized water. In this study, two different concentrations of alumina nanoparticle suspensions, 20mg/mL and 50mg/mL, were used in the experiments. A three-step procedure was used to disperse the aluminum oxide nanoparticles into deionized water: a) First, 20mg or 50mg nanoparticles were added into 1mL deionized water in a beaker. b) Then the nanoparticles were dispersed by placing the beaker into an ultrasonic cleaner for 8 minutes. c) Finally, 20μL ethanol was added into the nanoparticle suspension. The ethanol acts as an inducer, which can make sure enough nanoparticles are trapped at the oil-water interface [113,114].

Mineral oil was used to generate oil droplets. In order to observe the redistribution of the nanoparticles on the droplet in response to the applied electrical field, it is desirable to avoid the unwanted effects of the droplet motion; therefore, the oil droplets were anchored onto a solid surface as sessile drops. To form a sessile oil droplet immersed in deionized water, a plastic petri dish and a piece of cover glass slide were used, and the procedures are as follows: a) Pour deionized water into the petri dish and make the water level is around 5 mm from the bottom; b) Put the cover glass slide on the surface of water, due to the surface tension, the cover glass slide floats on water surface without sinking; c) Deposit a drop of the mineral oil on the floating cover glass slide;

d) Push the glass slide into water. As the oil droplet has already attached on the surface of the glass, it will not detach and float; a sessile drop of oil in water is formed in this way. As shown in Figure 3-1(a), the contact angle of water of the sessile oil droplet system is 45° (on the water side) and remains unchanged before and after applying electric field, which was measured with a side view microscope (Nikon, SMZ800).

The experimental system used in this study is shown in Figure 3-1(b). It consists of a microscope and image system, a DC power supply and a petri dish. In the experiment, the petri dish which holds deionized water and oil droplet was fixed on the stage of the microscope (Ti-E, Nikon, Japan). The DC power supplier (CSI12001X, Circuit Specialist Inc., USA) was used to apply the electrical field via the electrodes. The Nikon Ti-E microscope was used to monitor the redistribution of nanoparticles on oil droplets. The images were captured by a digital camera (DS-Qi1Mc ,Nikon) and sent to a computer to be displayed and saved.

Once the oil droplet is formed in water, as described above, the aluminum oxide nanoparticles are deposited onto the droplet surface by releasing a certain amount of the nanoparticle suspension over it with a digital micro-pipette. As the aluminum oxide nanoparticles carry positive charges, they will adhere at the negatively charged oil-water interface, forming a uniform coverage on the droplet surface. However, due to the inter-particle cohesion forces, the nanoparticles aggregate and form small clusters uniformly distributed over the oil droplet surface. When a DC electric field is applied to the droplet, the positively charged particles on the droplet surface will be forced to move and accumulate to one side of the oil droplet. A Janus droplet partially covered with aluminum oxide nanoparticles is formed in this way. The total amount of nanoparticles adhering on the oil droplet surface can be adjusted by varying the concentration of the nanoparticle suspension. All of the experiments in this study were conducted at room temperature (23-25℃).

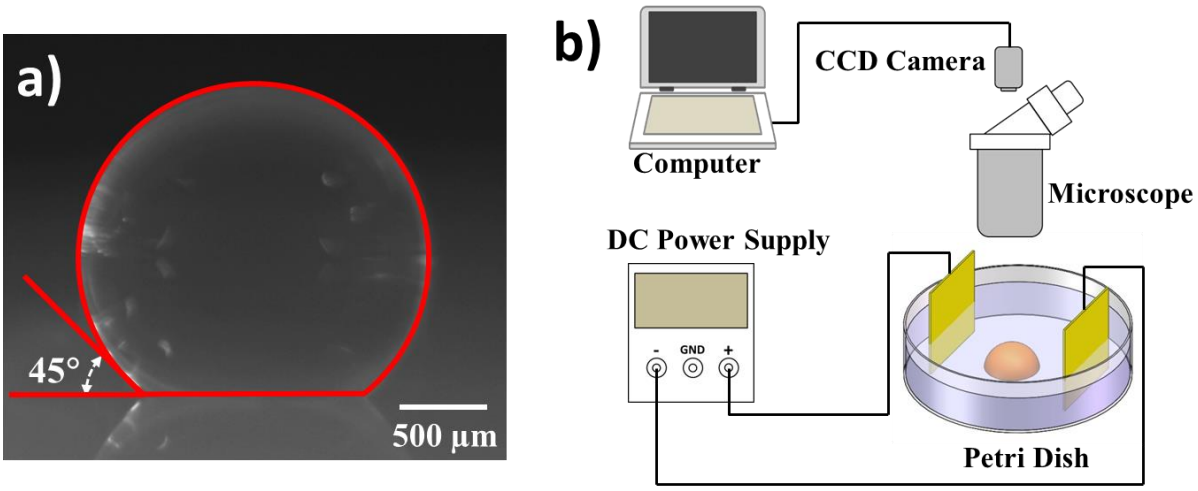

Figure 3-1. (a) Side view image of a sessile oil droplet with a diameter of 1.9 mm on a glass surface immersed in deionized water. (b) Schematic diagram of the experimental system in fabricating sessile Janus droplets.

3.2.2 Fabrication of Suspended Electrically Induced Janus Droplets

3.2.2.1 Materials

Aluminum oxide passivated aluminum nanoparticles with the mean diameter of 18nm were provided by US Research Nanomaterials, Inc., USA. The thickness of the aluminum oxide shell wrapping the aluminum core was 2~5nm. Tween 20 (nonionic surfactant, impurities ≤ 3.0%) was purchased from Sigma-Aldrich which was used without further treatment. The oil was vegetable oil (pure canola oil from Mazola Corporation) with the density of 918.7kg/m^3. Solid potassium chloride (KCl) of 99% purity was purchased from Sigma-Aldrich. Deionized water was obtained from a Milli-Q reagent water system. The resistance of the deionized water was 18.2MΩ·cm at 25℃.

3.2.2.2 Preparation of Pickering Emulsion

Method A

Aluminum oxide nanoparticles and nonionic surfactant (Tween 20) were used as stabilizers to prepare oil-in-water Pickering emulsion. First, aluminum oxide nanoparticles were dispersed into deionized water using an ultrasonic cleaner (Cody Technology Limited Co., China) in the following way: a) Put certain amount of aluminum oxide nanoparticles into a glass bottle with a volume of 15mL (21mm (*d*) × 70mm (*h*)); b) Add deionized water (5mL) into the bottle followed by ultrasonic treatment for 8min. After the generation of nanoparticle suspension, put 100μL Tween 20 and 1mL oil into the bottle. Emulsification could be made by vibrating the mixture with a vortexer (VWR Scientific) at the speed of 3200rpm for 2min. The nonionic surfactant served as emulsifier to speed up emulsification and stabilize emulsion without changing the electrical property of the oil-water interface. As the zeta potential of aluminum oxide nanoparticles was positive from pH 2.5 to pH 8, they adhered on the negatively charged oil droplets automatically and Pickering emulsion formed finally (Figure 3-2(a)). Let the emulsion stand for 48 hours, the extra nanoparticles in the water phase would sink to the bottom of the bottle and separate from the droplets by gravity.

Method B

Apart from the method shown above, the Pickering emulsion droplets can also be prepared by adding suspended oil droplets into the nanoparticles suspension. The oil-in-water emulsion droplets were prepared by vibrating the mixture of 5 mL deionized water, 1 mL canola oil (Mazola Corporation) and 100 μL Tween 20 with a vortexer (VWR International, Canada) at its highest speed of 3200 rpm for 2 min. After this, 500 μL emulsion droplets were sucked from the top layer of the oil-water emulsion carefully with a digital pipette, and added into the nanoparticle suspension. Then, the mixture was vibrated with the lab dancer for 2 min at medium speed (approximately 1600 rpm). The vibration process is essential for making the oil droplets uniformly coated with nanoparticles. After this, leave the emulsion standing for one day to separate the Pickering emulsion droplets and extra nanoparticles in water through gravity. The droplets floated to the top to form a black layer while the nanoparticles sank to the bottom.

3.2.2.3 Formation of Janus Droplets

The EIJDs can be formed easily by applying direct current electric field to the Al_2O_3 nanoparticle-stabilized Pickering emulsion droplets. As shown in Figure 3-2(a), after applying an electric field,

the nanoparticles attaching on the droplet surface move and accumulate to one side of the droplet. Because of the accumulation of the nanoparticles, the nanoparticle film forms on the oil droplet while leaving the other side without the presence of nanoparticle. In this study, as the positively charged alumina nanoparticles were employed, the EIJD therefore has one side with a positively charged nanoparticle film and another side with a negatively charged oil-water interface in deionized water. The microscopic image of an EIJD is shown in Figure 3-2(b). The dark region is coated with the nanoparticle film.

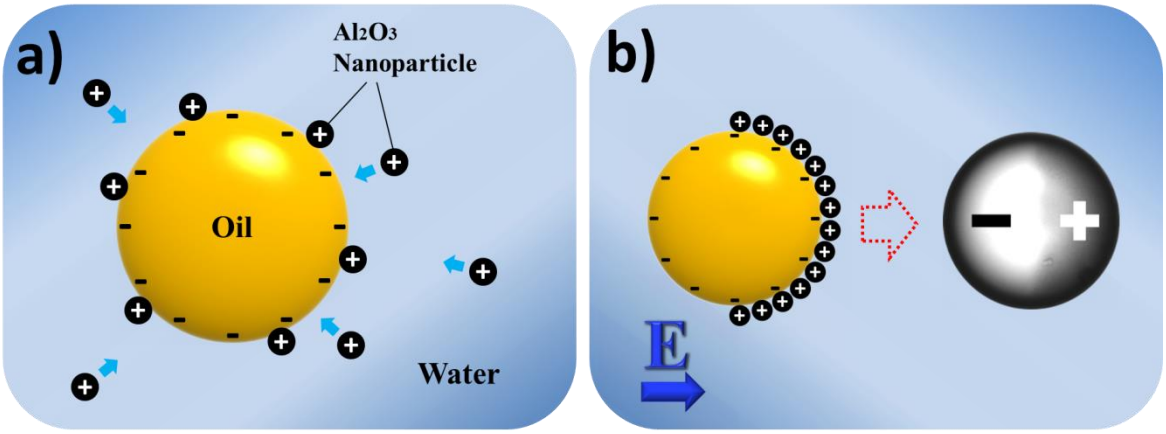

Figure 3-2. (a) Schematic diagram of the formation of Al_2O_3-nanoparticle-stabilized Pickering emulsion. (b) Schematic diagram of the fabrication process of EIJDs under electrical field.

3.2.2.4 Calculation of Nanoparticle Coverage

The nanoparticle coverage of suspended EIJDs can be calculated under a bright-field microscope (Nikon Ti-E) with the assistance of imaging analysis software. The nanoparticle coverage variation of EIJDs was monitored by the microscope, and the images were recorded and sent to the compute by a charge-coupled device (CCD) camera. Under a bright-field microscope, the nanoparticle coated side of the EIJDs is black, while the other side without the presence of nanoparticle indicates as white. The two segments of EIJDs can be distinguished easily from the recorded images. By using imaging analysis software, the angle between two edge lines of the nanoparticle

film (θ) can be measured; hence, the nanoparticle coverage of EIJDs (γ) can be calculated with following equation:

$$\gamma = \frac{1-\cos(\theta/2)}{2} \quad (3\text{-}1)$$

3.2.3 Fabrication of Janus Droplets and Droplets with Multiple Heterogeneous Nanoparticle Strips in Microchannels

3.2.3.1 Fabrication Mechanism

A simple approach for fabricating Janus droplets and droplets with homogeneous and heterogeneous coatings of nanoparticles in a crossing microchannel was developed. As shown in Figure 3-3(a), two different nanoparticle suspensions, nanoparticle A and B, are driven through the two inlet channels, and the DC electric field is applied along the central channel and the main channel. An oil droplet is anchored in the main channel which serves as the substrate for adhering nanoparticles. When nanoparticles flow through the main channel, they adsorb on the droplet surface and are assembled under electric field. By controlling the delivery of the two nanoparticle suspensions, droplets with one hemisphere coated with a nanoparticle film (Figure 3-3(b) and 3-3(c)), with a homogeneous nanoparticle film (Figure 3-3(d)), with two different nanoparticle films on the two hemispheres (Figure 3-3(e)), and with multiple strips of different nanoparticles (Figure 3-3(f)), can be fabricated easily. These Janus droplets and droplets with heterogeneous surface strips possess specific electrokinetic properties.

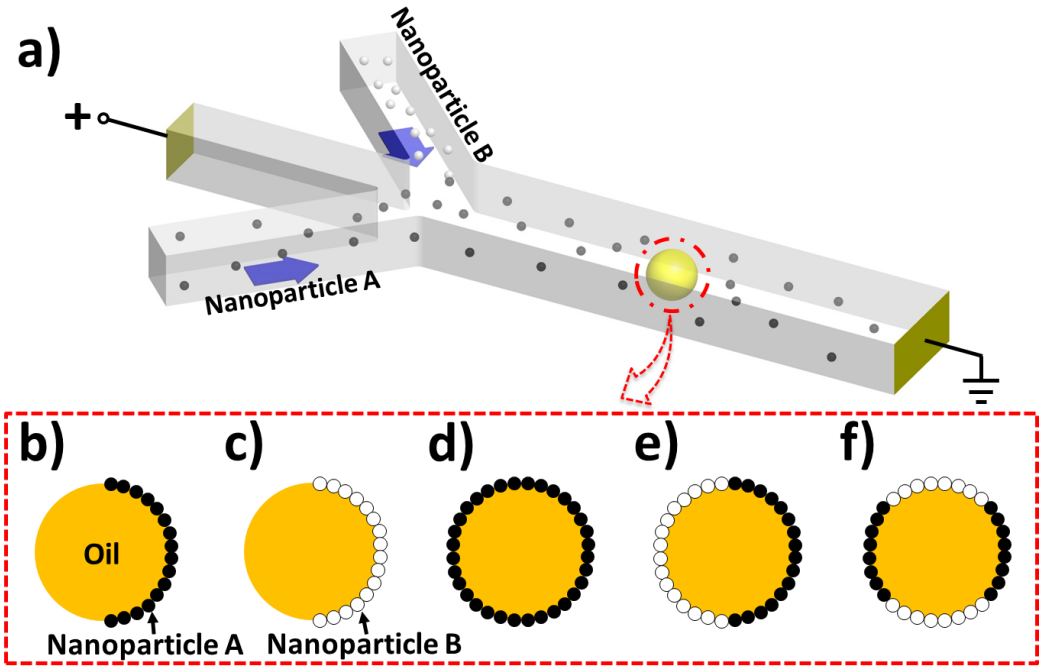

Figure 3-3. Schematic diagrams: (a) the fabrication of Janus droplets with nanoparticles in a microchannel; (b) Janus droplet fabricated with nanoparticle A; (c) Janus droplet fabricated with nanoparticle B; (d) homogeneously coated droplet with nanoparticle A; (e) Janus droplet with two hemispheres consisting of different nanoparticles; (f) droplet with multiple strips of different nanoparticles.

3.2.3.2 Fabrication of Microfluidic Chip

The microfluidic chip was prepared by combining a top PDMS (polydimethylsiloxane) layer to a VWR® glass substrate. The PDMS layer contains the microchannel structure, which was prepared by traditional soft lithography method. Briefly, after the processes of spin-coating, soft bake, ultraviolet (UV) light exposure, post exposure bake and development, a master with raised features was fabricated. Then, pour degassed PDMS-curing agent mixture (10:1, w/w, Sylgard 184, Dow Corning) onto the master, and the PDMS layer formed in a curing process. A permanent bond between the PDMS layer and the substrate was created after plasma treatment (HARRICK PLASMA, Ithaca, NY, USA).

In order to fabricate Janus droplets and droplets with multiple heterogeneous strips, a cross microchannel was designed, as shown in Figure 3-4(a). The cross microchannel consists of three inlet branches and a main channel. The main channel is 1 cm in length and 500 μm in width, and the size of the three inlet branches is 1 cm × 250 μm (length × width). A circular confinement chamber with a diameter of 8 mm is connected to the central inlet branch, which is used to hold the oil droplet. At the rear end of the confinement chamber, a 1.5 mm-in-diameter electrode insert port is punched for placing the electrode. To anchor the droplet, a pair of circular pillars is designed in the middle of the main channel (labelled with red rectangle in Figure 3-4(a)). The diameter of the pillars is 25 μm and the distance between them (from center to center) is 60 μm. The microchannel has uniform height of 80 μm.

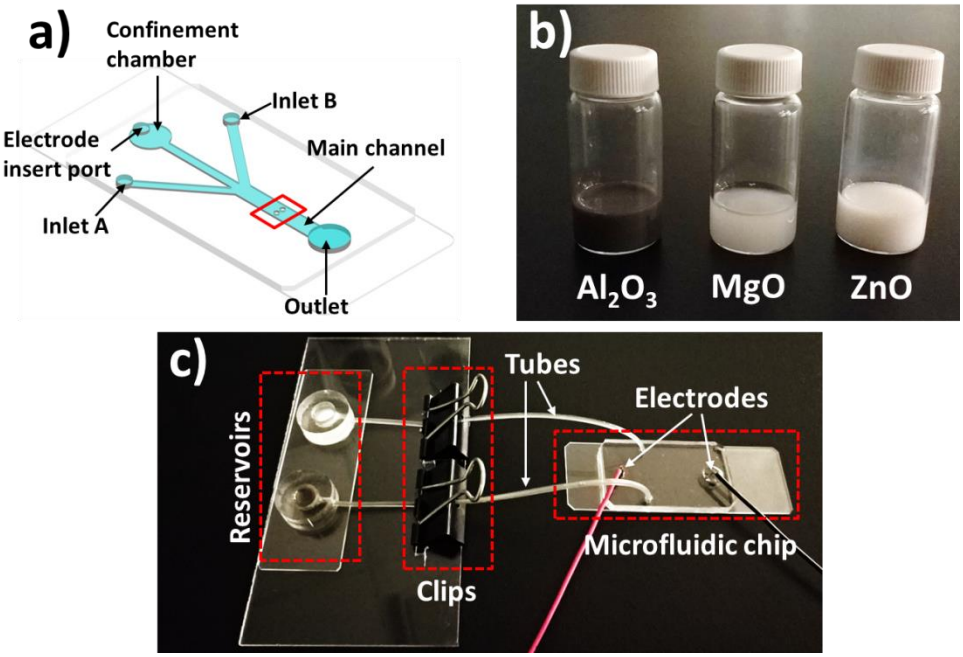

Figure 3-4. (a) Schematic of the microfluidic chip for Janus droplet fabrication. (b) Photograph of the nanoparticle suspensions: Al_2O_3, MgO and ZnO (from left to right). (c) Photograph of the fabrication system.

3.2.3.3 Preparation of Nanoparticle Suspensions

The Al_2O_3, MgO and ZnO nanoparticle suspensions were prepared through ultrasonic treatment by following the subsequent steps: i) weight certain amount of nanoparticles into a glass vial with a volume of 15 mL; ii) add 5 mL deionized water (18 MΩ·cm, Milli-Q) and 100 μL nonionic surfactant, Tween 20 (impurities ≤ 3.0%, Sigma-Aldrich), into the vial with digital pipettes (Eppendorf, Germany); iii) use ultrasonic wave to treat the mixture for 8 minute to disperse the nanoparticles (Cody Technology Limited Co., China). As shown in Figure 3-4(b), by this method, the Al_2O_3, MgO and ZnO nanoparticle suspensions with the concentrations of 6 mg/mL, 10 mg/mL and 10 mg/mL were produced, respectively. The Al_2O_3, MgO and ZnO nanoparticles were provided by US Research Nanomaterials Inc. with the mean diameters of 18 nm (for Al_2O_3) and 10 nm (for MgO and ZnO), respectively.

3.2.3.4 Preparation of Sessile and Suspended Oil Droplets

The sessile droplet in a microchannel can be prepared with the following steps: i) attach a tiny piece of Duck® tape onto the glass substrate; ii) after plasma treatment, peel off the tap and drop canola oil (Mazola Corporation) onto the glass substrate; iii) align the microchannel on the PDMS layer to the oil droplet under the Nikon Ti-E microscope (Nikon, Japan) and push the PDMS layer and the glass substrate together; iv) after filling the microchannel with deionized water, the sessile oil-in-water droplet is formed inside of a microchannel.

The suspended oil-in-water emulsion droplets were prepared by vibrating the mixture of 5 mL deionized water, 1 mL canola oil (Mazola Corporation) and 100 μL Tween 20 with a vortexer (VWR International, Canada) at its highest speed of 3200 rpm for 2 min.

3.2.3.5 Fabrication of Sessile Janus Droplets and Droplets with Heterogeneous Strips

A simple experimental setup consisting of two liquid reservoirs, a microfluidic chip and a DC voltage source was built up to fabricate sessile Janus droplets and droplets with heterogeneous strips, as shown in Figure 3-4(c). The two reservoirs are used to hold different nanoparticle suspensions, and are connected to the two inlets of the microfluidic chip (inlet A and B, Figure 3-4(a)) through soft tubes. Binder clips are applied in the middle of the tubes, and the liquid motion

inside of the tubes can be controlled by opening or closing the clips. The DC voltage source composing of four serial DC power supplies (CSI12001X, Circuit Specialist Inc., USA) provides voltages to the microchannel through two platinum electrodes, and the strength of the electric field in the microchannel is adjusted by changing the DC voltage source output voltage.

To fabricate the sessile Janus droplets and droplets with heterogeneous strips, a sessile droplet was generated first in the main channel of the microfluidic chip by following the procedure described in the last section. Then, the soft tubes and electrodes were placed into the inlet wells, outlet wells and electrode insert port on the microfluidic chip, respectively; and an electric field of 150 V/cm was applied to the main channel. After opening the clip, the nanoparticle suspension was forced to move through the microchannel in response to the pressure difference of 110 Pa (controlled by the liquid levels) between the reservoirs and the outlet. As these positively charged metal oxide nanoparticles flew through the sessile oil droplet with negative surface charges, the nanoparticles attached on the surface on the droplet. These positively charged nanoparticles further moved and accumulated to the rear end of the droplet to form compact nanoparticle layer under the effect of electrical field. By adjusting the opening time of the two clips, the amount and the types of the nanoparticles packed on the surface of the droplet will change, and the droplets covered with one type of nanoparticle film, the Janus droplets partially covered with nanoparticles, and droplets covered with two or more strips of different nanoparticle films can be fabricated. During fabrication, the process was monitored under a Nikon Ti-E microscope.

3.2.3.6 Fabrication of Suspended Janus Droplets and Droplets with Heterogeneous Strips

Similar experimental setup as described above was employed to fabricate the suspended Janus droplets and suspended droplets with heterogeneous surface strips. The fabrication procedure includes: i) inject oil-in-water emulsion droplets into the main channel through the microchamber, and one of the oil droplets can be anchored by the two circular pillars in main channel; ii) apply electric field of 150 V/cm in main channel through electrodes inserted in the electrode insert port and outlet; iii) manipulate the clips to control the nanoparticles delivery and assembly on the oil droplet surface. By following this procedure, the suspended droplets with designed surface patterns can be fabricated.

3.3 Results and Discussion

3.3.1 Sessile Janus Droplets: Micro-size and Macro-sized Janus Droplets

By using the method described above, micro-sized Janus droplets and macro-sized Janus droplets can be made. An example of a micro-sized Janus droplet and an example of a macro-sized Janus droplet are shown in Figure 3-5, respectively. For the micro-sized droplet shown in Figure 3-5, it has a diameter of 67 μm and was covered with the nanoparticles by depositing 2.5 μL nanoparticle suspension with a concentration of 20 mg/mL over it. As shown in Figure 3-5(a), before applying electric field, the nanoparticles on the surface of the droplet were uniformly distributed. Then an electric field (E = 15 V/cm) was applied from left to right. Under the applied electric field, the positively charged nanoparticles moved along the direction of the electric field and accumulated to the right side of the oil droplet. The area with accumulated nanoparticles becomes constant after 30 seconds. A Janus droplet which was partially covered with nanoparticles was formed (Figure 3-5(b)). The position of the accumulation region of the nanoparticles depends on the direction of the electric field. As shown in Figure 3-5(c), when the electric field was reversed, i.e., from right to left, the nanoparticles moved and accumulated to the left hemisphere of the oil droplet, reaching the final state as shown in Figure 3-5(c).

The same phenomenon can also be observed for the macro-sized Janus droplets. Figure 3-5(d)-(f) show a droplet with a diameter of 1.1 mm. In this case, 12.5 μL 50 mg/mL nanoparticle suspension was deposited over 5 times near the top of the droplet to make sure enough nanoparticles adhered on the droplet. As seen from Figure 3-5(d), initially the particles distribute uniformly over the drop surface. Then an electric field of 25 V/cm was applied from left to right, the nanoparticles moved towards right and eventually reached a final state after 2 minutes (Figure 3-5(e)). Similarly, under the reversed electric field, the nanoparticles moved in the opposite direction and accumulated to the left hemisphere of the oil droplet (Figure 3-5(f)).

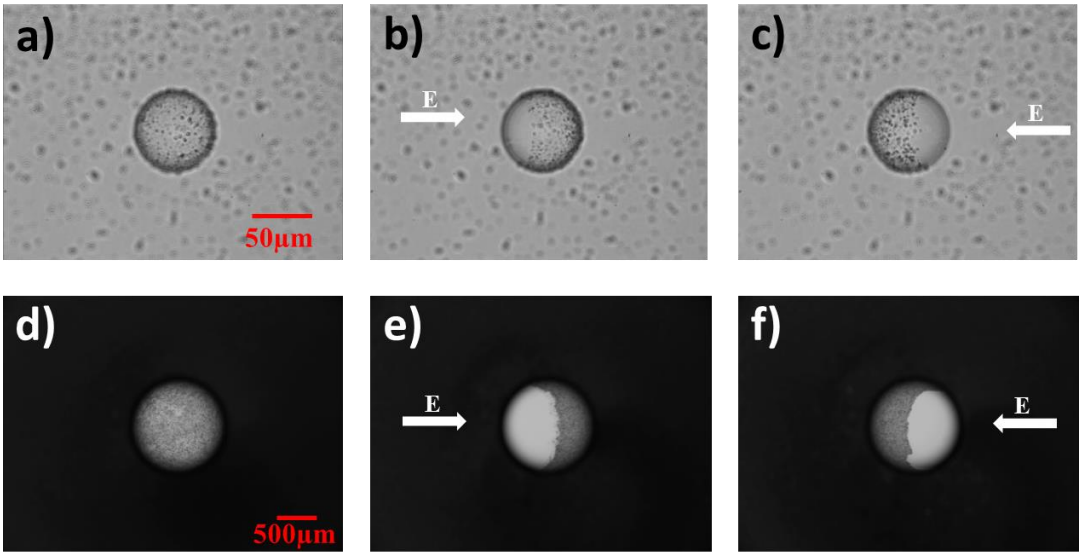

Figure 3-5. The formation of a micro-sized Janus oil droplet ((a)-(c)) and a macro-sized Janus droplet with a diameter of 1.1 mm ((d)-(f)) under externally applied electric field. (a) Before the electric field was applied, the nanoparticles were distributed uniformly on the surface of the oil droplet with a diameter of 67 μm. (b) The nanoparticles were accumulated to the right hemisphere of the oil droplet after the electric field from left to right was applied for approximately 30 seconds. (c) The nanoparticles were accumulated to the left hemisphere of the droplet under leftward electric field. The externally applied electric field was 15 V/cm, and 2.5 μL nanoparticle suspension with a concentration of 20 mg/mL was released over the oil droplet. (d) Before the electric field was applied, the nanoparticles distributed uniformly on the surface of the oil droplet. (e) The nanoparticles accumulated to the right hemisphere of the oil droplet after the electric field from left to right was applied for approximately 2 minutes. (f) After reversing the direction of the electric field, the nanoparticles accumulated to the left hemisphere. The externally applied electric field was 25 V/cm, and 12.5 μL nanoparticle suspension with a concentration of 50 mg/mL was released over the oil droplet.

The comparison of the fabrication of micro-sized Janus droplet and macro-sized Janus droplet clearly shows that the motion and accumulation of the nanoparticles in response to the applied electric field is the same for both micro-sized droplets and macro-sized droplets. However, it's relatively difficult to generate micro-sized droplets with accurately controlled size. Furthermore,

it is difficult to introduce the same amount of nanoparticles onto the surface of smaller micro-sized droplets. Therefore, macro-sized droplets were used to carry out the studies of the effects of the concentration of the nanoparticle suspension, the electric field and the size of the droplets on the topology of Janus droplets.

3.3.2 Sessile Janus Droplets: Effect of the Concentration of the Nanoparticle Suspension

To study the effect of the concentration of the nanoparticle suspension on the topology of Janus droplets, aluminum oxide nanoparticle suspensions with different concentrations, 20mg/mL and 50mg/mL, were used to cover the oil droplets, respectively. In these experiments, the diameter of the oil droplets (d =1.1 mm) and the applied electric field (E =25 V/cm, from left to right) were kept constant.

When the concentration of the suspension is 20 mg/mL, the redistribution of the positively charged aluminum nanoparticles under applied electric field is shown in Figure 3-6, as an example. Before the electric field was applied, $t = 0$, the nanoparticles on the surface of the oil droplet are distributed uniformly and motionless with the nanoparticle surface coverage ratio γ = 100%, as shown in Figure 3-6(a). After the electric field was applied from left to right, the positively charged particles moved in the same direction as that of the electric field and the coverage ratio decreases from 100% to 20.75% as time went by (Figure 3-6(b)~(e)). At the final state, all of the nanoparticles accumulated in a small area on the right side of the droplet, leaving a large "blank" oil-water interface behind, and a Janus droplet with γ = 20.75% was formed finally, as shown in Figure 3-6(f). The sequence of images in Figure 3-7 shows an example of the redistribution of nanoparticles on the oil droplet when the concentration of the nanoparticle suspension is 50 mg/mL. The similar phenomenon can be observed from the images in Figure 3-7. That is, the original uniformly-distributed nanoparticles moved and accumulated to the right side of the oil droplet in response to the externally applied electric field. The comparison of Figure 3-6(f) with Figure 3-7(f) indicates that when the concentration increases from 20 mg/mL to 50 mg/mL, at the finial state, the nanoparticle coverage ratio increases significantly from 20.75% to 50%. As the increase of the concentration of the nanoparticle suspension, the total amount of the nanoparticles adhering on the surface of the oil droplet increases. This can be seen by comparing the original states of the oil droplets as shown in Figure 3-6(a) and Figure 3-7(a). Obviously, the more nanoparticles at the oil-

water interface, the larger the final accumulation area. Therefore, the following conclusion can be drawn: the surface area of the Janus droplet that is covered with nanoparticles enlarges with the increase of the concentration of the nanoparticle suspension. Under this set of specific conditions, when the concentration of the nanoparticle suspension is 50 mg/mL, a Janus droplet whose whole right hemisphere is covered with aluminum nanoparticles (γ = 50%) can be obtained.

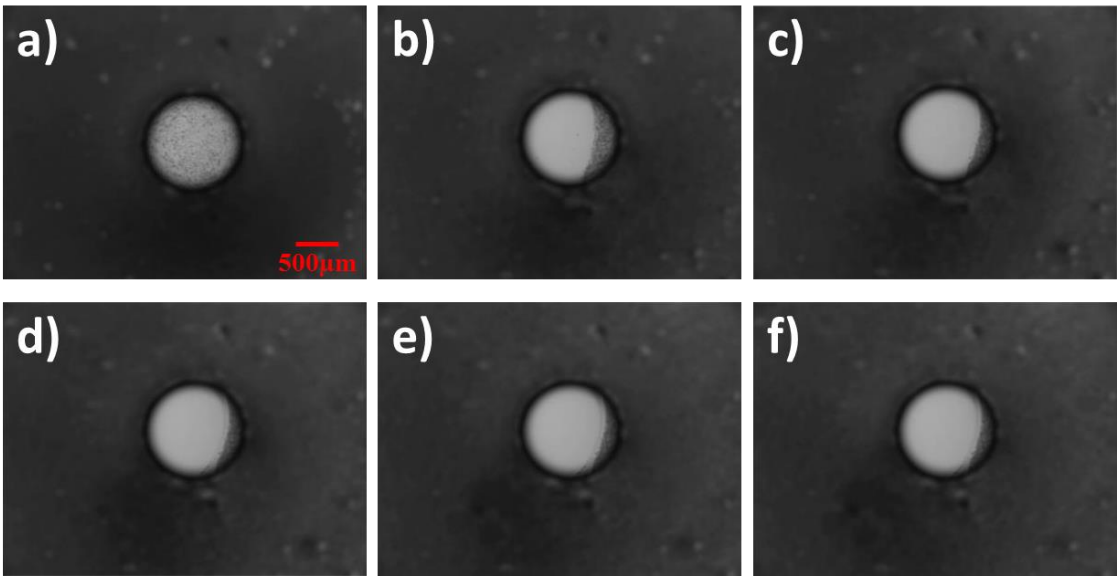

Figure 3-6. The redistribution of aluminum oxide nanoparticles on the surface of an oil drop of 1.1 mm in diameter under E = 25 V/cm at different time. 12.5 μL 20 mg/mL nanoparticle suspension was released over the oil droplet. Two minutes after applying electric field, nanoparticles reached the final state when the coverage ratio (γ) remained unchanged, γ = 20.75%. (a) t = 0 min, γ = 100%; (b) t = 1 min, γ = 31.96%; (c) t =2 min, γ = 20.75%; (d) t =3 min, γ = 20.75%; (e) t =4 min, γ = 20.75%; (f) t = 5 min, γ = 20.75%.

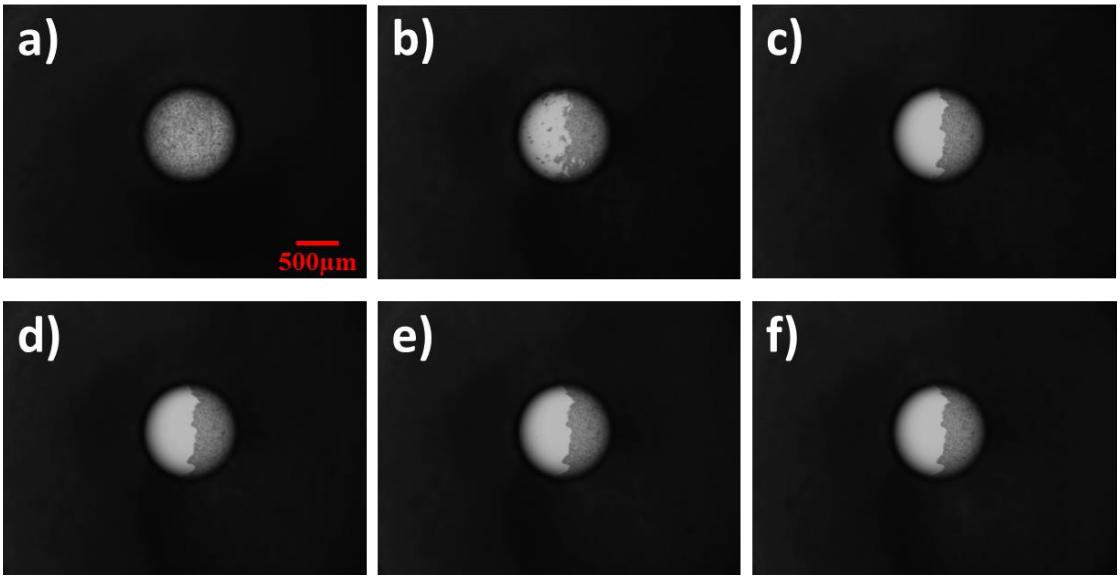

Figure 3-7. The redistribution of aluminum oxide nanoparticles on the surface of an oil drop of 1.1 mm in diameter under E = 25 V/cm at different time. 12.5 µL 50 mg/mL nanoparticle suspension was released over the oil droplet. Two minutes after applying electric field, nanoparticles reached the final state when the coverage ratio (γ) remained unchanged, γ = 50%. (a) t = 0 min, γ = 100%; (b) t = 1 min, γ > 50%; (c) t = 2 min, γ = 50%; (d) t = 3 min, γ = 50%; (e) t = 4 min, γ = 50%; (f) t = 5 min, γ = 50%.

3.3.3 Sessile Janus Droplets: Effect of the Applied Electric Field

The strength of the externally applied electric field is another factor that will affect the topology of Janus droplets. The effect of the applied electric field on the redistribution of nanoparticles on the surface of the oil droplet can be understood as follows. Under externally applied electrical field, the positively charged nanoparticles will be pushed by the external electrical field force and move to the side of the oil droplet facing the negative electrode. Once the nanoparticles get closer, they start to repel each other due to the electrostatic repulsive force between the particles. At final state, the two forces acting on the particles will be balanced, and the nanoparticles are confined in an area. When the external electric field changes, the electric field force will change, hence affect the balance with the electrostatic repulsive force between the nanoparticles, and consequently, the

distance between the nanoparticles. Therefore, the final accumulation area of the nanoparticles changes with the applied electric field.

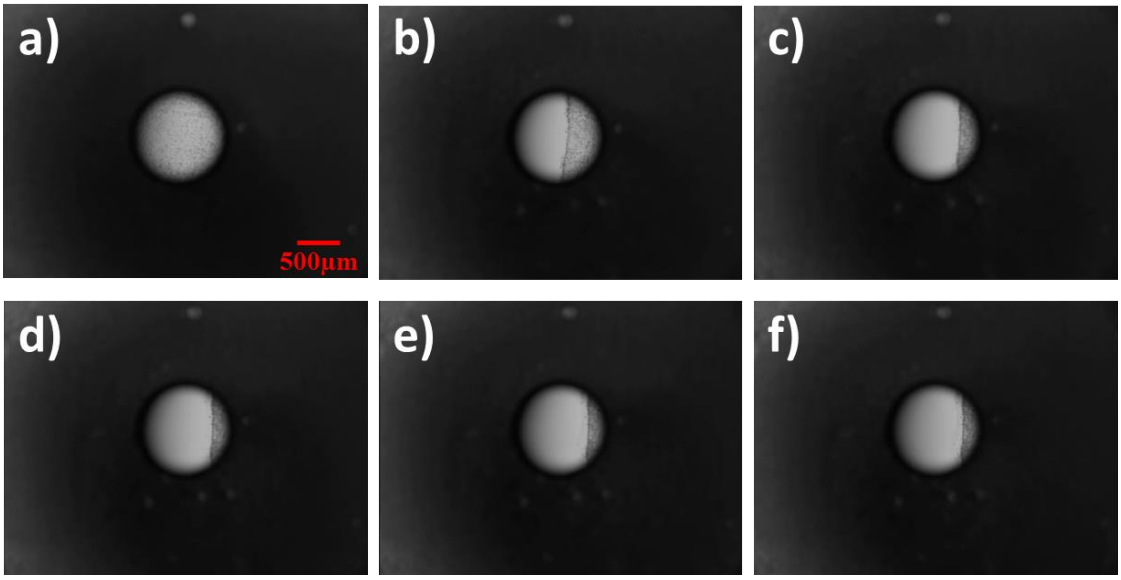

Figure 3-8. The redistribution of aluminum oxide nanoparticles on the surface of an oil drop of 1.1 mm in diameter under E = 15V/cm at different time. 12.5 µL 20 mg/mL nanoparticle suspension was released over the oil droplet. When t = 6min, nanoparticles reached the final state with γ = 28.81%. (a) t = 0 min, γ = 100%; (b) t = 2 min, γ = 43.12%; (c) t = 4 min, γ = 30.05%; (d) t = 6 min, γ = 28.81%; (e) t = 8 min, γ = 28.81%; (f) t = 10 min, γ = 28.81%.

Figure 3-8 and Figure 3-9 shows the redistribution processes of the alumina nanoparticles on the surface of the oil droplet of 1.1 mm in diameter under different electric field, 15 V/cm and 35 V/cm, respectively. It is clearly shown in these figures that, at the final state, the nanoparticle coverage ratio r decreases from 43.17% to 17.16% when the electric field increases from 15 V/cm to 35 V/cm, which means the final accumulation area of the nanoparticles becomes smaller as the externally applied electric field increases. Recall that Figure 3-6 shows the redistribution processes of the alumina nanoparticles on the surface of the same sized oil droplet under 25 V/cm. By comparing Figures 3-6, 3-8 and 3-9, the following can be concluded:

(1) The final surface coverage of Janus droplets by the nanoparticles decreases with the applied electric field, e.g., 43.17% for 15 V/cm, 20.75% for 25 V/cm and 17.16% for 35V/cm.

(2) For an oil droplet with a fixed size and the same amount of nanoparticles covered on its surface, the particles move faster and the time required to reach the final state is shorter if the applied electrical field is stronger. For example, when E = 15 V/cm, it takes more than 6 minute for the nanoparticles to reach the final state (Figure 3-8). While it takes around 2 minute under E = 35V/cm (Figure 3-9).

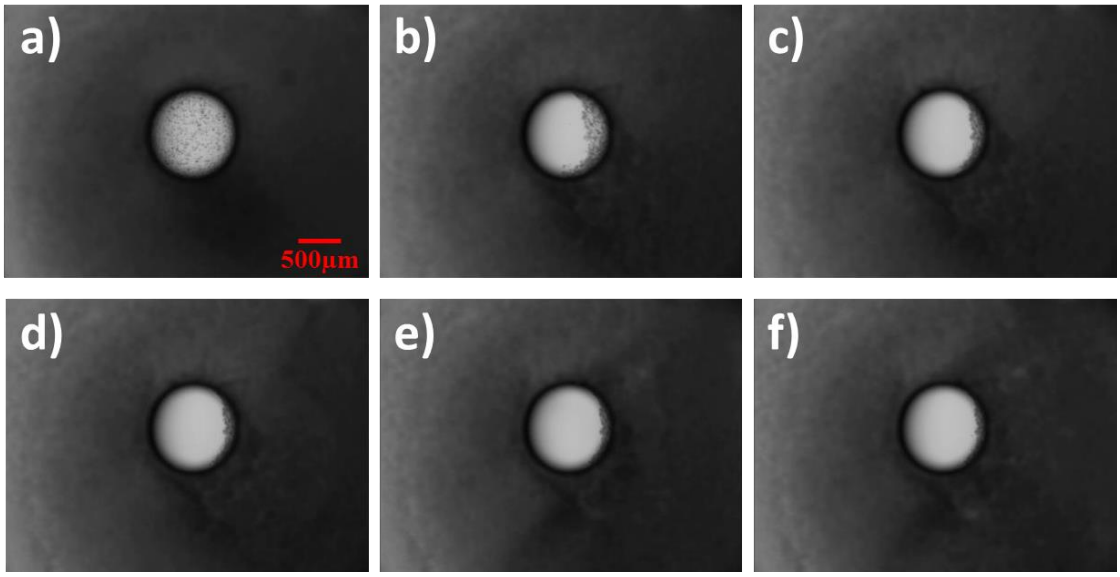

Figure 3-9. The redistribution of aluminum oxide nanoparticles on the surface of an oil drop of 1.1 mm in diameter under E = 35V/cm at different time. 12.5 µL 20mg/mL nanoparticle suspension was released over the oil droplet. When t = 3 min, nanoparticles reached the final state with γ = 17.16%. (a) t = 0 min, γ = 100%; (b) t = 1min, γ = 31.17%; (c) t = 2min, γ = 17.16%; (d) t = 3min, γ = 17.16%; (e) t = 4 min, γ = 17.16%; (f) t = 5 min, γ = 17.16%.

3.3.4 Suspended Janus Droplets: Effect of Nanoparticle Suspension

Figure 3-10 shows the variation of surface coverage of Janus droplets by Al_2O_3 nanoparticles, γ, with the concentration of the nanoparticle suspension, *C*. The Janus droplets shown in this section were developed from the Pickering emulsion droplets prepared from method A (section 3.2.2.2). The microscope image over each bar is the picture of Janus droplet generated with the corresponding nanoparticle suspension under electrical field of 50V/cm. It is seen in this figure that γ increases with *C*. This phenomenon can be understood as follows. With other parameters unchanged, when high concentration of nanoparticle suspension is used to generate Pickering emulsion, the total number of nanoparticles adsorbed on the surface of oil droplets increases, which results in Janus droplets with a large surface coverage by nanoparticles under a given electric field. It should be noted that, as the nanoparticle coverage region of small Janus droplets cannot be seen clearly, only the Janus droplets with a diameter larger than 40 μm were chosen to measure the surface coverage. Under each condition, 10 independent measurements were conducted.

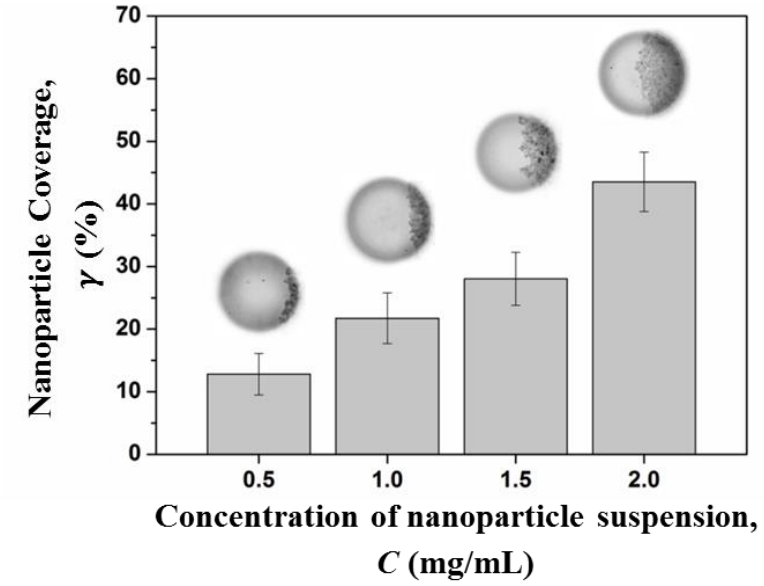

Figure 3-10. The variation of the surface coverage of Janus droplets by nanoparticles (γ) with the concentration of the nanoparticle suspension (*C*). The microscope images over each bar are the pictures of Janus droplets generated with the corresponding nanoparticle suspensions under 50 V/cm electric field.

3.3.5 Suspended Janus Droplets: Effect of Electric Field Strength

The electric field affects the nanoparticle coverage of EIJDs by changing the distances between nanoparticles attached on the droplet surface. The separation distance between two spherical nanoparticles can be predicted with the well-known DLVO (Derjaguin-Landau-Verwey-Overbeek) theory [115–119]. Based on the DLVO theory, without the presence of externally applied electric field, the interaction between two nanoparticles is composed of the Van der Waals (vdW) interaction and the electric double layer (EDL) interaction, as shown in Figure 3-11(a). The Van der Waals force ($\vec{F}_{vdW}$) is attractive force which trends to drag the nanoparticles together, while the EDL interaction force ($\vec{F}_{EDL}$) is repulsive force towards the opposite direction. The variations of $\vec{F}_{vdW}$, $\vec{F}_{EDL}$ and the total force ($\vec{F}_{total}$, $\vec{F}_{total} = \vec{F}_{vdW} + \vec{F}_{EDL}$) with the distance between two nanoparticles are shown in Figure 3-11(c). As shown in this figure, the steady state is reached at point A, where the total force is equal to zero. After applying electric field from left to right, the electrostatic force, F_e, exerts on the positively charged nanoparticles, which is toward the cathode of the electric field. As shown in Figure 3-11(b), the direction of $\vec{F}_e$ is identical to that of the attractive Van der Waals force. With the presence of $\vec{F}_e$, the balance between the $\vec{F}_{vdW}$ and $\vec{F}_{EDL}$ is broken, the two nanoparticles move closer to each other until a new force balance is reached. The final distance between the two nanoparticles is determined by the strength of the externally applied electric field. Generally, as the strength of the electric field increases, the distance decreases to generate equivalent repulsive $\vec{F}_{total}$ to balance the electric force, as shown in Figure 3-11(c). However, as $\vec{F}_{total}$ decreases sharply with the distance, the further increase of electric force only leads to limited decrease of the separation distance.

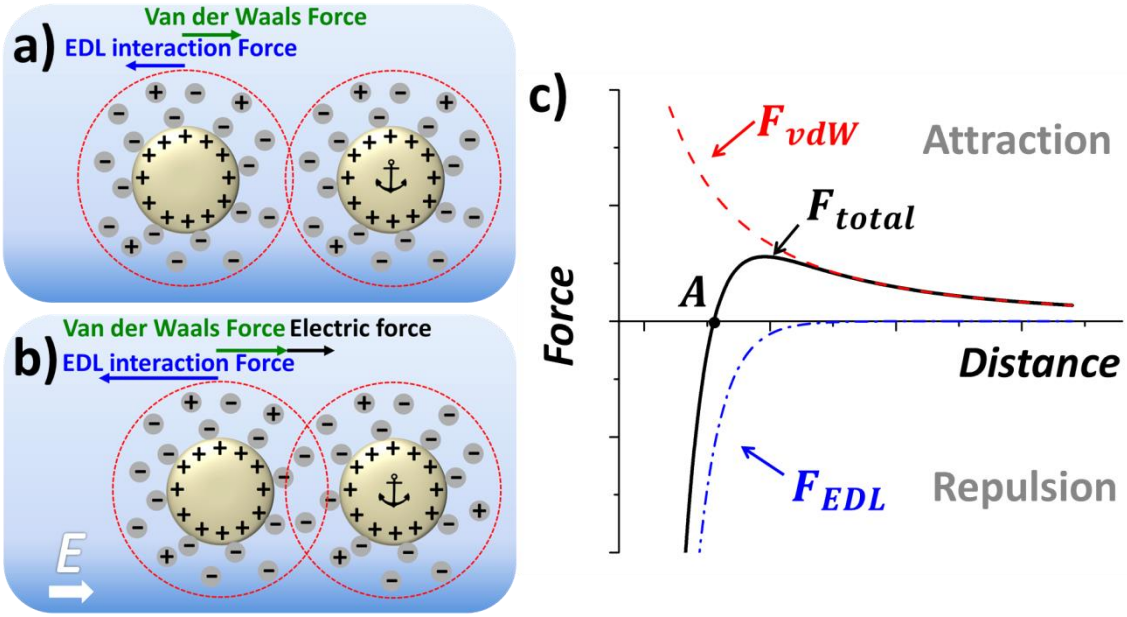

Figure 3-11. (a)-(b) Schematic diagrams of the forces acting on the left nanoparticle with (b) and without (a) the presence of electric field. The right nanoparticle gets anchored, while the left one is free to move. (c) Schematic diagram of the variation of Van der Waals Force, EDL interaction force and total force with the distance between two nanoparticles.

In the study of the effect of electric field strength on nanoparticle coverage of the EIJDs, The Al_2O_3 nanoparticle-stabilized Pickering emulsion was prepared with the method B shown in section 3.2.2.2. After the preparation of the Pickering emulsion droplets, the EIJDs can be formed easily by applying direct current electric field to the Al_2O_3 nanoparticle-stabilized Pickering emulsion droplets. To study the variation of nanoparticle coverage of the EIJDs with the strength of electric field, nanoparticle suspensions with different concentrations of nanoparticle, 0.5 mg/mL, 1 mg/mL and 1.5 mg/mL, were formed for generating Pickering emulsion droplets and then fabricating EIJDs, respectively.

The variation of the nanoparticle coverage of the EIJDs with the electric field strength is shown in Figure 3-12. As an example, the microscope images of the EIJD formed from 1 mg/mL nanoparticle suspension under different electric fields are presented in Figure 3-12(a). As indicated in the serial images, with the increase of the electric field strength, the area of the nanoparticle film

decreases. The variation of the nanoparticle coverage is significant under relative weak electric field, ranging from 10 V/cm to 50 V/cm. Once the electric field becomes larger than 50 V/cm, further increasing of the electric field only leads to very limited area reduction of the nanoparticle film. To characterize the relationship between electric field strength and the nanoparticle coverage of EIJDs quantitatively, the nanoparticle coverages of EIJDs fabricated from different concentrated nanoparticle suspensions were measured under different electric fields. Three typical examples of the variation of nanoparticle coverage of EIJDs (γ) in terms of the strength of electric field (E) are plotted in Figure 3-12(b). It is clearly shown in this figure that for all of the three EIJDs carrying different amount of nanoparticles, both γ and the variation rate of γ decreases as E increases. Under the electric field of 10 V/cm, the nanoparticle coverage of the EIJD generated from 1 mg/mL (indicated by red rectangular points in Figure 3-12(b)) is around 50%. When E increases to 50 V/cm, γ reduces to 38%. However, with the further increase of the electric field from 50 V/cm, γ almost remains constant which only decreases from 38% to 35%. This phenomenon can be understood based on the DLVO theory shown above. Under an externally applied electric field, the extra electrostatic force applies to the nanoparticles and the nanoparticles get redistributed by moving closer to each other; therefore, the nanoparticle coverage of the EIJDs decreases. However, as the repulsion force increases sharply with the smaller separation distance between nanoparticles, the reduction of the separation distance between nanoparticles decreases under high electric field; hence, the variation rate of the nanoparticle coverage decreases with the further increase of the electric field.

In describing the relationship between nanoparticle coverage and electric field quantitatively, two normalized parameters, relative coverage (γ_r) and relative electric field (E_r), were introduced:

$$\gamma_r = \frac{\gamma}{\gamma_{@10\,V/cm}} \tag{3-2}$$

$$E_r = \frac{E}{10\,V/cm} \tag{3-3}$$

where $\gamma_{@10\,V/cm}$ is the nanoparticle coverage of the EIJDs under electric field of 10 V/cm. Based on Equation 3-2 and 3-3, both the nanoparticle coverage and the electric field are normalized. The variation of γ_r as a function of E_r was plotted in Figure 3-12(c), and an empirical equation was derived to give the relationship between nanoparticle coverage and electric field strength:

$$\gamma_r = 0.66 + 0.41 \times 0.84^{E_r} \quad (3\text{-}4)$$

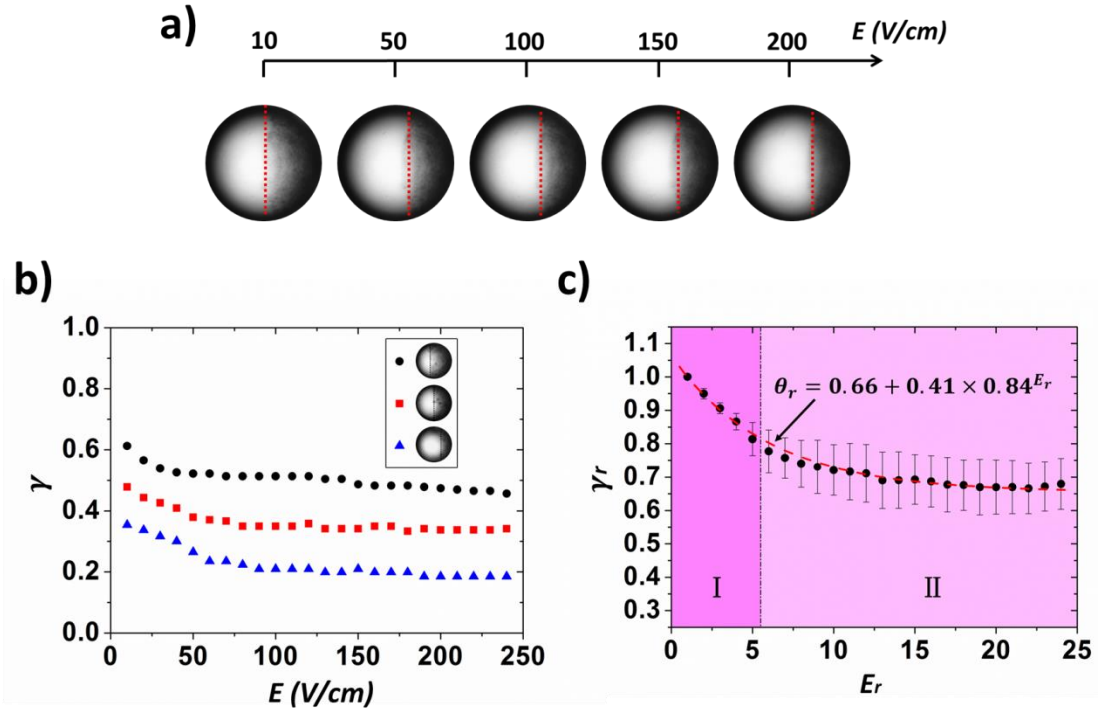

Figure 3-12. (a) Microscope images of the EIJD fabricated from 1 mg/mL nanoparticle suspension under different electric field strengths; (b) three typical examples of the variations of nanoparticle coverage as a function of the electric field strength for the EIJDs carrying different amount of nanoparticles. The circular point, rectangular point and triangular point refer to the EIJDs generated from 1.5 mg/mL, 1 mg/mL and 0.5 mg/mL nanoparticle suspensions, respectively; (c) the variation of relative coverage, γ_r, with the relative electric field, E_r. The diameters of the EIJDs range from 50 μm to 75 μm.

At least ten independent measurements were conducted to check the reliability of the results. The consistency of the measurements of the nanoparticle coverage variation confirms the reproducibility of the findings. The adjusted coefficient of determination between the experimental results and the empirical equation is 0.998, which allows for accurate and precise prediction of γ_r with the empirical equation. As shown in Figure 3-12(c), based on the reduction rate of γ_r, the

variation of γ_r can be divided into two stages: a sharp descent stage (Ⅰ) and a gentle descent stage (Ⅱ). In the first stage, E_r ranges from 0 to 5, and the decline of γ_r is significant with the increase of E_r. For E_r larger than 5, the second stage is reached. In this stage, the variation of γ_r is limited and γ_r approaches a constant with the increase of E_r. The EIJDs with the diameter ranging from 50 μm to 75 μm were chosen.

3.3.6 Microfluidic Method: Sessile Janus Droplets and Droplets with Heterogeneous Strips

The fabrication of sessile Janus droplets with different nanoparticles, Al_2O_3 and MgO, are shown in Figure 3-13. As the metallic oxide nanoparticles and the oil droplet carry surface charges of opposite signs ("+" for nanoparticles, "−" for oil droplet), when nanoparticles flow by the surface of oil droplet, they are attracted and attach on the droplet. Under DC electric field, the nanoparticles adhering on the oil droplet are driven to move on the oil-water interface along the electric field direction and accumulate to the rear end of the oil droplet. Under the applied electric field, the nanoparticles accumulate to form compact nanoparticle film on the surface of the droplet. It's clearly shown in the time-lapse sequences of Figure 3-13 that, as time goes by, more and more nanoparticles assemble on the oil droplets and the accumulation areas of nanoparticles increases. Within 1 min, the Janus droplets partially coated with nanoparticles form. Generally, the time needed to form a certain size of the nanoparticle film on the oil droplet will be shorter when the nanoparticle mass flow rate is higher. As both Al_2O_3 and MgO nanoparticles are positively charged, the resulting Janus droplets are electrically anisotropic, that the part covered by the nanoparticles carries positive charges and the oil surface without the nanoparticle coverage has negative surface charges. The nanoparticles on the right hemisphere of the Janus droplet form a packed nanoparticle film under the electric field of 150 V/cm. Furthermore, if the nanoparticles are continuously transported through the microchannel, more nanoparticles will deposit on the oil droplet surface, and finally, the droplet will be covered completely by a homogeneous nanoparticle film.

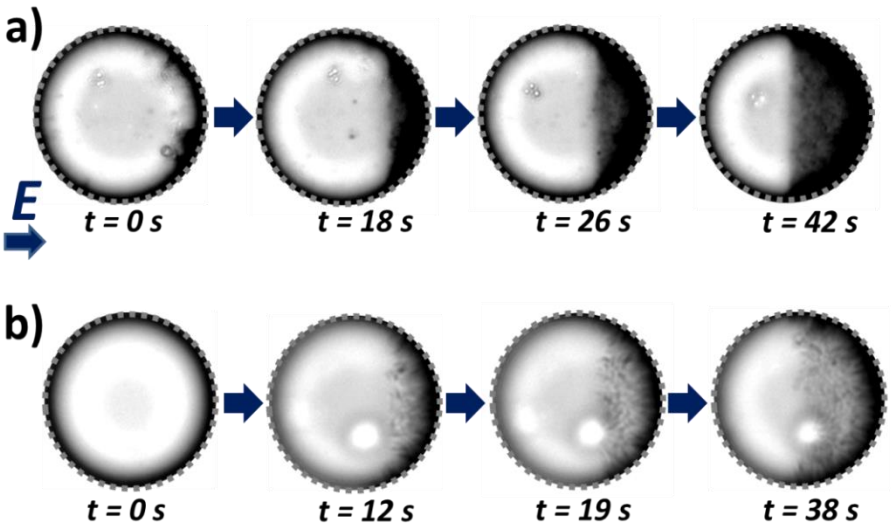

Figure 3-13. Time-lapse sequences of the sessile Janus droplets formation with (a) Al_2O_3 nanoparticles and (b) MgO nanoparticles under externally applied electric field of 150 V/cm. The diameters of the droplets are approximately 50 μm.

Figure 3-14(a) displays time-lapse images for the formation of multiple strips of different nanoparticles on the surface of sessile oil droplet under the electric field of 150 V/cm. The Al_2O_3 nanoparticles and MgO nanoparticles are employed in this fabrication. In this figure, the Al_2O_3 nanoparticle strip shows dark color and MgO nanoparticle strip shows white color. One can see that, by transporting different nanoparticles in sequence to the sessile oil droplet, nanoparticles accumulate orderly and strip patterns can be generated on the surface of the oil droplet. The width of each nanoparticle stripe can be easily modulated by changing the amount of nanoparticle suspension injected into the microchannel while fabricating. By controlling nanoparticles delivery, the Janus droplets and droplets with different strips can be fabricated. Figure 3-14(b) shows a Janus droplet with one hemisphere coated with Al_2O_3 nanoparticles and the other hemisphere coated with MgO nanoparticles. Figure 3-14(c) displays a droplet coated with three strips by assembling Al_2O_3, MgO and Al_2O_3 nanoparticles on the oil droplet in turns. As the ZnO nanoparticles also carry positive surface charges in pH = 7 buffer solution, it is possible to produce ZnO nanoparticle films on oil droplets. Figure 3-14(d) and (e) show a ZnO-Al_2O_3 Janus droplet and a droplet with Al_2O_3-ZnO-Al_2O_3 three strips, respectively. The Al_2O_3, MgO and ZnO nanoparticles have

different physical and chemical properties, which give these droplets specific functions in potential applications.

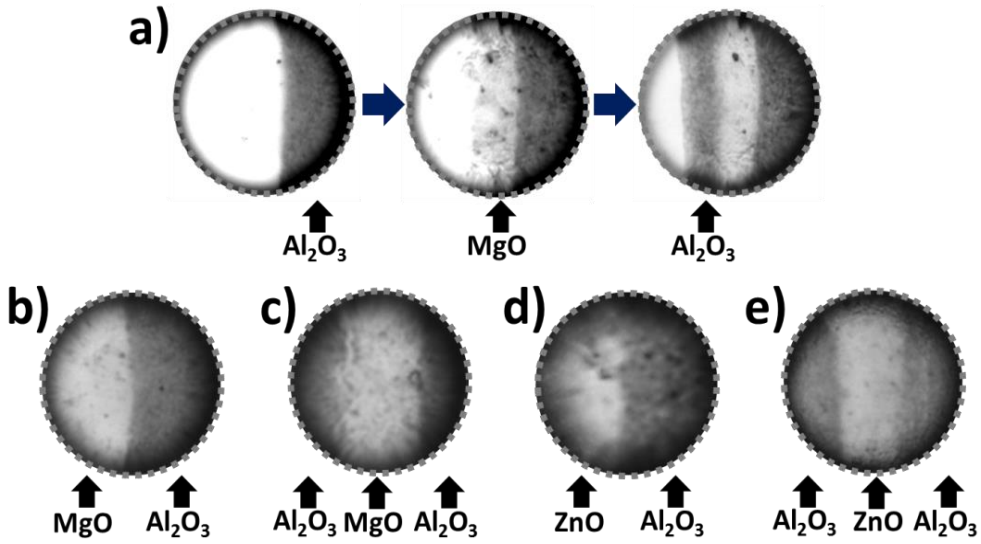

Figure 3-14. (a) Accumulation of different nanoparticles on sessile oil droplet to form multiple strips; (b) MgO-Al_2O_3 Janus droplet; (c) droplet with Al_2O_3-MgO-Al_2O_3 three strips; (d) ZnO-Al_2O_3 Janus droplet; (e) droplet with Al_2O_3-ZnO-Al_2O_3 three strips. The electrical field applied to the droplets while fabricating is 150 V/cm. The diameter of these droplets ranges between 45 μm and 75 μm.

3.3.7 Microfluidic Method: Suspended Janus Droplets and Droplets with Heterogeneous Strips

Similar to the fabrication of sessile Janus droplets, nanoparticle delivery and electrical field assembly are essential in producing suspended droplets. To hold a suspended oil droplet stationary while the nanoparticles are moving in the microchannel, the suspended oil droplet is transported with the flow into the microchannel and blocked by a pair of circular pillars. In Figure 3-15, the time-lapse images are captured from a video for the formation of suspended oil droplet covered by

a homogeneous film of Al_2O_3 nanoparticles. Initially, the oil droplet is anchored between the two pillars. When the nanoparticles are delivered with flow and the electrical field is applied, the oil droplet is covered by the positively charged nanoparticles from the right side gradually. At t = 42 s, a suspended Janus droplet with the right hemisphere covered with the positively charged nanoparticles forms; and at t = 128 s, the oil droplet is fully coated by the nanoparticles and a droplet covered with a homogeneous film of positively charged nanoparticles is formed. The formation process of MgO or ZnO nanoparticle film on an oil droplet is similar.

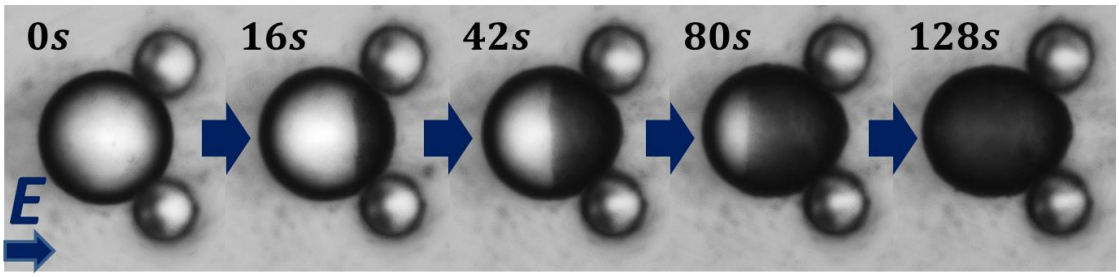

Figure 3-15. Time-lapse sequences of the formation of Al_2O_3 nanoparticle film on a suspended oil droplet in a microchannel under externally applied electric field of 150 V/cm. The diameter of the droplet is approximately 50 μm.

The microscope images of suspended droplets covered with two or three different nanoparticle films are shown in Figure 3-16. Under the electric field of 150 V/cm, the different nanoparticle films on a single suspended droplet are formed by controlling the sequence of nanoparticle delivery in a process similar to that described for Figure 3-15. Figure 3-16(a) and (c) indicate two Janus droplets with the right hemispheres coated by Al_2O_3 nanoparticles and the left hemispheres covered with MgO nanoparticles and ZnO nanoparticles, respectively. The droplets covered with three strips: Al_2O_3-MgO-Al_2O_3 or Al_2O_3-ZnO-Al_2O_3, are also fabricated successfully, as shown in Figure 3-16(b) and (d). As the nanoparticle strips possess different physical and chemical properties, the droplets covered with multiple nanoparticle strips are anisotropic. Based on the color anisotropy and electrical anisotropy properties, the droplets can be employed as pixel elements in fabricating electronic paper and indicators to show the direction of electrical field. The

droplets can also be used as self-propelled micromotor to deliver cargos relying on the selective reaction between one of the strips and the surrounding buffer solution. Furthermore, the droplets have great potentials in material science, which can be regarded as build blocks to fabricate superstructures through self-assembly.

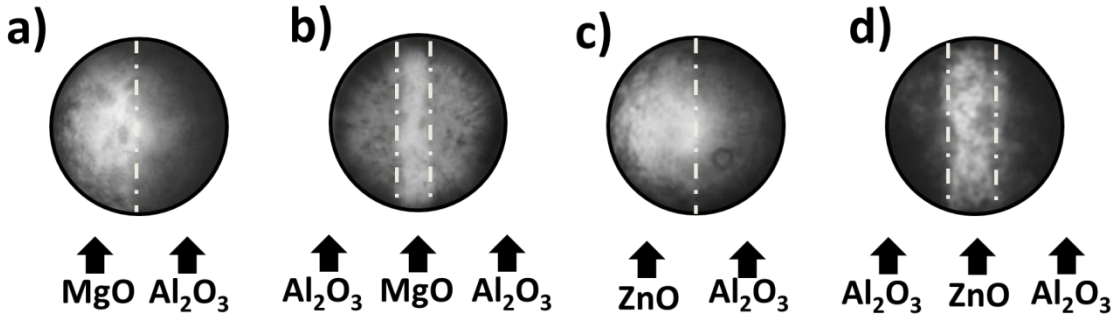

Figure 3-16. Microscope images of suspended droplets covered with more than one nanoparticle films. (a) MgO-Al_2O_3 Janus droplet; (b) droplet with Al_2O_3-MgO-Al_2O_3 three strips; (c) ZnO-Al_2O_3 Janus droplet; (d) droplet with Al_2O_3-ZnO-Al_2O_3 three strips. These droplets are fabricated under the electric field of 150 V/cm and the diameter ranges from 40 μm to 60 μm.

3.4 Conclusions

This chapter presents novel techniques for fabricating EIJDs and droplets with heterogeneous strips with nanoparticles under electric field. In the fabrication of sessile Janus droplets, both the micro-sized and macro-sized EIJDs can be produced. The final surface area that is covered by the nanoparticles varies with the concentration of the nanoparticles suspension and the applied electric field. Generally, a higher concentration of nanoparticle suspension results in a Janus droplet with a larger particle accumulation area. Increase in the applied electric field concentrates the charged particles in a smaller area on the Janus droplets. The suspended EIJDs are developed from nanoparticle-stabilized Pickering emulsion droplets by accumulating the nanoparticles to one side of the droplets under electric field. Similar to sessile EIJDs, the nanoparticle coverage of the

suspended ones is also dependent on the concentration of nanoparticle suspension and the electric field strength that the nanoparticle coverage increases with the increase of the concentration of the nanoparticle suspension and the decrease of the electric field strength. Based on the experimental results, an empirical equation has been derived for calculating the nanoparticle coverage of suspended EIJDs as a function of the electric field. With the microfluidic method, the sessile and suspended Janus droplets and droplets with designed heterogeneous strips were formed by controlling the delivery of nanoparticles to the surfaces of oil droplets. The fabrication techniques shown in this chapter are simple, effective and economical, which can be conducted in many labs. The electrokinetic properties of the EIJDs will be numerically and experimentally studied in the following chapters.

CHAPTER 4. Fundamental Research I: Electroosmotic Flow Field around EIJDs*

4.1 Introduction

In the previous chapter, the fabrication of the electrically induced sessile Janus droplet is studied and a guideline is provided to generate the electrically induced Janus droplets with controllable coverage area by nanoparticles. For an EIJD composed of a negatively charged surface on one side and a positively charged surface on the other side, vortices around the Janus droplet may be expected. The vortices around Janus droplets have many potential applications. For example, mixing inside microchannels is a challenge due to small Reynolds number, and the vortices around Janus droplets can enhance the mixing and the Janus droplets may be regarded as micro-mixers.

In this chapter, the electroosmotic flow fields around sessile EIJDs under externally applied DC electrical field are studied. A numerical model is set up to simulate the flow field around the Janus droplet in electric field. The effects of the strength of the electrical field and the surface coverage by the positively charged nanoparticles on the flow field are studied. The numerically predicted results are further validated experimentally by visualizing the flow fields with tracing particles. Furthermore, as the Janus droplets are generated in electrical field, the surface coverage by the nanoparticles depends on the strength of the electric field; therefore, the effect of the electric field on the nanoparticle coverage of the Janus droplet and the flow field is analyzed.

4.2 Material and Methods

4.2.1 Theoretical Model and Numerical Simulation

Consider an EIJD, one side with positive surface charges, the other side with negative surface charges (Figure 4-1(a)), immersed in an infinitely large aqueous solution, electroosmotic flow will be generated around the droplet under electric field. Due to the opposite signs of zeta potentials on

* A similar version of this chapter was submitted or published as:
Li, M.; Li, D. Vortices around Janus Droplets under Externally Applied Electrical Field. *Microfluid. Nanofluid.* **2016**, 20, 79. https://link.springer.com/article/10.1007/s10404-016-1741-2

different sides of the Janus droplet, vortices will be produced in vicinity of the droplet because of the opposite directions of electroosmotic flow on the two sides of the Janus droplet. A multi-physics model is employed to simulate the EDL field, electric field and flow field of the system, as described in the following sections.

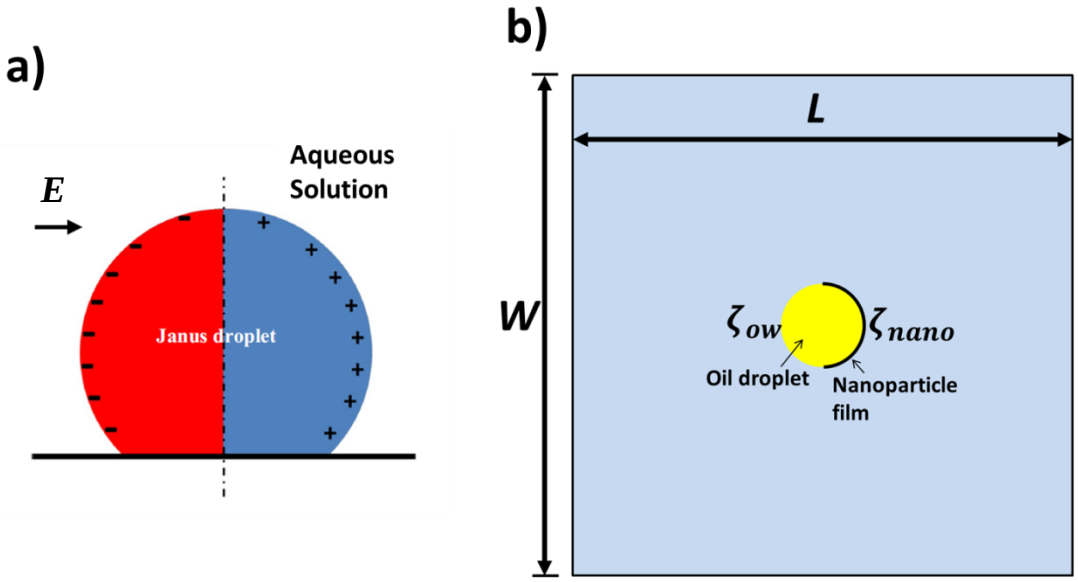

Figure 4-1. (a) Schematic diagram of a sessile Janus droplet which is anchored on a solid surface in an aqueous solution. (b) Schematic diagram of the geometry of the simulation model.

4.2.1.1 EDL Field

The Poisson-Boltzmann equation is employed to describe the potential of EDL field ψ [67]:.

$$\nabla^2\psi = \frac{2zen_\infty}{\varepsilon_0\varepsilon_w} sinh(\frac{ze\psi}{k_bT}) \quad (4\text{-}1)$$

In this equation, z is the valence of ions, n_∞ is the concentration of ions in the bulk aqueous solution, e is the elementary charge, ε_0 is the electric constant, ε_w is the permittivity of the aqueous solution, k_b is the Boltzmann constant and T is the temperature.

The boundary conditions in different positions are set:

$$\psi = \zeta_{ow} \qquad \text{oil-water interface} \qquad (4\text{-}2)$$

$$\psi = \zeta_{nano} \qquad \text{nanoparticle film} \qquad (4\text{-}3)$$

here, ζ_{ow} and ζ_{nano} are the zeta potentials of the oil-water interface and nanoparticle film, respectively.

4.2.1.2 Electric Field

After applying the electric field to the system, the electric potential ϕ in the liquid can be determined by solving the Laplace's equation:

$$\nabla^2 \phi = 0 \qquad (4\text{-}4)$$

The corresponding boundary conditions are:

$$\vec{n} \cdot \nabla \phi = 0 \qquad \text{at the oil droplet surface} \qquad (4\text{-}5)$$

$$\phi = \phi_0 \qquad \text{at the electric field inlet} \qquad (4\text{-}6)$$

$$\phi = 0 \qquad \text{at the electric field outlet} \qquad (4\text{-}7)$$

where $\vec{n}$ is the unit vector normal to the boundary. ϕ_0 is the voltage applied to the inlet of the microchannel.

4.2.1.3 Flow Fields

At steady state, the flow field of the water phase ($\vec{u}_w$) is described with reduced Navier-Stokes equation and the continuity equation [120]:

$$\nabla P = \eta_w \nabla^2 \vec{u}_w + \vec{E}_o \rho_e \qquad (4\text{-}8)$$

$$\nabla \cdot \vec{u}_w = 0 \qquad (4\text{-}9)$$

here, η_w is the viscosity of the water phase, P is the pressure. $\vec{E}_o$ is the local electric field and ρ_e is the local net charge density in the water phase, which can be calculated:

$$\vec{E}_o = -\nabla\phi \tag{4-10}$$

$$\rho_e = -2n_\infty ze sinh(\frac{ze\psi}{k_b T}) \tag{4-11}$$

As the oil phase is electrically neutral, the NS equation of the flow field of the oil droplet ($\vec{u}_o$) is further simplified by neglecting the electrical body force term:

$$\nabla P = \eta_o \nabla^2 \vec{u}_o \tag{4-12}$$

$$\nabla \cdot \vec{u}_o = 0 \tag{4-13}$$

The boundary conditions of the flow fields are:

$$\vec{u}_w = 0 \qquad \text{nanoparticle film in water phase} \tag{4-14}$$

$$\vec{n} \cdot \nabla \vec{u}_w = 0 \qquad \text{far field boundaries} \tag{4-15}$$

$$\vec{u}_o = 0 \qquad \text{nanoparticle film in oil phase} \tag{4-16}$$

Due to the mobility of the oil-water interface, the motion of the interface is described by the electric double layer + surface charges (EDL+SC) model with considering both velocity continuity and shear force conservation [121–124]:

$$\vec{u}_w = \vec{u}_o \qquad \text{oil-water interface} \tag{4-17}$$

$$\frac{\partial \vec{u}_w}{\partial \vec{n}} - \frac{\eta_o}{\eta_w}\frac{\partial \vec{u}_o}{\partial \vec{n}} + \frac{\sigma_s \vec{E}_o}{\eta_w} = 0 \qquad \text{oil-water interface} \tag{4-18}$$

In Equation (4-18), σ_s is the local surface charge density:

$$\sigma_s = \frac{4n_\infty ze}{\kappa} sinh(\frac{ze\zeta_d}{2k_b T}) \tag{4-19}$$

$$\kappa = \sqrt{2n_\infty z^2 e^2 / \varepsilon_0 \varepsilon_w k_b T} \tag{4-20}$$

4.2.1.4 Numerical Simulation

Based on the theoretical analysis shown above, the multi-physics simulation was conducted with commercial finite element software, COMSOL 4.3b. The geometry of the model is shown in Figure 4-1(b). For meshing the computation domain, extremely fine mesh elements were employed at the oil-water interface and the microchannel wall to simulate the liquid motion inside EDL. The total number of meshes used in this simulation is 131,034. The parameters used in this simulation are listed in Table 4-1.

Table 4-1. Parameters used in the simulation

Parameters	Values
Permittivity of vacuum ε_0 (C/V m)	8.854×10^{-12}
Dielectric constant of water ε_w	80
Viscosity of water η_w (Pa·s)	0.001
Density of water ρ_w (kg/m^3)	1000
Viscosity of oil η_o (Pa·s)	0.05
Density of oil ρ_o (kg/m^3)	900
Diameter of the droplet d (μm)	200
Length of the computation domain L (μm)	4000
Width of the computation domain W (μm)	4000
Temperature T (K)	298
Zeta potential on positively charged surface of the Janus droplet ζ_{nano} (mV)	60
Zeta potential on negatively charged surface of the Janus droplet ζ_{ow} (mV)	–40

4.2.2 Experimental Setup

The sessile EIJDs were generated with the method shown in section 3.2.1. In order to visualize the fluid flow around the sessile Janus droplet, spherical polystyrene particles (Bangs Laboratories Inc., IN, USA) with the diameter of 1 μm were used as the tracing particles. The experimental

system is shown in Figure 4-2: a petri dish to hold a sessile oil droplet covered with aluminum oxide nanoparticles in water, a DC power supply (CSI12001X, Circuit Specialist Inc., USA), a microscope imaging system (Ti-E, Nikon, Japan). During the experiment, the petri dish was put on the stage of the microscope. The electric field was applied by the DC power supply through two electrodes immersed in the aqueous solution. The strength of the electric field can be adjusted by controlling the output voltage of the DC power supply. The microscope with a digital camera (DS-Qi1Mc, Nikon) was taken to visualize the trace particles' motion around the Janus droplet. The images can be captured by the digital camera and send to a computer to be saved and analyzed.

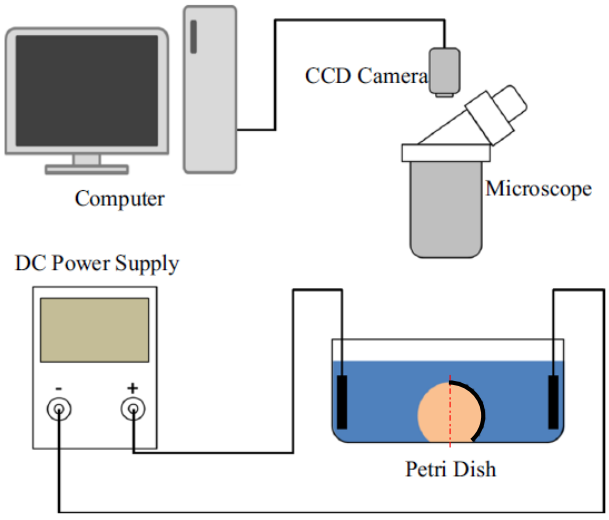

Figure 4-2. Schematic diagram of the experimental system for studying electroosmotic flow field around a Janus droplet.

4.3 Results and Discussion

For a sessile EIJD with one side carrying positive surface charges and the other side carrying negative surface charges, vortices can be formed in the neighborhood of the Janus droplet under externally applied electrical field. Figure 4-3(a) shows the typical flow stream patterns around a Janus droplet of 200 μm in diameter under applied electric field 40 V/cm. In this case, the positive surface charges are on the right-hand side of the droplet; and the negative surface charges are on

the left-hand side of the droplet. As one can see in this figure, two vortices were generated around the droplet because of the zeta potential difference between the two sides of the droplet. Because the absolute value of zeta potential on the right hemisphere (+60 mV) is larger than that on the left hemisphere (−40 mV), the electroosmotic flow on the right hemisphere dominates the flow and hence the two vortices stay on the left side. Verification experiment was conducted at the same electric field of 40 V/cm. A Janus droplet with the diameter of 170 μm was generated by following the procedures described above. As shown in Figure 4-3(b), two vortices formed on the left side of the Janus droplet. The comparison of Figures 4-3(a) and (b) indicates that the numerical prediction agrees well with the experimental observation.

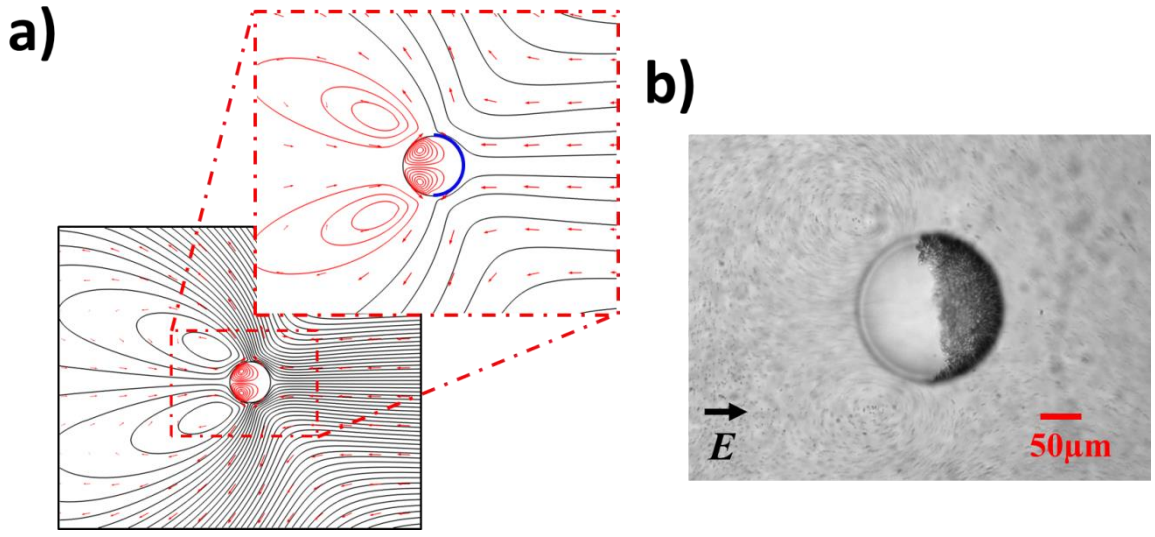

Figure 4-3. Flow field around a Janus droplet under the electrical field of 40 V/cm. (a) Numerical result with the red section carries negative charges and the blue section carries positive charges; (b) experimental observation of a sessile Janus droplet partially covered with positively charged aluminum oxide nanoparticles under the same electric field.

4.3.1 Effect of the Applied Electric Field

It is well known that electroosmotic velocity is directly proportional to the applied electric field. To study how the vortices vary with electric field, the numerical simulations for three different

strengths of electric fields were conducted. Figure 4-4(a), (b) and (c) shows the flow fields around the same Janus droplet under three different electric fields, 40V/cm, 50V/cm and 60V/cm, respectively. It can be seen from these figures that two vortices were formed on the left-hand side (negatively charged surface) of the Janus droplet under different applied electrical fields. Comparison of the three cases in Figure 4-4(a), (b) and (c) clearly shows that when the surface coverage of the Janus droplet by the nanoparticles is fixed, 50% in this case, the externally applied electrical field has no appreciable effect on the location and size of the vortices. As the electric field increases, the velocity of the two opposite electroosmotic flows from the two hemisphere surfaces all increases. Therefore, the locations of the vortices remain the same. However, the rotation speed of the vortices becomes larger.

In order to experimentally verify the prediction of the above numerical simulations, an oil droplet covered with aluminum oxide nanoparticles was generated in a plastic petri dish. To make the accumulation area of the nanoparticles unchanged under different externally applied electrical fields, the electric field of 60 V/cm was applied from left to right for a period of 2~3 minutes. This electrical field was strong enough to push the nanoparticles to accumulate to the right hemisphere of the oil droplet and make them tightly packed with each other; so that, when the external electrical field was reduced to 50 V/cm or 40 V/cm, the aggregated nanoparticles were kept in the original area (the right hemisphere). In this way, a Janus droplet with a fixed surface coverage by the nanoparticles under different applied electric fields can be studied. Figure 4-4(d) to (f) show the vortices around the Janus droplet of 170 μm in diameter under different applied electrical fields. In order to see the vortices clearly, only the vortices near the up-left quarter of the droplet were shown. All of the three pictures presented in Figure 4-4(d), (e) and (f) were taken with the same exposure time of 200 ms. Therefore, the strength of the vortices under different applied electric field can be obtained by comparing the length of the streak lines of the tracing particles. By comparing the three pictures in this figure, the same conclusion can be obtained: as the electric field increases, the strength of the vortices increases while the location and size of the vortices remains unchanged.

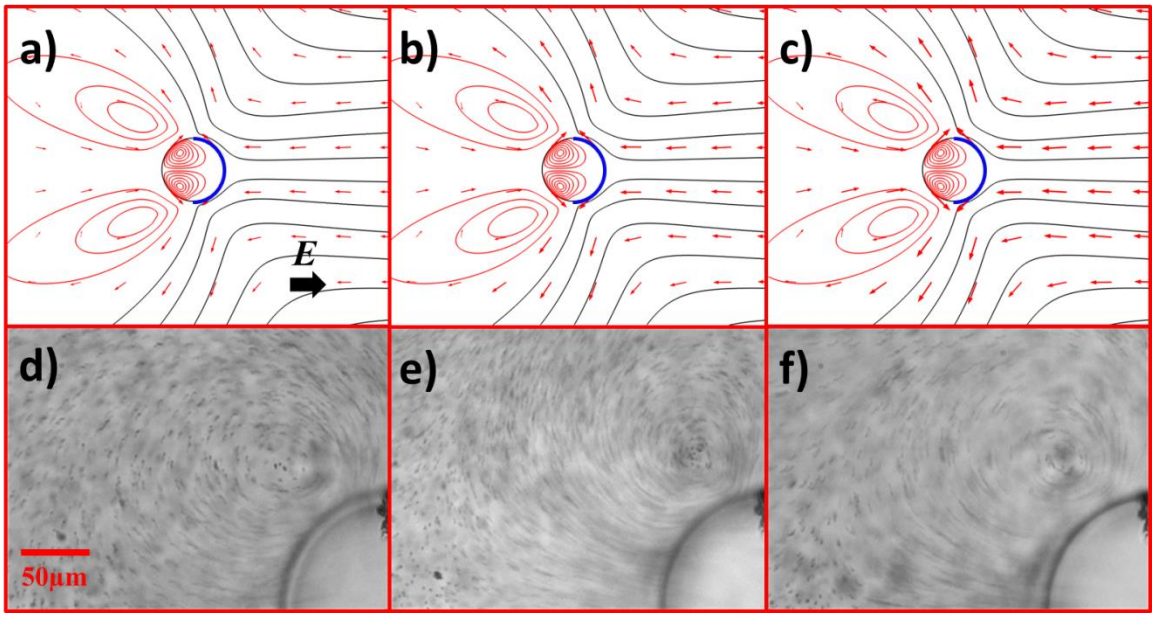

Figure 4-4. (a)-(c) Vortices around a Janus droplet under different applied electrical fields as predicted by numerical simulation. The red hemisphere carries negative surface charges and the blue hemisphere carries positive surface charges. (a) E = 40 V/cm; (b) E = 50 V/cm; (c) E = 60 V/cm. The direction of red arrows represents that of the fluid flow, and the length of red arrows is proportional to logarithmic flow velocity of the fluid. (d)-(f) Experimentally observed vortices around the Janus droplet with the diameter of 170μm under electric fields of 40 V/cm (d), 50 V/cm (e) and 60 V/cm (f).

4.3.2 Effect of the Surface Coverage of the EIJDs

The surface coverage of the Janus droplet by the nanoparticles is another factor that will affect the vortices. As mentioned above, when the nanoparticle surface coverage of the Janus droplet is 50%, because the absolute value of the zeta potential on the surface of aluminum oxide nanoparticles is larger than the zeta potential of the oil-water interface, the electroosmotic flow on this hemisphere covered with nanoparticles will dominate the flow around the droplet, and two vortices will be generated on the other hemisphere of the droplet. When the accumulation area of the nanoparticles is larger, the electroosmotic flow on the positively charged surface becomes dominant over the opposite electroosmotic flow generated on the negatively charged surface. This results in vortices

on the negatively charged side of the droplet. However, when the accumulation area of the positively charged nanoparticles is small enough, the electroosmotic flow on the negatively charged surface will dominate the flow field around the droplet and the two vortices will be positioned on the positively charged side of the droplet. Figure 4-5 shows the vortices around Janus droplets with different surface coverage by the positively charged nanoparticles. As shown in Figure 4-5(a), when the positively charged section (blue line) is larger than the negatively charged section (black line), the electroosmotic flow from the blue area is stronger which forced two vortices to be formed on the other side of the oil droplet. However, the vortices will occur on the positively charged side when the surface coverage by the positively charged nanoparticles becomes sufficiently small and the electroosmotic flow from the negatively charged section becomes dominant, as shown in Figure 4-5(b).

Figure 4-5(c) and (d) shows the experimentally observed change of the vortices position with the surface coverage of the droplet by positively charged nanoparticles. The Janus droplets with different surface coverage were generated by depositing different volumes of nanoparticle suspension over the oil droplet. Applying a larger volume of the nanoparticle suspension results in a larger number of nanoparticles on the droplet surface. With the externally applied electric field unchanged, at the final state, the larger number of nanoparticles leads to a larger accumulation area on the droplet surface. As can be seen in Figure 4-5(c), when $\theta \approx 110°$, i.e., the positively charged nanoparticles cover the majority of the droplet surface, vortices form on the side of the pure oil-water interface. However, when $\theta \approx 60°$, i.e., the positively charged nanoparticles cover only a small fraction of the droplet surface on the right-hand side, vortices occur on the side of the droplet facing the negative electrode, as shown in Figure 4-5(d). In order to show the vortices clearly, only one vortex and one quarter of the droplet were shown in these two figures. Clearly, the predicted results by numerical simulation and the experimental observation are in good agreement.

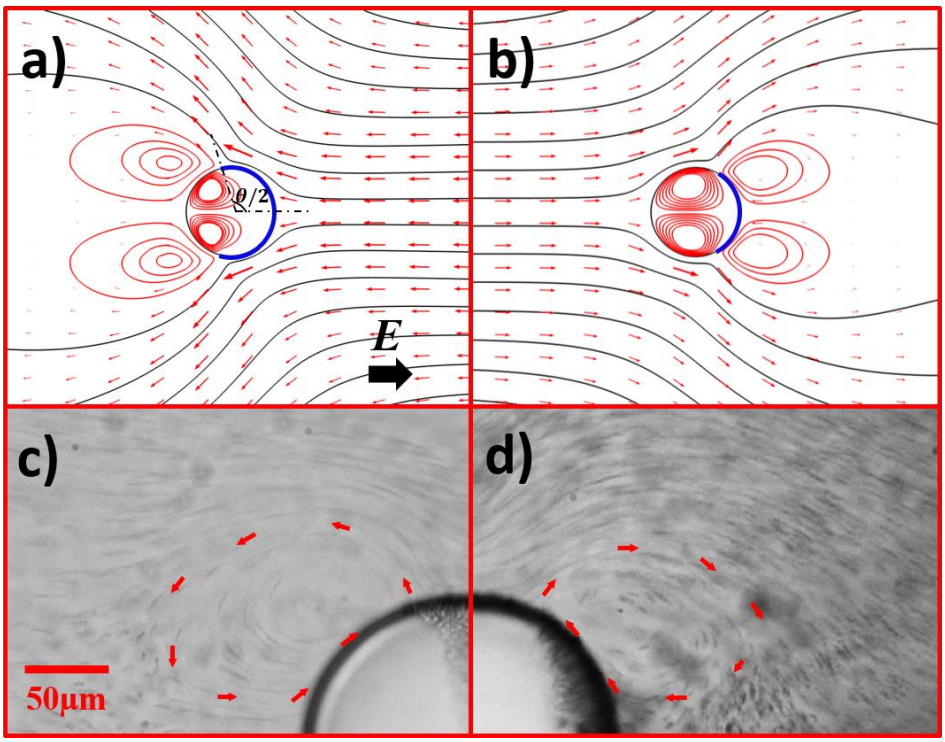

Figure 4-5. (a)-(b) Vortices around Janus droplets with different surface areas covered by positive surface charges under electrical field 60V/cm. The blue line carries positive surface charges. The surface coverage is $\theta/2 = 110°$ (a) and $\theta/2 = 60°$ (b). (c)-(d) Experimentally observed vortices around Janus droplets with different surface coverages by the positively charged nanoparticles under electrical field 60 V/cm. The surface coverage is $\theta/2 \approx 110°$ (c) and $\theta/2 \approx 60°$ (d).

4.3.3 Effect of the Electric Field on the Surface Coverage of the EIJDs and Vortices

In section 4.3.1, to analyze the influence of applied electric field on the vortices, we kept the surface coverage of the Janus droplet unchanged by making the nanoparticles tightly packed with each other under high electric field. However, under relative low electric field for limited time, the nanoparticles and cluster won't aggregate with each other, and the nanoparticle surface coverage of the Janus droplet is dependent on the applied electric field. When the external electrical field is applied, the positively charged nanoparticles move at the interface under the external electrical field force and accumulate to one polar of the oil droplet. As the accumulation of these

nanoparticles, the electrostatic repulsive force between the particles gets larger. At final state, the two forces acting on the nanoparticles, external electric force and repulsive force, are balanced, and the surface coverage by nanoparticles of the Janus droplet remains unchanged. However, once the strength of the electric field changes, the electric force acting on the nanoparticles changes, which will result in the variation of the nanoparticle surface coverage. For example, when the electric field increases, the electric force will increase and the distance between the nanoparticles will decrease; therefore, the nanoparticle surface coverage decreases finally.

Figure 4-6 shows the variation of the surface coverage by nanoparticles and vortices around the same Janus droplet under different electric fields, 40V/cm and 60V/cm. As shown in Figure 4-6(a), under the electric field 40V/cm, the nanoparticles are pushed to accumulate to the right side of the oil droplet and leave the pure oil-water interface on the left side. Small vortex forms on the side of the pure oil-water interface. When the electric field increases to 60V/cm (Figure 4-6(b)), the accumulation area of the nanoparticles decreases and leave a larger blank area on the other side; therefore, the vortex get larger and stronger.

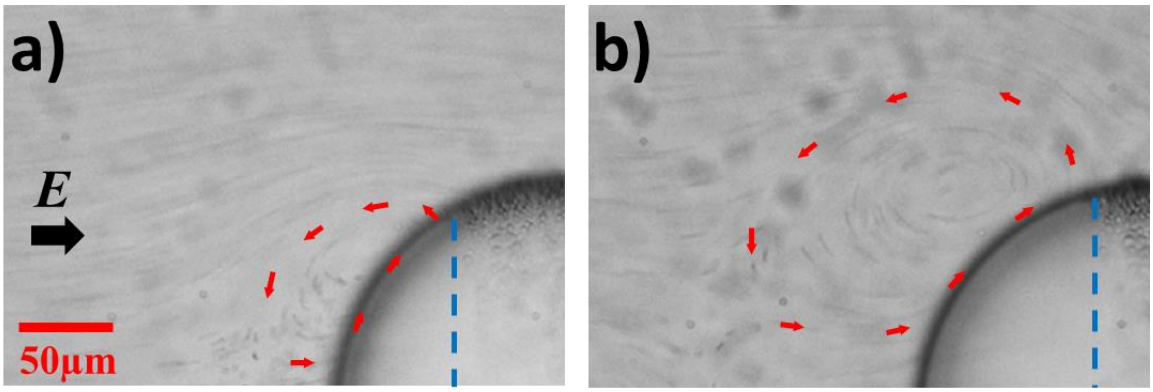

Figure 4-6. The variation of the surface coverage of the Janus droplet and vortices around it with different strengths of externally applied electrical fields (droplet diameter d = 215 μm). (a) E = 40V/cm; (b) E = 60V/cm.

4.4 Conclusions

Vortices around Janus droplets are studied in this paper. The results of the numerical simulations show that two vortices can be generated in the surrounding area of the Janus droplet under externally applied electric field. By comparing the numerical results under different circumstances, the following two conclusions can be drawn:

(a) If the surface coverage of the Janus droplet by the positively charged nanoparticles is the same, the strength of the vortices increases with the applied electric field;

(b) The variation of the surface coverage of the droplet by the positively charged nanoparticles will result in the change of the size and the location of the vortices.

(c) As the Janus droplets are generated under electric field, the strength of the externally applied electric field affects the accumulation area of the particles on the droplet (the surface coverage) within a certain range of the electric field. Generally, the accumulation area of positively charged particles decreases as the increase of the strength of the electric field; therefore, the size, position and strength of vortices vary with the electric field.

These findings are validated experimentally by visualizing the vortices around Janus droplets that are partially covered with positively charged aluminum oxide nanoparticles. The studies in this paper are important which can be used to develop novel technology for sorting and separation.

CHAPTER 5. Fundamental Research II:Nonlinear Electrokinetic Motion of EIJDs in Microchannels under a Relatively Weak Electric Field*

5.1 Introduction

As one of the electrokinetic phenomena, electrophoresis has been used as an efficient analytical technique in many fields, such as biomedical science [125,126], biochemistry [127–129] and colloidal science [130]. For example, Huang et al. [128] separated different size DNA molecules successfully in a micro-post array based on the electrophoresis of the DNA molecules. By applying asymmetric pulsed electric fields, the DNA molecules with different sizes undergo different electrophoretic velocities in the array and are sorted in different directions. Generally, for a uniformly charged particle with a thin electric double layer (EDL), the electrophoretic velocity of the particle in a bulk stationary liquid ($\vec{U}_{ep}$) is proportional to the strength of the externally applied electric field ($\vec{E}$), which is given by the well-known Helmholtz-Smoluchowski equation [131]:

$$\vec{U}_{ep} = \frac{\varepsilon_0 \varepsilon_w}{\eta_w} \zeta_p \vec{E} = \mu_{ep} \vec{E} \tag{5-1}$$

where ε_0 and ε_w are the permittivity of vacuum and the bulk liquid, respectively. η_w is the viscosity of the liquid, ζ_p is the zeta potential of the particle, and μ_{ep} is called the electrophoretic mobility. When the particle is injected into a microchannel, the motion of the particle results from both the electrophoresis of the particle and the electroosmotic flow (EOF) of the bulk liquid in the microchannel. The velocity of the electrokinetic motion, $\vec{U}_{ek}$, is characterized by:

$$\vec{U}_{ek} = \frac{\varepsilon_0 \varepsilon_w}{\eta_w} (-\zeta_w + \zeta_p) \vec{E} \tag{5-2}$$

where ζ_w is the zeta potential of the microchannel wall. According to Equation (5-2), the electrokinetic velocity of the charged particle also has linear relationship with the electric field.

---

* A similar version of this chapter was submitted or published as:

Li, M.; Li, D. Nonlinear Electrokinetic Motion of Electrically Induced Janus Droplets in Microchannels. *Submitted to **Journal of Colloid and Interface Science***.

For the electrophoresis of droplets with uniformly surface charges, both experimentally and theoretically studies have been reported extensively. Theoretically, Booth [132] first derived a formula for the electrophoretic velocity of charged droplets in terms of the applied electric field by retaining spherical shape of the droplets and neglecting the retardation effect. However, the formula disagrees with the experimental findings [133]. Later, Baygents and Saville [134] studied the electrophoresis of non-conducting droplets. They found that the liquid droplet performs as solid particle with the adsorption of ionic solutes and polarization. The expression of the electrophoretic mobility of a droplet in a salt-free medium was derived by Ohshima [135], which is a function of the size, viscosity and zeta potential of the liquid droplet. Experimentally, the effects of the concentration of surfactant, pH value and ion strength on the electrophoresis of charged oil droplets were studied in some published papers, respectively [136–139]. Overall, the concentration of surfactant, pH value and ion strength affect the electrophoretic motion by changing the zeta potential of the oil droplets. While keeping the above-mentioned parameters fixed, the electrophoretic mobility remains a constant value regardless of the electric field strengths; therefore, the electrophoretic velocity increases proportionally with the electric field strength.

As illustrated in Chapter 3, the EIJDs were fabricated by partially covering oil droplets with nanoparticles. As the nanoparticle coverage of the EIJDs is electric-responsive, the electrophoretic mobility of the Janus droplet varies with electric field, which leads to nonlinear relationship between the electric field and the electrokinetic velocity. In this chapter, nonlinear electrokinetic motion of the EIJDs in a microchannel was studied under both constant and time-varying electric fields. The lag of the variation of nanoparticle coverage of the EIJDs behind the change of electric field was characterized by measuring the evolution time of the nanoparticle film under different electric field strengths and by comparing the variations of nanoparticle coverage under different time-varying electric fields. In the study of the electrokinetic motion of the EIJDs in a microchannel, the electrokinetic velocities of the EIJDs under different electric field strengths and different time-varying electric fields were measured, respectively.

5.2 Experimental Section

5.2.1 Preparation of EIJDs

The EIJDs can be formed easily by applying direct current electric field to the Al_2O_3 nanoparticle-stabilized Pickering emulsion droplets. Briefly, prepare Al_2O_3 nanoparticle suspensions by adding Al_2O_3 nanoparticles (US Research Nanomaterials Inc., 18 nm in average diameter) into water and dispersing the nanoparticles with ultrasonic wave. Then, emulsify oil (canola oil, 100% pure, Mazola Corporation) into continuous water phase through vibration. The Al_2O_3 nanoparticle-stabilized Pickering emulsion can be formed by adding 500 μL emulsion droplets into Al_2O_3 nanoparticle suspension. Finally, the suspended EIJDs can be formed by applying electric field to the Pickering emulsion droplets.

5.2.2 Fabrication of Microfluidic Chip

The microfluidic chip was prepared with soft lithography method. In brief, a master with the designed patterns was structured first by following the processes of spin-coating, baking, exposuring and developing. After the master was fabricated, the pattern was duplicated by pouring PDMS-curing agent mixture (10:1, w/w, Sylgard 184, Dow Corning) onto it and heating at 80 ℃ for 1 h. After peeling off the cured PDMS layer from the master, and the microfluidic chip was formed by bonding the PDMS layer onto a glass substrate (VWR, VWR International) following plasma treatment (Harrick Plasma).

In the study of the effect of the electric field strength on the nanoparticle coverage of EIJDs and the electrokinetic velocity of EIJDs, a straight microchannel was designed and fabricated. The schematic diagram of the microchannel is shown in Figure 5-1(a). The size of the channel is 1 cm × 500 μm (length × width) with its two ends connecting to the confinement chamber and the outlet, respectively. The confinement chamber is circular with the diameter of 8 mm for holding the emulsion droplets. An inlet well is punched on the confinement chamber. While studying the nanoparticle coverage, the target EIJD should remain stationary for measurement. Therefore, to block the movement of EIJD under electric field, a pair of circular pillars (25 μm in diameter) is set in the downstream of the channel, as labelled in Figure 5-1(a). The center-to-center distance between the two pillars is 60 μm. The height of the microchannel is 80 μm.

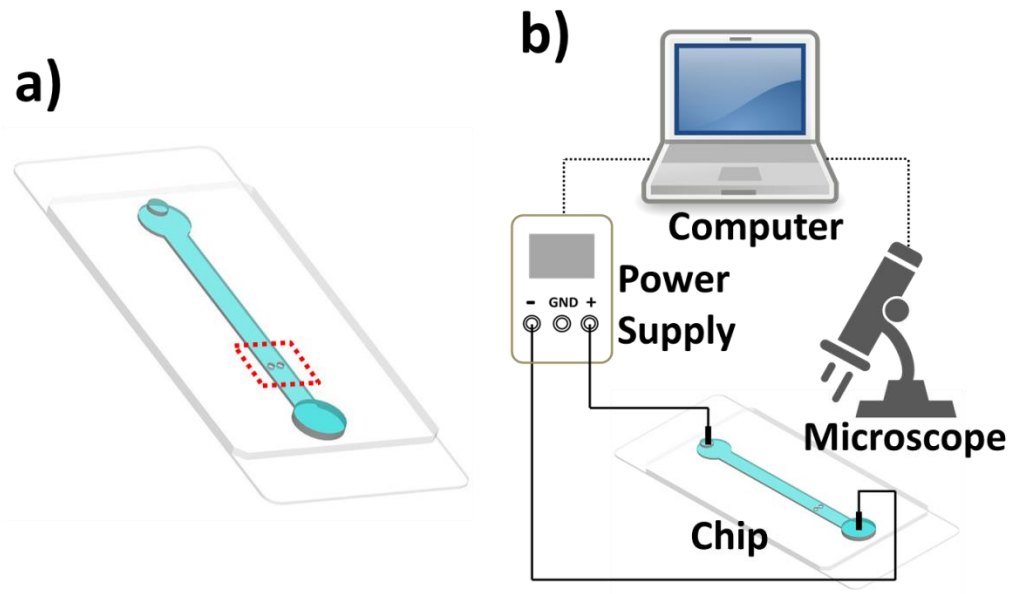

Figure 5-1. (a) Schematic diagram of the structure of the microfluidic chip; (b) schematic diagram of the experimental setup.

5.2.3 Analysis of Nanoparticle Coverage Evolution with Electric Fields

The nanoparticle coverage of the EIJDs can be detected under a microscope with the method and equation shown in section 3.2.2.4. The experimental setup consists of a microfluidic chip, a direct-current (DC) power supply, a bright-field microscope (Nikon Ti-E) and a computer. The electric field was provided by the DC power supply through two platinum electrodes, the strength of which is adjustable by changing the output voltages of the power supply (Figure 5-1(b)). In the experiments, the microchannel was wetted first by adding deionized water of 10 µL into the outlet. Then, 5 µL Al_2O_3 nanoparticle-stabilized emulsion droplets were added through the confinement chamber. Following this, deionized water of 50 µL was added into the inlet well. Due to the liquid level difference between the inlet well and the outlet well, the droplets was driven to move into the main channel, and one of the droplets can be trapped by the pillars in the downstream of the channel. Afterwards, the liquid level of the wells was balanced carefully by dropping deionized

water into the outlet well gradually. The electric field was applied by a power supply through the electrodes inserted in the wells. In the studies of the effect of the electric field strength on the nanoparticle coverage at steady state and the evolution time of the nanoparticle film under different electric field strengths, four serially connected DC power supplies (CSI12001X, Circuit Specialist Inc.) were employed to provide the voltage. In the study of the variation of nanoparticle coverage under time-varying electric fields, the pulsed electric fields were generated with a programmable power supply (BK Precision 1698, Yorba Linda, USA). In the experiments, the images of EIJDs were taken continuously by the microscope for later measurement and calculation.

5.2.4 Measurement of Electrokinetic Velocity

The electrokinetic velocities of EIJDs under different electric fields in a microchannel were determined by measuring the moving distance of EIJDs within a certain time interval. Briefly, the electric field, directed from inlet well to outlet well, was applied to the trapped droplet to fabricate EIJD. After this, the direction of the electric field was switched, directed from outlet well to inlet well, to drive the EIJD moving away from the pillars. As the EIJD is electrically anisotropic, with the switching of the electric field, the EIJD rotates to make its nanoparticle coated side backward the electric field constantly. Following this, the electrokinetic motions of the EIJD in the upstream of the microchannel under different electric fields were recorded at a rate of 25 frames/s. The accuracy of this system in determining the position of droplets was approximately ± 2 pixels corresponding to ± 1.1 μm. By analyzing the recordings, the electrokinetic velocities of the EIJDs were obtained finally. The electrokinetic velocities of EIJDs in both directions (towards both inlet well and outlet well) were measured, respectively, to eliminate the hydrostatic pressure effect. In the studies of the electrokinetic motion of EIJDs under different electric field strengths, four serially connected DC power supplies were employed to provide the voltage. While in the study of the electrokinetic motion of EIJDs under time-varying electric fields, the programmable power supply was used to generate time-varying electric fields. To indicate the effect of time-varying electric field on the electrokinetic motion, pulse electric fields with different variation speed were applied to the microchannel.

5.3 Results and Discussion

5.3.1 Evolution Time of the Nanoparticle Film

After applying electric field to the Al_2O_3 nanoparticle-stabilized Pickering emulsion, electrostatic forces are exerted on the nanoparticles, and the nanoparticles undergo electrokinetic motion on the oil droplets. The moving direction of the nanoparticles is identical to that of the electric field. The moving velocity of the nanoparticles depends on the electric field [140]. Generally, as the electric field strength increases, the velocity of the nanoparticles increases. Furthermore, as shown above, the variation rate of the nanoparticle coverage and hence the moving distance of the nanoparticles decreases with the further increase of the electric field when the applied electric field becomes relatively higher. Due to the combined effects of the increased velocity and the decreased moving distance, the evolution time of the nanoparticle film decreases with the increase of the electric field.

To study the effect of the electric field on the evolution time of the nanoparticle film of the EIJDs, the electric field applying to the EIJDs was increased gradually from 10 V/cm to 50 V/cm with the interval of 10 V/cm. Under a given electric field strength, the variation of the nanoparticle film was recorded, and the evolution time was measured with the recorded videos. The variation of the evolution time with the electric field is plotted in Figure 5-2. As shown in this figure, the time decreases significantly with the increase of the strength of the electric field. Initially, with E = 10 V/cm, it takes approximately 35 s for the nanoparticles to accumulate to the steady state. However, when E increases to 50 V/cm, only 5 s is needed for the EIJDs to reach the steady state. It should be noted that, the evolution time of nanoparticle film of the EIJDs were measured and analyzed only in the electric field increasing period. When the electric field starts to decrease gradually from 50 V/cm, the nanoparticle coverage changes very slowly, and the nanoparticles get dispersed quickly only under weak electric field (smaller than 10 V/cm). Therefore, it's hard to measure the evolution time of the nanoparticle film in the decreasing period of the electric field. Each test was repeated 10 times to calculate the average time and standard deviation.

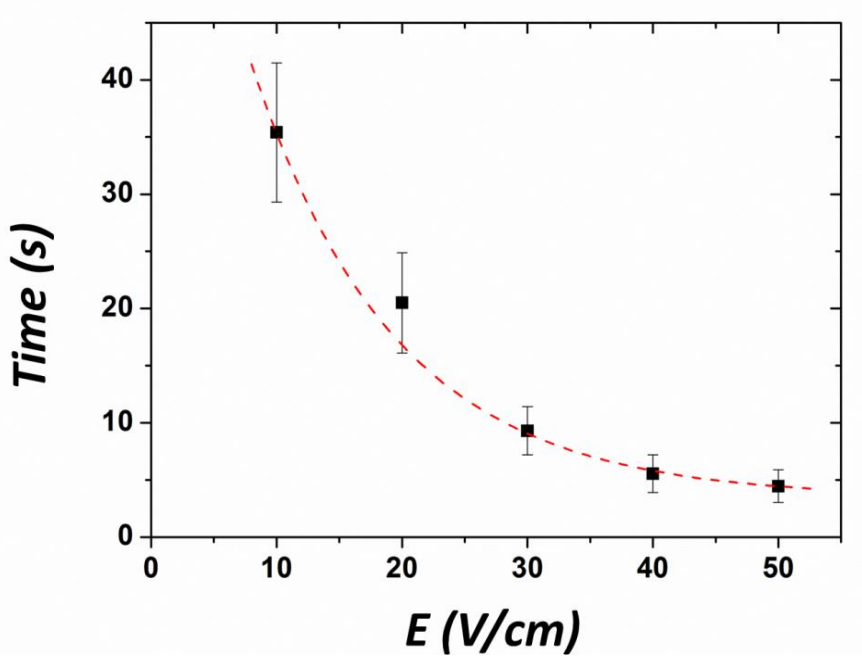

Figure 5-2. Effect of the strength of the electric field on the evolution time of the nanoparticle film of the EIJDs. The diameters of the EIJDs range from 50 μm to 75 μm. The EIJDs are formed from 1 mg/mL nanoparticle suspension.

5.3.2 Variation of Nanoparticle Coverage of EIJDs under Time-varying Electric Field

The variation of nanoparticle coverage of the EIJDs is different under different time-varying electric fields. As the evolution of the nanoparticle film of the EIJDs takes time, the variation of nanoparticle coverage lags behind the variation of the electric field. The lag of the variation of nanoparticle coverage is dependent on the speed of the electric field. Generally, the faster the variation speed of the electric field, the more significant the lag of the nanoparticle coverage variation. The variations of the nanoparticle coverage of an EIJD under different time-varying electric fields are shown in Figure 5-3(a), (b) and (c), respectively. The electric fields are pulsed, which increase from 0 to 50 V/cm then decrease to 0 within a time period t. As shown in these figures, the variation of γ (nanoparticle coverage) is different between the increasing and the decreasing periods of the electric field. Under the same strength of electric field, γ in the increasing period is larger than that in the decreasing period. This is because that, in comparison to the

accumulation of the nanoparticles in the electric field increasing period, the dispersion of the nanoparticles with the decrease of the electric field is very slow. Hence, the lag of the variation of γ is more significant in the decreasing process. To make convenient comparison, the fitting curves of γ under the time-varying electric fields with t = 20 s, 40 s and 60 s are plotted in the same figure (Figure 5-3(d)). As shown in this figure, with the decrease of t, the lag of γ becomes more significant. As a result, in the increasing process (the upper side of each curve), γ increases with the decrease of t under the same electric field strength. For the decreasing process, the variation trend is adverse that γ decreases with t. It should be noted that, to make accurate comparison, the same EIJD was employed and analyzed under the three different electric fields. 5 measures were conducted at each point to get the average nanoparticle coverage and the standard deviation.

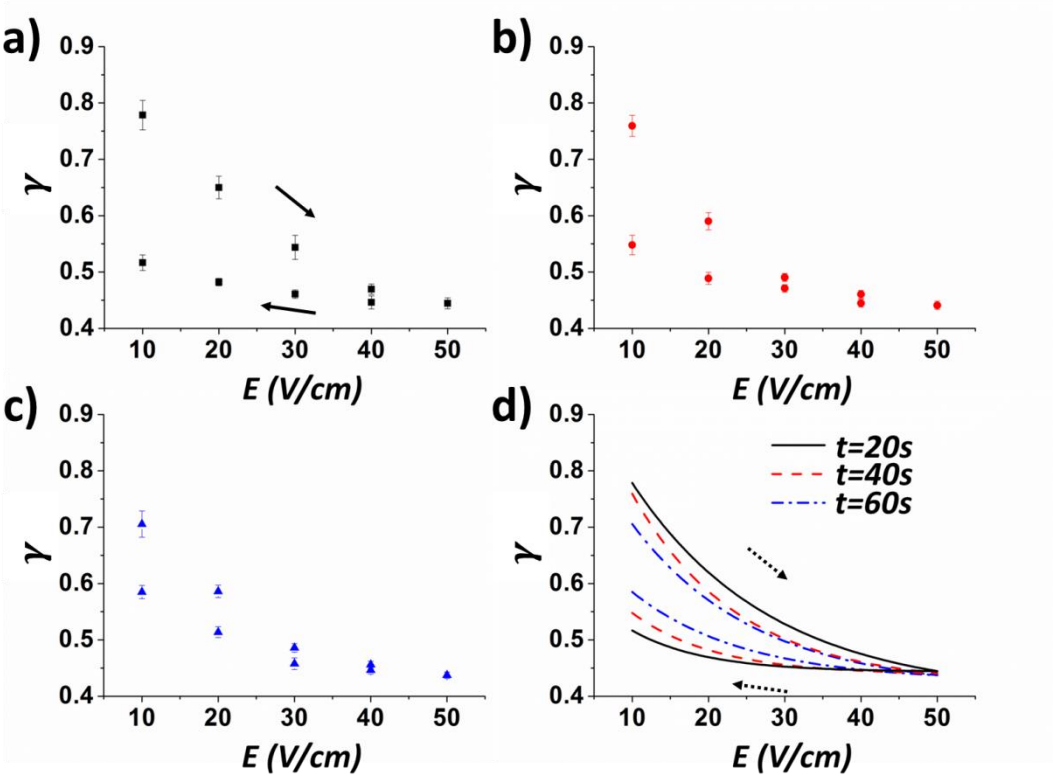

Figure 5-3. (a)-(c) The variation of nanoparticle coverage under different time-varying electric fields with t = 20 s (a), t = 40 s (b) and t = 60 s (c). (d) The fitting curves of θ under different time-varying electric fields. The EIJD is developed from 1 mg/mL nanoparticle suspension with the diameter of approximately 70 μm.

5.3.3 Electrokinetic Motion of EIJDs in a Microchannel

The electrokinetic motion of EIJDs in a microchannel is determined by the effects of the electrophoresis (EP) of the EIJDs and the electroosmotic flow (EOF) in the microchannel. Generally, for the droplets with fixed topology, both the EOF and EP have linear relationship with the electric field strength; therefore, the combined electrokinetic velocity increases proportionally with the electric field. However, for the EIJDs, the nanoparticle coverage changes with the electric field, as shown in Figure 3-12. This leads to nonlinear variation of the electrokinetic velocity of the EIJDs with the electric field. The experimentally measured electrokinetic velocities of EIJDs generated by using 1 mg/mL nanoparticle suspension under different electric fields are shown in Figure 5-4. As shown in this figure, the measured electrokinetic velocity increases with the electric field strength. When the electric field increases from 30 V/cm to 50 V/cm, the EOF in the microchannel increases with the electric field while the nanoparticle coverage of the EIJDs decreases significantly. When the electrophoresis of the EIJD is weaker than the EOF in the microchannel, the EIJD will carried by the EOF to move with the surrounding liquid. The increasing EOF leads to the increases of the electrokinetic velocity of EIJDs. The electrophoretic mobility is the ratio between the electrophoretic velocity and the electric field strength, as indicated in Equation (5-1). For an EIJD with surface area S and nanoparticle coverage of γ, the electrophoretic mobility of the EIJD is related to its average zeta potential ($\bar{\zeta}$). The average zeta potential of the EIJD is obtained by [85]:

$$\bar{\zeta} = \frac{1}{S}\int \zeta_0 dS = \zeta_{ow} \cdot (1-\gamma) + \zeta_{nano} \cdot \gamma \qquad (5\text{-}3)$$

where, ζ_0 is the local zeta potential, ζ_{ow} and ζ_{nano} are the zeta potentials of the oil-water interface and the nanoparticle film of the Janus droplet, respectively. In aqueous solution, ζ_{ow} is negative, while ζ_{nano} is positive [141–144]. Based on Equation (5-3), the reduction of nanoparticle coverage of the EIJDs (γ) with the electric field increase leads to both $\bar{\zeta}$ and hence the electrophoretic mobility of the EIJDs decreases. As a result, the increase of the electrokinetic velocity of the EIJDs slows down slightly as the electric field strength increases. When E is larger than 50 V/cm, the effect of electric field on the variation of the nanoparticle coverage is limited; therefore, the electrophoretic velocity increases almost linearly with the electric field. At least 20 measurements were applied under each condition.

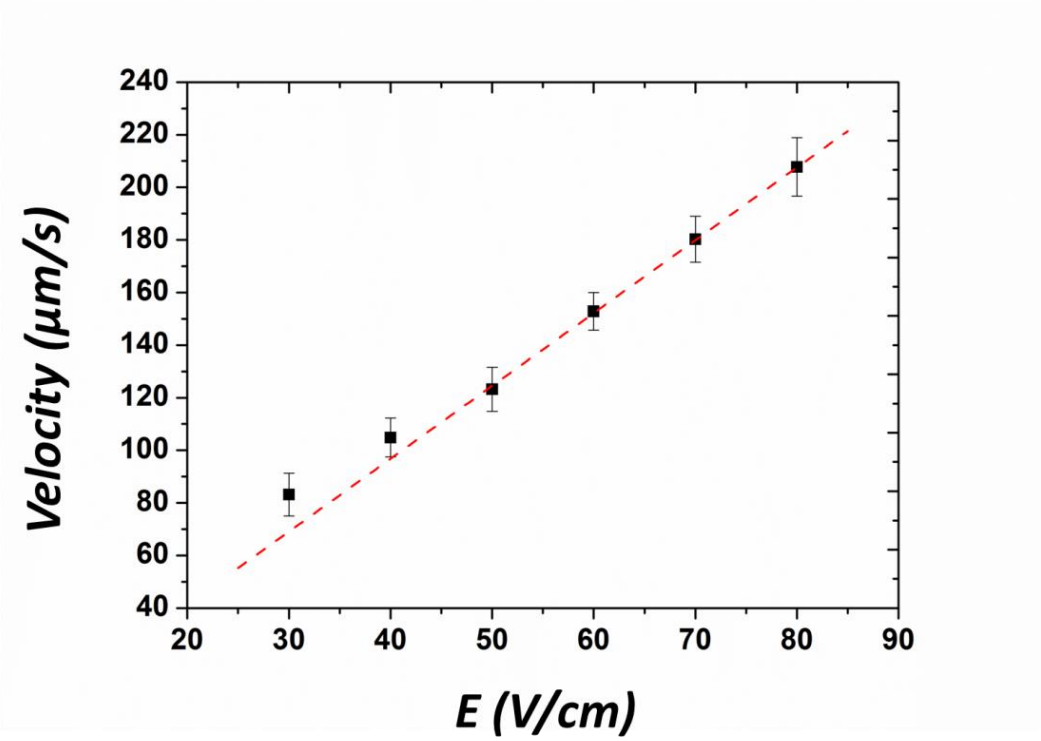

Figure 5-4. Experimental measured electrokinetic velocities of the EIJDs generated from 1 mg/mL nanoparticle suspension as a function of the electric field. The diameter of the EIJDs ranges from 50 μm to 75 μm.

5.3.4 Electrokinetic Motion of EIJDs under Time-varying Electric Fields

The variation of the electrokinetic velocity of the EIJD fabricated from 1 mg/mL nanoparticle suspension under time-varying electric fields is shown in Figure 5-5. The schematic diagram of the motion of an EIJD in a microchannel under pulsed electric field is shown in Figure 5-5(a). As the lag of the variation of nanoparticle coverage takes place under time-varying electric fields, the variations of the electrokinetic velocities of the EIJD are different under different electric fields. The variations of the electrokinetic velocity of the EIJD under different time-varying electric fields are shown in Figure 5-5(b) to (d), respectively.

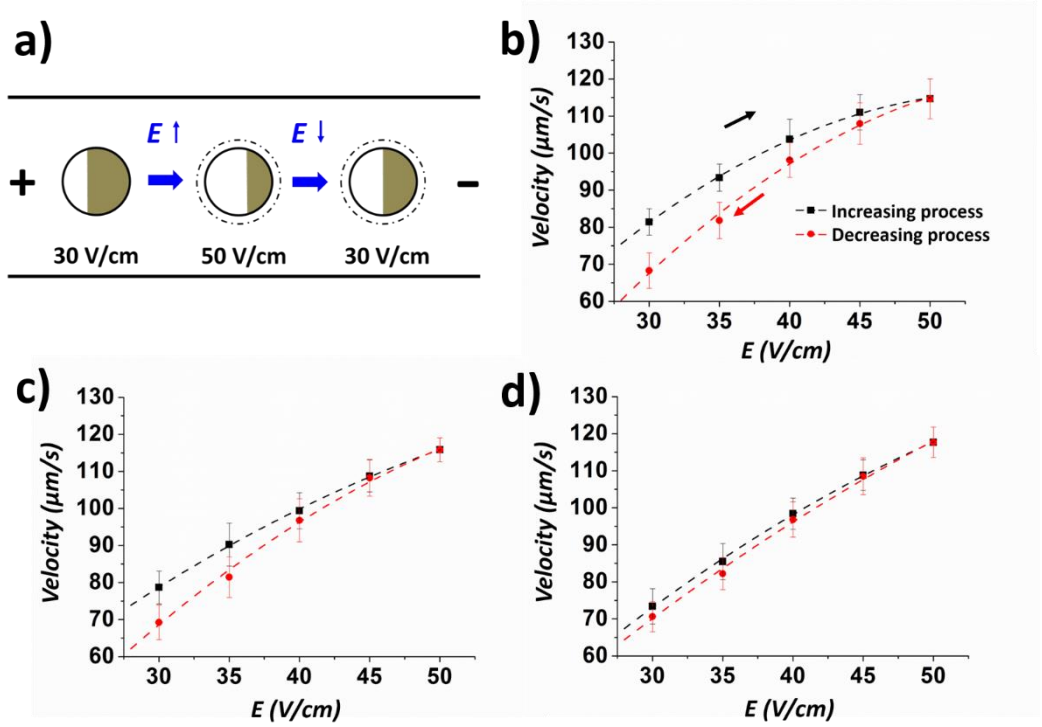

Figure 5-5. (a) Schematic diagram of the electrokinetic motion of the EIJD under time-varying electric field. (b)-(c) The variation of electrokinetic velocities of EIJDs under time-varying electric field with t = 20 s (b), t = 40 s (c) and t = 60 s (d). The diameter of the EIJD is approximately 70 μm. The black rectangular points represent the velocities at increasing period of electric field. The red circular points represent the velocities at decreasing period of electric field.

The electrokinetic velocities of the EIJD in the increasing period of electric field are shown by the black rectangular points, and those in the decreasing period are shown with the red circular points. As shown in this figures, at the increasing period, with the increase of the EOF in the microchannel, the electrokinetic velocity increases. However, due the reduction of the nanoparticle coverage of the EIJD as the electric field increases, the electrophoretic mobility decreases gradually. Therefore, the combined electrokinetic velocity increases with gradually decreasing slope. The situation is reversed in the decreasing period, that is, the electrokinetic velocity decreases with increasing rate.

This variation of the electrokinetic velocity results from the decrease of the EOF and the increase of the electrophoretic mobility of the EIJD with the decrease of the electric field strength. Due to the lag effect, the nanoparticle coverage of the EIJDs in the increasing period is larger than that in the decreasing period under the same strength of electric field. Hence, the electrokinetic velocity at increasing period is larger. The comparison between Figure 5-5(b), (c) and (d) indicates that with the increase of t, the lag effect becomes insignificant, and the difference between the velocities in different periods gets smaller. In the experiments, at least 20 measurements were applied under each condition.

5.4 Conclusions

The nonlinear electrokinetic motion of EIJDs in a microchannel was studied in this chapter. The EIJDs were fabricated by operating aluminum oxide nanoparticles to partially cover one side of the oil droplet under electric field. The nanoparticle coverage of the EIJDs was dependent on the electric field strength. Generally, as the electric field strength increases, the nanoparticle coverage of the EIJDs decreases. The lag of the variation of the nanoparticle coverage of the EIJDs with respect to the applied electric field was studied under different pulsed electric fields. The experimental results indicate that, due to the lag effect, the variation of the nanoparticle coverage is different between the increasing and the decreasing periods of the electric field. The faster the variation of the electric field, the more significant the lag effect. Because of the variation of the nanoparticle coverage of EIJDs, the electrokinetic velocities of EIJDs in a microchannel were affected. As the electric field increases, the electrokinetic velocity of the EIJDs increases while the electrophoretic mobility decreases. Therefore, the electrokinetic velocity of the EIJDs increases nonlinearly with the electric field strength. Under time-varying electric fields, due to the lag effect, the variations of the electrokinetic velocity are different in the increasing and decreasing periods of the electric field. Under the same electric field strength, the electrokinetic velocity of the EIJDs in the increasing period is larger than that in the decreasing period.

CHAPTER 6. Fundamental Research III: Electrokinetic Motion of EIJDs in Microchannels under a Relatively High Electric Field[*]

6.1 Introduction

In chapter 5, the electrokinetic motion of the EIJDs under a relatively weak electric field is studied. Under the electric field smaller than 50 V/cm, the nanoparticle coverage of the EIJDs changes significantly with the electric field strength; therefore, the electrokinetic velocity of the EIJDs is nonlinearly proportional to the electric field strength. However, this situation is different under electric field higher than 50 V/cm. As shown in section 3.3.6, the nanoparticle coverage of the EIJDs almost remains constant when the electric field becomes larger than 50 V/cm. As a result, the electrokinetic motion of the EIJDs under a relatively high electric field is different.

In this chapter, the electrokinetic motion of the EIJDs with fixed nanoparticle coverage was studied both numerically and experimentally. Numerically, a theoretical model is constructed to calculate the electrokinetic velocity of the Janus droplet by considering the force balance on the surface of the Janus droplet at steady state. In the model, the effects of the electric double layer and surface charges on the motion at the oil-water interface are considered. The effects of five parameters on the electrokinetic motion of the Janus droplets are studied: the strength of the electric field, the ratio of the zeta potential of the positively charged side of the Janus droplet to that of the negatively charged side, the ratio of the viscosity of the oil phase to that of the water phase, the nanoparticle coverage of the Janus droplet, and the ratio of the diameter of the Janus droplet to that of the cylindrical microchannel. To confirm the numerical findings, the electrokinetic motion of the EIJDs in a microchannel under electric field larger than 50 V/cm is studied, and the numerical results and the experimental results are compared.

---

[*] A similar version of this chapter was submitted or published as:

(a) Li, M.; Li, D. Electrokinetic Motion of an Electrically Induced Janus Droplet in Microchannels. *Microfluid. Nanofluid.* **2017**, 21, 16. https://link.springer.com/article/10.1007/s10404-016-1838-7

(b) Li, M.; Li, D. Fabrication and Electrokinetic Motion of Electrically Anisotropic Janus Droplets in Microchannels. *Electrophoresis.* **2017**, 38, 287-295. https://onlinelibrary.wiley.com/doi/abs/10.1002/elps.201600310

6.2 Theoretical Model

We consider an electrically induced Janus oil droplet with one side covered with a compact layer of positively charged nanoparticles in a circular microchannel filled with an aqueous solution, as shown in Figure 6-1(a). The oil-water interface of the droplet without the nanoparticles carries negative surface charges. To simplify the model, the gravity effect is neglected and the Janus droplet is suspended at the center of the microchannel. As two sides of the Janus droplet carries opposite surface charges, a dipolar electric double layer (EDL) forms in the vicinity of the Janus droplet. Under externally applied electrical field, electroosmostic flows are generated in opposite directions on different sides of the Janus droplet, which results in vortices around the droplet and affects the electrophoresis of the Janus droplet (Figure 6-1(b)). The interaction between the electric field and the net charges in the EDL of the channel wall generates electroosmotic flow (EOF) in the microchannel. Both the electroosmotic flow in the microchannel and the electrophoresis of the Janus droplet contributes to the motion of the Janus droplet. Furthermore, the oil-water interface on the side of the Janus droplet without the presence of the nanoparticles is mobile; therefore, the external bulk EOF in the microchannel and the EOF along the oil-water interface will induce axisymmetric vortexes inside the droplet, which also affect the droplet motion. It should be noted that under electrical field, the EIJD is aligned with the positively charged side facing the cathode and the negatively charged side facing the anode. At steady state, the Janus droplet moves along the microchannel translationally without rotation.

As shown in Figure 6-1, the cylindrical coordinate system is set up with the origin point, *O*, located at the center of the moving droplet; therefore, relative to the coordinate, the Janus droplet keeps stationary and the channel wall moves with the velocity of $-\vec{U}_d$ where $\vec{U}_d$ is the velocity of the droplet motion. The angle between the center line of the microchannel and the radial-vector from the center of the Janus droplet to the boundary of the nanoparticle covered area is defined as $\theta/2$. This angle $\theta/2$ is used to indicate the nanoparticle coverage on the Janus droplet.

To simplify the model, the following assumptions have been made: (1) Compared with the diameter of the oil droplet, the thickness of the nanoparticle film is negligible; (2) the oil droplet and the mcirochannel wall are considered as electrically non-conducting; (3) the electric double

layer around the Janus droplet is thin, so that the retardation effect is neglected; (4) the gravity effect is neglected; (5) under weak electric field, the Janus droplet is considered non-deformable.

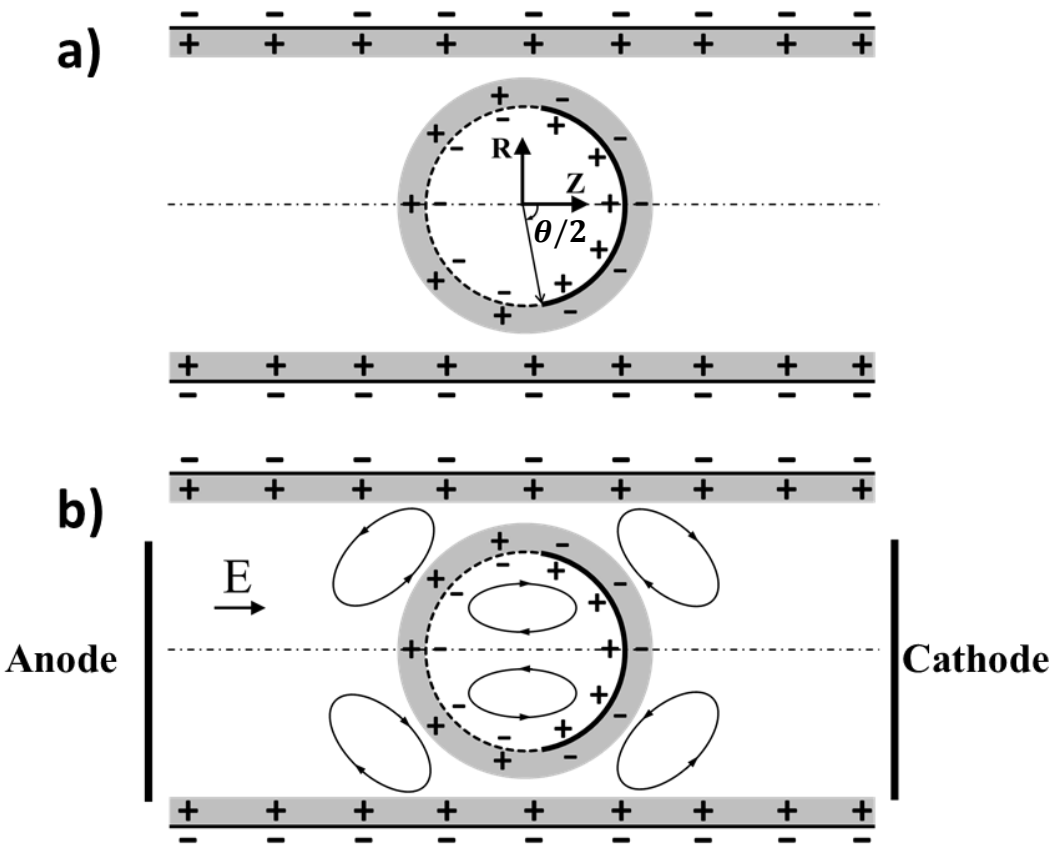

Figure 6-1. The schematic diagram of a spherical Janus droplet in a cylindrical microchannel with a circular cross section. (a) The geometry and the coordinate of the system. (b) The flow fields inside and outside of the Janus droplet in electric field.

6.2.1 EDL Field

When contacting with an aqueous solution, the channel wall, the oil-water interface and the nanoparticle film carry surface charges. The charged surfaces attract counter-ions from the liquid

and EDLs form in the water phase. The potential of EDL field ψ is described by the well-known Poisson-Boltzmann equation [67]:

$$\nabla^2\psi = \frac{2n_\infty ze}{\varepsilon_0\varepsilon_w} sinh(\frac{ze\psi}{k_bT}) \quad (6\text{-}1)$$

where n_∞ is the ionic concentration of the aqueous solution, z is the absolute value of the ionic valence, e is the elementary charge, k_b is the Boltzmann constant, T is the absolute temperature, ε_0 and ε_w are the permittivity of vacuum and the solution, respectively.

The boundary conditions are:

$$\psi = \zeta_w \quad \text{at the channel wall} \quad (6\text{-}2)$$

$$\psi = \zeta_{ow} \quad \text{at the negatively charged side of the droplet} \quad (6\text{-}3)$$

$$\psi = \zeta_{nano} \quad \text{at the positively charged side of the droplet} \quad (6\text{-}4)$$

where ζ_w is the zeta potential of the channel wall, ζ_{ow} is the zeta potential on the negatively-charged side of the Janus droplet and ζ_{nano} is the zeta potential on the positively-charged side of the Janus droplet.

According to the theory of electrokinetics, the local net charge density in the aqueous electrolyte solution ρ_e is given by:

$$\rho_e = -2n_\infty zesinh(\frac{ze\psi}{k_bT}) \quad (6\text{-}5)$$

6.2.2 Electric Field

As shown in Figure 6-1(b), the electric field is applied from left to right through two ends of the microchannel. The Laplace's equation is used to determine the distribution of the applied electrical potential ϕ in the solution:

$$\nabla^2\phi = 0 \quad (6\text{-}6)$$

With the consideration that both the Janus droplet and the channel wall are non-conducting, the following boundary conditions are set in the model:

$\phi = \phi_0$ at the inlet of the channel (6-7)

$\phi = 0$ at the outlet of the channel (6-8)

$\vec{n} \cdot \nabla \phi = 0$ at the droplet surface and the channel wall (6-9)

here $\vec{n}$ is the unit normal vector at the channel wall and the surface of the Janus droplet.

6.2.3 Flow Field

The fluids inside and outside of the Janus droplet are incompressible, and the flow fields can be described by the Navier-Stokes equation and the continuity equation:

$$\rho \left[\frac{\partial \vec{u}}{\partial t} + \vec{u} \cdot \nabla \vec{u}\right] = -\nabla P + \eta \nabla^2 \vec{u} + \vec{F}_e \quad (6\text{-}10)$$

$$\nabla \cdot \vec{u} = 0 \quad (6\text{-}11)$$

where ρ and η are the density and viscosity of the liquid, respectively. ∇P is the pressure gradient, and $\vec{F}_e$ is the body force which is cause by the interaction between the applied electric field and the net charges in the liquid:

$$\vec{F}_e = \vec{E}_o \rho_e \quad (6\text{-}12)$$

where $\vec{E}_o = -\nabla \phi$ is the local applied electrical field; and ρ_e is the local net charge density in the aqueous electrolyte solution, as given by Equation (6-5).

At steady state, the flow field doesn't change with time; therefore, the time item $\frac{\partial \vec{u}}{\partial t}$ can be neglected. As the flow speed in microchannels is very low, the inertia term $\vec{u} \cdot \nabla \vec{u}$ is negligible. For the water phase, the Navier-Stokes equation (Equation (6-10)) is reduced to:

$$\nabla P = \eta_w \nabla^2 \vec{u}_w + \vec{F}_e \quad (6\text{-}13)$$

The oil is electrically neutral (no net change); therefore, the Navier-Stokes equation can be further simplified by removing the electrical body force item, F_e. Hence, for the oil phase,

$$\nabla P = \eta_o \nabla^2 \vec{u}_o \tag{6-14}$$

where η_w and η_o are the viscosities of water and oil, and $\vec{u}_w$ and $\vec{u}_o$ are the velocities of water and oil, respectively. As illustrated above, the cylindrical coordinate system is set in the oil droplet. Relative to the coordinate system, the mobile Janus droplet remains stationary, and the microchannel wall moves with the opposite velocity of the droplet motion, $-\vec{U}_d$, which leads to the boundary condition of Equation (6-15). The no-slip boundary condition, Equation (6-16), is applied to the positively charged side of the Janus droplet (i.e., the rigid nanoparticle film). The inlet and outlet of the microchannel are set as open boundaries without the effect of pressure gradient and viscous stress (Equation (6-17)).

$$\vec{u}_w = -\vec{U}_d \qquad \text{at the channel wall} \tag{6-15}$$

$$\vec{u}_w = 0 \qquad \text{at the positively charged side of the Janus droplet} \tag{6-16}$$

$$\vec{n} \cdot \nabla \vec{u}_w = 0 \qquad \text{at the inlet and outlet} \tag{6-17}$$

For the negatively charged side of the Janus droplet, the pure oil-water interface is mobile. Under the applied electric field, the boundary condition of the oil-water interface is given by the electric double layer and surface charges (EDL+SC) model by considering the shear stress continuity at the oil-water interface [121–124]:

$$\vec{u}_w = \vec{u}_o \tag{6-18}$$

$$\frac{\partial \vec{u}_w}{\partial \vec{n}} - \frac{\eta_o}{\eta_w}\frac{\partial \vec{u}_o}{\partial \vec{n}} + \frac{\sigma_s \vec{E}_o}{\eta_w} = 0 \tag{6-19}$$

σ_s is the local surface charge density at the interface, which is given by:

$$\sigma_s = \frac{4 n_\infty z e}{\kappa} sinh\left(\frac{ze\zeta_0}{2k_b T}\right) \tag{6-20}$$

here, κ is the Debye-Hückel parameter ($\kappa = \sqrt{2n_\infty z^2 e^2 / \varepsilon_0 \varepsilon_w k_b T}$).

6.2.4 Droplet Velocity

Under externally applied electrical field, the charged Janus droplet experiences the electrostatic force $\vec{F}_{e,J}$. Meanwhile, the fluid flow around the droplet exerts hydrodynamic force on the Janus droplet $\vec{F}_h$. The hydrodynamic force can be divided into two parts: the hydrodynamic force generated by the fluid flow outside of EDL ($\vec{F}_{ho}$) and the hydrodynamic force generated by the fluid flow inside of EDL ($\vec{F}_{hin}$). The net force $\vec{F}_{net}$ acting on the Janus droplet is:

$$\vec{F}_{net} = \vec{F}_{e,J} + \vec{F}_{ho} + \vec{F}_{hin} \tag{6-21}$$

To calculate the force acting on the Janus droplet, the water phase is divided into two regions, the inner region and the outer region. The inner region is defined as the electrical double layer on the Janus droplet, and the outer region is the remainder of the water phase. For fully developed EOF in the EDL around the Janus droplet, it can be shown that $\vec{F}_{e,J} = -\vec{F}_{hin}$ [78]. Therefore, at stable state, $\vec{F}_{net}$ is equal to $\vec{F}_{ho}$. Without considering the gravity effect, $\vec{F}_{net}$ is given by [145]:

$$\vec{F}_{net} = \vec{F}_{ho} = -\oint\left\{-P\bar{\bar{I}} + \eta_w[(\nabla\,\vec{u}_w) + (\nabla\,\vec{u}_w)^T]\right\}\cdot\vec{n}dS \tag{6-22}$$

where $\bar{\bar{I}}$ is identity tensor. It should be noted that in Equation (6-22), $\vec{u}_w$ is the velocity of water outside of the EDL around the Janus droplet. The net force acting on the Janus droplet can be obtained by substituting the calculated flow field of the outer region into Equation (6-22).

At steady state, the net force acting on the Janus droplet should be equal to zero [76]:

$$\vec{F}_{net} = -\oint\left\{-P\bar{\bar{I}} + \eta_w[(\nabla\,\vec{u}_w) + (\nabla\,\vec{u}_w)^T]\right\}\cdot\vec{n}dS = 0 \tag{6-23}$$

While solving the above-described model numerically, different values of $-\vec{U}_d$ (Equation (6-15)) are used in an iterative method. The one that satisfies Equation (6-23) is the electrokinetic velocity of the Janus droplet $\vec{U}_{ek}$.

Table 6-1. Values of parameters used in the simulation

Parameters	Values
Dielectric constant of water ε_w	80
Permittivity of vacuum ε_0 (C/V m)	8.854×10^{-12}
Viscosity of water η_w (Pa·s)	0.001
Density of water ρ_w (kg/m^3)	1000
Density of oil ρ_o (kg/m^3)	900
Length of the channel L (μm)	500
Diameter of the channel D (μm)	150
Zeta potential of the channel wall ζ_w (mV)	−60
Zeta potential of the negative side of the oil droplet ζ_{ow} (mV)	−25

6.2.5 Numerical Simulation

As described above, in order to evaluate the electrokinetic velocity of the Janus droplet, a multi-physics model is developed to simulate the EDL field, the electric field and the flow fields inside and outside of the Janus droplet. As the geometry of the model is symmetric around the z-axis (see Figure 6-1(a)). Therefore, a 2D axisymmetric multi-physics model is built with the commercial software COMSOL. In the model, the length of the microchannel is 500 μm and the diameter of it is 150 μm. The zeta potential on the channel wall is set to be −60 mV. Electric field E is applied to the microchannel through the inlet and outlet of the microchannel. The Janus oil droplet with the diameter of d is placed at the center of the circular microchannel. The zeta potential of the positively charged side of the Janus droplet is ζ_{nano} and that of the negatively charge side is ζ_{ow}. As the EDLs in vicinity of the charged microchannel and the Janus droplet are very thin, extremely fine mesh elements were used in these regions. The total number of mesh elements used for calculation is 104,477. The values of the parameters used in the simulation are shown in Table 6-1.

6.3 Experimental Section

6.3.1 Formation of EIJDs in a microchannel

In this study, the microfluidic chip was made by the soft lithograph method by bonding a polydimethylsiloxane (PDMS) layer with a microchannel on a glass substrate. Briefly, the master of the PDMS microstructure was fabricated first by coating photoresist (SU-8 2075, MicroChem, USA) onto a silicon wafer. Then, a film carrying the pattern was placed on top of the wafer coated with a SU8 film after soft baking. And expose them to ultraviolet (UV) light. With the post exposure baking and the developing processes, a master with microchannel pattern on the silicon wafer was obtained. The mixture of PDMS and the curing agent (10:1 (w/w)) was poured on the master and heated at 80℃ for 1h. The PDMS layer with the microchannel structures was then peeled off carefully from the master and put into a plasma cleaner (HARRICK PLASMA, Ithaca, NY) with a glass slide for 1min. Finally, the microfluidic chip was assembled by placing the PDMS layer on the top of the glass slide. As shown in Figure 6-2(a), the microfluidic chip comprises a straight microchannel with a size of 1cm × 150μm × 80μm (length × width × height) for the formation and motion of Janus droplets and a confinement chamber with a size of 0.5cm × 1cm × 80μm (length × width × height) for holding droplets. An electrode insert port with the diameter of 1.5mm is set next to the joint between the confinement chamber and the microchannel for placing electrode. The effect of the droplets in the confinement chamber on the electric field can be eliminated by inserting the electrode into this port rather than into the inlet well. Another electrode is inserted in the outlet well.

After the microfluidic chip was fabricated, 10μL buffer solution was added into the outlet well first to wet the microchannel. Then 5μL Pickering emulsion droplets (prepared with the procedures shown in Section 3.2.2) was added into the inlet well and the droplets would flow into the droplet confinement chamber. Due to the limitation of the height of the confinement chamber, only those droplets with the diameter smaller than 80μm could enter it. Afterwards, 100μL buffer solution was loaded into the inlet well and outlet well, respectively. The electrical field was applied to the microchannel with a DC power supply (CSI12001X, Circuit Specialist Inc., USA) via two platinum electrodes inserted in the electrode insert port and outlet well, respectively. Under electrical field, the oil droplets entered the microchannel from the confinement chamber and

moved through it. At the same time, the positively charged Al_2O_3 nanoparticles adsorbed on the oil droplet were accumulated to one side of the oil droplet back to the electric field. Janus droplets partially covered with Al_2O_3 nanoparticles could be formed in this way, as shown in Figure 6-2(b). The images of a droplet with uniformly covered Al_2O_3 nanoparticles before applying electrical field and a Janus droplet with Al_2O_3 nanoparticles covered on one side after applying the electric field are shown in Figure 6-2(c). As shown in this figure, after applying DC electrical field of 50V/cm from left to right, the positively charged nanoparticles move to the right-hand side of the droplet and a color and electrically anisotropic Janus droplet forms.

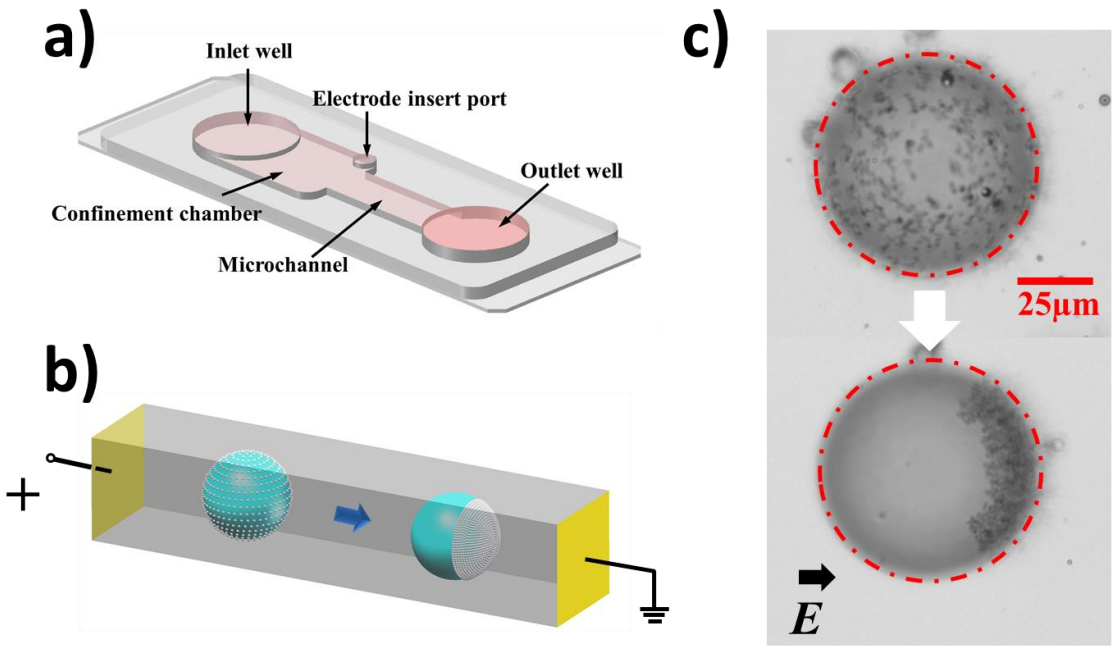

Figure 6-2. (a) Schematic diagram of the structure of the microfluidic chip. (b) Schematic diagram of the generation of an EIJD under applied DC electric field. (c) The formation of the EIJD under electric field of 50 V/cm.

6.3.2 Visualization of Vortices

Spherical polystyrene particles of 1μm in diameter (Bangs Laboratories Inc., IN, USA) were employed as tracers to indicate the flow fields around Janus droplets. The experimental system, as shown in Figure 6-3, is composed of the microfluidic chip, a DC power supply, an optical microscope (Ti-E, Nikon) and imaging system. In the experiment, the microfluidic chip which held nanoparticle covered oil droplets was fixed on the microscope stage, and the liquid levels in the inlet and outlet wells were carefully balanced by injecting certain amount of tracing particle suspension with a digital pipette. Then apply electric field to the microchannel via two platinum electrodes inserted in the electrode insert port and the outlet well. Under this electrical field, Janus droplets formed quickly in the microchannel and the surface coverage (γ) remained constant under the given electric field. The flow fields around Janus droplets were observed in the electrical field of 30V/cm. The images of the flow fields around Janus droplets were taken by a charge coupled device (CCD) camera (DS-Qi1Mc ,Nikon) assembled in the microscope, and were stored in a computer. Generally, the flow field changes with the variation of the topology of the Janus droplets. The flow fields around Janus droplets with different surface coverage generated with 1mg/mL and 2mg/mL nanoparticle suspension were observed, respectively.

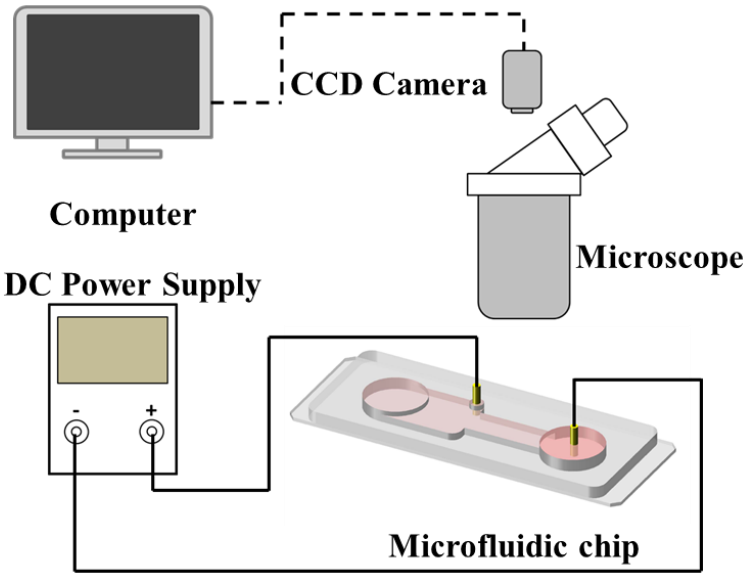

Figure 6-3. Schematic diagram of the experimental setup.

6.3.3 Measurement of the Electrokinetic Velocity of the EIJDs

The electrokinetic motions of oil droplets and Janus droplets were measured with the same experimental system as shown in Figure 6-3. The motions of oil droplets/Janus droplets were recorded by the CCD camera at the frame rate of 25 fps under externally applied electrical field. The accuracy of this system in determining the position of droplets was approximately ± 2 pixels corresponding to ± 1.1 μm. By measuring the travelling distance under certain time for an individual droplet with imaging analysis software, the velocity of the Janus droplet could be obtained. Under each condition, 30 independent measurements were conducted. The experiments were carried out at room temperature (23-25℃).

Furthermore, to minimize the effect of hydrostatic pressure on the electrokinetic motion of Janus droplets, two measures were adopted: a) Large inlet and outlet wells were used to minimize the water level difference caused by electroosmotic flow in microchannel; b) After applying the electrical field for 30~40 s, the electric field was reversed to balance the water level of the wells.

6.4 Numerical Results and Discussion

As mentioned above, the translational movement of an EIJD in a microchannel under electric field is studied in this paper. By setting up a 2D axisymmetric model, the EDL field, electric field, the flow fields and finally, the electrokinetic velocity of the Janus droplet at steady state are calculated with the finite element method (FEM). In this study, the effects of the strength of the electric field (E), the zeta potential of the positively charged side of the Janus droplet (ζ_{nano}), the viscosity of the droplet (η_o), the surface coverage of the positively charged side ($\theta/2$, the relationship between θ and γ is given in Equation (3-1)), as well as the size of the Janus droplet on the electrokinetic velocity of the Janus droplet are analyzed. To make the results more general, the following parameters are non-dimensionalized:

$$\zeta_r = |\zeta_{nano}/\zeta_{ow}| \quad \text{zeta potential ratio} \tag{6-24}$$

$$\eta_r = \eta_o/\eta_w \quad \text{viscosity ratio} \tag{6-25}$$

$$r = d/D \qquad \text{size ratio} \tag{6-26}$$

$$U_{ek}^{*} = \left|\vec{U}_{ek}/U_{ref}\right| \quad \text{dimensionless velocity} \tag{6-27}$$

where U_{ref} is the reference velocity which is set to be 10^{-4} m/s. In simulations, to completely study the effects of these influence factors on EK motion, the values of these factors are set to change in a wide range. For example, in the study of the effect of the nanoparticle coverage on the EK motion, the nanoparticle coverage changes from $\frac{\theta}{2} = 0$ (homogeneous oil droplet) to $\frac{\theta}{2} = 180°$ (Pickering emulsion droplet).

6.4.1 Model Validation

For a negatively charged solid particle immersed in a bulk aqueous solution, under externally applied DC electric field, the particle moves towards the anode. This phenomenon is called electrophoresis. The electrophoretic velocity $\vec{U}_{ep}$ of such a particle with thin EDL can be calculated by the well-known Helmholtz-Smuluchowski equation:

$$\vec{U}_{ep} = \frac{\varepsilon_0 \varepsilon_w \zeta_p}{\eta_w} \vec{E} \tag{6-28}$$

where ζ_p is the zeta potential of the negatively charged solid particle. The dimensionless electrophoretic velocity can be derived from this equation as:

$$U_{ep}^{*} = \left|\frac{\vec{U}_{ep}}{U_{ref}}\right| = \frac{\varepsilon_0 \varepsilon_w \zeta_p}{\eta_w U_{ref}} \left|\vec{E}\right| \tag{6-29}$$

A homogeneous negatively-charged solid particle can be regarded as a special Janus droplet with $\eta_o \to \infty$ and $\theta = 0°$. Therefore, the model presented in this chapter can be used to calculate the electrophoretic velocity of a homogeneous solid particle in an infinitely large aqueous solution by considering that the zeta potential of the microchannel wall is zero and the diameter of the microchannel is greatly larger than the size of the particle. The comparison between the numerical simulation and the Helmholtz-Smuluchowski equation is shown in Figure 6-4. The solid line represents the analytical solution obtained from the Helmholtz-Smuluchowski equation, and the circular points are the numerical solutions of the model developed in this work. It's clearly shown

in this figure that for the solid particle with ζ_p = −25 mV and the particle diameter d = 60 μm, the numerical solution and the analytical solution of the Helmholtz-Smuluchowski equation match very well with each other.

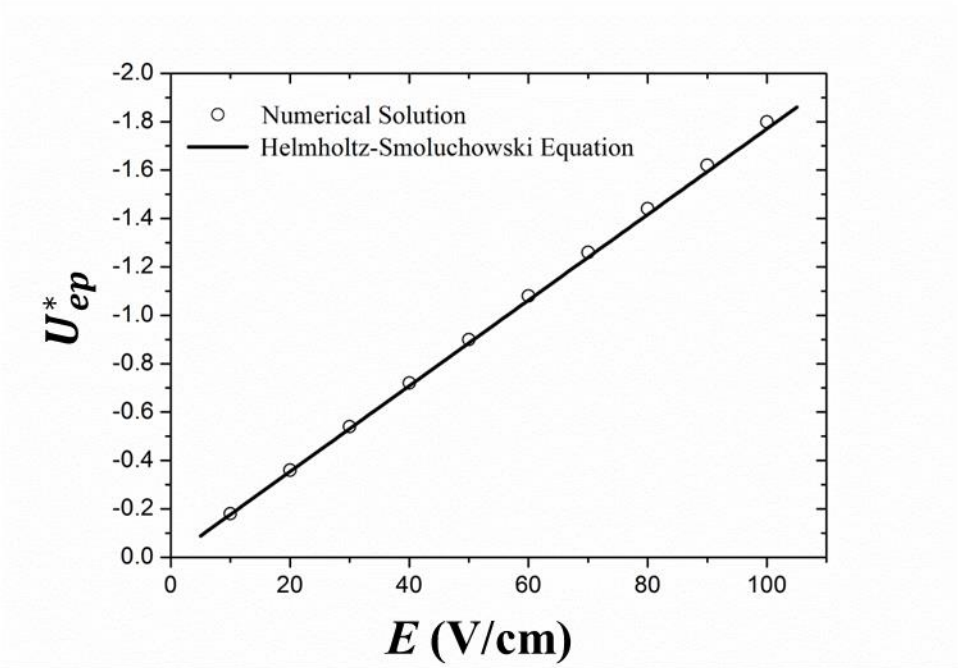

Figure 6-4. The comparison of the dimensionless particle electrophoretic velocity, U_{ep}^*, versus the strength of the applied electrical field, *E*, between the numerical solution and the Helmholtz-Smoluchowski equation, with ζ_p = −25 mV and d = 60 μm. In this model, the computation domain is set to be square. The length of side is 10 times larger than the droplet diameter. The boundary condition of the square is set to be open boundary.

The electrokinetic motion of a charged particle in a circular microchannel is considered as another case to test this model. For a charged particle moving along the center line of a straight circular microchannel, the electrokinetic velocity of the particle ($\vec{U}_{ep}$) can be evaluated by the approximate formula derived by Keh et al. [75]:

$$\vec{U}_{ek} = [1 - 1.28987r^3 + 1.89632r^5 - 1.02780r^6 + o(r^8)]\frac{\varepsilon_0\varepsilon_w\zeta_p}{\eta_w}(1 - \frac{\zeta_w}{\zeta_p})\vec{E} \qquad (6\text{-}30)$$

where r is the ratio between the diameter of the particle d and that of the microchannel (D). The dimensionless electrophoretic velocity U_{ek}^* can be obtained by dividing $\vec{U}_{ek}$ by U_{ref}.

Figure 6-5 shows the comparison of the non-dimentional electrokinetic velocity of a charged particle in a circular microchannel between Keh's formula and the numerical simulation results of the model presented in this paper at ζ_w = −60 mV, ζ_p = −25 mV and r = 0.4. As can be seen, the numerical solution and the approximation solution are in good agreement.

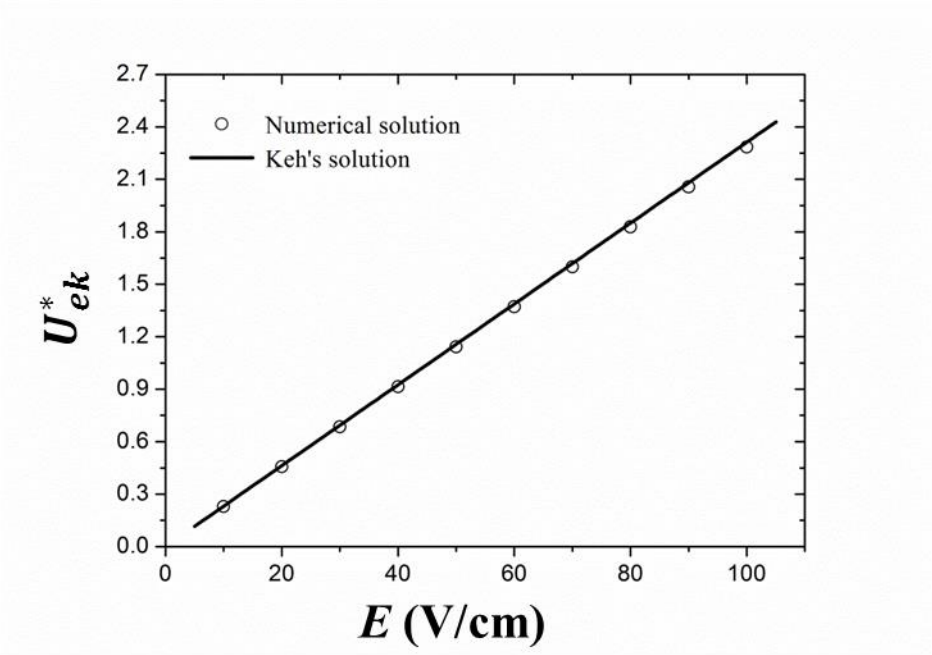

Figure 6-5. The comparison of the non-dimentional electrokinetic velocity of a charged particle in a cylindrical microchannel, U_{ek}^*, versus the strength of the applied electrical field, E between the numerical solution and the Keh's solution, with ζ_w = –60 mV, ζ_p = –25 mV and r = 0.4. In the numerical simulation, the viscosity of the oil droplet is set to be infinitely large without considering the motion of the oil-water interface; therefore, the oil droplet performs as solid particle.

6.4.2 Effect of the Strength of the Electric Field

Figure 6-6 shows the non-dimensional electrokinetic velocity versus the strength of the electrical field for Janus droplets with different surface coverage under the condition of the zeta potential ratio ζ_r = 1, the viscosity ratio η_r = 1000, and the size ratio r = 0.4. The electrokinetic velocities for Janus droplets with $\theta/2$ = 60°, 90° and 120° are indicated by rectangular points, circular points and triangular points, respectively. It's clearly shown in Figure 6-6 that the electrokinetic velocity of Janus droplet increases linearly with the strength of the electric field. It is not difficult to understand that the electrokinetic motion of the Janus droplet in a microchannel results from the combined effect of the electrophoresis of the droplet and the electroosmosis of the surrounding liquid in the channel. The expression of the electrokinetic velocity of the Janus droplet $\vec{U}_{ek}$ can be written as:

$$\vec{U}_{ek} = \vec{U}_{eof} + \vec{U}_{ep} = (\mu_{eof} + \mu_{ep}) \cdot \vec{E} \tag{6-31}$$

where $\vec{U}_{eof}$ and μ_{eof} are the velocity and mobility of the electroosmotic flow in the microchannel, $\vec{U}_{ep}$ and μ_{ep} are the velocity and mobility of the electrophoresis of the Janus droplet. It's clearly shown in Equation (6-31) the electrokinetic velocity of the Janus droplet is linearly proportional to the strength of the applied electrical field.

Figure 6-6 also shows that under the same electrical field, the electrokinetic velocity of the Janus droplet increases with $\theta/2$. This can be understood as the following. When the coverage of the positively charged surface area is small, i.e., $\theta/2 < 90^o$, the net surface charge of the Janus droplet is negative. For a negatively charged droplet in a microchannel with negatively charged walls, the electroosmotic flow of the liquid in the microchannel and the electrophoretic motion of the Janus droplet are in opposite directions. Therefore, the net velocity of the Janus droplet is smaller. However, when the coverage of the positively charged surface area is larger, i.e., $\theta/2 > 90^o$, the net surface charge of the Janus droplet is positive. For a positively charged droplet in a microchannel with negatively charged walls, the electroosmotic flow of the liquid in the

microchannel and the electrophoretic motion of the Janus droplet are in the same directions. Therefore, the net velocity of the Janus droplet is larger.

It should be noted that, the simulation was conducted under the assumption of fixed nanoparticle coverage. Generally, this assumption is valid when the externally applied electric field is larger than 50 V/cm. However, to reveal the effect of the electric field, the nanoparticle coverage of the EIJD was assumed to be fixed regardless of the electric field strength.

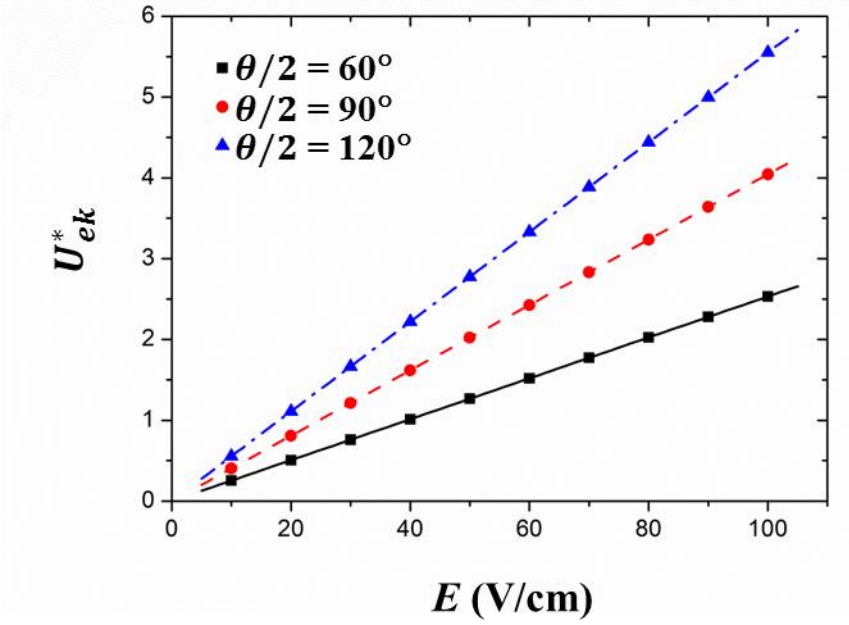

Figure 6-6. The non-dimensional Janus droplet electrokinetic velocity, U^*_{ek}, versus the strength of the electrical field, E, with ζ_r = 1, η_r = 1000 and r = 0.4.

6.4.3 Effect of the Zeta Potential Ratio

The zeta potential ratio between two sides of the Janus droplet is another factor that affects the electrokinetic velocity of the Janus droplet. Figure 6-7 shows the calculated non-dimensional electrokinetic velocity versus the zeta potential ratio ($\zeta_r = |\zeta_{nano}/\zeta_{ow}|$) for Janus droplets with different surface coverage by nanoparticles under the externally applied electric field of 50V/cm. The other parameters are fixed with η_r = 1000 and r = 0.4. The rectangular points, circular points and triangle points represent the electrokinetic velocities of the Janus droplets with the surface

coverage of 60°, 90° and 120°, respectively. It can be seen from the figure that the dimensionless electrokinetic velocity increases with the zeta potential ratio (ζ_r). For Janus droplet with larger surface coverage by nanoparticles, the effect of ζ_r on U_d^* is more significant.

Under electrical field, the electrical force $\vec{F}_{e,J}$ acting on the Janus droplet can be calculated:

$$\vec{F}_{e,J} = (Q^- + Q^+)\vec{E} \tag{6-32}$$

here Q^+ and Q^- are the total number of surface charges on the positive and negative sides of the Janus droplet, respectively. Under thin EDL assumption, for the Janus droplet with the positively charged nanoparticle coverage of $\theta/2$, Q^+ and Q^- can be obtained:

$$Q^+ = \sigma_s^+ \cdot S^+ = \frac{2n_\infty(ze)^2}{\kappa K_b T}\zeta_{nano}S^+ = \frac{2n_\infty(ze)^2}{\kappa K_b T}\zeta_r|\zeta_{ow}|S^+ \tag{6-33}$$

$$Q^- = \sigma_s^- \cdot S^- = \frac{2n_\infty(ze)^2}{\kappa K_b T}\zeta_{ow}S^- \tag{6-34}$$

where σ_s^+ and S^+ are the local surface charge density and the surface area of the positively charged side of the Janus droplet. σ_s^- and S^- are the local surface charge density and the surface area of the negatively charged side. Substituting Equation (6-33) and (6-34) into Equation (6-32):

$$\vec{F}_{e,J} = Q^-(1 - \zeta_r\frac{S^+}{S^-})\vec{E} \tag{6-35}$$

As indicated in this equation, when other parameters are fixed, $\vec{F}_e$ decreases with the increase of ζ_r; hence the electrophoretic velocity of the Janus droplet decreases. Recall Equation (6-31), with the reduction of the electrophoresis of the Janus droplet, its electrokinetic velocity increases. For a Janus droplet with large nanoparticle coverage, S^+/S^- is large; therefore, with the increase of ζ_r, $\vec{F}_{e,J}$ decreases more substantially, and the electrokinetic velocity of the Janus droplet increases more significantly than those with smaller $\theta/2$.

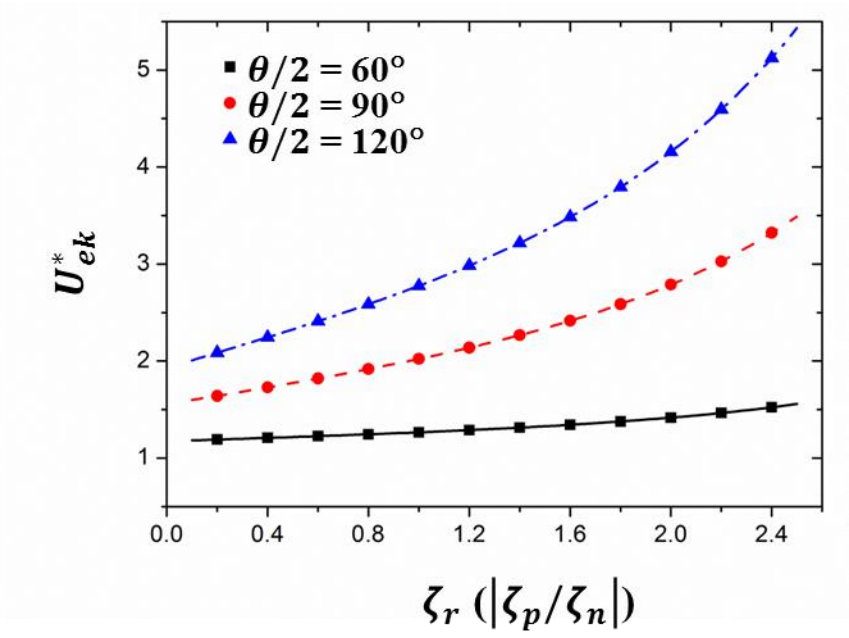

Figure 6-7. The non-dimensional Janus droplet electrokinetic velocity, U^*_{ek}, versus the zeta potential ratio, ζ_r, with E = 50 V/cm, η_r = 1000 and r = 0.4.

6.4.4 Effect of the Viscosity Ratio

The variation of the dimensionless electrokinetic velocity of the Janus droplets with the viscosity ratio η_r (η_o/η_w) is shown in Figure 6-8. Three different Janus droplets with different nanoparticle coverage ($\theta/2$ = 60°, 90° and 120°) are analyzed under the condition of E = 50 V/cm, ζ_r = 1 and r = 0.4. As shown in Figure 6-8, for Janus droplets with the nanoparticle coverage larger than 90°, the electrokinetic velocity of the Janus droplets is essentially independent of the viscosity ratio η_r (η_o/η_w). For Janus droplets with a smaller nanoparticle coverage, for example, $\theta/2$ = 60°, the electrokinetic velocity of the Janus droplets increases with the viscosity ratio η_r (η_o/η_w) when the viscosity ratio is low, and becomes a constant when the viscosity ratio is high. The electrophoresis of oil droplet has been studied in some papers [134,146]. Under externally applied electrical field, the oil droplet moves with axisymmetric vortex formed inside of it. The presence of the vortex reduces the hydrodynamic force acting on the droplet and hence the electrophoretic velocity of the oil droplet is larger than that of the solid particle under the same conditions. For the Janus droplet studied in this paper, vortex also forms inside of the droplet when it moves in a microchannel

under electrical field, as shown in Figure 6-9. Because of symmetry, only a half of the droplet is shown. The comparison between Figure 6-9(a) and (b) indicates that the vortex inside of the Janus droplet becomes weaker as the increase of the viscosity ratio between the oil phase and the water phase. Therefore, for a Janus droplet with larger viscosity ratio, the electrophoretic velocity of it is slower. Based on Equation (6-31), the electrokinetic velocity of the high viscosity ratio Janus droplet is higher than that of the Janus droplet with low viscosity ratio under the same condition. However, for a Janus droplet with large nanoparticle coverage area, for example, $\theta/2$ = 120° (triangular points in Figure 6-8), the viscosity effect is too weak to be seen. As the most part of the Janus droplet is covered with a compact nanoparticle film, only a small region on the droplet surface is mobile and the Janus droplet behaviors as a solid particle regardless of the viscosity of the oil phase.

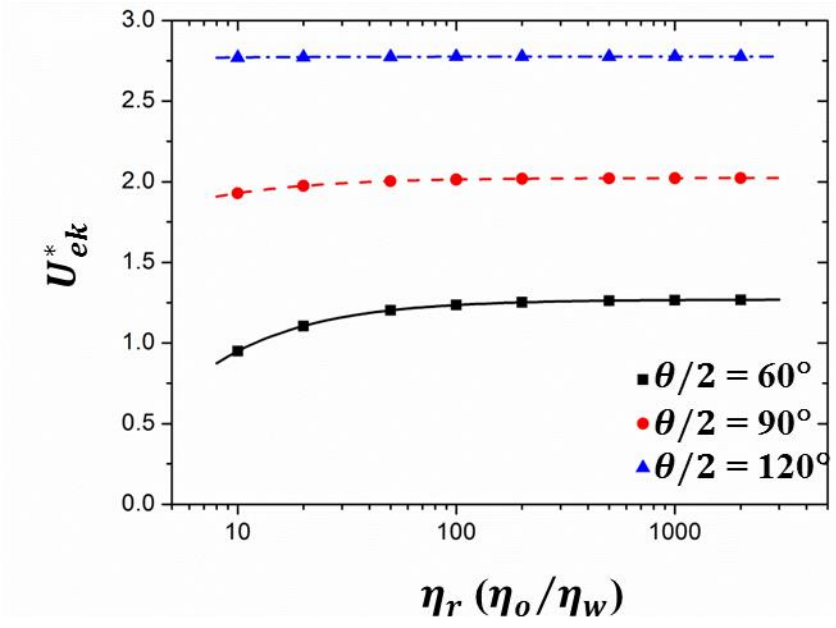

Figure 6-8. The non-dimensional Janus droplet electrokinetic velocity, U^*_{ek}, versus the viscosity ratio, η_r, with E = 50 V/cm, ζ_r = 1 and r = 0.4.

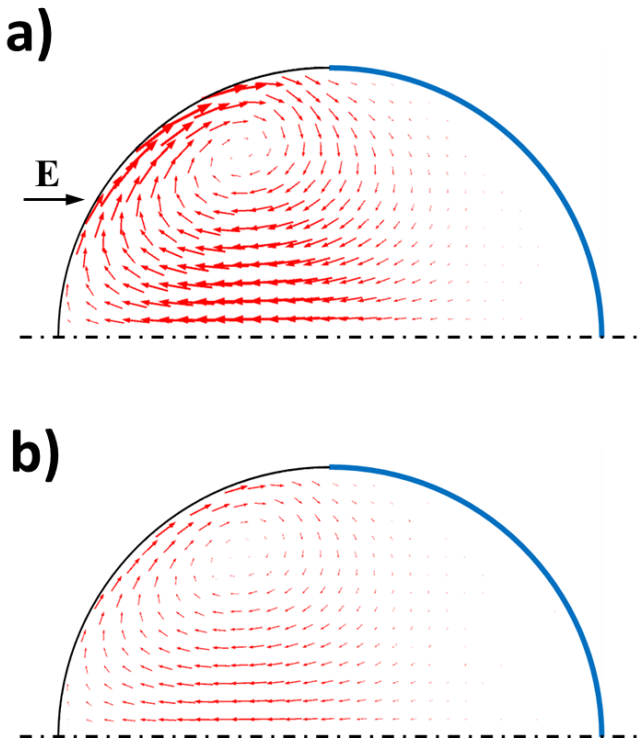

Figure 6-9. Flow fields inside Janus droplets with the viscosity ratio of (a) η_r = 500 and (b) η_r = 1000. E = 50 V/cm, ζ_r = 1, $\theta/2$ = 90° and r = 0.4. Because of symmetry, only one side of the droplet is shown. The length of the arrow is proportional to the local flow velocity and the direction of it represents the local flow direction.

6.4.5 Effect of the Nanoparticle Coverage

The non-dimensional electrokinetic velocity of Janus droplets versus the nanoparticle coverage $\theta/2$ are shown in Figure 6-10. As can be seen, the dimensionless electrokinetic velocity of the Janus droplet increases with the nanoparticle coverage $\theta/2$ which reaches the maximum at $\theta/2 = 180°$. The velocity increases first and then approaches a plateau. Furthermore, for the Janus droplet with a larger zeta potential ratio (ζ_r), the influence of $\theta/2$ on U_{ek}^* is more significant. With the increase of $\theta/2$ and ζ_r, the net charges on the Janus droplet get reduced; therefore, under the same electrical field, the electrostatic force acting on the Janus droplet decreases. With the reduction of the electrostatic force, the electrophoretic velocity decreases and the electrokinetic velocity of the Janus droplet increases.

The flow fields inside and outside of the Janus droplet for $\theta/2$ = 90° and 60° are shown in Figure 6-11, respectively. For symmetry, only half of the droplet and the flow field are shown. Figure 6-11(a) shows two axisymmetric vortices form around the Janus droplet and one axisymmetric vortex inside of it. The vortices in the water phase are generated due to the opposite EOF on different segments of the Janus droplet surface. When $\theta/2$ decreases from 90° to 60°, the rightward EOF on the oil-water surface of the Janus droplet becomes dominant, and only the vortex on the positively charged side remains (Figure 6-11(b)).

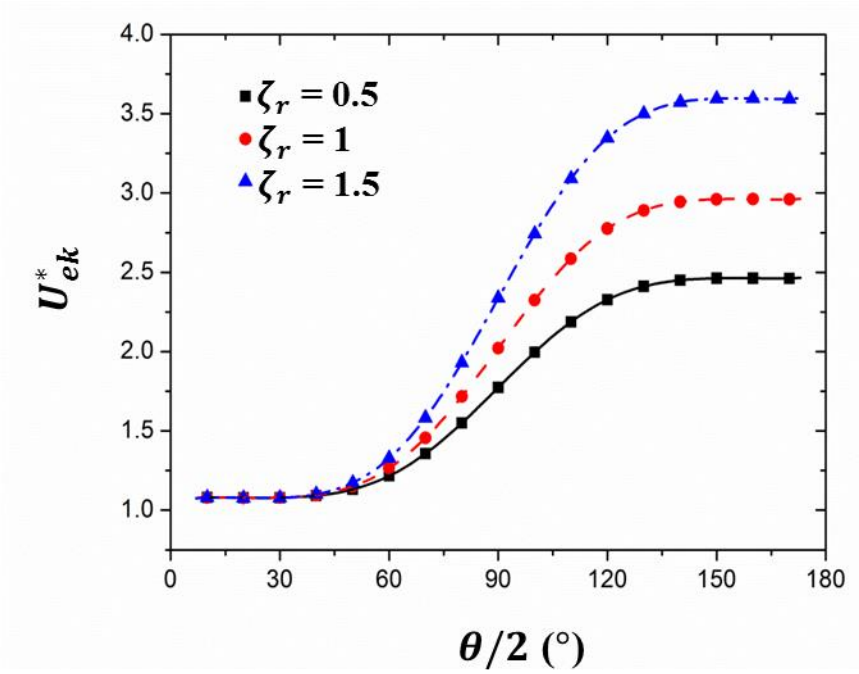

Figure 6-10. The non-dimensional Janus droplet electrokinetic velocity, U^*_{ek}, versus the nanoparticle coverage, $\theta/2$, with E = 50 V/cm, η_r = 1000 and r = 0.4.

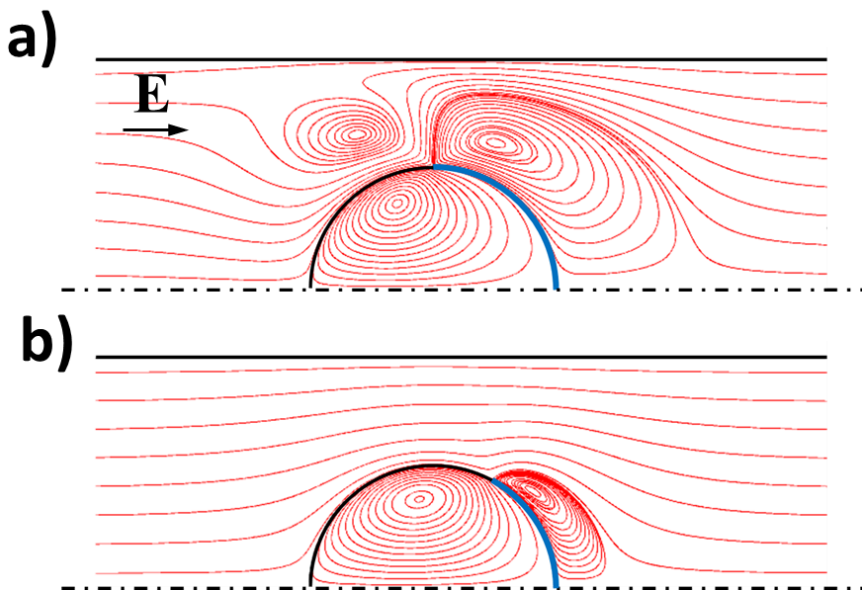

Figure 6-11. Flow fields inside and outside Janus droplets with the nanoparticle coverage of (a) $\theta/2$ = 90° and (b) $\theta/2$ = 60°. E = 50 V/cm, ζ_r = 1, η_r = 1000 and r = 0.4.

6.4.6 Effect of the Size Ratio

Figure 6-12 shows the non-dimensional electrokinetic velocity of Janus droplet versus the size ratio (r = *d/D*) with E = 50 V/cm, η_r = 1000. It's clearly shown in this figure that for the Janus droplet with ζ_r = 1 and $\theta/2$ = 90°, the calculated non-dimensional electrokinetic velocity first decreases mildly until reaching a minimum value around r = 0.7, then increases sharply with r. The variation of U_{ek}^* with r can be explained by considering the competing effects of the electric field and the viscous retardation when the Janus droplet approaches the channel wall [147]. On the one hand, the squeezed electric field in the small gap between the channel wall and the droplet is stronger and hence generates stronger electroosmotic flow, which trends to promote the motion of the Janus droplet. On the other hand, the viscous retardation effect in the small gap tends to reduce the droplet motion. For r < 0.7, the viscous retardation effect is dominant, leading to the decrease of the droplet velocity. Further increasing the size of the Janus droplet to r > 0.7, the effect of the increased local electric field overcomes the viscous retardation effect and drive the Janus droplet to move faster. This phenomenon is called wall enhance effect [71,72].

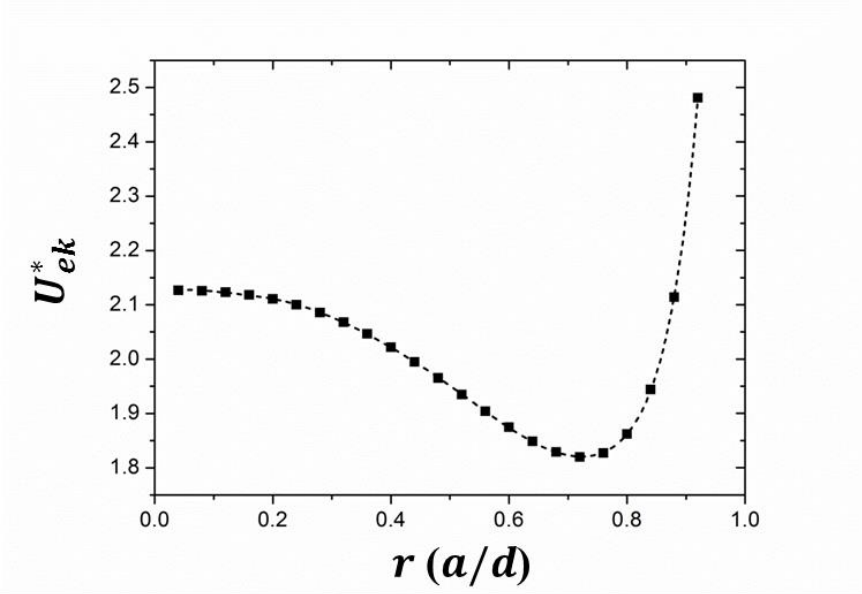

Figure 6-12. The non-dimensional Janus droplet electrokinetic velocity, U^*_{ek}, versus the size ratio, r, with ζ_r = 1, E = 50 V/cm, η_r = 1000, and $\theta/2$ = 90°.

6.5 Experimental Verification

6.5.1 Vortices in Vicinity of EIJDs

In this study, the flow fields around two Janus droplets with the same size (the diameter d = 78 μm) and different surface coverage (γ = 40.6% and 21.1%) were examined. The flow fields around these Janus droplets under electric field of 30 V/cm are shown in Figure 6-13. It clearly indicates in Figure 6-13(a) that four vortices are generated around the mobile Janus droplet with γ = 40.6% under the rightward electric field. The two vortices are on the left side, while the other two stay on the right side. Figure 6-13(b) shows the flow field around the Janus droplet with smaller surface coverage by nanoparticles, γ = 21.1%. As shown in this figure, under the same applied electrical field, only the two vortices on the right side of the Janus droplet exist, and the size of the vortices are smaller. With the decrease of the surface coverage of the Janus droplet, the electroosmotic flow

on this side gets weaker and the electroosmotic flow on the other side becomes dominant; therefore, only the two vortices on the right side exist. This experimental finding confirms the numerical results shown in Figure 6-11.

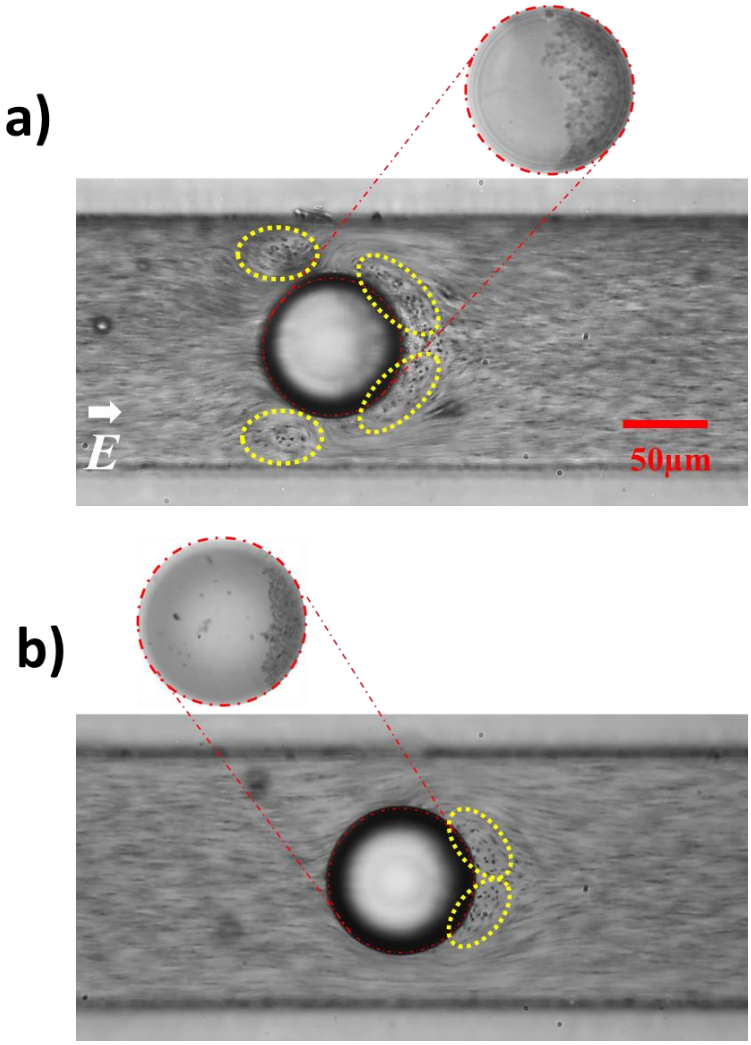

Figure 6-13. Vortices are generated around Janus droplets moving in a microchannel under externally applied DC electrical field of 30V/cm. (a) d = 78 µm, γ = 40.6%, generated with 2 mg/mL nanoparticle suspension; (b) d = 78µm, γ = 21.1%, generated with 1mg/mL nanoparticle suspension. The exposure time of the microscope is 400 ms.

6.5.2 Electrokinetic Motion of the EIJDs

6.5.2.1 Effects of the Applied Electric Field and the Nanoparticle Coverage

In order to study the effects of the electric field strength and the nanoparticle coverage on the electrokinetic velocities of the EIJDs, Janus oil droplets and pure oil droplets of 75 μm ± 3 μm in diameter were chosen in the experimental investigation. The electrokinetic velocities of Janus droplets with different surface coverage by aluminum oxide nanoparticles and oil droplets in terms of the electrical field are shown in Figure 6-14. The experiments were conducted under the electric field larger than 50 V/cm. Clearly, the velocity of Janus droplets is larger than the velocity of oil droplets under identical DC electrical field. And the larger the surface coverage of the Janus droplet by nanoparticles (γ), the faster the electrokinetic motion in a microchannel. Furthermore, the results also indicate the effect of the electric field strength on the electrokinetic motion of oil droplets and Janus droplets. As shown in this figure, the velocities of oil droplets and Janus droplets increase with the applied DC electrical field linearly.

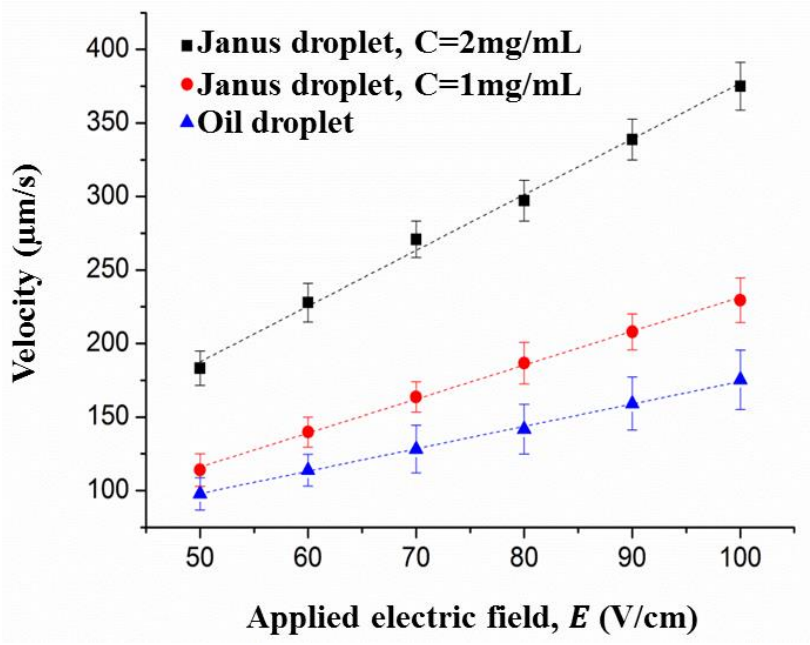

Figure 6-14. The electrokinetic velocities of the Janus droplets generated with different concentrations of nanoparticle suspensions and oil droplets as a function of electrical field. The diameter of different types of droplets *d* is 75 μm ± 3 μm.

6.5.2.2 Effect of Droplet Size

The electrokinetic motion of Janus droplets in a microchannel can also be affected by the size of them. The electrokinetic velocities of Janus droplets with two different sizes, d = 75 µm ± 3 µm and d = 45 µm ± 2 µm were measured and compared. These droplets were generated with a nanoparticle suspension of C = 2 mg/mL. As shown in Figure 6-15, under the same applied electrical field, the larger Janus droplets move faster than the smaller ones. For a larger droplet, the gaps between the droplet and the channel walls are smaller. Consequently, the electrical lines are squeezed further in the smaller gap, and the electrical field is stronger in this region. The stronger electrical field in the smaller gaps will generate stronger electroosmotic flow, which promotes the motion of the Janus droplet. As illustrated in Section 6.4.6, this phenomenon is caused by the "wall effect". The comparison of the velocities between EIJDs with different sizes proves the simulation findings shown in Figure 6-12.

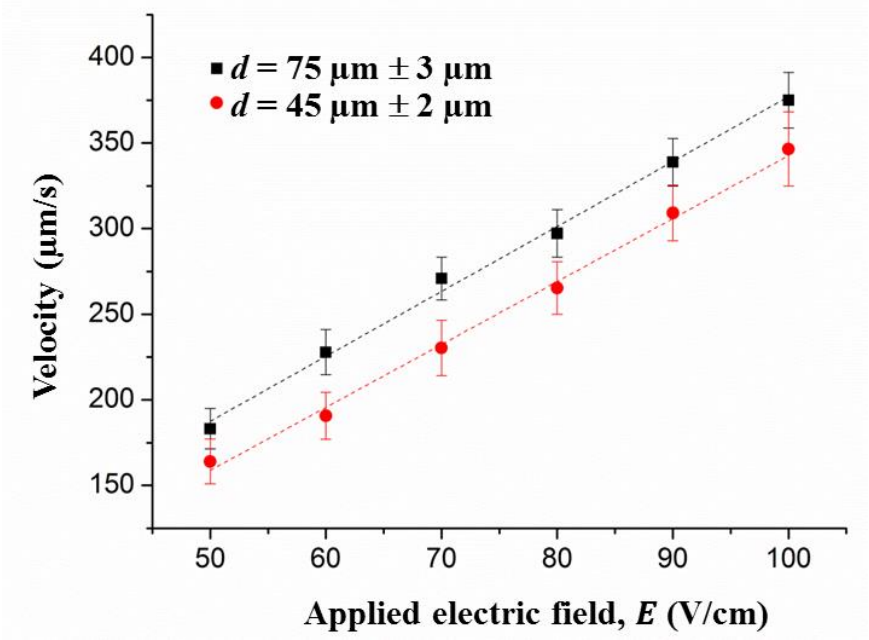

Figure 6-15. The electrokinetic velocity of Janus droplets with a diameter of 75 µm ± 3 µm and 45 µm ± 2 µm generated with nanoparticle suspension of C = 2 mg/mL as a function of applied DC electrical field.

6.5.2.3 Effect of the Electrolyte Concentration

The effect of the electrolyte concentration on the electrokinetic velocity of Janus droplets was also investigated. The buffer solution used is 1mM KCl solution which was prepared by dissolving solid potassium chloride into deionized water. The electrokinetic velocities of Janus droplets in deionized water and 1mM KCl solution are shown in Table 6-1. By comparing the data shown in Table 6-1, it can be seen that the electrokinetic velocity decreases significantly when the buffer solution is changed from deionized water to 1mM KCl solution. For example, under applied electrical field of 50 V/cm, the average electrokinetic velocity of the Janus droplets in deionized water is 183.2 μm/s. However, in 1mM KCl solution, the average velocity decreases to 46.2 μm/s.

Table 6-2. The average values of the measured electrokinetic velocity of Janus droplets generated with nanoparticle suspension of C = 2 mg/mL under different electric field. (A) in deionized water; (B) in 1 mM KCl solution. The diameter of the Janus droplets is d = 75 μm ± 3 μm.

(A) Deionized Water						
Electric field (V/cm)	50	60	70	80	90	100
Electrokinetic velocity (μm/s)	183.2	227.8	270.8	297.2	338.8	375.0
Standard deviation	11.8	13.1	12.5	13.8	13.8	16.3
(B) 1 mM KCl Solution						
Electric field (V/cm)	50	60	70	80	90	100
Electrokinetic velocity (μm/s)	46.2	55.2	66.0	75.0	79.3	88.8
Standard deviation	4.6	6.1	7.9	9.2	8.8	9.3

It is well-known that the absolute value of zeta potential decreases when contacting with high-concentration buffer solution. For example, in deionized water, the zeta potential for PDMS microchannel is –60mV [148]. The zeta potential reduces to –20mV in 1mM KCl solution [149].

Therefore, under applied electrical field of 50V/cm, the electroosmotic flow velocities in a microchannel for deionized water and 1mM KCl solution can be calculated to be 236.1μm/s and 78.7μm/s, respectively. The comparison between the calculated electroosmotic flow velocities and the measured electrokinetic velocities of Janus droplets clearly shows that the reduction of the electrokinetic velocity of Janus droplets is mainly caused by the decrease of electroosmotic flow velocity in the microchannel.

6.5.3 Comparison Between Numerical and Experimental Results

The comparsions between the simulation results and the experimental results for the electrokinetic velocities of Janus droplets under different conditions are shown in Figure 6-16. The electrokinetic velocities of the Janus droplet with d = 76 μm and $\theta/2$ = 83.5° in deionized water and 1mM KCl solution are shown as case A and D, respectivley. For case B, the diameter of the Janus droplet is 45 μm with the nanoparticle coverage of 83.5°. Case C is for the Janus droplet with the diameter of 76 μm and the nanoparticle coverage of 55°. As shown in Figure 6-16, the simulation results and the experimental results are in good agreement for case B. However, for cases A, C and D, the simulation results are larger than the experimental results under given electric field. The explanation for the difference between the simulation results and the experimental results of large Janus droplets (d = 76 μm) is that the wall enhance effect is overly signified in the model simulation. As explained above, in the experiment, the Janus droplet with a diameter of 76 μm moves in a rectangular microchannel with 150 μm in width and 80 μm in height, and only the top and bottom walls contributes to the wall enhance effect. However, the circular microchannel with 80 μm in diameter is used in the numerical simulation. In the model simulation, the channel wall surrounding the Janus droplet in all directions influences the motion of the Janus droplets. Therefore, under the same applied electrical field, the Janus droplet moves faster in a smaller circular microchannel than in a larger rectangular microchannel. However, for a Janus droplet with a smaller size moving along the center line of the microchannel, the gap between the droplet and the microchannel wall is relatively large, and thus the wall effect is limited in both the rectangular microchannel and the circular microchannel. Hence, the simulation results match well with the experimental results for case B.

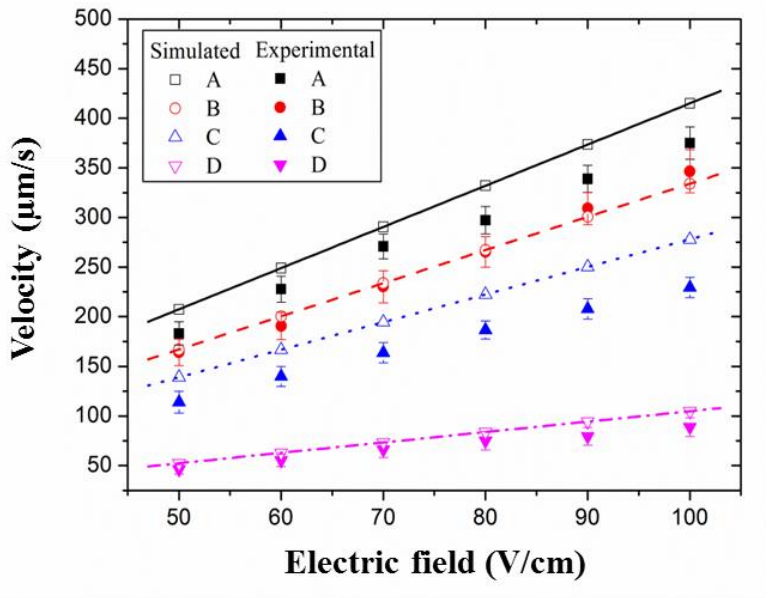

Figure 6-16. Comparisons between the numerical simulation results and the experimental results for the electrokinetic velocities of Janus droplets. Case A is for the Janus droplet with d = 76 μm and $\theta/2$ = 83.5° immersed in deionized water. Case B is for the Janus droplet with d = 45 μm and $\theta/2$ = 83.5° immersed in deionized water. Case C is for the Janus droplet with d = 76 μm and $\theta/2$ = 55° immersed in deionized water. Case D is for the Janus droplet with d = 76 μm and $\theta/2$ = 83.5° immersed in 1 mM KCl solution.

6.6 Conclusions

In this paper, the electrokinetic motion of an electrically induced Janus droplet along the center line of a circular microchannel was studied numerically and experimentally. Numerically, we considered the oil droplet partially covered by positively-charged nanoparticles. The nanoparticle coverage of the EIJD remains fixed. The positively-charged surface area on the Janus droplet is immobile and the negatively-charged oil-water interface is mobile. The effect of the mobile oil-water interface is considered by the EDL+SC model. A 2D axisymmetric model was constructed to numerically simulate the electrokinetic velocity of the Janus droplet at steady state. The simulated results reveal that:

(a) The electrokinetic velocity of the Janus droplet increases linearly with the strength of the externally applied electrical field.

(b) The larger the zeta potential ratio between the positive side and the negative side, the larger the electrokinetic velocity.

(c) For a Janus droplet with a smaller nanoparticle coverage, its electrokinetic velocity increases with the viscosity ratio between the oil phase and water phase. However, for the Janus droplet with a larger coverage by nanoparticles, the viscosity effect can be neglected.

(d) The electrokinetic velocity increases with the nanoparticle coverage.

(e) Due to the wall effect, the electrokinetic velocity of Janus droplet first decreases gradually then increases sharply with the increase of its size.

To confirm these findings, experiments were conducted. First, the flow fields around EIJDs with different nanoparticle coverages were visualized. The existence of the vortices in vicinity of EIJDs in a microchannel under the electric field due to the opposite electroosmotic flow on different sides of the droplet was demonstrated. The number of vortices is dependent on the nanoparticle coverage. Then, the electrokinetic velocities of the EIJDs were measured. By comparing the electrokinetic velocities of Janus droplets under different conditions, the findings in the numerical part were proved.

CHAPTER 7. Fundamental Research IV: Wall-induced Dielectrophoresis and Separation of EIJDs in Microchannels*

7.1 Introduction

Emulsion with one phase dispersed into the other immiscible phase has extensive applications in many fields, such as chemistry, biology, medicine as well as material science. For example, the emulsion droplets can be used for synthesizing solid particles [150,151], carrying out chemical reactions [152–154], encapsulating cells and DNAs [155–157], building up artificial cells [158,159]. Traditionally, the emulsion droplets are prepared by shaking or stirring the mixture, which results in droplets with wide range of size distribution. As a new division of emulsion droplets, the Janus droplets are the droplets with two hemispheres carrying different properties. Due to their novel properties, the Janus droplets have attracted increasing attention in recent years [160–162]. Generally, the Janus droplets with uniform size and morphology are essential in these applications. However, the Janus droplet fabrication methods mentioned in Chapter 2 are difficult to have precise control over the size and morphology that limits the droplets' practical applications. Therefore, research in the separations of oil droplets and Janus droplets are highly desirable.

Recently, the development of microfluidic technology provides a new approach for the separation of emulsion droplets. The methods for sorting homogeneous droplets in microchannel include dielectrophoresis (DEP) [163,164], Marangoni effect [165–167], mechanical microvalve [168,169], surface acoustic wave[170–172], etc. Due to the dielectric property difference between the droplets and the suspension liquid, under non-uniform electrical field (induced by the varying shape of microchannels or by non-symmetric electrodes), DEP forces are generated and drive the droplets to move. As the DEP force is dependent on the droplets size, the emulsion droplets can be separated by size with this method [83]. For example, Ahn et al. [173] developed a high-throughput droplet sorting microfluidic device by DEP, the sorting rate could reaches 1.6 kHz. Marangoni effect is also used for sorting emulsion droplets. For a droplet with surface tension

---

* A similar version of this chapter was submitted or published as:

Li, M.; Li, D. Separation of Janus Droplets and Oil Droplets in Microchannels by Wall-induced Dielectrophoresis. *J. Chromatogr. A.* **2017**, 1501, 151-160. https://www.sciencedirect.com/science/article/pii/S0021967317305800

gradient along its surface, Marangoni flow is generated on the surface of the droplet and consequently the droplet moves towards the side of the low interfacial tension. By generating a temperature gradient or a surfactant gradient around the droplet, the interfacial tension gradient is created to drive the droplet towards specific direction and the sorting of the droplets can be achieved [166]. The emulsion droplets can also be separated with mechanical microvalves assembled in microfluidic chips. For example, Abate et al. [168] fabricated a single-layer membrane valve to control the fluid flow at the bifurcating channel junction. By switching the valve with a solenoid, the droplets flow into different outlets and are separated. The surface acoustic wave method uses a piezoelectric substrate to generate the surface acoustic wave which propagates along the microchannel wall and drives the droplets towards the direction that the wave spreads. Therefore, the droplets can be manipulated to move to different branches by controlling the piezoelectric substrate positioned at the junction of microchannels. However, compared with the numerous researches on separating homogeneous emulsion droplets, the study of the separation of Janus droplets/particles is limited [174].

In addition to the separation methods discussed above, the wall-induced DEP has been proven to be an efficient method to separate particles/droplets continuously by size and surface charge in microfluidics. For a particle/droplet nearby a planar dielectric wall, under externally applied electrical field, a DEP force is generated due to the non-uniform electrical field around the particle/droplet. The negative DEP force pushes the particle/droplet away from the wall. Theoretically, Young and Li [175] first derived the accurate expression of the wall-induced DEP force by integrating the Maxwell stress along the surface of the particle. It was found that the DEP force increases with the reduction of the distance between the particle and the planar wall. Later, Yariv [176,177] derived the leading-order expression of the wall-induced DEP force. Similar studies were also presented by Zhao and Bau [178] in their theoretical paper. Recently, Kang [179] numerically studied the wall-induced DEP motion of a particle from a nearby planar wall under the electrical field parallel to the wall. He found that the wall-induced lateral migration velocity of the particle is dependent on the distance between the particle and the adjacent planar wall. Experimentally, Liang et al. [180,181] first demonstrated the existence of the wall-induced DEP force by visualizing the lateral migration of the polystyrene particles in a rectangular microchannel under DC electric field. It has been found that the lateral migration of the dielectric particle increases with the electric field and the size of the particle. Then, by detecting the gap between the

dielectric particles and the dielectric wall with the evanescent wave-based particle-tracking velocimetry, Kazoe et al. [182] proved that the wall-induced DEP force is proportional to the square of the electric field and the size of the particle but is independent of the zeta potential of the particle. Later, Liang et al. [183] controlled the separation distance between the particle and the wall by using the electric field to adjusting the DEP force acting on the particle. Recently, the wall-induced DEP separations of particles and cells have been studied by Xuan's group [184,185]. Through experimental analysis, they found that the particles with different sizes and different surface charges can be separated due to their different migration distances while moving through a straight microchannel. Based on the features of wall-induced DEP, this separation method is applicable in separating EIJDs with size and nanoparticle coverage.

In this chapter, we studied the wall-induced DEP of the oil droplets and EIJDs. The lateral migrations of the oil droplets and Janus droplets in a straight microchannel under different electric fields were experimentally measured first, and the experimental results were compared with the theoretical predications. Then, the oil droplets with different sizes, Janus droplets with different sizes, oil droplets and Janus droplets with the same size were separated respectively in a microchannel by using the wall-induced DEP method. The purpose of this study is to demonstrate the feasibility of this method, for the first time to our knowledge, for separating both oil droplets and Janus droplets which has potential in industrial and research applications.

7.2 Theoretical Analysis

7.2.1 Mechanism of the Wall-induced DEP

The wall-induced DEP is caused by an asymmetric electric field around a spherical droplet nearby a dielectric planar wall. As shown in Figure 7-1, a spherical droplet with the radius of a is located near a dielectric channel wall, and the separation distance between the center of the droplet and the channel wall is y_d. Under the electric field parallel to the wall, the electric field lines are distorted around the sphere, and squeezed in the gap space between the droplet and the channel wall. Therefore, the electric field is non-uniformly distributed around the droplet in the normal direction to the wall (y direction), and the magnitude of the electrical field in the gap region is larger than that on the opposite side of the droplet. The asymmetric electric field in the y-direction generates the DEP force F_{wDEP} on the droplet, which repels the droplet from the wall.

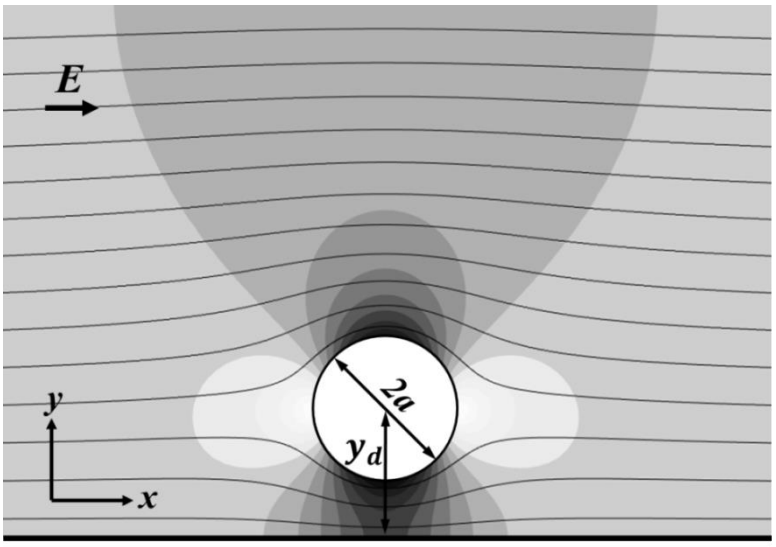

Figure 7-1. The schematic diagram of the electric field lines around a droplet close to a dielectric planar wall. The color of the background represents the magnitude of the electrical field. The darker the color, the larger the magnitude of the electrical field.

7.2.2 Calculation of Droplet Trajectory

For a droplet in a straight microchannel, it experiences electrokinetic motion in the x-direction (channel length direction) and the wall-induced dielectrophoretic lateral migration in the y-direction under electric field. In the x-direction, the position of the center of the droplet x_d in term of time *t* can be written as:

$$x_d = \mu_{ek} E t \tag{7-1}$$

where E is the strength of the electric field. μ_{ek} is the electrokinetic mobility of the droplet in a microchannel.

According to Equation (7-1), within finite time $\mathrm{d}t$, the variation of x_d ($\mathrm{d}x_d$) is obtained:

$$\mathrm{d}x_d = \mu_{ek} E \mathrm{d}t \tag{7-2}$$

In the y-direction, the analytical expression of the wall-induced DEP force acting on the droplet F_{wDEP} has been derived by Yariv [177] with the Maxwell stress tensor method, which is independent of the surface charge of the droplet:

$$F_{wDEP} = \frac{3\pi}{16}\varepsilon_0\varepsilon_w a^2 E^2(\tau)^4 \tag{7-3}$$

where ε_0 and ε_w are the permittivity of vacuum and the surrounding liquid, respectively. a is the radius of the droplet, E is the strength of the electrical field, τ is the ratio between the radius of the droplet (a) and the distance from the center of the droplet to the channel wall (y_d). Thus, the wall-induced dielectrophoretic lateral migration velocity of the droplet (U_{wDEP}) can be obtained by considering the balance between the electric force and the flow friction force [181]:

$$U_{wDEP} = \frac{\varepsilon_0\varepsilon_w}{32\eta_w} aE^2(\tau)^4 \tag{7-4}$$

here, η_w is the dynamic viscosity of the surrounding liquid. The lateral migration of the droplet within finite time ($\mathrm{d}y_d$) can be obtained:

$$\mathrm{d}y_d = U_{wDEP}\mathrm{d}t = \frac{\varepsilon_0\varepsilon_w}{32\eta_w} aE^2(\tau)^4\mathrm{d}t \tag{7-5}$$

Substituting Equation (7-2) into Eq. (7-5), the expression of $\mathrm{d}y_d$ in terms of $\mathrm{d}x_d$ can be obtained:

$$\mathrm{d}y_d = \frac{\varepsilon_0\varepsilon_w}{32\eta_w}\frac{Ea}{\mu_{ek}}(\tau)^4\mathrm{d}x_d \tag{7-6}$$

Integrating Equation (7-6), the expression of y_d can be obtained:

$$y_d = \frac{\varepsilon_0\varepsilon_w}{32\eta_w}\frac{Ea}{\mu_{ek}}\int_0^{x_d}(\tau)^4\mathrm{d}x_d \tag{7-7}$$

As shown in Equation (7-7), the lateral migration of the droplet is related to the dielectric constant (ε_w) and the viscosity (η_w) of the surrounding medium, the radius (a) and the electrokinetic mobility (μ_{ek}) of the droplet, and the strength of the externally applied electrical field (E). While holding the other parameters fixed, the increase of the electric field and the size of the droplet leads to the increase of the lateral migration. Oppositely, with the increase of the electrokinetic mobility of the droplet, the lateral migration decreases. As the electrokinetic mobility of the partially

negatively charged Janus droplet is larger than that of a homogeneous negatively charged oil droplet, the lateral migration of the oil droplet is larger than that of the Janus droplet when they travel through the same distance in the x-direction. In this study, the deionized water was used as the buffer solution. Thus, ε_w is set to be 80 and η_w is taken as 0.001 Pa·s. In chapter 6, the electrokinetic mobility of oil droplets and Janus droplets in a microchannel was measured experimentally, which were 1.75×10^{-8} $m^2/(V\ s)$ and 3.75×10^{-8} $m^2/(V\ s)$, respectively.

7.3 Experimental Studies

7.3.1 Preparation of Microfluidic Chip

The microfluidic chip was comprised of a top polydimethylsiloxane (PDMS) layer with microchannels and a flat substrate. The PDMS layer with microchannel structures was fabricated by soft lithography method. And the microfluidic chip can be formed by putting the PDMS layer on top of the substrate after plasma treatment.

In the study of the wall-induced dielectrophoretic lateral migrations of oil droplets and Janus droplets, a Y-shaped microchannel was used, as shown in Figure 7-2(a). The Y-shaped microchannel is composed of a main channel, two inlet branches and a confinement chamber. The microchannel has the uniform height of 80 μm. The main channel is 8.5 mm in length and 430 μm in width, and is used for measuring the wall-induced lateral migrations of the oil droplets and Janus droplets. The sheath fluid inlet branch has the size of 1.5 mm × 430 μm (length × width), while the sample inlet branch is 1 cm long and 150 μm wide. The confinement chamber between the sample inlet well and the sample inlet branch is used for holding oil droplets and Janus droplets, and has the size of 6mm × 6 mm (length × width).

For separating oil droplets and Janus droplets, the structure of the microfluidic chip is shown in Figure 7-2(b) and (c). It has a confinement chamber, a main channel, two inlet and two outlet branches. The main channel, where the droplet separation takes place, has the length of 1 mm and the width of 250 μm. The sizes of the sheath fluid inlet branch and the sample inlet branch are 1 mm × 250 μm (length × width) and 5 mm × 150 μm (length × width), respectively. The two outlet branches are each 9 mm in length, with the upper outlet branch (outlet branch A) 120 μm in width and the down outlet branch (outlet branch B) 180 μm in width. Similarly, the confinement chamber

is set before the sample inlet branch with the size of 6mm × 6 mm (length × width). The entire channel has a fixed height of 80 µm. Due to the limit of the height of the confinement chamber, only the droplets with the diameter smaller than 80 µm can enter into the confinement chamber and pass through the microchannel.

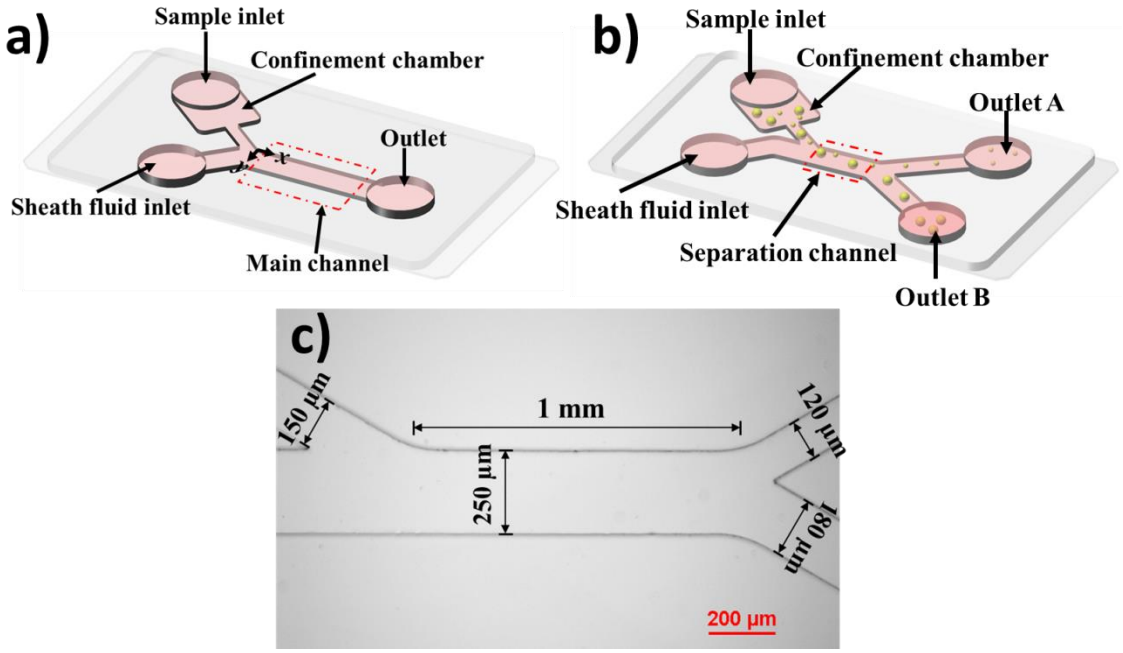

Figure 7-2. (a) Schematic diagram of the microfluidic channel for measuring the wall-induced dielectrophoretic lateral migration of droplets. (b) Schematic diagram of the microfluidic channel for droplets separation. (c) Microscopic image of the microchannel for separation.

7.3.2 Preparation of Oil-in-water Emulsion and EIJDs

The oil-in-water emulsion used in this study was prepared by mixing the pure canola oil (Mazola Corporation) and deionized water with the nonionic surfactant Tween 20 (Sigma Aldrich) used as the stabilizer. The oil-in-water emulsion was fabricated by adding 5 mL deionized water, 1 mL oil and 100 µL surfactant into a glass bottle (15 mL in capacity) and stirring the mixture with a vortexer (VWR Scientific) at the speed of 3200 rpm for 2 minutes.

The EIJDs were fabricated from Al_2O_3-stabilitized Pickering emulsion droplets. The fabrication process of the Pickering emulsion droplets is available in Section 3.2.2 (method A). After the generation of the Pickering emulsion, inject the emulsion droplets into a microchannel and apply a direct current (DC) electric field. Under electrical field, the positively charged Al_2O_3 nanoparticles adsorbing on the oil droplet move and accumulate to the side of the droplet back to the electrical field to form EIJDs.

7.3.3 Experimental Operation

For measuring the lateral migration of the oil droplets and Janus droplets, the Y-shaped microchannel was used, as mentioned above. In the experiment, 10 μL deionized water was added into the microchannel from the outlet well first to wet the microchannel. Then, 5 μL emulsion (oil-in-water emulsion or Pickering emulsion) was injected into the sample inlet well. The droplets would enter into the adjoining confinement chamber automatically. Due to the restriction of the height of the microchannel, only the droplets smaller than 80 μm in diameter can flow into the confinement chamber. The lateral migrations of the droplets can be affected if two or more droplets get close to each other in the main channel; therefore, dilute emulsion samples should be used here to make the droplets pass through the main channel one by one. Following this, 200 μL deionized water was added into the sample inlet well, sheath fluid inlet well and outlet well, respectively. After platinum electrodes were inserted into the three wells, the electrical field was applied to the microchannel with DC power supplies (CSI12001X, Circuit Specialist Inc., USA). Four DC power supplies were connected in series here and the strength of the electric field can be controlled by adjusting the output voltages of the power supplies. Under the electric field, the oil droplets would flow into the sample inlet branch from the confinement chamber. When the droplets covered with aluminum oxide nanoparticles moved through the sample inlet branch, the positively charged nanoparticles were accumulated to one side of the droplets and the Janus droplets formed in this process. While the droplets move from the sample inlet branch into the main channel, the liquid from the sheath flow inlet branch pushed the droplets close to the wall at the entrance of the main channel. Then, the droplets migrated away gradually from the wall when moving along the main channel due to the effect of the wall-induced DEP force. The migrations of the oil droplets and the Janus droplets in the main channel were visualized with an optical microscope (Ti-E, Nikon), and

the images were recorded by a charge coupled device (CCD) camera (DS-Qi1Mc, Nikon) at a rate of 25 frames per second, which can be used to do measurement later.

In the investigation of the separations of the oil droplets and Janus droplets, the same experimental setup and procedures were used. The microfluidic chip used in this experiment comprises four wells, sample inlet, sheath fluid inlet, outlet A and B, as shown in Figure 7-2(b). Therefore, after wetting the microchannel, injecting the emulsion into the confinement chamber and adding the deionized water into the wells, four platinum electrodes were inserted into the four wells respectively and electrical field was applied to the microchannel via the DC power supplies connecting to the electrodes. In this part, the separation of oil droplets of different sizes and the separation of Janus droplets with different sizes were conducted, respectively. It should be noted that, in order to compare the separation difference between oil droplets and electrically induced Janus droplets, the droplets with three different sizes, d = 25 μm, 50 μm and 75 μm, were chosen and separated in the experiments. Then, based on the experimental results, the separation of oil droplets and Janus droplets with the same size was demonstrated by injecting the mixed oil-in-water emulsion and Pickering emulsion into the microchannel. In this paper, all experiments were conducted at room temperature (23–25 ℃).

Furthermore, to minimize the effect of pressure driven flow, two measures were taken in the experiments: (a) Very large reservoirs (wells) were used to minimize the liquid level difference generated by electroosmotic flow in microchannel. (b) The liquid levels in the wells were carefully balanced before each test. (c) Each test was completed within 2 minutes.

7.4 Results and Discussion

7.4.1 Lateral Migration of Oil Droplets and Janus Droplets

The wall-induced dielectrophoretic lateral migrations of oil droplets and Janus droplets in the straight main channel were measured experimentally and calculated theoretically. The examples of the trajectories of an oil droplet and a Janus droplet with d = 75 μm ± 3 μm under the electrical field of 375 V/cm are shown in Figure 7-3(a) and (b), respectively. Figure 7-4 shows the trajectories of the oil droplets and the Janus droplets with different sizes under different electric fields in the main channel. The lateral migrations of the droplets under different conditions were

obtained by measuring the distances from the center of the droplets to the microchannel wall in the recorded images. Data at each point was measured at least three times in three different chips. The calculation of the trajectories of oil droplets and Janus droplets was carried out with MATLAB by using Equation (7-7) derived in Section 7.2. For this calculation, the iteration method was conducted by developing a computer program in MATLAB. It's clearly shown in Figure 7-4 that the calculated results match well with the experimental results.

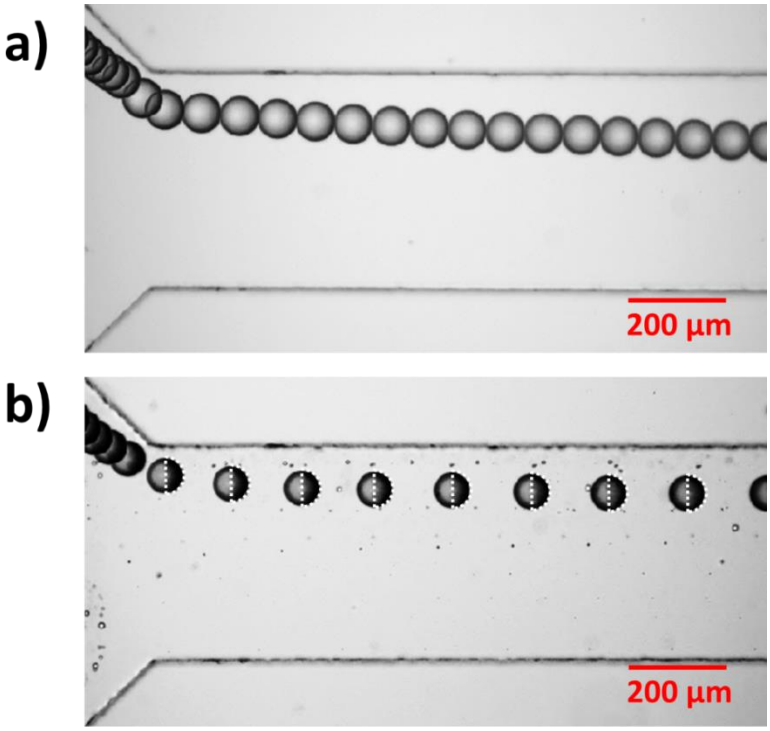

Figure 7-3. Trajectories of oil droplet and Janus droplet under the electrical field of 375 V/cm in the main channel. (a) Oil droplet, d = 75 µm ± 3 µm; (b) Janus droplet, d = 75 µm ± 3 µm. As visual aid, the dots are added to the Janus droplet to indicate the nanoparticle accumulated area.

7.4.1.1 Varying Lateral Migration with the Axial Moving Distance

As shown in Figure 7-3 and 7-4, due to the wall-induced lateral migration, both the oil droplets and Janus droplets move away from the microchannel wall gradually while they travel through the

main microchannel. It's obviously shown in this figure that the migration in the upstream section is more significant than that in the downstream section. For example, as shown in Figure 7-4(a), the trajectory of the oil droplet with the diameter of 75 μm under electrical field of 125 V/cm was indicated by the triangle points and the dot-dash line. The lateral migration of the droplet is approximately 30 μm in the y-direction when it travels through the first 200 μm length in the main channel, and then the lateral migration velocity decreases and the migration distance is less than 30 μm while traveling through the next 800 μm length in the main channel. This decelerated lateral migration is due to the dependence of the migration velocity (U_{wDEP}) on the ratio of the droplet radius to the distance from the center of the droplet to the channel wall ($\tau = a/y_d$), as shown in Equation (7-4). This is because, as the droplet moves away from the microchannel wall gradually, the wall-induced DEP force decreases; hence, the lateral migration velocity decreases.

7.4.1.2 Effect of Droplet Size

The effect of droplet size on the lateral migration can be found by comparing the trajectories of the droplets with different sizes, as shown in Figure 7-4(a) and (c). In each experiment set, the droplets with certain sizes (d = 25 μm ± 3 μm, 55 μm ± 3 μm and 75 μm ± 3 μm) were chosen and their lateral migrations in the main channel were measured respectively. It is obvious from these figures that the lateral migration of large droplets is always more apparent than that of small droplets for both oil droplets and Janus droplets. As the size of the droplet increases, the distortion of the electric field around the droplet becomes more serious, which generates stronger DEP force on the droplet (F_{wDEP}) and larger lateral migration velocity (U_{wDEP}). The same conclusion can also be obtained by examining Equation (7-7). Therefore, while moving through the same section of the microchannel, the larger the droplet, the more apparent the lateral migration.

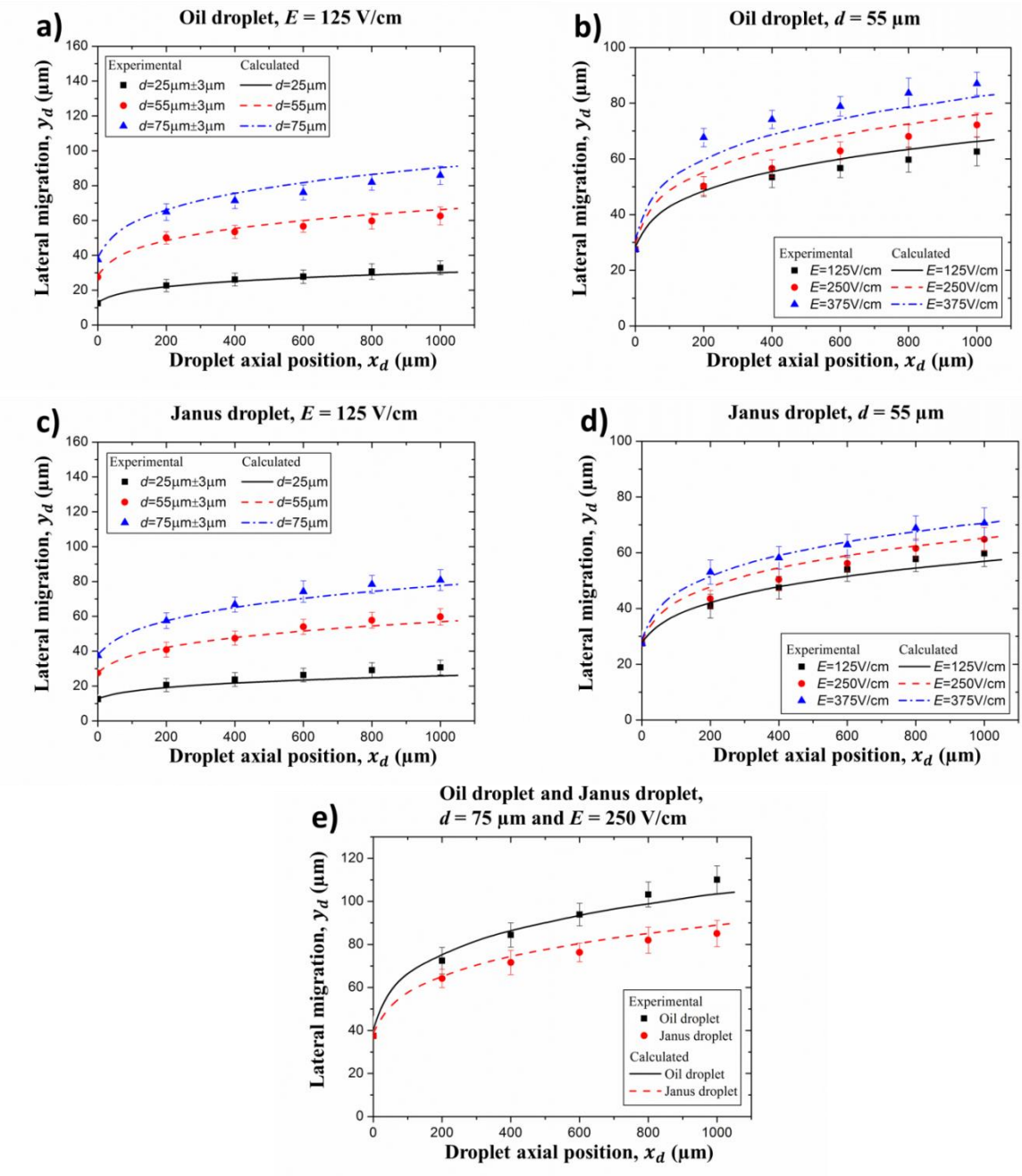

Figure 7-4. Comparison between the calculated results and experimental results for the trajectories the oil droplets and the electrically induced Janus droplets in the main channel under externally applied electrical field. (a) Oil droplets, E = 125 V/cm; (b) Oil droplets, d = 55 μm; (c) Janus droplets, E = 125 V/cm; (d) Janus droplets, d = 55 μm; (e) Oil droplets and Janus droplets, d = 75 μm and E = 250 V/cm.

7.4.1.3 Effect of Electric Field

The strength of the electrical field is another factor that affects the lateral migrations of oil droplets and Janus droplets. When the strength of the electric field increases, the DEP force acting on the droplet (F_{wDEP}) increases, as shown in Equation (7-3); therefore, the lateral migration of the droplet increases. Figure 7-4 (b) and (d) show the trajectories of the oil droplets and Janus droplets with the same size under the electrical fields of 125 V/cm, 250 V/cm and 375 V/cm. The comparison of the trajectories of oil droplets or Janus droplets with d = 55 μm under different electrical fields indicates that the lateral migrations of both oil droplet and Janus droplet increases with the strength of the externally applied electrical field. As indicated in Figure 7-4(d), the lateral migration of Janus droplet is approximately 57 μm at x_d = 1000 μm under the electrical field of 125 V/cm. If the electric field *E* is increased to 375 V/cm, the lateral migration can reach 70 μm at the same section.

7.4.1.4 Effect of Electrokinetic Mobility

The lateral migration of a droplet also changes with the droplet electrokinetic mobility, which can be understood as follows. When the electrokinetic mobility of the droplet changes, the time needed for the droplet to move through a certain section of the microchannel changes, which affects the lateral migration of it. Generally, when other parameters are fixed, if the electrokinetic mobility of the droplet increases, the time for the droplet moving through the main channel becomes shorter, and the lateral migration of the droplet decreases. This conclusion can be demonstrated by reviewing Equation (7-7) which shows the inverse relationship between y_d and μ_{ek}. As illustrated above, the electrokinetic mobility of the Janus droplets is approximate two times larger than that of the oil droplets (μ_{ek} = 3.75 × 10^{-8} m^2/(V s) for Janus droplets, μ_{ek} = 1.75 × 10^{-8} m^2/(V s) for oil droplets); therefore, the lateral migration of the Janus droplets is shorter than that of the oil droplets when moving through the same section of the main channel. It should be noted that the electrokinetic mobility difference between the oil droplets and the Janus droplets is caused by the surface charge [120,186]. In this study, the electrically induced Janus droplet is fabricated by partially covering a negatively charged oil droplet with positively charged Al_2O_3 nanoparticles. With the presence of the Al_2O_3 nanoparticles, the total number of negative charges on the droplet decreases. Therefore, under the same condition, the electrophoresis of the Janus droplet is slower

than that of the homogeneous negatively charged oil droplet. In a microchannel, the electrokinetic motion of a droplet originates from the combined effects of the electrophoresis of the droplet and the electroosmosis of the bulk liquid which are opposite in direction; thus, the electrokinetic motion of the Janus droplet is larger than that of the oil droplet.

The analysis shown above can be proven by comparing the trajectories of the Janus droplet and oil droplet with the same size under the same electrical field. As shown in Figure 7-4(e), under electrical field of 250 V/cm, the experimental measured lateral migration of the oil droplets with d = 75 μm ± 3 μm at x_p = 1000 μm is approximately 110 μm. However, for the Janus droplets with the same size, the lateral migration at x_p = 1000 μm is only 85 μm.

7.4.2 Separation of Oil Droplets by Size

As discussed above, the lateral migration of oil droplet is dependent on the droplet size. Therefore, the droplets of different sizes can be diverted into different streams and separated when they move through the straight main channel (as shown in Figure 7-2(b)). The example of separation of oil droplets by size is shown in Figure 7-5, which is obtained by superimposing the recorded images of the moving droplets. Initially, the oil droplets move into the sample inlet branch from the confinement chamber as a single stream. While reaching the entrance of the main channel, due to the push of the sheath fluid from the other inlet branch, the droplets are forced to move close to the channel wall. While the droplets pass the main channel, the wall-induced lateral migration takes place and the droplets are diverted into different streams with the large droplets moving closer to the center of the main channel. By adjusting the voltages applied to the outlet A and B, the large oil droplets move into the outlet branch B and the small droplets move into the outlet A. As shown in Figure 7-5(a), under $\phi_A = \phi_B$ = 0 V (ϕ_A and ϕ_B represent the voltages applied to the outlet A and outlet B, respectively), the electric fields in outlet branch A and B are the same with $E_A = E_B$ = 277 V/cm. Under this electric field, the larger oil droplet with d = 50 μm moves into the outlet branch B, while the smaller droplet (d = 25 μm) enters into the outlet branch A. To separate the oil droplet with d = 50 μm and the oil droplet with d = 75 μm, the voltage applied to the outlet B (ϕ_B) should be increased. With the increase of ϕ_{oB}, the proportion of the liquid moving from the main channel into the outlet branch B decreases. Under certain ϕ_{oB}, the oil droplet with d = 50 μm will move into the outlet branch A meanwhile the larger oil droplet (d = 75 μm) will move

into the outlet branch B. The experimental result indicates that the oil droplets with different diameter sizes, 50 µm and 75 µm, can be successfully separated under ϕ_B = 50 V (E_A = 283 V/cm, E_B = 236 V/cm), as shown in Figure 7-5(b).

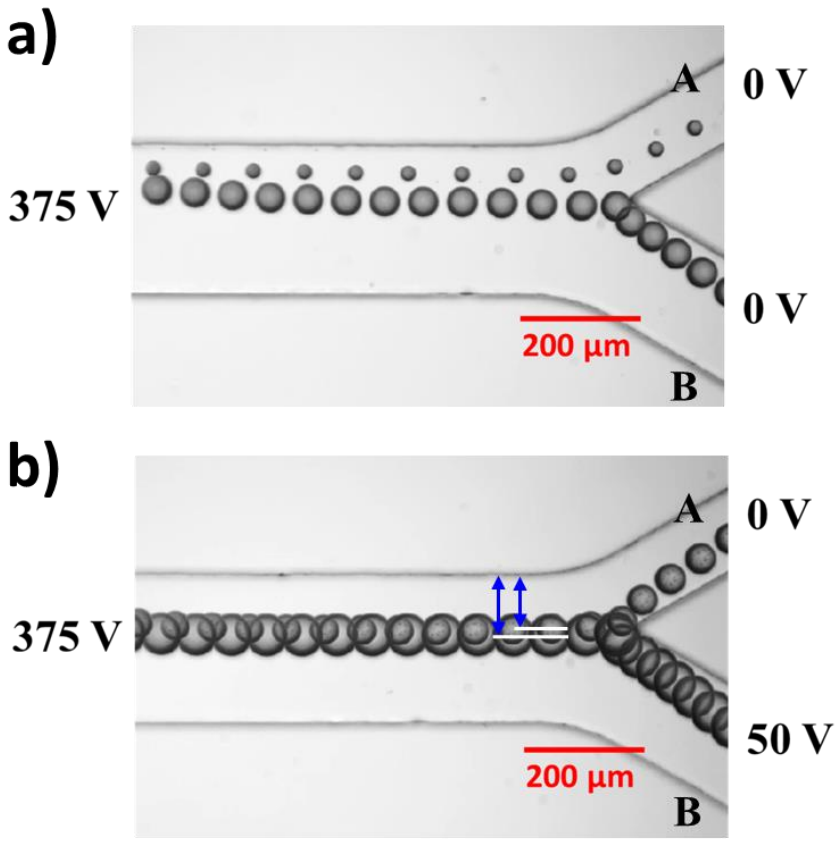

Figure 7-5. Separation of the oil droplets by size. (a) Separation of 25 and 50 µm diameter oil droplets, ϕ_{sample} = ϕ_{sheath} = 375 V, ϕ_A = ϕ_B = 0 V; (b) Separation of 50 and 75 µm diameter oil droplets, ϕ_{sample} = ϕ_{sheath} = 375 V, ϕ_A = 0 V, ϕ_B = 50 V. ϕ_{sample}, ϕ_{sheath}, ϕ_A and ϕ_B represent the voltages applying to the sample inlet reservoir, the sheath fluid inlet reservoir, outlet A and outlet B, respectively. The time scale between two droplet positions Δt is 0.08s.

Clearly, the separation of oil droplets by size can be accomplished with the wall-induced DEP method, and the separation of the droplets depends on the voltages applied to the two outlet wells.

Changing the relative values of applied voltages at the two outlet wells will lead to the variation of the proportion of the liquid moving from the main channel into each of the outlet channels, and hence enable the further separation of the droplets with different lateral migrations. The optimal values of the applied voltages at the two outlet wells can be obtained by experimental calibration for a target droplet size. It should be noted that without the presence of droplet, the electric field is always uniformly distributed inside the main channel when the values of applied voltages change; therefore, the wall-induced DEP theory shown in the theory part can still be used here to estimate the lateral migrations of droplets in the main channel.

7.4.3 Separation of Janus Droplets by Size

The wall-induced lateral migration of EIJDs is also sensitive to the droplets size; hence, the Janus droplets can also be separated by size. As two examples, Figure 7-6 shows the separation of the electrically induced Janus droplets by size. It should be noted that, in these figures, as visual aid, the dots are added to each Janus droplet to indicate the nanoparticle accumulated area. Figure 7-6 (a) shows the separation of a 75 μm diameter Janus droplet from the smaller one (d = 50 μm) under $\phi_{sample} = \phi_{sheath}$ = 375 V and $\phi_A = \phi_B$ = 0 V. It can be seen that the separation process of Janus droplets is similar to that of oil droplets. When Janus droplets with different sizes move through the main channel, the droplets are diverted into different trajectories by size and the separation takes place at the joint between the main channel and the two outlet branches. Figure 7-6(b) shows the separation of the 50 μm diameter Janus droplet from the smaller one (d = 25 μm). In this separation, to make the 50 μm diameter Janus droplet flow into the outlet branch B, the voltage applied to the outlet A, ϕ_A, increases gradually until reaching 200 V. Under this electrical field, the strength of the electrical field in outlet branch A becomes weaker than that in outlet branch B with E_A = 104 V/cm and E_B = 294 V/cm, and more liquid flows into the outlet branch B from the main channel; thus, the Janus droplet with d = 50 μm moves into outlet branch B rather than outlet branch A. In this way, the Janus droplet with 50 μm diameter is separated from the smaller one.

By comparing Figure 7-5(a) and Figure 7-6(a), we can easily find that the oil droplet and the Janus droplet with 50 μm in diameter enter into different outlet branches under the same electrical field, which is caused by the electrokinetic mobility difference between them. Therefore, it is possible to separate the oil droplet and the Janus droplet with the same size in this microfluidic chip.

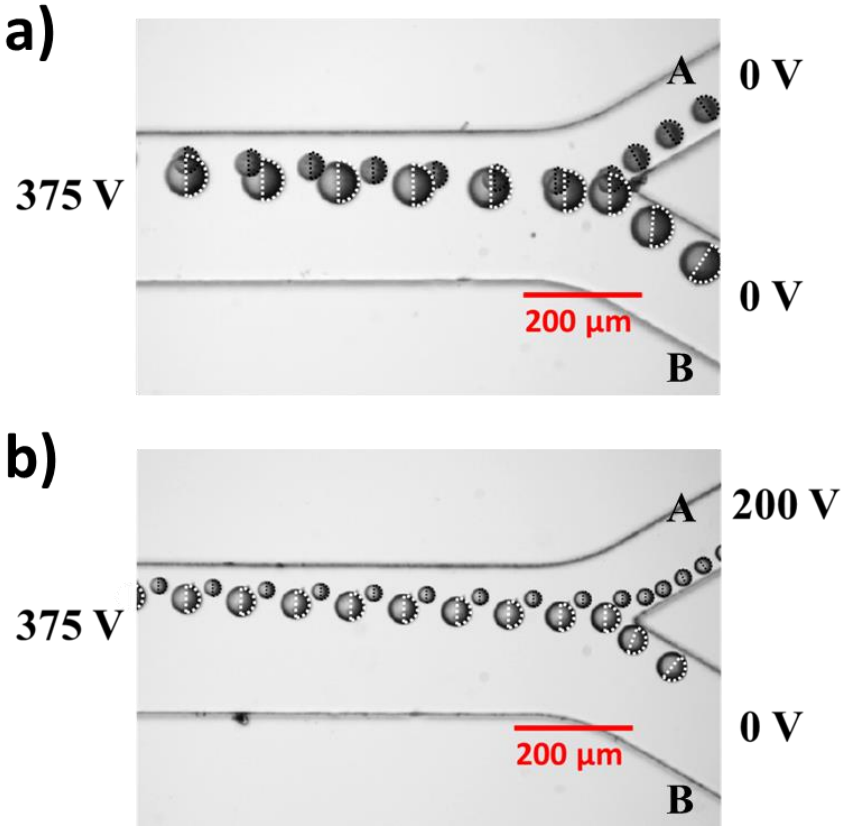

Figure 7-6. Separation of the Janus droplets by size. (a) Separation of 50 and 75 µm diameter Janus droplets, ϕ_{sample} = ϕ_{sheath} = 375 V, ϕ_A = ϕ_B = 0 V; (b) Separation of 25 and 50 µm diameter oil droplets, ϕ_{sample} = ϕ_{sheath} = 375 V, ϕ_A = 200 V, ϕ_B = 0 V. ϕ_{sample}, ϕ_{sheath}, ϕ_A and ϕ_B represent the voltages applying to the sample inlet reservoir, the sheath fluid inlet reservoir, outlet A and outlet B, respectively. As visual aid, the dots are added to each Janus droplet to indicate the nanoparticle accumulated area. The time scale between two droplet positions Δt is 0.08 s.

7.4.4 Separation of Oil Droplets and Janus Droplets with the Same Size

The separation of oil droplets and electrically induced Janus droplets of the same size were conducted. Figure 7-7 shows the trajectories of a Janus droplet of 50 µm in diameter and an oil droplet of 50 µm in diameter under the condition of ϕ_{sample} = ϕ_{sheath} = 375 V, ϕ_A = ϕ_B = 0 V (E_A = E_B = 277 V/cm). As the electrokinetic mobility of the Janus droplet is larger than that of the

oil droplet, the wall-induced lateral migration of the oil droplet is further than that of the Janus droplet while moving through the main channel. At the exit of the main channel, the oil droplet moves closer to the central region of the microchannel; eventually, the oil droplet moves into the outlet branch B while the Janus droplet enters the outlet branch A. It should be noted that this is just one example of the separation of Janus droplets and oil droplets with the same diameter. By adjusting the voltages applied to the two outlets of the microchannel, the oil droplet and Janus droplet with other sizes can be separated. The relationship between the voltages and the separation size of the oil droplets and the Janus droplets can be easily obtained through experiment.

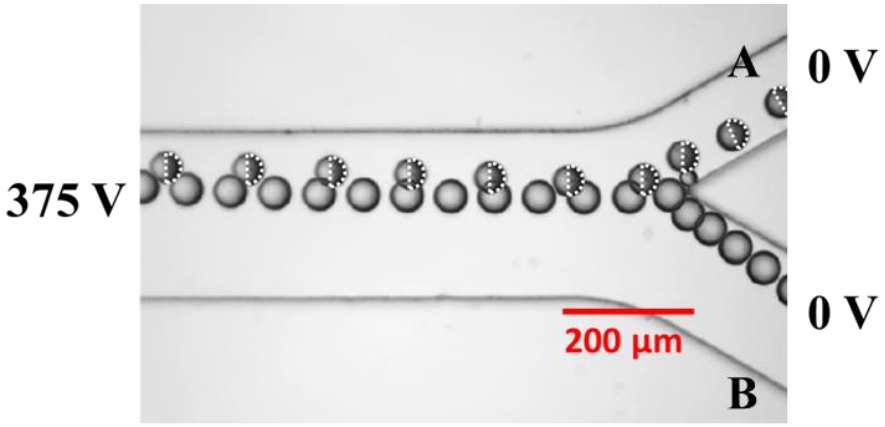

Figure 7-7. Separation of Janus droplet and oil droplet with 50 µm in diameter under ϕ_{sample} = ϕ_{sheath} = 375 V, ϕ_A = ϕ_B = 0 V. ϕ_{sample}, ϕ_{sheath}, ϕ_A and ϕ_B represent the voltages applying to the sample inlet reservoir, the sheath fluid inlet reservoir, outlet A and outlet B, respectively. As visual aid, the dots are added to each Janus droplet to indicate the nanoparticle accumulated area. The time scale between two droplet positions Δt is 0.08 s.

Although the wall-induced DEP method has advantages in separating oil droplets and Janus droplet, it possesses limitation. The limitation results from the property of wall-induced DEP. As discussed above, the wall-induced DEP is dependent on the droplet size, electric field strength and electrokinetic mobility of the droplet. If keeping the other two factors fixed and changing one factor, the lateral migration of the droplet can be controlled. Therefore, the droplets can be

separated based on this factor. For example, the separation of oil droplets and Janus droplets by size. However, if two factors change simultaneously, the lateral migration becomes uncertain, and under some specific conditions, the lateral migration will remain fixed regardless of the variations of these influence factors. Generally, with the increase of the droplet size, the lateral migration increases, while the lateral migration decreases with the increase of the droplet electrokinetic mobility. Therefore, for smaller oil droplets and larger Janus droplets, the lateral migrations of them could be the same under certain conditions, that limits the separation between them.

7.5 Conclusions

In this chapter, the wall-induced DEP lateral migrations of both EIJDs and oil droplets were studied, and the separation of oil droplets and Janus droplets in a microchannel by the wall-induced DEP method was demonstrated for the first time. The wall-induced dielectrophoretic lateral migrations of both oil droplets and electrically induced Janus droplets in a straight microchannel were studied first. The experimental results indicate that the migration of the droplets from the channel wall is dependent on the strength of the electric field, the size and electrokinetic mobility of the droplet. The increases of the strength of the electric field and the size of the droplet lead to further lateral migration. On the contrary, the lateral migration decreases with the increase of the electrokinetic mobility of the droplet; therefore, under the same condition, the lateral migration of the Janus droplet is smaller than that of the oil droplet. The experimental measured lateral migrations of oil droplets and Janus droplets were also compared with the theoretical predicted results, and good agreement was found. Then, the wall-induced DEP separation method was successfully demonstrated through separation of oil droplets by size, separation of electrically induced Janus droplets by size, and separation of oil droplets and Janus droplets with the same size in a microchannel with two inlet branches and two outlet braches. The experimental results indicate that the separation of target droplets can be easily accomplished by varying the applied voltages at the ends of the two outlet branches.

The wall-induced DEP droplet separation method presented in this chapter has the advantages of simple structure and easy operation, which can be used to sort the target droplets with fixed size and morphology for specific applications after they are fabricated. This method holds promise in the applications of industrial and research fields.

CHAPTER 8. Application I: Fabrication of Microvalve Using Electrokinetic Motion of EIJD*

8.1 Introduction

Microfluidics has wide applications in various areas, such as biotechnology, chemistry and life science, due to less reagent consumption, short reaction time, low cost and compact size [187–191]. As one of the most important microfluidic components, microvalves are designed to carry out flow regulation and flow switching [164,192,193]. Generally, microvalves can be categorized into five major classes based on their actuation originalities: pinch, pneumatic, phase change, capillary and electrokinetic. Pinch microvalves are operated by compressing a flexible membrane with an external mechanical force. Magnetic [194–196], electric [197,198,106,199] and thermal [200–205] actuations are universally used to realize the compression. For example, in 1979, Terry et al. [194] first developed a magnetic pinch valve to control the motion of gas by placing a solenoid plunger on top of a nickel diaphragm. Normally, the plunger presses the diaphragm onto the micromachined silicon valve seat and the valve closes. Once the solenoid is powered on, the plunger moves upward to release the diaphragm to open the valve. By turning on and off the solenoid, the magnetic microvalve can be operated. Despite the simple actuation principles of the pinch microvalves, it is difficult to fabricate them because of their complicated structures. Generally, a pinch microvalve consists of diaphragm, valve seat, sealing ring and actuator. By assembling these components together, a pinch microvalve always contains multiple layers and films, that causes unavoidable leakage [164]. Pneumatic microvalves, introduced firstly by Quake's group [206], are the most widely used valves in microfluidics nowadays [207–209]. The microvalve consists of a fluidic channel and a control channel with an elastomeric membrane separating the two channels. The membrane is actuated by external air pressure via the control channel. With the deformation of the membrane, the fluid in the fluidic channel is displaced and the channel gets sealed. However, apart from the liquid driven system, the external actuation

* A similar version of this chapter was submitted or published as:

Li, M.; Li, D. Microvalve Using Electrokinetic Motion of Electrically Induced Janus Droplet. *Anal. Chim. Acta*. **2018**, 1021, 85-94. https://www.sciencedirect.com/science/article/pii/S0003267018303660

system, such as air pump, is essential in fabricating pneumatic microvalve, which makes the microsystem complex and limits its further miniaturization. Phase change microvalves are developed based on the phase transition of the actuator materials. When phase transition takes place in response to changes in temperature or pH value, the volume of the actuator material changes, which forces the material flowing into the microchannel or actuates the deformation of the adjacent microchannel to control the fluid flow inside the channel. Ice [210], hydrogel [211–213], paraffin[214–216] and polyethylene glycol [217] have been proven as viable actuator materials for fabricating phase change microvalves. As phase transition needs time, the response time of the phase change microvalve is longer, from several seconds to several minutes, which restricts its applications in slow-response conditions. Capillary microvalves manipulate the fluid flow inside microchannels by changing the capillary forces. For a passive capillary valve, a sudden geometry expansion is set in the microchannel, which causes a pressure barrier and traps the fluid to form a meniscus until extra driving force is applied to open the valve [218–220]. Apart from the abrupt geometry change strategy, the electrocapillary and thermocapillary effects are also able to control the capillary force by generating electrical potential difference and temperature gradient on the microchannel wall, which have been proven to be efficient methods to fabricate capillary microvalves [221–223]. The advantages of the capillary microvalve are that it does not have any moving parts and can be fabricated easily; however, this valve is hard to recover once opened, which restricts its further application. Electrokinetic valves use electroosmotic flow to drive liquid moving to target microchannels by changing the electrical field applied to each microchannel [224–232]. The major issue of this type of valves is that the ion/molecular diffusion cannot be neglected since the microchannels are opened and connected at all times.

In general, there are shortcomings and challenges in the traditional microvalves, for example: (a) leakage, (b) large size, (c) long responsive time, (d) bulky and complex external actuation system, (e) complicated structure and fabrication process. These shortcomings restrict the miniaturization and efficiency of the microfluidic devices. Therefore, research in developing new microvalves with novel strategies is highly desirable.

Recently, the development of Janus materials provides a new direction for fabricating microvalves. A Janus material has two sides carrying distinct properties. Due to their anisotropic property, the Janus materials have found potential applications in mechanics [2,233,234], chemistry [235,236],

biology [237–239] and pharmaceutics [240–242]. In the fabrication of microvalve with Janus materials, Daghighi et al. [96] first introduced a microvalve using the electrokinetic motion of metallo-dielectric Janus particle (with a metallic hemisphere and a dielectric hemisphere) and analyzed the feasibility of using such a Janus particle to form a microvalve numerically. This microvalve consists of a microchamber, three microchannels, four electrodes and a Janus particle. When applying electrical field, vortices are introduced in the vicinity of the Janus particle and drive the particle to move in the microchamber and block the entrance of the target microchannel. By switching the electrical field, the Janus particle moves and blocks different microchannels. However, in practice, the surface of the microparticles, the surface of the wall of the valve chamber and the entrance of the microchannels cannot be perfect spherical and smooth. Therefore, the solid microparticle cannot fully block the entrance of the microchannels, resulting in leakage. Later, Wang et al. [243] fabricated a no-moving part microvalve with N-isopropylacrylamide (NIPAM)/16-mercaptohexadecanoic acid (MHA) Janus elliptical nanopillar arrays. This Janus nanopillar array is wet anisotropically which only allows water to move along the hydrophilic direction. Based on this mechanism, they developed a one-way microvalve by combining a T-shaped microchannel with the Janus pillar arrays for gas-liquid separation.

In this chapter, we reported a microvalve fabricated with EIJDs. Because such a Janus droplet can move in response to the change of the applied electric field and can deform in shape slightly under the applied electric field force (and hence can block the entrance of a microchannel well), it is possible to achieve the function of the microvalve by utilizing the electrokinetic motion of such a Janus droplet. In this study, the application of such a Janus droplet in fabricating electrically responsive microvalve is demonstrated. The electrokinetic motion of the Janus droplet in a circular microchamber under switching electric field was examined first. Then, the microvalve was fabricated by injecting an EIJD into a three dimensional (3D) microchannel, and the performance of the microvalve, including switching time, flow rate and leakage, was analyzed. In addition, the EIJD was compared with an isotropic oil droplet, and the sealing performance of the oil droplet-based microvalve was tested.

8.2 Materials and Methods

8.2.1 Preparation of EIJDs

The EIJDs were prepared from the Al_2O_3-nanoparticle-stabilized Pickering emulsion under the induction of externally applied direct current (DC) electric field. First, emulsion oil droplets were prepared through vibration by following the steps shown in section 3.2.3.4. The Pickering emulsion droplets are formed by adding the emulsion oil droplets into Al_2O_3 nanoparticle suspension. In the experiment, the Pickering emulsion droplets were first injected into a microchannel. Under the electric field, the positively charged nanoparticles adhering at the oil-water interface were induced to move and accumulate on one side of the droplets. Finally, a compact nanoparticle film was formed on the side of each droplet facing the cathode of the electric field. The EIJDs with half-half geometry can be generated with 1.5 mg/mL nanoparticle suspension.

8.2.2 Fabrication of Voltage Control Unit

A voltage control unit, including four serial voltage-adjustable DC power supplies (CSI12001X, Circuit Specialist Inc., USA), signal relays (G5V-2, Omron, Canada) and data-acquisition (DAQ) device (NI USB6259, National Instruments, USA), were used to control the voltages applied to the microfluidic chips (Figure 8-1). This unit can be easily controlled with LabVIEW software (National Instruments, USA). In this unit, the serial power supplies connected to the signal relays were set to provide voltages ranging from 0 V to 500 V. The DAQ device received the order from the computer and sent out signals to operate the relays. By turning on/off the relays, the output voltage at each outlet end of the unit can be switched.

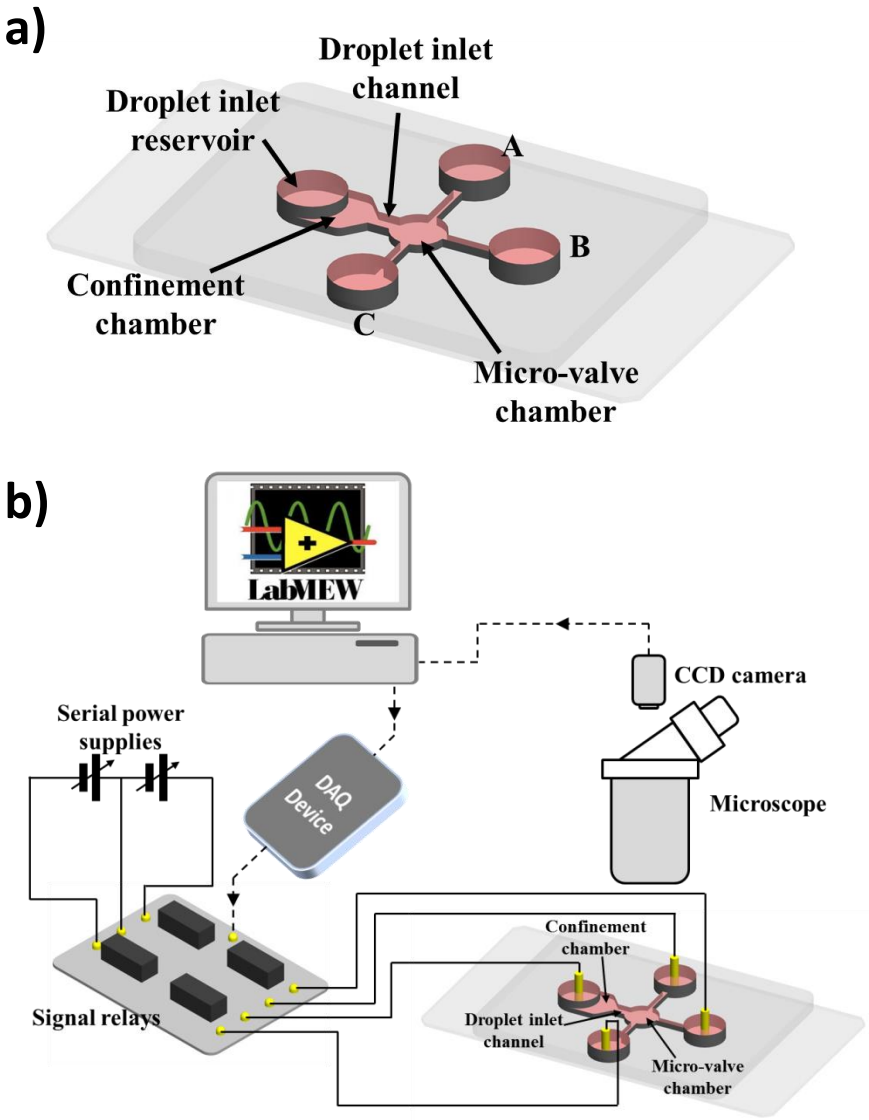

Figure 8-1. (a) Schematic diagram of the microchannel for detecting the electrokinetic motion of the EIJD. (b) Schematic diagram of the system setup for analyzing electrokinetic property of the EIJDs.

8.2.3 Analysis of Electrokinetic Property of the EIJDs

The electrokinetic property of the EIJDs was analyzed in a PDMS microfluidic chip under switching electric field. The whole analysis system consists of three major units: microfluidic chip, optical visualization, and voltage control unit (Figure 8-1(a)). The microfluidic chip was fabricated by a standard soft lithography technique, which contains a patterned top PDMS layer and a flat PDMS substrate. A cross-shaped microchannel with uniform height of 80 μm was designed, composed of a circular micro-valve chamber, four branch channels, and a confinement chamber. The micro-valve chamber (200 μm in diameter), connecting four branch channels, was located at the center of the microchannel. The channel connecting the confinement chamber and the micro-valve chamber was 500 μm long and 100 μm wide for transporting the Janus droplet, while the dimensions of the other three channels were 5 mm × 30 μm (length × width). The confinement chamber was used to hold the Pickering emulsion droplets after they were injected from the reservoir. The electric field was applied to the microchannel through four platinum electrodes inserted in the reservoirs.

While analyzing the electrokinetic property of EIJDs, 10 μL deionized water was added into the microchannel first. After injecting 5 μL Pickering emulsion droplets into the confinement chamber, 50 μL deionized water was added into each reservoir, respectively. The electrodes were inserted into the reservoirs, and the electric field was applied to the microchannel by the voltage control unit. Initially, the electric field was applied to the confinement chamber and the droplet inlet channel; this is to induce the nanoparticles to accumulate to one hemisphere of the droplet to form EIJDs and to drive the droplets to flow towards the micro-valve chamber. When one Janus droplet entered into the circular microchamber, the electric field applied to the microchannel was switched continuously by using LabVIEW software to operate the voltage control unit. Under the switching electric field, the electrokinetic motion of the Janus droplet in the circular micro-valve chamber was observed with the Nikon Ti-E optical microscope and recorded through a charge coupled device (CCD) camera (DS-Qi1Mc, Nikon) at 25 fps (Figure 8-1(b)).

8.2.4 Fabrication of Multilayer Microfluidic Chip

The microfluidic chip used in fabricating microvalve includes two layers, top PDMS layer and bottom PDMS layer. The chips were made by the soft lithography technique. The process included

the following steps: top layer master fabrication, bottom layer master fabrication and assembly of PDMS layers (Figure 8-2(a)). The top layer master has a three-dimension (3D) photoresist structure. To fabricate it, a layer of photoresist (SU-8 2015, MicroChem, USA) with the thickness of 20 μm was first spin-coated onto a silicon wafer, followed by soft baking at 65 ℃ for 2 min and 95 ℃ for 3.5 min. Then, the SU-8 coated wafer was exposed to ultraviolet (UV) light with mask #1 placed on top it. After post exposure baking (65 ℃ for 3 min and 95 ℃ for 4.5 min), the second layer of photoresist (SU-8 2025, MicroChem, USA) with the thickness of 40 μm was spin-coated onto the wafer, followed by soft baking (65 ℃ for 3 min, 95 ℃ for 6 min). Before UV exposure, the mask #2 was put on the wafer and aligned to the first layer photoresist pattern through an optical microscope (Nikon SMZ800, Nikon, Japan). With post exposure baking (65 ℃ for 1 min and 95 ℃ for 6 min) and development, the top layer master with 3D photoresist structures was formed. The bottom layer master was fabricated via the single-layer soft lithography method. In brief, the wafer was spin-coated by the photoresist layer (SU-8 2025, MicroChem, USA) with the thickness of 40 μm and baked at 65 ℃ for 3 min and at 95 ℃ for 6 min. After the processes of UV exposure, post exposure bake and development, the pattern was transferred from the mask to the wafer. After fabricating the masters, the degassed polydimethylsiloxane PDMS (10:1 (w/w) ratio of precursor and curing agent) was poured onto the masters and heated at 80 ℃ for 1 hour. Then the PDMS slabs with the designed microstructures were peeled off and four reservoirs were punched on the top PDMS layer. After plasma treatment (HARRICK PLASMA, Ithaca, NY, USA), the top PDMS layer was aligned to the bottom PDMS layer under the Nikon Ti-E microscope and the 3D microchannel was formed.

The 3D microchannel was composed of a micro-valve chamber, four branch channels and a confinement chamber (Figure 8-2(b) and (c)). The micro-valve chamber located at the center of the microchannel was 300 μm in diameter, which was used for connecting the branch channels and holding the Janus droplet. The droplet inlet channel with 100 μm width and 500 μm length was set between the confinement chamber and the micro-valve chamber to transfer the EIJD. The confinement chamber was designed for holding the Pickering emulsion droplets and also served as a filter to block the entry of large emulsion droplets due to its limited height. The confinement chamber, droplet inlet channel and micro-valve chamber had uniform height of 100 μm. The

dimensions of the other three branches, inlet channel, outlet A and B, were 5 mm × 20 μm × 20 μm (length × width × height), and the angle between the two outlet channels was 45°.

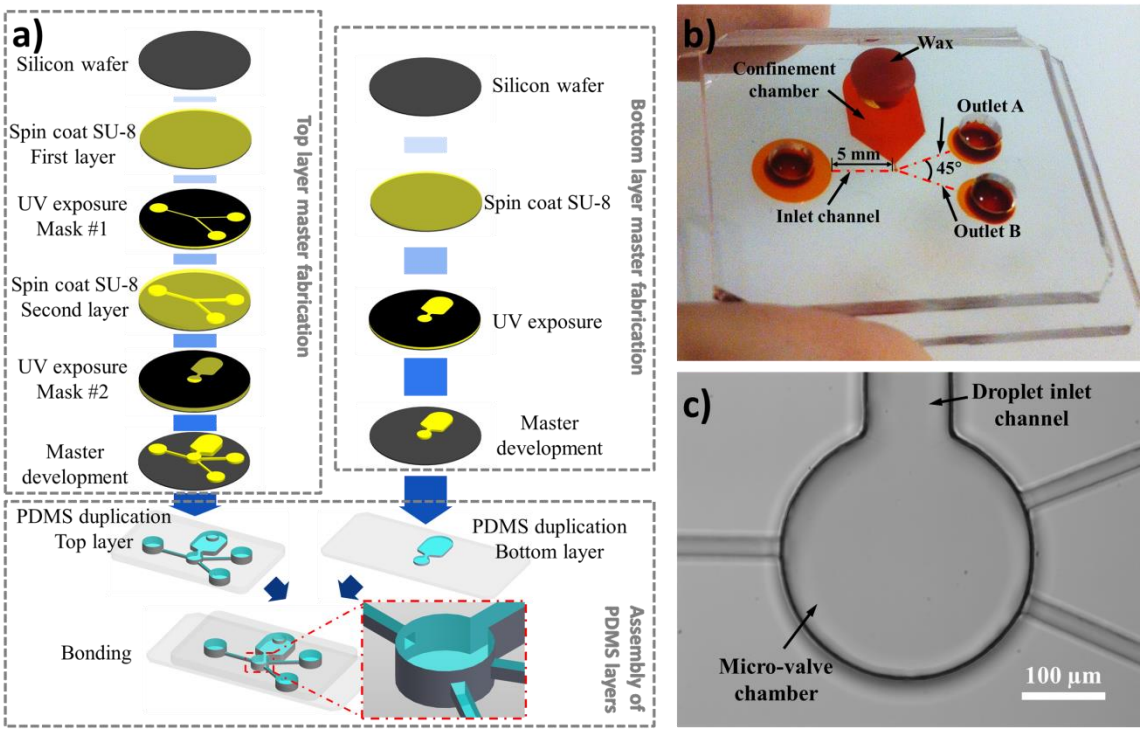

Figure 8-2. (a) Schematic diagram of the fabrication of multilayer microfluidic chip. (b) Picture of the microfluidic chip (filled with methyl orange solution for clarity). (c) Optical microscopic image of the microchannel.

8.2.5 Function Test of the Microvalve

To test the function of the electrically responsive EIJD microvalve, experiments were conducted by using the experimental setup as described previously, including the microfluidic chip, voltage control unit and optical visualization. However, as seen in Figure 8-3, the microfluidic chip used in this part has a configuration different from the chip shown in Figure 8-1. After adding 10 μL deionized water into the microchannel for wetting, injecting 5 μL Pickering emulsion droplets into the confinement chamber and adding 50 μL deionized water into each reservoir, four platinum

electrodes connecting to the voltage control unit were inserted into the reservoirs. Voltages were applied from the droplet inlet reservoir (ϕ_d) to the outlet reservoirs (ϕ_A and ϕ_B) with $\phi_d = 250\ V$ and $\phi_A = \phi_B = 0V$. Under this electric field, the positively charged nanoparticles attached on the Pickering emulsion droplets accumulated to the side of the droplets facing the cathode and, meanwhile, the droplets moved towards the droplet inlet channel. After one Janus droplet flew into the micro-valve chamber from the droplet inlet channel, the electric field was switched to control the motion of the Janus droplet, so that the Janus droplet would move towards and block a target channel to achieve the function of the microvalve. To avoid the effect of the liquid motion between the confinement chamber and the droplet inlet channel during the operation of the microvalve, hot wax was introduced to seal the droplet inlet reservoir after injecting the Janus droplet to the micro-valve chamber. In this experiment, the motions of the Janus droplet in the micro-valve chamber under different strengths of electric field were visualized with the Nikon Ti-E microscope and recorded by the CCD camera for later measurement and analysis.

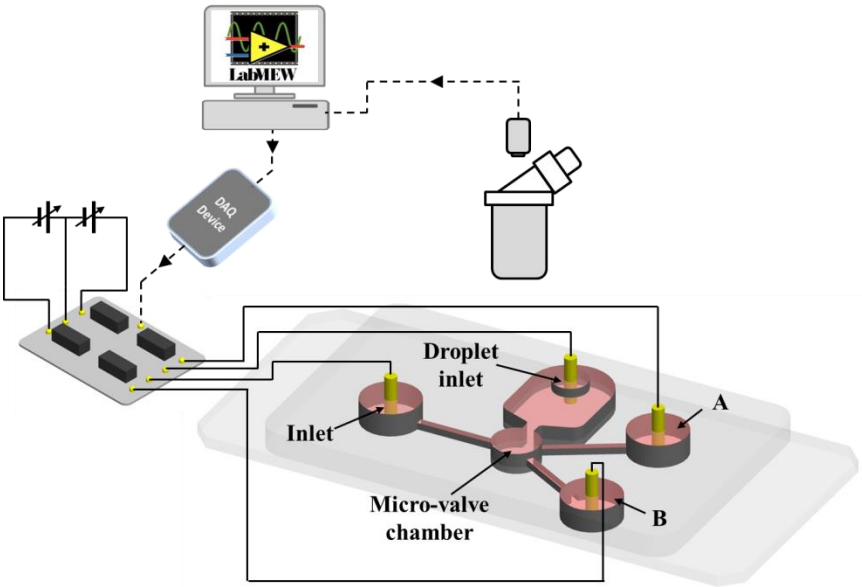

Figure 8-3. Schematic diagram of the experimental setup for testing the function of the microvalve.

8.2.6 Evaluation of Sealing Performance of the Microvalve

The sealing of the target outlet channel in the microvalve was evaluated by using fluorescent nanoparticles (23 nm in diameter, Fluoro-Max Dyed Red Aqueous Fluorescent Particles, Thermo Scientific Inc., Fremont, California, USA). Briefly, after one of the outlet channels was blocked by the Janus droplet, the fluorescent nanoparticle suspension was injected into the microchannel through the inlet reservoir. By visualizing the nanoparticle streams under a fluorescent microscope (Nikon Ti-E), the moving direction of the liquid inside microchannel and the sealing effectiveness of the microvalve were examined. To make comparison, the sealing performance of the microvalve using an isotropic oil droplet was also detected by using the fluorescent nanoparticles by following the same procedure under the same experimental conditions.

8.3 Results and Discussion

8.3.1 Rotation of the EIJD under Switching Electric Field

Under externally applied electric field, the Janus droplet experiences electrokinetic motion in a microchannel. Different from the isotropic droplet, the Janus droplet carries surface charges of opposite signs on its two hemispheres (the Al_2O_3 nanoparticle film is positively charged and the oil-water interface is negatively charged), the electrostatic forces exerting on the two hemispheres ($\vec{F}_{e,J}^{+}$ and $\vec{F}_{e,J}^{-}$) are in opposite directions. If the Janus droplet is unaligned with the electric field (the normal vector at the interface of its two hemispheres has an angle with the electric field), the electrostatic forces will generate torques to rotate the Janus droplet until it gets lined up with the electric field (Figure 8-4(a)). Once it reaches such a steady state, the Janus droplet moves along the electric field with the positively charged hemisphere facing the cathode and the negatively charged hemisphere facing the anode.

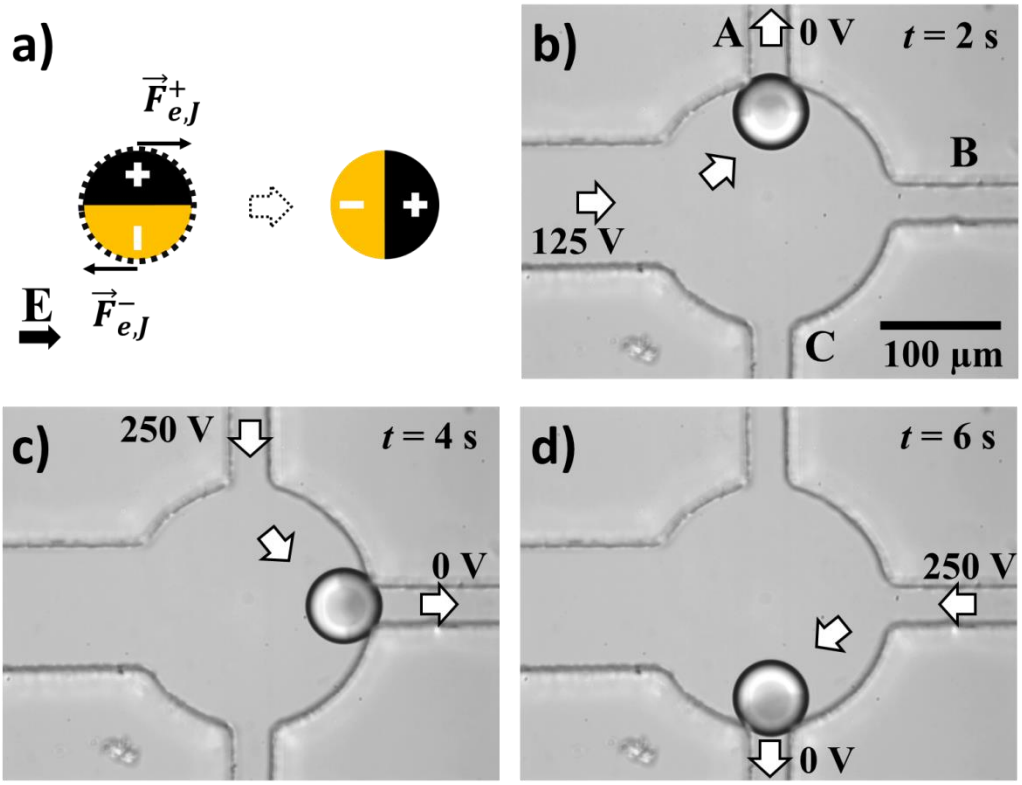

Figure 8-4. (a) Schematic diagram of the alignment of Janus droplet to the electric field. (b)-(d) The rotation and motion of an EIJD with the diameter of approximately 60 µm in a circular micro-valve chamber under switching electric field. The diameter of the micro-valve chamber is 200 µm in diameter. Arrows in pictures (b)-(d) represent the electric field direction.

In this study, a Janus droplet with approximately 60 µm in diameter was injected into the micro-valve chamber and its electrokinetic motion in response to the switching electric field was observed. Figure 8-4(b) to (d) indicates the rotation of the Janus droplet in the microvalve chamber while the direction of the electric field keeps changing. As shown in Figure 8-4(b), initially, the electric field was applied to the microchannel from the droplet inlet channel to outlet A with $\phi_i = 125\,V$ and $\phi_A = 0\,V$ (ϕ_i and ϕ_A are the voltages applied to the droplet inlet reservoir and reservoir A). Under this electric field, electroosmotic flow is generated in the microchannel and pushes the Janus droplet to move towards the entrance of outlet A. While moving, the electrostatic forces acting on the Janus droplet rotates it and aligns it with the electric field. Finally, the Janus droplet reaches the entrance of outlet A with the nanoparticle-coated hemisphere facing the

entrance (the direction of the cathode of the electric field). After this, the electric field is switched by sending out signals to control the signal relays. Under $\phi_A = 250\,V$ and $\phi_B = 0\,V$ (ϕ_B represents voltage applied to reservoir B), the Janus droplet rotates and leaves the entrance of outlet A, and moves to the entrance of outlet B with the positively charged hemisphere facing the cathode of the electric field (Figure 8-4(c)). To drive the Janus droplet moving from outlet B to outlet C, the electric field is switched again with $\phi_B = 250\,V$ and $\phi_C = 0\,V$ (ϕ_C represents voltage applied to reservoir C) (Figure 8-4(d)).

8.3.2 Operation of the Microvalve

The strategy of the microvalve is using a droplet to block one of the outlet channels and driving the liquid to move into the other one. This is achieved by the electrokinetic motion of the electrically induced Janus droplet and the electroosmotic flow in the microchannel. The valve operation process is shown in Figure 8-5, and the voltages applied to the microvalve at each step are listed in Table 8-1. As shown in Figure 8-5(a), initially, the Janus droplet stays next to the entrance of outlet B. To drive the Janus droplet to outlet A, the electric field was applied from the inlet channel and the outlet B to the outlet A with $\phi_i = 250\,V$, $\phi_A = 0\,V$ and $\phi_B = 250\,V$ (ϕ_i, ϕ_A and ϕ_B represent the voltages applied to inlet, outlet A and outlet B reservoirs). Under this electric field, electrokinetic motion of the Janus droplet is generated, and the Janus droplet moves to the entrance of the outlet A and rotates gradually to align up with the electric field (Figure 8-5(b)). Under this specific electric field, it takes approximately 5 s for the Janus droplet to move from its initial location to the entrance of outlet A. After 5 s, the voltage applied to outlet B was turned down to 0 V ($\phi_B = 0\,V$). As the entrance of outlet A is blocked by the Janus droplet, under this electric field ($\phi_i = 250\,V$, $\phi_A = 0\,V$ and $\phi_B = 0\,V$), the liquid is pumped from the inlet channel to the outlet B by electroosmosis (Figure 8-5(c)); this process lasts for 9 s. In the next step (step 3 in Table 8-1), the microvalve was switched by transporting the Janus droplet to block outlet B. To accomplish this, the voltage applied to outlet A (ϕ_A) was increased from 0 V to 250 V. As a result, the Janus droplet detaches from the entrance of outlet A first (Figure 8-5(d)), then rotates and moves in the micro-valve chamber responding to the electric field (Figure 8-5(e)). Under this specific electric field, within 5 s, the Janus droplet reaches outlet B and blocks its entrance with the positively charged hemisphere facing the cathode of the electric field. After this, ϕ_A was set to be 0 V to drive the liquid to move to the opened outlet A (Figure 8-5(f)).

As the liquid in the microvalve is pumped by electroosmosis, the flow rate of the liquid can be easily adjusted by changing the applied electric field. The electroosmotic flow velocity ($\vec{U}_{eof}$) on a charged surface can be calculated by [67]:

$$\vec{U}_{eof} = -\frac{\varepsilon_o \varepsilon_w \zeta_w}{\eta_w} \vec{E} \tag{8-1}$$

where ε_o and ε_w are the permittivities of vacuum and surrounding electrolyte solution, respectively. $\vec{E}$ is the electric field, ζ_w is the zeta potential of the surface and η_w is the liquid viscosity. For a microchannel with the cross sectional area of A, the electroosmotic volume flow rate (V_{eof}) is given by:

$$V_{eof} = \left|\vec{U}_{eof} \cdot A\right| = \frac{\varepsilon_o \varepsilon_m |\zeta_w|}{\eta_m} EA \tag{8-2}$$

E is the electric field strength in the microchannel. The zeta potential of PDMS microchannel wall in contact with deionized water is –60 mV [148]. The cross-section areas of the inlet channel, outlet A and B are the same, $S = 400\ \mu m^2$. While outlet B is blocked (Figure 8-5(f)), under the electric field of $\phi_i = 250\ V$, $\phi_A = 0\ V$ (the distance between the electrodes is 1 cm; therefore, the strengths of the electric fields in the inlet channel and outlet B are $E_i = E_A = 250\ V/cm$), the liquid volume flow rate in the microvalve from inlet channel to outlet A can be estimated with Equation (8-2) to be approximately 0.425 nL/s. It is clearly shown in Equation (8-2) that, when the other parameters remain fixed, the electroosmotic volume flow rate is linearly correlated to the strength of the electric field. For example, if ϕ_i is increased 1.5 times to 375 V ($E_i = 375\ V/cm$), the volume flow rate will increase to 0.638 nL/s. Therefore, after the target outlet is blocked, the flow rate of the liquid pumped into the other outlet can be adjusted easily via changing the electrical field applied to the inlet and outlet branches. The microvalve tested here is fabricated with PDMS, and the function of the microvalve can also be accomplished when the microfluidic chip is fabricated with other materials, such as, PMMA and PVDF.

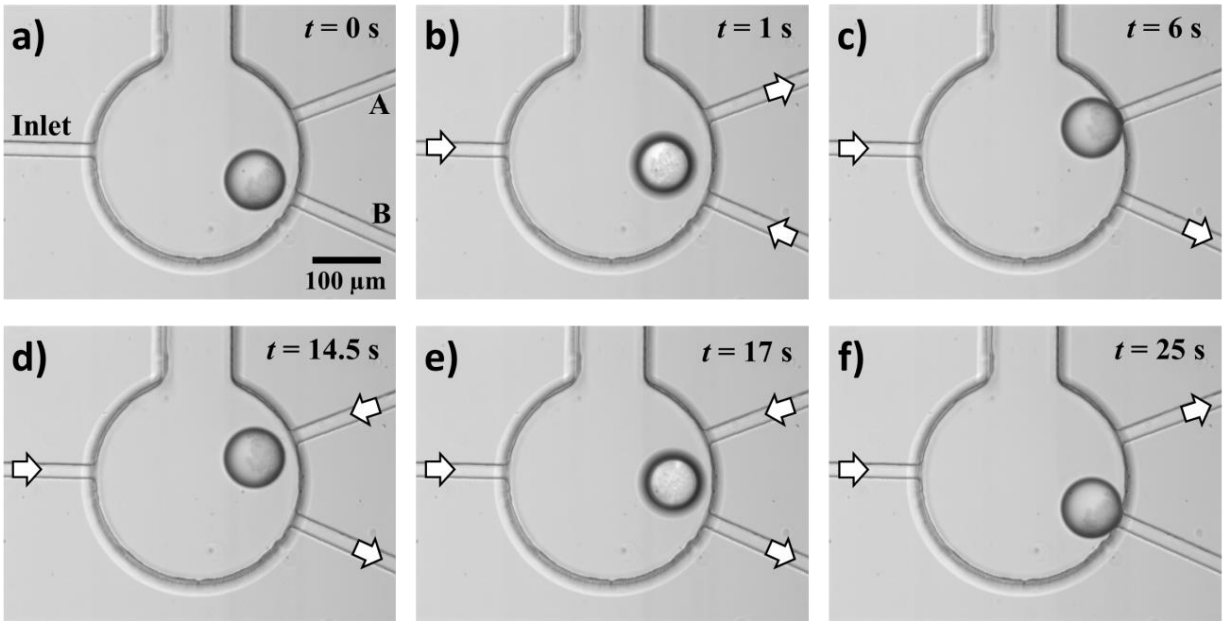

Figure 8-5. An example of operation of the microvalve under the externally applied electric field. (a) The initial state of the microvalve, t = 0 s. (b) Electrokinetic motion of the Janus droplet to block outlet A, t = 1 s. c, Liquid transportation from inlet channel to outlet B, t = 6 s. (d)-(e) Microvalve switching by blocking outlet B, t = 14.5 s and t = 17 s. (f) Liquid transportation from inlet channel to outlet A, t = 25 s. The arrows in the pictures indicate the electric field direction. The diameter of the Janus droplet is 85 µm.

Table 8-1. The steps for operating the microvalve.

Step	ϕ_i (V)	ϕ_A (V)	ϕ_B (V)	t (s)	Function
1	250 V	0 V	250 V	0-5	Block outlet A
2	250 V	0 V	0 V	5-14	Liquid transport to outlet B
3	250 V	250 V	0 V	14-19	Block outlet B
4	250 V	0 V	0 V	19-28	Liquid transport to outlet A

ϕ_i, ϕ_A and ϕ_B represent the voltages applied to the reservoirs of inlet, outlet A and outlet B, respectively.

8.3.3 Effect of the Electric Field Strength on Microvalve Switching Time

The effect of the strength of the electric field on microvalve switching time (the time required for the Janus droplet to move from one outlet to the other) results from the electrokinetic motion of the Janus droplet in the micro-valve chamber. The electrokinetic motion of EIJDs in microchannels has been studied numerically and experimentally in Chapter 6. The electrokinetic motion of a Janus droplet in a microchannel ($\vec{U}_{ek}$) develops from the effects of the electroosmotic flow of the surrounding liquid and the electrophoresis of the droplet. The electrokinetic velocity ($\vec{U}_{ek}$) can be expressed as:

$$\vec{U}_{ek} = \vec{U}_{eof} + \vec{U}_{ep} = (\mu_{eof} + \mu_{ep}) \cdot \vec{E} \tag{8-3}$$

where μ_{eof} and $\vec{U}_{eof}$ are the electroosmotic mobility and the electroosmotic flow velocity of the surrounding liquid, μ_{ep} and $\vec{U}_{ep}$ are the electrophoresis mobility and the electrophoretic velocity of the Janus droplet. This equation clearly indicates that $\vec{U}_{ek}$ is positively correlated to the strength of the electric field. Consequently, for the microvalve, when the strength of the electric field increases, the electrokinetic velocity of the Janus droplet in the microchamber increases and the microvalve switching time decreases.

To study the effect of the strength of the electric field on microvalve switching time experimentally, the voltages applied to the inlet reservoir and one of the outlet reservoirs were set to be the same value, ranging from 150 V to 375 V, while the voltage in the other outlet reservoir was 0 V. For example, in Figure 8-5(d), the voltage of 250 V was applied to the inlet and outlet A to drive the Janus droplet to block outlet B. In this study, under different applied voltages, the switching times of the microvalve were measured by analyzing the recorded videos with imaging analysis software. The correlation between the applied voltage and the microvalve switching time is plotted in Figure 8-6. It can be seen from this figure that the microvalve switching time decreases with the increase of the applied voltage. For example, under the voltage of 150 V, the average switching time of the microvalve is 6.5 s, which decreases to 1.8 s when the applied voltage increases to 350 V. However, due to large size difference between the branches and the microvalve chamber, the increase of electric field in the chamber is limited by increasing the voltages applied in the reservoirs. For example, under the applied voltages of $\phi_i = 375\ V$, $\phi_A = 0\ V$ and $\phi_B = 375\ V$, the electrical

field in the center of the chamber is just approximately 10 V/cm. To overcome this effect, one can reduce the size difference between the branches and the microvalve chamber, or embed plane electrodes under branches next to the entrances and apply electric field directly to the microvalve chamber.

It should be noted that the switching time was measured on the specific microchannel shown in the paper. The geometry of the microchannel can be changed based on the applications of the microvalve; therefore, the switching time changes accordingly. As the microvalve relies on the electrokinetic motion of the EIJD in the microvalve chamber, the switching time can be shorten by reducing the distance between the two entrances. For the microchannel used in this paper, the distance between the two entrances is approximately 120 μm, and the switching time can be reduced significantly if the distance is reduced. In conclusion, the switching time is related to the distance between two entrances of the outlets and the strength of the electric field applied to the Janus droplet. By reducing the distance and increasing the electric field, the switching time becomes shorter.

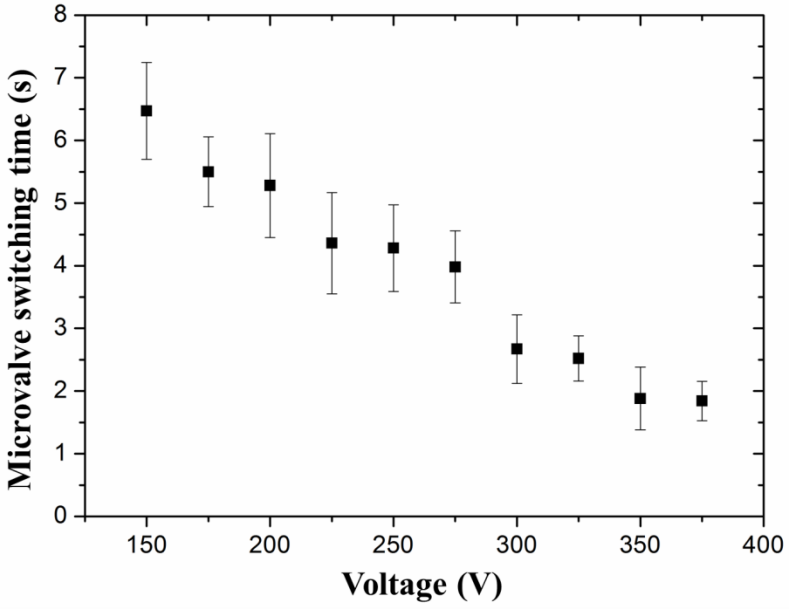

Figure 8-6. Variation of the microvalve switching time with the externally applied voltage.

8.3.4 Sealing Performance of the Microvalve

The sealing performance is one of the critical factors to evaluate a microvalve. To examine the sealing performance of the EIJD microvalve, the fluorescent nanoparticles with an average diameter of 23 nm were used as tracers to indicate the motion of the aqueous solution in the microvalve. Figure 8-7(a) shows the fluorescence microscopy images of the microvalve when the outlet A is blocked. As shown in this figure, under the electric field of $\phi_i = 250\ V$, $\phi_A = 0\ V$ and $\phi_B = 0\ V$, the liquid is pumped from the inlet channel to the outlet channel B. As the outlet A is blocked by the Janus droplet, no fluorescent nanoparticles can enter the outlet channel A; therefore, under the fluorescence microscope, the outlet channel A is black. Figure 8-7(b) indicates the distribution of fluorescent intensity along the straight line drawn in Figure 8-7(a). The line goes through both outlet A and B. It can be seen from this figure that, only one peak shows up in the region of outlet B, and the fluorescent intensity doesn't change when moving through the blocked outlet A.

It should be noted that the microchannel was fabricated with the standard soft lithography technique and the shape of the cross section of the microchannels were square (20 μm × 20 μm). When the Janus droplet (80 μm in diameter) is applied to block the target outlet entrance, it overcomes the shape difference by deforming itself to fit the square entrance and by pressing itself against the entrance wall, under the applied electric field. Apparently, using a rigid solid particle cannot have the ability to seal the entrance due to the shape difference.

Due to the size difference between the micro-valve chamber and the outlet channels, the electric field is non-uniformly distributed in the micro-valve chamber, especially near the entrance of the outlet channels. This non-uniform electric field generates dielectrophoresis (DEP) force (F_{DEP}) on the Janus droplet towards the lower electric field gradient. For a Janus droplet moving close to one of the outlet entrances, the DEP force trends to oppose the approaching of the Janus droplet to the entrance. In addition to the DEP force, hydrodynamic force ($\vec{F}_h$) and electrostatic force ($\vec{F}_{e,J}$) also exert on the Janus droplet. It should be realized that the side of the Janus droplet facing the outlet entrance is covered with positively charged nanoparticle film; and the applied electric field generates a strong electrostatic force on the positively charged nanoparticles to pull the Janus droplet towards the outlet entrance. The summation of these forces ($\vec{F}_h + \vec{F}_{e,J}$) is towards the outlet

entrance and is stronger than the DEP force [96]. Consequently, under the applied electric field, the Janus droplet is able to be transferred to the entrance and block it.

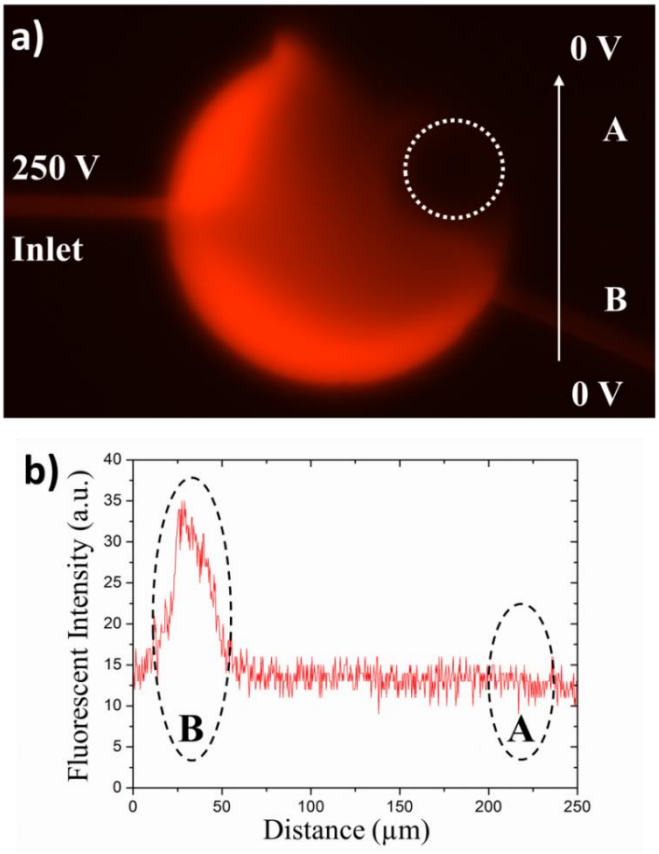

Figure 8-7. (a) The fluorescence microscopy image of the microvalve with outlet A blocked by a Janus droplet. (b) The distribution of fluorescent intensity along the straight line drawn in Figure 8-7(a). Red fluorescent nanoparticles with the diameter of 23 nm are used as indicators. The applied voltages are $\phi_i = 250\ V$, $\phi_A = 0\ V$ and $\phi_B = 0\ V$. The diameter of the Janus droplet is approximately 80 μm.

However, the situation is different for an isotropic oil droplet. When an oil droplet moves towards an outlet entrance, the DEP force acting on it increases significantly as the droplet gets closer to the entrance. Furthermore, as both the oil droplet and the wall of microvalve chamber carry negative surface charges, the electric double layer (EDL) interaction force is generated when they get closer [175]. The two forces (DEP and EDL) prevent the oil droplet from getting close to the wall. Therefore, at stable state, a small gap exists between the oil droplet and the outlet entrance.

To prove this, a microvalve using an oil droplet is fabricated and the sealing performance of the microvalve is examined by using 23 nm fluorescent nanoparticles (Figure 8-8). It's clearly shown in this figure that the liquid flows into the "should-be-blocked" outlet under the electric field of $\phi_i = 250\,V$, $\phi_A = 0\,V$ and $\phi_B = 0\,V$. The valve function cannot be achieved by using an isotropic oil droplet.

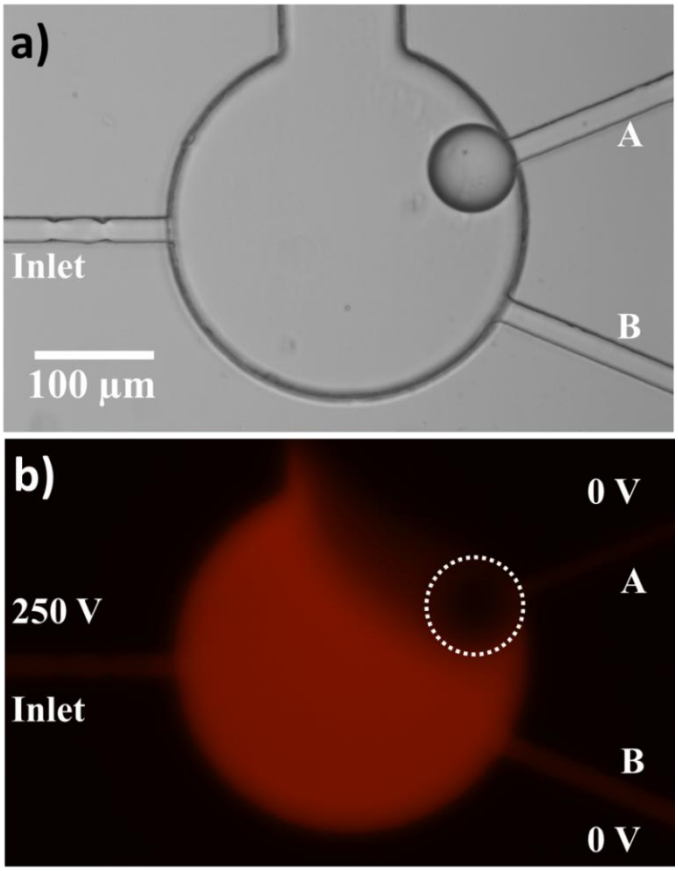

Figure 8-8. (a) The optical microscopy image of the microvalve using an oil droplet. (b) The fluorescent microscopy image of the microvalve with an oil droplet blocking the outlet A. Red fluorescent nanoparticles with the average diameter of 23 nm are used as indicators. The applied voltages are $\phi_i = 250\,V$, $\phi_A = 0\,V$ and $\phi_B = 0\,V$. The diameter of the oil droplet is approximately 75 µm.

In comparison with the existing microvalve technologies (shown in the introduction part), the microvalve fabricated with EIJD has the characteristics of simple structure, easy operation and easy integration. The microvalve consisting of a microchannel and a Janus droplet can be constructed easily, that the microchannel is fabricated with standard soft lithography technique, while the Janus droplet is formed spontaneously under electric field. For operation, electric field is the only source needed to transport liquid through the microchannel and switch the microvalve; therefore, the microvalve can be easily controlled by adjusting the applied electrical field. Furthermore, without setting additional actuation system, the microvalve is easy to integrate with microfluidic system. Due to the features shown above, the microvalve has potential in many areas. For example, with this microvalve, the biological or chemical samples can be injected into different outlets to undergo different processes without interaction. Furthermore, the microvalve can also be used in separation and sorting.

8.4 Conclusions

A novel microvalve using the EIJD was developed in this chapter. The electrokinetic motion of the EIJD in a circular microchamber under direction-switching electric field was studied first. The experimental results indicate that, while moving along the electric field, the Janus droplet rotates in the micro-valve chamber with the positively charged hemisphere facing the cathode constantly. Then, the microvalve was fabricated by injecting an EIJD into a 3D microchannel produced with the standard soft lithography technique. The microvalve is electrically responsive and is operated by controlling the electrokinetic motion of the Janus droplet to block one outlet and pumping out the liquid through the opening outlet by electroosmosis. The liquid flow rate and the switching time of the microvalve can be flexibly adjusted by changing the strength of the applied electric field. Generally, with the increase of the electric field, the liquid flow rate increases while the switching time reduces. The sealing performance of the microvalve was also examined experimentally by using fluorescent nanoparticles as indicator. The result shows that the Janus droplet can successfully block the target outlet. For comparison, a microvalve using oil droplet was fabricated, and the leakage check results showed that the oil droplet cannot block the entrance of outlet channel due to the effects of DEP force and EDL interaction. The EIJD-based microvalve shown in this paper has the advantages of easy operation, simple structure and easy integration.

CHAPTER 9. Application II: Fabrication of Self-propelled Janus Micromotors with Janus Droplets*

9.1 Introduction

Manipulation of liquid droplets plays an important role in various applications, such as, mixing and separation, controllable drug delivery and food products dispersion [244–246]. However, the existing manipulation techniques rely on complex systems, including passive elements (channels) and external actuation systems (valves and pumps) [247–249]. The self-propelled motion of droplets provides a promising alternative pathway for manipulating droplets. The self-propulsion mechanisms of the droplets can be divided into the following categories: chemical reaction [250,251], solubilization [252,253], phase separation [254–256] and external stimuli [257–264]. For the mechanism of chemical reaction, the spontaneous motion of droplets results from the chemical reaction involving surfactants. Due to the reaction of the surfactant molecules on the oil-water interface, the interfacial tension along the surface of droplets becomes inhomogeneous, which leads to Marangoni flow at the interface and eventually drives the droplets to move in the continuous phase. For example, Toyota et al. [250] studied the self-propulsion of 4-octylaniline droplets containing catalyst in an aqueous surfactant solution. Reacting with the catalyst from the inside of the droplet, the surfactant molecules at the interface were hydrolyzed, breaking the interfacial symmetry and generating the spontaneous motion of the droplets. As the surfactant molecules from the bulk aqueous solution transfer to the interface continuously, the droplets keep moving by the reaction with the consumption of the surfactant molecules at the interface.

The solubilization mechanism of the self-propelled motion of droplets involves dissolving the droplets into surfactant micelles in the continuous phase. For a droplet immersed in a surfactant solution with the concentration significantly higher than the critical micelle concentration (CMC), some molecules of the droplet dissolve into the surfactant micelles and the size of the droplet decreases. As some surfactant molecules on the droplet are transferred together with the droplet

---

* A similar version of this chapter was submitted or published as:

Li, M.; Li, D. Self-propulsion of Aluminum Particle-coated Janus Droplet in Alkaline Solution. *J. Colloid Interface Sci.* **2018**, 532, 657-665. https://www.sciencedirect.com/science/article/pii/S0021979718309494

molecules, a surfactant depletion region in vicinity of the droplet may occur. Generally, the solubilization process takes place non-uniformly, the surfactant along the surface of the droplet is distributed heterogeneously. Consequently, the Marangoni flow forms on the droplet, which in turn actuates the motion of the droplet. In 2011, Pimienta et al. [253] experimentally studied the spontaneous motion of water-saturated dichloromethane droplet in a cetyltrimethylammonium bromide (CTAB) solution. After dropping the droplet onto the surface of the aqueous phase, the droplet moves due to the solubilization of the droplet molecules. By studying the effect of CTAB concentration on droplet motion systematically, they found that the spontaneous motion of the droplet can be generated only when the surfactant concentration of the aqueous phase is above the CMC value.

In addition, the droplets in a continuous phase can move spontaneously in a non-thermal equilibrium state. For an emulsion system, consisting of immiscible dispersed and continuous phases, when the system is in a far-from-thermal-equilibrium state, mass and momentum transfers on the droplet surfaces induce convection and spontaneous motion of the droplets. Self-propulsion of pure hexadecane droplet in acetone-rich phase was demonstrated by Molin's group [254]. Moreover, the motion of droplets can also be actuated by inducing interfacial tension gradient along suspended droplets with external stimuli, such as, heating [257], light illumination [258–260], electrical field [261,262] and chemical gradient field of the aqueous phase [263,264]. For example, Florea et al. [260] studied the spontaneous motion of a droplet under white light. In their system, a light-sensitive spiropyran sulfonic acid was dissolved into the aqueous phase. Under light irradiation, the H^+ ions are released and the local pH value of the aqueous phase decreases. With the generation of pH gradient in the aqueous phase between the light region and the dark region, the droplet moves away from the light source.

Recently, the development of Janus materials provides a new strategy in generating self-propelled micromotor. Janus materials possess asymmetrical structures with two sides carrying different physical or chemical properties. Therefore, under external stimuli or chemical reaction with the surrounding solution, the forces acting on the two sides of the Janus materials are unbalanced, which leads to the motion of the micromotors [265–267]. Based on the propulsion mechanism, the Janus micromotors can be divided into three major groups: self-electrophoresis [268,269], self-thermophoresis [270,271] and bubble propulsion. For self-electrophoresis, the two ends of the

Janus micromotor are made from different conducting materials with different chemical potentials. After adding the motor into a buffer solution, due to the chemical reaction between the Janus micromotor and the buffer solution, a local current loop is generated between two ends of the micromotor; thus, the Janus micromotor is driven to move by electrophoresis. Self-thermophoresis generally uses a laser beam to induce a temperature gradient in the vicinity of the micromotor based on different absorptivity of its two sides, which in turn causes thermophoresis of the micromotor. Compared with these two mechanisms, the bubble propulsion mechanism is most commonly used in actuating the motion of Janus micromotors. As the name suggests, the bubble propulsion motion results from the directional bubble ejection from the micromotor. By placing the Janus micromotor into chemical "fuel", one side of the micromotor starts a reaction and bubbles are ejected, i.e., via catalytic reaction or replacement reaction, to propel the micromotor towards the inactive side. The micromotor keeps moving until the chemical reactants are exhausted. For example, Gao et al. [272] showed the spontaneous motion of Al/Pd Janus microparticles in acid, alkaline and hydrogen peroxide solutions. In acid and alkaline solutions, hydrogen bubbles are generated in the Al side which drives the particle to move towards the Pd side; reversely, in hydrogen peroxide solution, catalytic reaction takes place on the Pd side to generate oxygen bubbles and the micromotor is propelled to move towards opposite direction.

However, most of the Janus micromotors reported in literatures are solid particles, which have the shortcomings of limited cargo loading capability and poor biodegradability. Therefore, research in developing new Janus droplet micromotors, combining the advantages of Janus materials and self-propelled droplets together, is highly desirable. In this chapter, for the first time, the self-propulsion of the EIJDs in alkaline solutions is demonstrated. The influence factors, including time, pH value of the surrounding solution, particle coverage of the Janus droplet and surfactant on the spontaneous motion of the micromotor are studied experimentally. Furthermore, the directionally controlled transportation of the Janus droplets is accomplished by using an electric field.

9.2 Materials and Methods

9.2.1 Materials and Chemicals

Non-ionic surfactants of Triton X-100 and Tween 20, cationic surfactant of CTAB and anionic surfactant of SDS, sodium hydroxide (NaOH) were purchased from Sigma-Aldrich. All the

chemicals were of reagent grade and used without further treatment. Aluminum particles with an average diameter of 10 μm were purchased from US Research Nanomaterials, Inc. Oil used in the analysis was canola oil (100% pure, Mazola Corporation). Deionized water (18.2 MΩ·cm) was obtained from Milli-Q purification system (Japan Millipore, Japan).

9.2.2 Preparation of Al Particle-coated Janus Droplets

The Janus droplets were prepared by dispersing oil containing Al particles into an aqueous solution, as shown in Figure 9-1. This method includes four steps. First, in order to prepare the particle-in-oil dispersion phase, 10 μm Al particles and 5 mL oil were added into a 15 mL-in-volume glass bottle. After vibrating the mixture with a lab dancer (VWR Scientific) at the maximum speed of 3200 rpm for 2 minutes, the particles are dispersed into oil uniformly. Then, 100 μL of the oil was dropped into the other glass bottle containing 5 mL Triton X-100 aqueous solution (2% (v/v)). The final position of the oily phase in the aqueous phase, floating at the top, suspending in the middle, or sinking at the bottom, is dependent on the amount of Al particles in it. After this, the three-phase mixture was shaken with the lab dancer at 3200 rpm for 30 seconds to form oil-in-water emulsion. Due to the vibration, the particles moved to the surface of emulsion droplets, and the Al particle film formed on the surface of each oil droplet. Because of the shield of the passivation oxide layer on the surfaces of the Al particles, the reaction between the aqueous phase and the Al particles is hampered. After vibration, the mixture was kept stationary for 10 min. Over this period of time, the Al particles were concentrated to the bottom of the droplets under gravity effect, and finally, the Janus droplets with the bottom side hemisphere covered with Al particles were formed.

The particle coverage of the Janus droplets generated with this method depends on the amount of particles on the surface of droplets. To generate Janus droplets with different particle coverages, particle-in-oil dispersions with different Al particle concentrations, ranging from 40 mg/mL to 280 mg/mL, were employed in fabricating the Janus droplets. The bright-field optical microscope (Nikon Ti-E, Nikon, Japan) was employed to examine the Janus droplets.

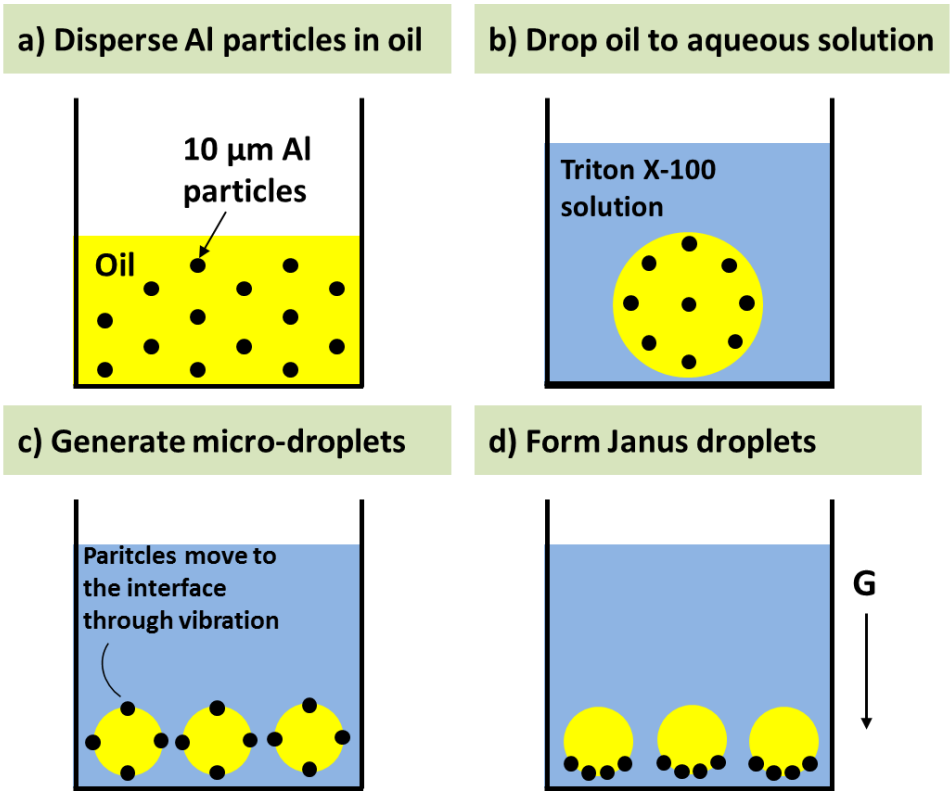

Figure 9-1. Schematics of the synthesis of Janus droplets with Al particles. (a) First, the Al particles with 10 μm in diameter are dispersed in oil through vibration; (b) Then, the oil phase are added in an aqueous Triton X-100 solution with the concentration of 2% (v/v); (c) Emulsion oil droplets are formed by vibrating the mixture with a lab dancer, and the Al particles move to the surface of the oil droplets; (d) Let the emulsion system stand for 10 min to make the particles concentrated to the bottom side of the droplets under gravity effect.

9.2.3 Analysis of the Spontaneous Motion of the Janus Droplets

The experiments for the study of the spontaneous motions of the Janus droplets were carried out in the NaOH solutions. The experiments were conducted in a chamber with the size of 1 cm × 1 cm × 0.5 mm (Length × Width × Height), as shown in Figure 9-2(a). The chamber was fabricated by bonding a PDMS layer containing chamber structure and a glass substrate (VWR Scientific) together after plasma treatment (HARRICK PLASMA, Ithaca, NY, USA). In the experiments, after filling the reaction chamber with NaOH solution, the Janus droplets were added into the

chamber with a digital pipette (Eppendorf Research). The spontaneous motions of the Janus droplets in alkali solutions were observed with an optical microscope (Nikon Ti-E), and the images were recorded by a CCD camera (DS-Qi1Mc, Nikon) at the speed of 25 fps. The recorded videos were analyzed with imaging analysis software. The motion velocities of the droplets were obtained by measuring the moving distance of the droplets over a time interval. For each experiment, 30 measurements were conducted to obtain the average velocity and the standard deviation. The Janus droplets with the diameter ranging from 70 μm to 100 μm were chosen to conduct analysis.

The effects of time, pH value of the aqueous solution, particle coverage and surfactant on the spontaneous motion of the Janus droplets were studied experimentally. In these studies, without special declaration, the alkaline solutions containing 2% (v/v) Triton X-100 were used. The Janus droplets (generated from 280 mg/mL particle-in-oil dispersion) and pH=14 aqueous solution were used in detecting the time effect. To test the self-propulsion motion of the Janus droplets in different pH solutions, the aqueous solutions containing different concentrations of NaOH were utilized. The velocity and life time of the Janus droplets generated from 280 mg/mL particle-in-oil dispersion in alkali solutions with pH ranging from 12 to 14 were measured. In the study of particle coverage effect, Janus droplets were generated from different concentrations of particle-in-oil dispersions, 40 mg/mL, 120mg/mL, 200 mg/mL and 280 mg/mL. The moving velocities of these Janus droplets in pH 14 solution were detected, respectively. Apart from Triton X-100, the other three surfactants, Tween 20, SDS and CTAB, were also introduced into the aqueous solution to study the surfactant effect. In the experiment, the moving status of the droplets in the alkali solutions with 2% (v/v) Tween 20, 1.2% (w/v) SDS and 1% (w/v) CTAB were observed under microscope, respectively.

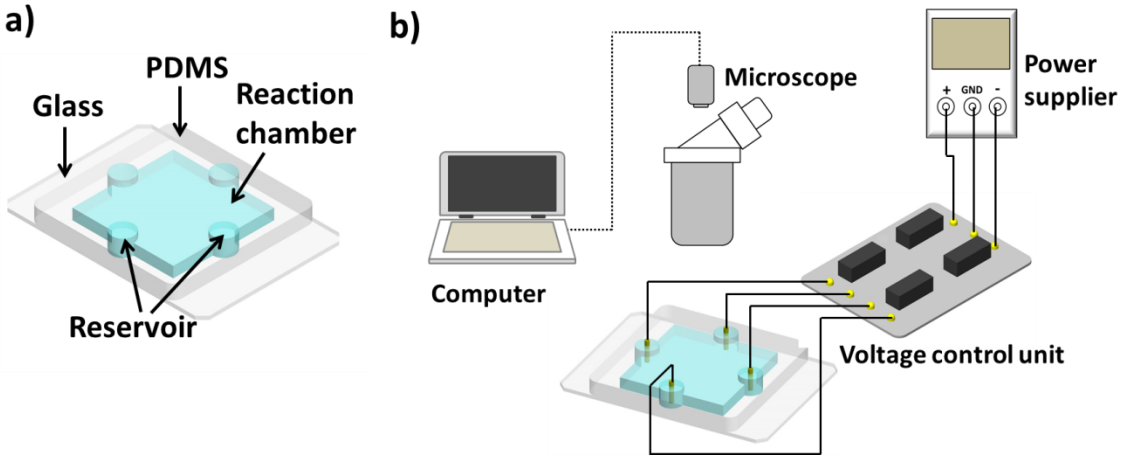

Figure 9-2. Schematics of the reaction chamber (a) and experimental setup (b).

9.2.4 Electrical Navigation of the Janus Droplets

To examine the electrical control of the motion of the Janus droplets, an experimental setup was built, which consists of a direct current (DC) power supplier, a voltage control unit, a reaction chamber and a Ti-E microscope, as shown in Figure 9-2 (b). The electric field was supplied by the DC power supplier (CSI12001X, Circuit Specialist Inc., USA) with adjustable output voltage ranging from 0V to 125V. The voltage control unit bridging between the power supplier and the reaction chamber was employed to control the direction of the electric field applied to the reaction chamber. The electric field was applied to the chamber through four electrodes inserted in the reservoirs. By placing the reaction chamber on the object stage of the microscope, the self-propulsion motion of the micromotors under the effect of electric field was observed by the microscope.

In the experiment, the reaction chamber was filled with aqueous alkali solution at pH 14 containing 2% (v/v) Triton X-100 first. After injecting the Janus droplet, the spontaneous motion of the droplet was triggered with bubble propulsion. By applying electric field of 25 V/cm to the reaction chamber, the droplet rotated to get aligned with the electric field because of the Al particle coating on one side of the droplet surface. Hence, the droplet moved along the electric field. Changing the direction of the electric field, the Janus droplet followed the orientation of the electric field, and the moving direction of it changed responsively. To avoid the electrolysis and Joule heating of the

aqueous electrolyte, the electric field was applied intermittently. The maximum time for turning on the electric field each time is 2 second. The directional motion of Janus micromotors in response to electric field was visualized and recorded by the optical microscope.

9.3 Results and Discussion

9.3.1 Generation of Janus Droplets with Different Particle Coverage

The Janus droplets are formed by moving the Al particles in the oil droplets initially to the oil-water interface through vibration, as shown in Figure 9-3(a). Under vibration, the oil phase is emulsified into small droplets, which are stabilized by the surfactant molecules in the aqueous. At the same time, the Al particles with the diameter of 10 μm moved to the oil-water interface. Generally, with the adsorption of one particle from the bulk phase to the oil-water interface, the free energy of the system decreases. The larger the reduction of the free energy, the more stable the particle at the interface. For a spherical particle with radius a at the oil-water interface, the reduction in the free energy ΔF is obtained [273,274]:

$$\Delta F = -\pi a^2 \gamma_{ow}(1 - cos\theta_w)^2 \quad \text{for } \theta_w < 90° \tag{9-1}$$

$$\Delta F = -\pi a^2 \gamma_{ow}(1 + cos\theta_w)^2 \quad \text{for } \theta_w > 90° \tag{9-2}$$

where, γ_{ow} is the specific interfacial free energy (i.e., interfacial tension) of the oil-water interface, θ_w is the contact angle of the particle in water. As shown in these equations, the reduction of the free energy (ΔF) increases with particle size a and oil-water interfacial free energy γ_{ow}. Therefore, by utilizing the micron sized particles, instead of nanoparticles, the adsorption of particles at the oil-water interface is energetically favorable. As demonstrated in the experimental studies of this paper, the Al particles can stay stably on the droplet surface in 2% Triton X-100 solutions with pH value ranging from 7 to 14. However, if replacing the micro-size Al particles with nanoparticles, the nanoparticles detach from the surface of the oil droplet in alkaline solution. Furthermore, the micromotor is propelled to move with the gas bubbles through the reaction between Al and OH^-. For nanoparticles, with the passivation of the surface, the effective amount of Al inside of the core-shell nanoparticles is small, which can't generate enough gas bubbles to drive the micromotor to move. Based on these, the micro-size Al particles are used for fabricating Janus droplets regardless

of nanoparticles. In this fabrication, after Al particles adsorb to the oil-water interface, they move and accumulate to the bottom side of each droplet under gravity effect. Finally, the particles are held together to form rigid layers of solid particles on the oil droplets. Due to the capillary forces between the solid particles, the attractive interactions between particles are strong, which is difficult to disperse them again once the particle film is formed [275].

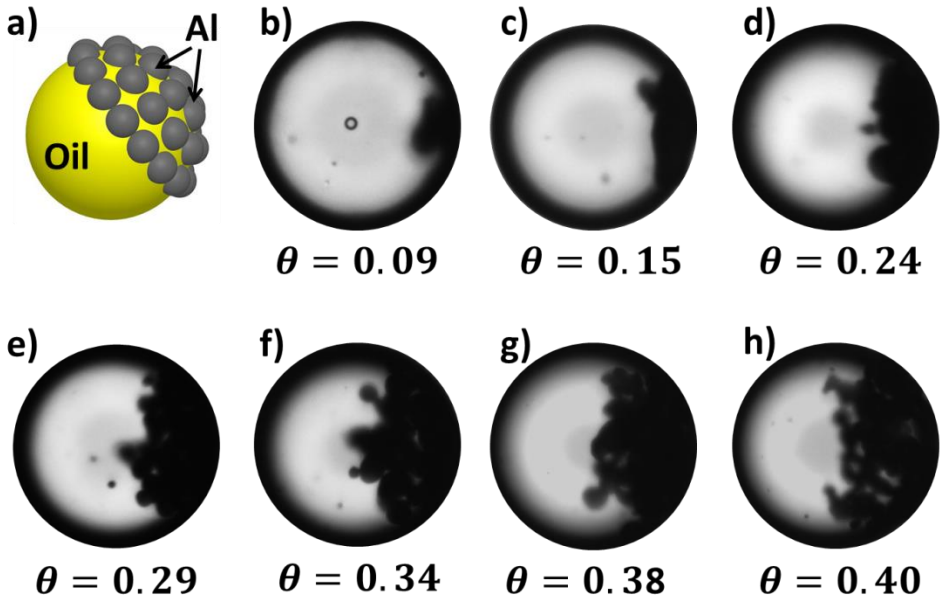

Figure 9-3. (a) Schematic diagram of the Janus droplet generated with Al particles. (b)-(h) Microscope images of Janus droplets generated with different concentrations of Al particle-in-oil dispersions: (b) 40 mg/mL, (c) 80 mg/mL, (d) 120 mg/mL, (e) 160 mg/mL, (f) 200 mg/mL, (g) 240 mg/mL and (h) 280 mg/mL. The diameter of the droplets ranges from 70 μm to 100 μm. θ is the particle coverage of the Janus droplets.

The particle coverage of the Janus droplets is dependent on the concentration of particle-in-oil dispersion. By comparing the microscope images of Janus droplets (shown in Figure 9-3(b) to (h)), it can be found that the particle coverage increases with the particle concentration of the dispersion. This can be understood easily. With other parameter fixed, as the particle concentration in the oil

phase increases, the total number of Al particles adsorbing on the oil droplets increases; therefore, after accumulation, the particle coverage of the Janus droplets increases. As shown in Figure 9-3(b), at the concentration of 40 mg/mL, only limited numbers of particles show up on the oil droplet. By increasing the particle concentration gradually, the amount of particles on the droplet surface increases, then the final particle accumulated area (indicated as the dark area in the microscope images) increases. When the concentration of the dispersion reaches to 280 mg/mL, almost half of the oil droplet is covered by particles, and a typical "half-half" Janus droplet is formed in this way. It should be noted that, in order to visualize the particle coverage of the Janus droplets clearly by using a top-down microscope, a slight pressure difference between the reservoirs of the reaction chamber was applied to drive the droplets to move very slowly with the hemisphere carrying the particle layer facing the flow field. That is why in Figure 9-3 the particle covered part of the droplet faces to the right side, instead to the bottom side. The relationship between the concentration of Al particle-in-oil dispersion and the particle coverage of the Janus droplet has been plotted as Figure 9-4. Under each condition, 20 independent measurements were conducted to obtain the average particle coverage and the standard deviation. As can be seen from this figure, the particle coverage highly depends on the concentration of the dispersion that the particle coverage increases significantly with the concentration of the dispersion.

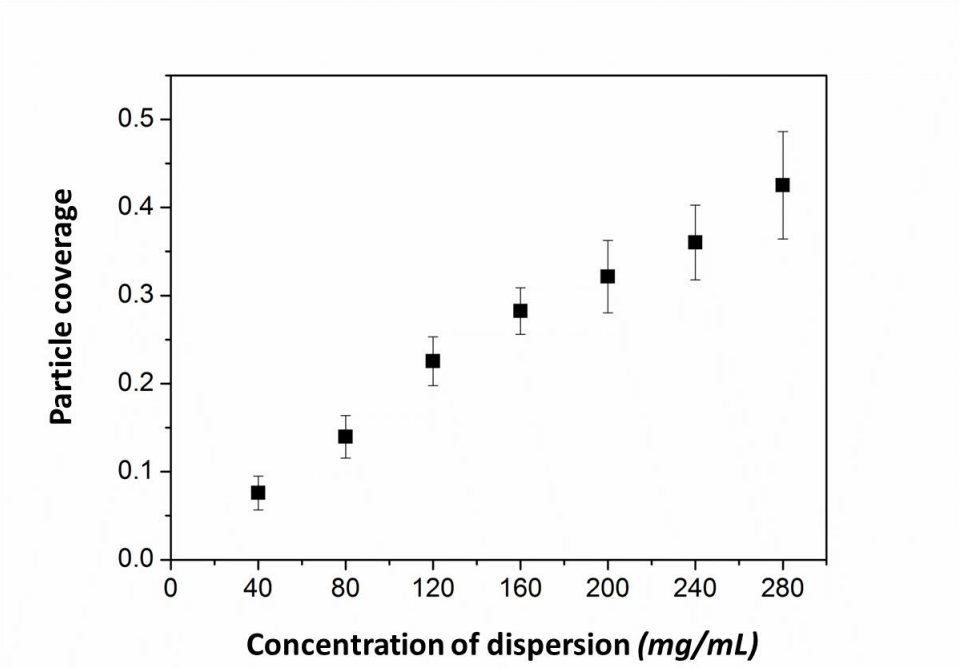

Figure 9-4. Dependence of the particle coverage of the Janus droplet on the concentration of Al particle-in-oil dispersion. The diameter of the Janus droplets ranges from 70 μm to 100 μm.

9.3.2 Spontaneous Motion of the Janus Droplets

The Janus droplet is propelled by the hydrogen bubbles that are generated by the reaction between the Al particles and the alkali solution. As illustrated in Figure 9-5(a), while the Janus droplet is injected into a strong alkaline medium, the protective oxide layer is removed, and the reaction between aluminum and the basic solution generates the hydrogen bubbles:

$$2Al + 2\,OH^- + 2\,H_2O \rightarrow 2\,AlO_2^- + 3\,H_2 \qquad (9\text{-}3)$$

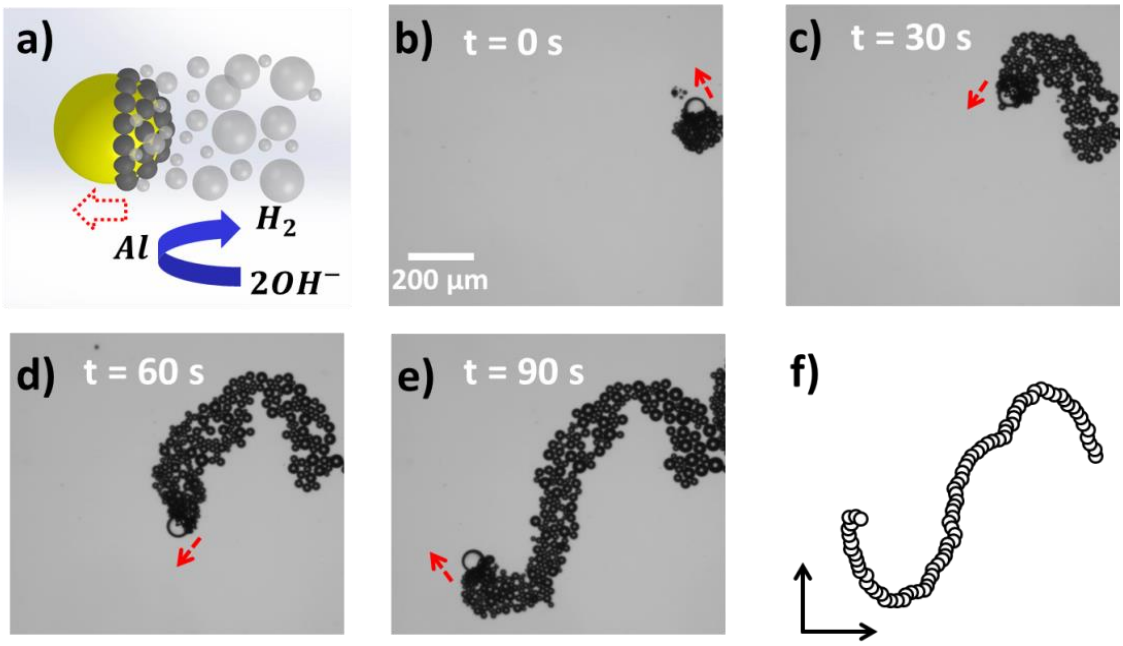

Figure 9-5. (a) Schematic diagram of the propulsion mechanism. (b)-(e) Time-lapse images of the spontaneous motion of a Janus droplet generated from 280 mg/mL particle-in-oil dispersion in pH 14 basic solution. (f) Trajectory of the spontaneous motion of the droplet. The diameter of the droplet is 85 μm. The concentration of Triton X-100 in the basic solution is 2% (v/v).

Because of the hydrogen bubbles released from the particle coated side of the droplet, a driving force exerts on the droplet and pushes the droplet to move. To demonstrate the spontaneous motion of the Janus droplets in alkali solution, a Janus droplet generated from 280mg/mL particle-in-oil dispersion was injected into pH 14 NaOH solution containing 2% (v/v) Triton X-100. The non-ionic surfactant, Triton X-100, was introduced to the alkaline solution to reduce the gas-water interfacial tension, which is essential for the self-propulsion of the Janus droplet. With the effect of Triton X-100, H_2 is ejected from the surface of the Janus droplet as small bubbles. As the propelling force is linearly proportional to the total number of bubbles detached from the Janus droplet per unit time, a large number of small bubbles can generate large enough propelling force for the motion of the Janus droplet [276]. The time-lapse images of the moving droplet are shown in Figure 9-5(b) to (e). As shown in these figures, a trail of bubbles is ejected continuously from the Al particle side of the Janus droplet, while no bubble shows up on the oil-water interface side of the Janus droplet. This particular droplet moves at an average speed of about 25 μm/s. The speed of the Janus droplet is dependent on the balance between the bubble propelling force and the viscous drag force. Therefore, increasing of the propelling force leads to the enhancement of the speed. The trajectory of the droplet is shown in Figure 9-5(f). As shown in this figure, the Janus droplet moves randomly in the buffer solution, i.e., without a constant direction, due to the non-uniform bubble generation of different Al particles. This behavior is identical for essentially all self-propelling droplets. However, most trajectories of the solid Janus particles are circular or linear as reported in some published papers [111,277,278].

9.3.2.1 Speed Evolution of the Droplet

The speed of the Janus droplet changes with time due to the variation of the bubble generation rate. Generally, with the increase of the number of bubbles detached from the droplet, the propelling force increases; hence, the speed of the droplet increases.

For an Al particle immersed in a basic solution, the reaction between them can be divided into three periods. As the Al particle is covered with a passivation oxide layer, when the particle starts contacting with the basic solution, the strong alkaline medium reacts with the oxide layer. With the removal of this passivation oxide layer, aluminum in the core of the particle is exposed to the solution and the reaction (Equation (9-3)) starts, generating hydrogen bubbles. In this period, the

bubble generation rate increases quickly with time. After the entire oxide layer is removed through corrosion, the reaction moves to a stable period and the bubble generation rate reaches the highest level. In the last period, the amount of aluminum in the particle reduces due to reaction; consequently, the bubble generation rate declines until all of the aluminum is consumed. Correspondingly, the self-propulsion of the Janus droplet undergoes three periods: initial development stage, stable stage and decline stage. The speed of the droplet increases initially, then remains constant for a while, and finally declines.

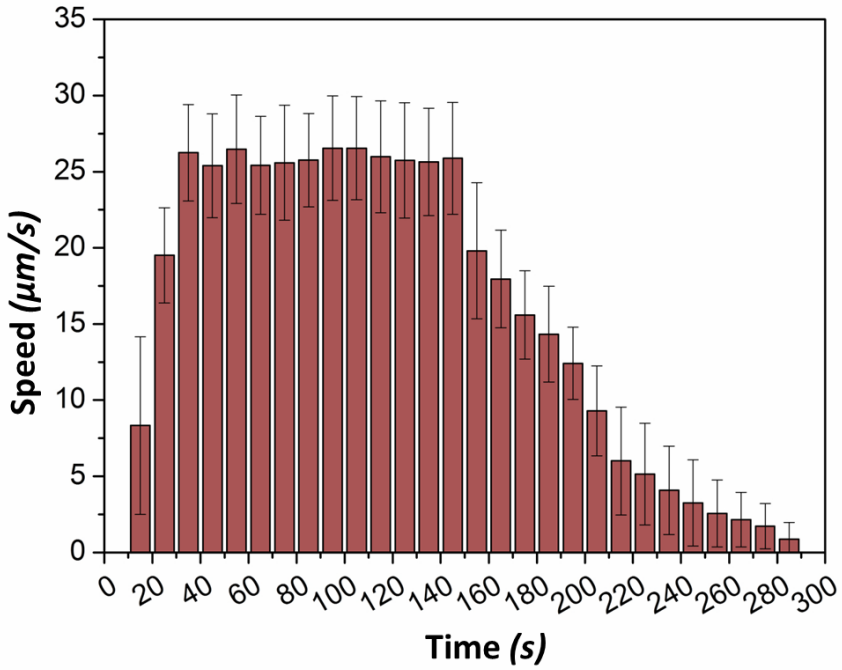

Figure 9-6. Speed evolution of the Janus droplets generated from 280 mg/mL particle-in-oil dispersion in pH 14 solution with 2% (v/v) Triton X-100. The diameter of the droplets ranges from 70 μm to 100 μm.

To study the speed variation with time, the Janus droplets generated from 280 mg/mL particle-in-oil dispersion were injected into basic solution at pH 14 with 2% (v/v) Triton X-100. The diameter of the Janus droplets ranges from 70 μm to 100 μm. The speed evolution of the droplets is plotted

in Figure 9-6. As shown in this figure, during the first 10 second, the reaction between the oxide layer and the alkaline medium takes place and the Janus droplets remain still. In the next 20 second, with the removal of the oxide layer, aluminum starts to react with the alkaline solution to generate hydrogen bubbles. As the bubble generation rate increases with time, the speed of the droplets increases quickly. After the oxide layer is removed, the reaction between Al particles and basic solution reaches a stable period, and the droplets move at a constant speed of about 25 μm/s. This stable period remains approximately for 2 minutes (from 30s to 150s). After this period, the amount of bubbles generated from the droplets decreases and the speed of the droplets declines gradually. The result shown in Figure 9-6 is an average of 5 independent Janus droplets.

9.3.2.2 Effect of pH on Speed and Lifetime of the Janus Droplet Motion

The speed and lifetime of the Janus droplet motion are strongly dependent on the pH value of the basic solution. The hydrogen generation from the reaction between aluminum and alkali solution has been studied in many published papers [279,280]. By immersing aluminum into alkali solutions with different concentrations and measuring the volume of hydrogen, it was found that in the same amount of time, more hydrogen can be generated with higher alkali concentration. Therefore, in a higher pH solution, the bubble generation rate from the Al particle layer is larger, which leads to larger propelling force and faster spontaneous motion of the Janus droplet. However, when the reaction between aluminum and alkali solution is faster, the aluminum on the droplet surface will be consumed more quickly, and hence the lifetime of the Janus droplet motion is reduced. The variations of the speed and the lifespan of the Janus droplet motion with the pH value of the alkali solution were investigated and the results are shown in Figure 9-7. As indicated in this figure, the spontaneous motion of the Janus droplets can be actuated only in strong enough alkaline medium with the critical pH value of 12.8. For the media with pH value larger than 12.8, the speed of the Janus motor has a positive relationship with the pH value while the lifetime has a negative relationship with it, which agrees with the analysis above. For pH smaller than 12.8, no bubble or only fewer bubbles are generated from the Janus droplet, and, the droplet remains stationary. It should be noted that, in this figure, in order to increase accuracy, the speeds of the droplets in the stable period were measured and analyzed.

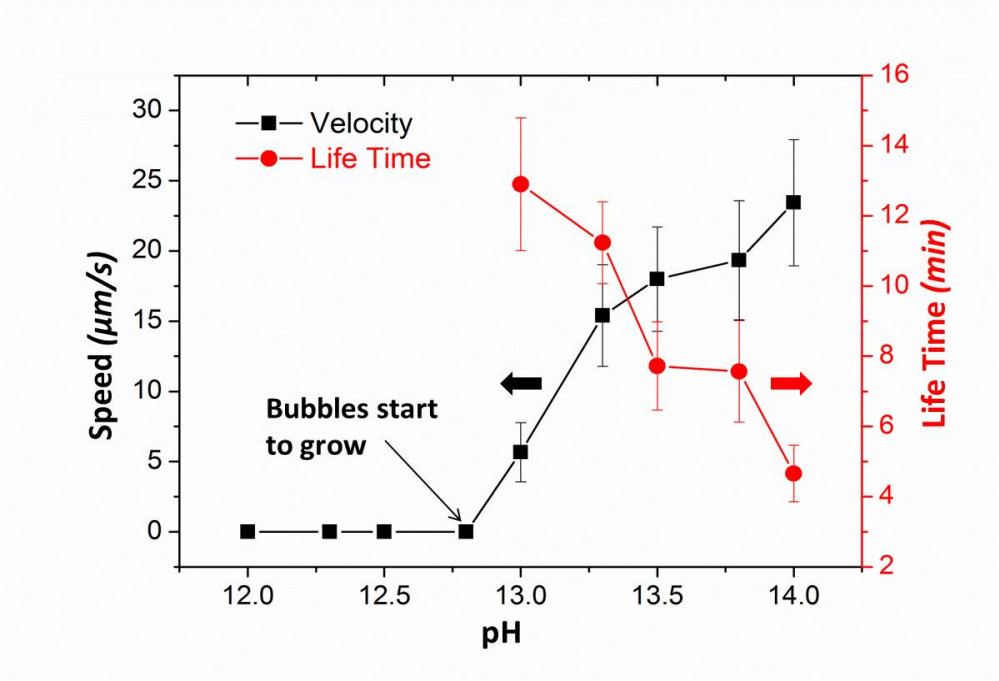

Figure 9-7. Dependence of the speed and lifetime of the Janus droplet motion on the pH value of the alkali solution. The Janus droplets are developed from 280 mg/mL particle-in-oil dispersion. The diameter of the Janus droplets is approximately 85 μm. The concentration of Triton X-100 in the alkali solutions is 2% (v/v).

9.3.2.3 Effect of Particle Coverage on Speed of the Janus Droplets

The particle coverage of the Janus droplet is another factor that affects the speed of it. Generally, with the increase of the particle coverage, more bubbles can be ejected from a larger Al particle layer. With the increase of the bubble generation rate, the bubble propelling force acting on the droplet becomes larger, which drives the Janus droplet to move faster. To examine the particle coverage effect, the Janus droplet generated from different concentrations of particle-in-oil dispersions were added into pH 14 alkali solution, respectively, and the stable speeds of them were measured and plotted in Figure 9-8. As shown in this figure, with the increase of the concentration of dispersion, the particle coverage increases, and the speed of the droplet increases. It should be noted that only limited number of particles show up on the droplets generated from 40 mg/mL particle-in-water dispersion. Therefore, the bubble generation rate from these droplets in the basic

solution is very low, and consequently, the bubble propelling force is too weak to drive the droplets to move.

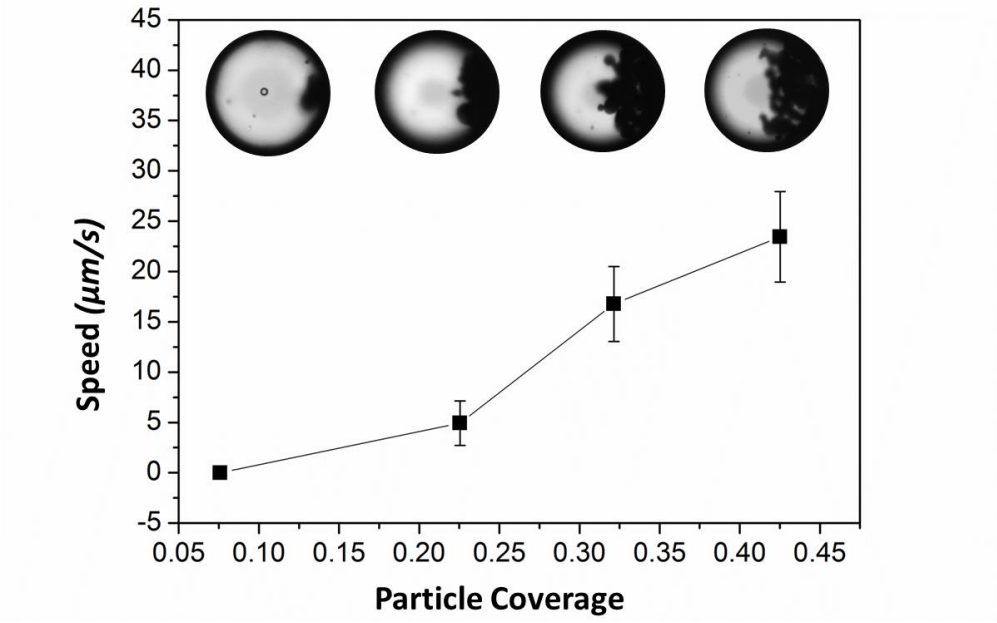

Figure 9-8. Dependence of the speed of the Janus droplet on the particle coverage. The Janus droplets with different particle coverages are generated from 40 mg/mL, 120 mg/mL, 200 mg/mL and 280 mg/m particle-in-oil dispersions, respectively. The surrounding alkali solution is at pH 14 and contains 2% (v/v) Triton X-100. The diameter of the Janus droplets ranges from 70 μm to 100 μm.

9.3.2.4 Effect of Surfactant

Surfactant plays a very important role in the bubble-propelled motion of Janus droplets. With the presence of surfactant, the interfacial tension is reduced, and that is essential for the detachment of bubble from the droplet. As shown in Wang's work [281], the speed of the micromotor keeps increasing with the surfactant concentration before reaching the critical micelle concentration (CMC). After CMC, the velocity of the micromotor remains constant. In this paper, to control the surfactant concentration effect, Triton X-100 solution with a concentration above CMC was employed for the studies of the effects of the time evaluation, pH and particle coverage.

The spontaneous motion of the Janus droplets differs significantly in different surfactant solutions. To study the effect of the surfactant type, the performances of the droplets in different surfactant

solutions of Tween 20 (nonionic), SDS (anionic) and CTAB (cationic) were tested, respectively, and the results were shown in Figure 9-9. As shown in Figure 9-9(a), in the presence of nonionic surfactant Tween 20, one large gas bubble is generated on the oil droplet. Since the bubble does not detach from the Janus droplet, the droplet does not move. This phenomenon results from the degradation of Tween 20 in alkaline solution [282–284]. Tween 20 is a polyoxyethylene sorbitol ester. In strong alkaline solutions, the hydrolysis of the ester bond takes place, which leads to the surfactant losing its functions. As shown in Figure 9-10(a), resulting from the ester hydrolysis, the mixture is solidified 1 hour after adding Tween 20 in a pH 14 solution. Due to the degradation of the surfactant, the interfacial tensions of oil-water interface and bubble-water interface becomes larger than that of oil-bubble interface, and the partial engulfment of the Janus droplet by the gas bubble occurs [14]. As shown in Figure 9-9(b), in SDS solution, the Janus droplet was surrounded by several larger gas bubbles and no significant translation of the Janus droplet was observed. Generally, in a strong NaOH solution, the presence of sodium ions affects the hydrolysis of SDS [285]. The SDS precipitation occurs in the solution and only limited amount of surfactant dissolves (as shown in Figure 9-10(b)). Therefore, the detachment of the bubbles was restrained due to relatively large interfacial tension and several large bubbles presented around the Janus droplet. As a result, no enough driving force can be generated to propel the Janus droplet to move. As shown in Figure 9-9(c), CTAB affects the Janus droplet by detaching Al particles from the oil-water interface. CTAB is cationic surfactant which can convert the zeta potential of the oil droplet surface from negative to positive [138]. As the oxide layer on the Al particle also carries positive charges in aqueous solution, the electrostatic interaction between the Al particle and the interface repels the particle away from the oil-water interface [143,286]. Compared with these three surfactants listed above, Triton X-100 performs well in the spontaneous motion of Janus droplets. Different from Tween 20 and SDS, the function of Triton X-100 remains stable in NaOH solution. As shown in Figure 9-5, in alkaline Triton X-100 solution, numerous small gas bubbles are ejected from the Al particles adhering on the Janus droplet. With the propulsion of these gas bubbles, the spontaneous motion of the Janus droplet was generated. In conclusion, except Triton X-100, the other three surfactants, Tween 20, SDS and CTAB, are unsuitable for generating the spontaneous motion of the Janus droplets.

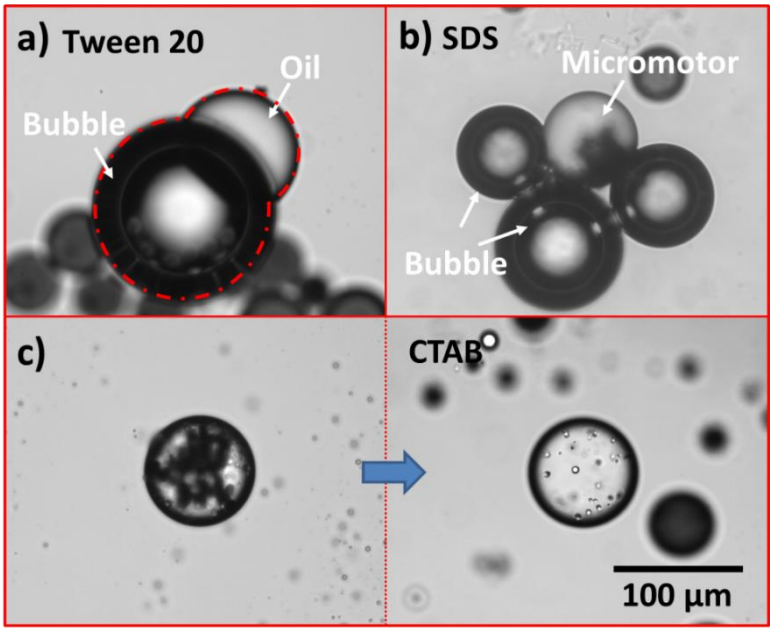

Figure 9-9. Effect of surfactant type on the Janus droplet. (a) A Janus droplet attached with a large gas bubble in 2% (v/v) Tween 20 solution; (b) A Janus droplet is surrounded by several large bubbles in 1.2% (w/v) SDS solution; (c) After adding 1% (w/v) CTAB solution, the particles adhering on the oil droplet surface are detached. The pH value of the surfactant solutions are 14.

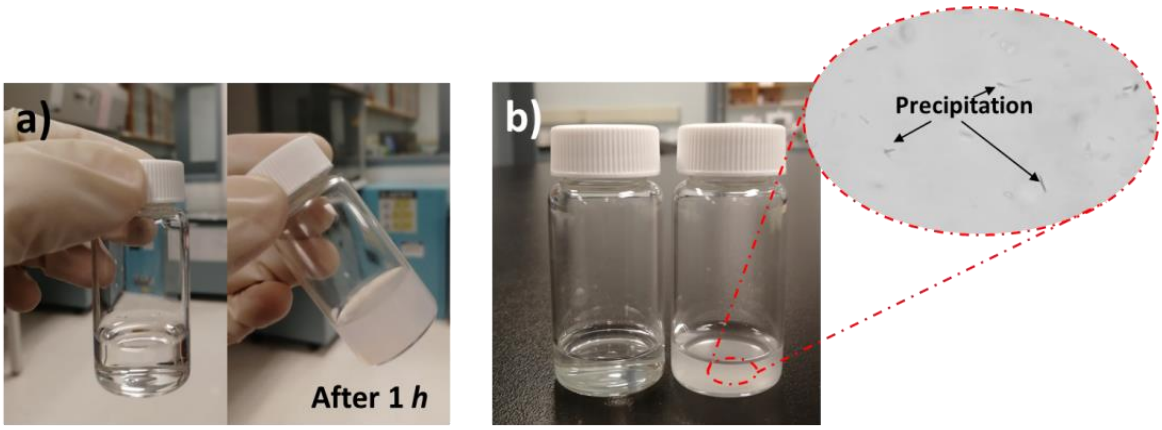

Figure 9-10. (a) Basic hydrolysis of Tween 20. Initially, the 2% (v/v) Tween 20 solution at pH 14 is clear (left). After 1 hour, the mixture is solidified due to hydrolysis of the ester bond (right); (b) SDS precipitation from alkaline solution. 1.2% SDS in deionized water is clear, while that in alkaline solution at pH 14 is opaque with lots of sediments showing up.

9.3.3 Directional Transport of the Janus Droplets by Electric Field

Controllable transport of droplets is essential in many applications, including chemical analysis, biological analysis and cargo delivery. For example, the droplet can be used as a micro-reactor for biochemical reaction and a carrier transporting organic substances and biomolecules. Furthermore, combining the motion of Janus droplets with the microfluidic technology offers the chance to develop novel droplet-based microfluidics systems for synthesis, analysis and detection without the need of external propulsion.

In this work, in order to direct the spontaneous motion of the Janus droplets, an external DC electric field was applied. As the Janus droplet has a higher density on the particle coated side than that of the other side ($\rho_{al} > \rho_o$), the accelerations of the two sides are different under the hydrodynamic force, and the lighter side moves faster than the heavier side. As a result, the Janus droplet rotates with the oil side forwarding the direction of the hydrodynamic force. Under externally applied electric field, electroosmotic flows are generated on the surfaces of the reaction chamber and the Janus droplet. With the effect of the electroosmotic flows, a hydrodynamic force is exerted on the Janus droplet, which forwards the Janus droplet to get aligned with the electric field, as shown in Figure 9-11(a). It should be noted that as the self-propulsion motion of the Janus droplet takes place in a strong alkaline solution, applying an electric field to the system continuously will cause electrolysis and Joule heating. To avoid these effects in the experiment, weak electric field of 25V/cm with a time interval of 2s was applied intermittently to control and adjust the moving direction. Figure 9-11(b) to(d) show the change of the moving direction of the Janus droplet under the applied electric field. It can be seen that by applying electric field intermittently, the Janus droplet rotates, changes its direction, and finally get aligned with the direction of the electric field.

The directionally controlled transportation of the Janus droplet was demonstrated by making the droplet to move linearly and to make a sharp turn. As shown in Figure 9-12(a), the Janus droplet moves linearly from left to right in response to the electric field. The motion of the droplet was monitored under a microscope, and the electric field was applied intermittently only when the Janus micromotor went out of the designed track. Therefore, the effect of electroosmotic flow on the motion of the droplet is limited. The turning of the Janus droplet was achieved by changing the direction of electric field. As shown in Figure 9-12(b) and (c), initially, the intermittent electric

field (E1) was applied transversely (from left to right), and the Janus droplet moves from left to right responsively. Then, the direction of the applied electric field was rotated 90° counterclockwise (E2). In response to the electric field of E2, the rotation of the Janus droplet took place and the Janus droplet moved vertically to its original direction.

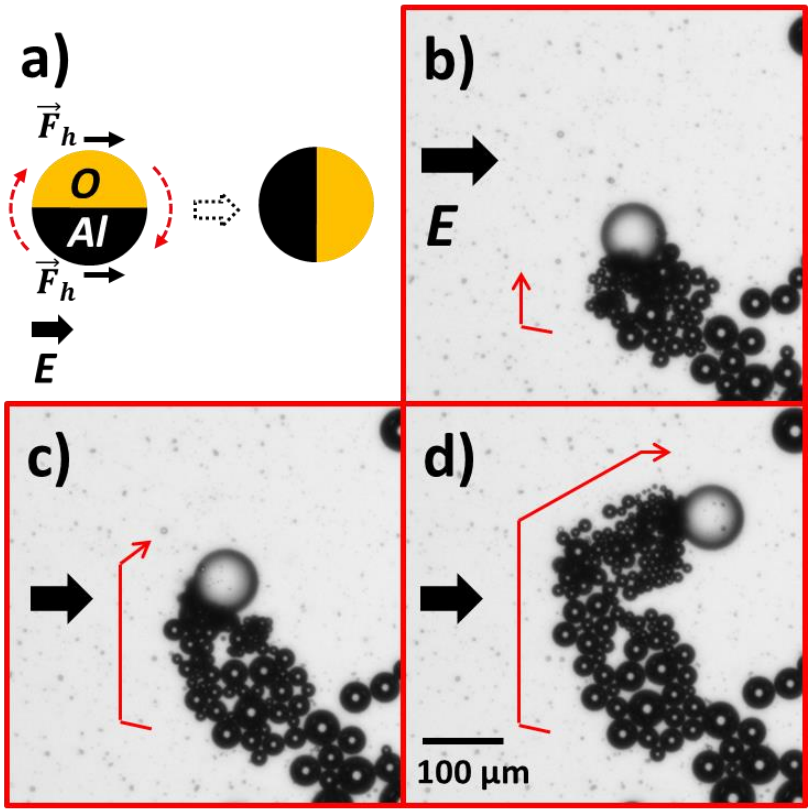

Figure 9-11. (a) Schematic of the rotation of the Janus droplet under electric field; (b)-(d) Time-lapse images of the direction change of the moving Janus droplet generated from 200 mg/mL particle-in-oil dispersion under intermittent applying electric field of 25 V/cm. The red lines in (b)-(d) indicate the trajectories.

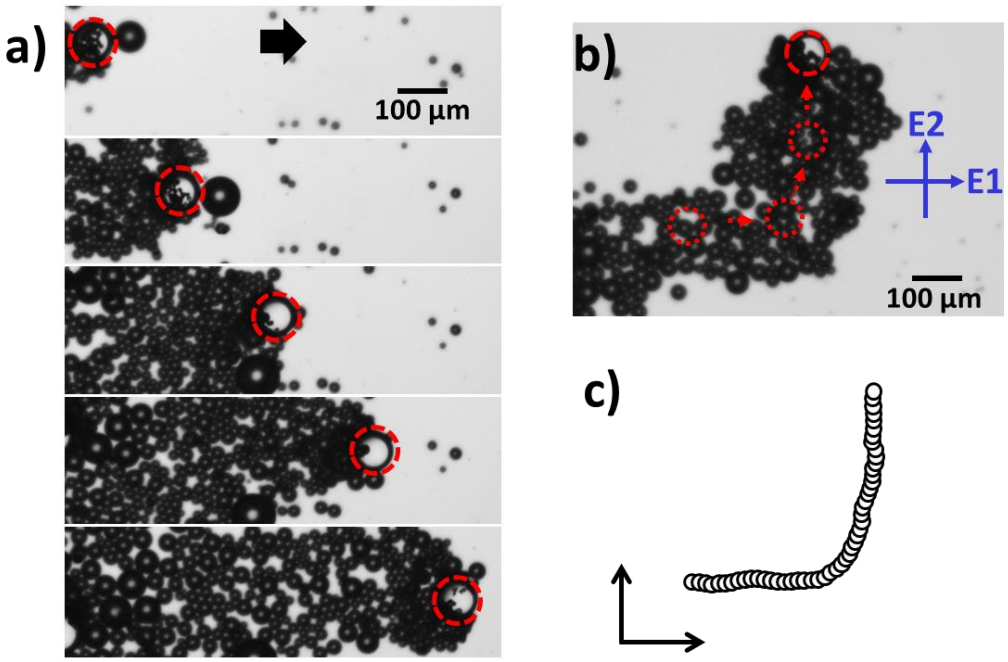

Figure 9-12. (a) Time-lapse images of the linear motion of a Janus droplet under the control of electric field. (b) 90° turning of the droplet with the direction change of the electric field. The blue arrows indicate the directions of the electric fields (c) Trajectory of the droplet turning 90° by changing the direction of the electric field 90° counterclockwise. In the experiments, the Janus droplets were developed from 200 mg/mL particle-in-oil dispersion and the strength of the control electric field is 25 V/cm.

9.4 Conclusions

In this chapter, the self-propelled micromotors are fabricated with Janus droplets, which are powered by the reaction of aluminum particles with alkaline solution. The Janus droplets are fabricated by covering one side of oil droplets with aluminum particles. The Janus droplets with different particle coverages are generated by using different concentrations of particle-in-oil dispersions. The particle coverage of the Janus droplets increases with the particle dispersion concentration. The spontaneous motion of the micromotor in NaOH solution is demonstrated. The gas bubbles are generated through the chemical reaction from the particle-coated side, the detaching of the gas bubble from the Janus droplet pushes the droplet to move towards the side

without the presence of particles. The effects of time, pH of the alkaline solution, particle coverage and surfactant in the solution on the speed of the Janus droplet are tested experimentally. Generally, over the course of time, the Janus droplet experiences three periods that the speed of the Janus droplet increases initially, then remains constant, and finally declines. The average moving speed of the Janus droplets increases with pH of the alkaline solution and the particle coverage of the droplet. In comparison with Tween 20, SDS and CTAB, surfactant Triton X-100 is most suitable for the generation of spontaneous motion of Janus droplets. The controlled directional motion of the Janus droplets by using electric field is also demonstrated successfully.

CHAPTER 10. Conclusions and Future Work

This chapter provides the summary of contributions of this thesis. Based on the findings and conclusions, the future research on the heterogeneous droplet fabrication, electrokinetic phenomena of the heterogeneous droplets, as well as the potentials of the heterogeneous droplets is introduced.

10.1 Summary of Contributions

This thesis presents a systematic study of Janus droplets, including fabrication, characterization and application. In the fabrication part, simple and controllable methods were developed to generate EIJDs and droplets with heterogeneous surface strips with nanoparticles using a DC electric field. By following the fabrication process, the sessile and suspended EIJDs can be generated with Al_2O_3 nanoparticles. The droplets with designed heterogeneous surface strips were prepared by controlling the delivery of nanoparticles to the surface of the droplets in a microchannel. The factors affect the topology of the EIJDs were studied. The electrokinetic phenomena of the EIJDs were investigated numerically and experimentally in the characterization part. The electroosmotic flow fluid around the EIJDs, the electrokinetic motion of the EIJDs under relative weak and relative high electric field, and the wall-induced electrophoresis of the EIJDs in a straight microchannel were studied, respectively. Finally, the applications of the Janus droplets in fabricating microvalve and micromotor were presented. For the EIJD-based microvalve, the performance of it was tested, including sealing, switching time and flow rate control. In comparison with other microvalves, the EIJD-based microvalve has the advantages of easy operation, simple structure and easy integration. The micromotor moved spontaneously in alkali solutions. The directional control of the micromotor using electric field was demonstrated. According to the research shown in this thesis, the major contributions are summarized and listed below:

1) A novel method was developed to fabricate sessile EIJDs with Al_2O_3 nanoparticles under an externally applied DC electric field.

2) The method for generating suspended EIJDs was developed and demonstrated. This method is simple and cost-effective, which produces EIJDs from Al_2O_3 nanoparticle-stabilized Pickering emulsion droplets under electric field.

3) A microfluidic system was set up to fabricate the droplets with multiple heterogeneous surface strips. The controllability of the formation of the strips on the droplets with this method was demonstrated. The droplets with designed patterns on their surfaces were generated.

4) The influence factors on the topology (nanoparticle coverage) of the EIJDs were studied, including the concentration of the nanoparticle concentration and the electric field.

5) A multi-physics model was set up to simulate the EOF fields around sessile EIJDs immersed in a bulk liquid. The vortices around the dipolar EIJDs were shown numerically.

6) With the particle tracing method, the vortices around the sessile EIJDs were visualized experimentally for the first time.

7) The effects of the electric field strength and the nanoparticle coverage of the sessile EIJDs on the size and location of the vortices were tested both numerically and experimentally.

8) The nonlinear electrokinetic motion of the suspended EIJDs in a microchannel under a relative weak electric field was demonstrated experimentally.

9) The lag of the variation of nanoparticle coverage of the EIJDs behind the change of electric field was characterized by measuring the evolution time of the nanoparticle film under different electric field strengths and by comparing the variations of nanoparticle coverage under different time-varying electric fields.

10) The difference of the variations of the electrokinetic velocity of the EIJDs under different time-varying electric fields was studied.

11) The flow fields around moving EIJDs under electric field were visualized for the first time with the particle tracing method. The results expand the understanding of the electrokinetic theory.

12) The electrokinetic motion of the EIJDs under relative high electric field was studied systematically. The effects of the electric field strength and the nanoparticle coverage of the EIJDs on the electrokinetic velocity were demonstrated experimentally.

13) The wall-induced DEP of the EIJDs was investigated systematically. The agreement between the theoretical results and the experimental data verifies the effects of electric field strength, droplet size and the nanoparticle coverage of the EIJDs on the wall-induced DEP lateral migration.

14) A microfluidic system was developed for the separation of target oil droplets and EIJDs by the wall-induced DEP, and the capability of the system in separation was demonstrated experimentally.

15) A microvalve based on the electrokinetic motion of the EIJDs was developed, and the performance of the microvalve, including sealing, switching time and flow rate control, was analyzed.

16) A self-propelled micromotor was fabricated with Janus droplet. The influence factors of the spontaneous motion of the micromotor were investigated. The directional motion of the micromotor under electric field was demonstrated.

10.2 Future Work

This thesis has demonstrated the fabrication of EIJDs and droplets with heterogeneous surface strips with nanoparticles. The electrokinetic phenomena and applications of the Janus droplets were studied comprehensively. However, additional questions still need to be explored in the future. The potential areas of research that could be conducted in the future are listed below.

10.2.1 Fabrication of Janus Droplets

In chapter 3, we introduced and demonstrated the methods in fabricating EIJDs and droplets with heterogeneous surface strips. However, the improvements are still essential to meet the requirements in different areas.

1) Generate large amount of EIJDs with uniform size. In practical applications, large amount of EIJDs with uniform size are generally essential. In this thesis, the suspended EIJDs are generated from Pickering emulsion droplets. However, the Pickering emulsion droplets are fabricated

through vibration, hence the size of the droplets varies. In order to generate EIJDs with uniform size, the microfluidic droplet device can be introduced to generate oil droplets with uniform size. The Pickering emulsion droplets and EIJDs with uniform size can be formed following.

2) Generate nanoscale Janus droplets. The Janus droplets studied in the thesis are in microscale. In comparison with the microscale Janus droplets, the Janus droplets in nanoscale may have unique electrokinetic properties which can find applications in specific areas. To prepare nanoscale Janus droplets, the emulsion droplets at nanometer can be generated with ultrasonic wave treatment, and the Janus droplets with nanoscale can be formed by partially covering the droplets with nanoparticles.

3) Prepare Janus droplets with some other nanoparticles. The property of the Janus droplets is dependent on the coated nanoparticle film. The Janus droplets generated from different nanoparticles have different properties, which may find specific applications. For example, the generation of Janus droplets with fluorescent nanoparticles may find applications in sensing and detection.

4) Generate aqueous Janus droplets immersed in continuous aqueous phase. Different from oil emulsion droplets, the water-in-water emulsion droplets have potentials in developing new controlled release system and fabricating artificial cells. The aqueous Janus droplets immersed in continuous aqueous phase can be fabricated by modifying the method developed in this thesis, which have potentials in drug delivery.

10.2.2 Characterization of the Janus Droplets

In the fundamental part, the electrokinetic properties of the Janus droplets were studied, including, EOF field, electrokinetic motion and wall-induced DEP. In these studies, the parameters we tested are not enough. Furthermore, the electrokinetic property is just one of the characters of the Janus droplets. Therefore, the studies of more influence factors and the other properties of the Janus droplet are essential.

1) Study the effect of ion size on the electrokinetic property of the Janus droplets. Generally, the ion size affects the EDL, and hence the EOF, EP and electrokinetic motion. Therefore, the study of the ion size on the electrokinetic property of the Janus droplet is suggested.

2) Study the effect of the pH value on the electrokinetic motion of the Janus droplets. The zeta potentials of the microchannel wall, oil-water interface and nanoparticle film are all pH responsive. With the variation of the pH value of the buffer solution, the electrokinetic motion of the Janus droplets changes. A series of experiments can be conducted to study this effect.

3) Study the effect of the microchannel shape on the electrokinetic motion of the Janus droplet. Based on the finding shown in this thesis, the shape of the microchannel can affect the electrokinetic motion of the Janus droplet. As a result, a systematical study of the effect of the microchannel shape on the electrokinetic motion of the Janus droplet is suggested.

4) Study the electrokinetic phenomena of nano-Janus droplets. The electrokinetic property of a charged particle, especially its electrokinetic motion, changes with the particle size. Therefore, the electrokinetic phenomena of the Janus droplets with nanometer size are different from that with micrometer size. The study of the electrokinetic performance of nano-Janus droplets may find some new phenomena.

5) Numerical and experimental examine how the electrokinetic motion of a Janus droplet is affected with the presence of neighboring Janus droplets. In practical applications of the microfluidic devices, the manipulation of multiple particles/droplets through a small microchannel at the same time is required. As a result, the electrokinetic motion of the particles/droplets can be affected by the presence of the other particles/droplets. For the EIJDs with dipolar EDL, vortices can be generated when they move in a microchannel under electric field. The existence of the vortices may enhance the interactions between EIJDs. Therefore, the study of the effect of the presence of other EIJDs on the electrokinetic motion of an EIJD is demand.

6) Study the assembly of the Janus droplets. The assembly of the Janus droplets has potential in material science, which can be applied to build up complex architectures. With the assembly of Janus droplets, the soft matter with novel structure and property can be formed.

10.2.3 Applications of the Janus Droplets

1) Improve the performance of the micromotor. The micromotor fabricated from Janus droplets can move spontaneous and directionally. However, the duration of the motion is limited and the

micromotor only takes effect in strong alkaline solution. Therefore, more efforts should be focused on improving the work efficiency and maximum the universality of the micromotor.

2) Generate micro-shutter with sessile EIJDs. The sessile EIJDs can be used as micro-shutter to control the light path. By using electric field to control the accumulation of the nanoparticles on the sessile oil droplet, the light path can be controlled.

3) Fabricate micro-sensor with EIJDs and droplets with heterogeneous surface strips. As the EIJDs are electrically responsive, the EIJDs can be applied as micro-sensors to indicate the direction and strength of the electric field. Furthermore, the EIJDs and droplets with heterogeneous surface strips fabricated from different functionalized nanoparticles can be used as biosensors to detect cells, bacteria and virus.

References

[1] Nisisako T, Torii T, Higuchi T. Novel microreactors for functional polymer beads. Chem Eng J 2004;101:23–9. doi:10.1016/j.cej.2003.11.019.

[2] Nisisako T, Torii T, Takahashi T, Takizawa Y. Synthesis of monodisperse bicolored janus particles with electrical anisotropy using a microfluidic co-flow system. Adv Mater 2006;18:1152–6. doi:10.1002/adma.200502431.

[3] Yu X, Zhang C, You S, Liu H, Zhang L, Liu W, et al. Microfluidic synthesis of multiferroic Janus particles with disk-like compartments. Appl Phys Lett 2016;108:3–8. doi:10.1063/1.4942365.

[4] Shepherd RF, Conrad JC, Rhodes SK, Link DR, Marquez M, Weitz DA, et al. Microfluidic assembly of homogeneous and janus colloid-filled hydrogel granules. Langmuir 2006;22:8618–22. doi:10.1021/la060759+.

[5] Xu K, Ge X, Huang J, Dang Z, Xu J, Luo G. A region-selective modified capillary microfluidic device for fabricating water–oil Janus droplets and hydrophilic–hydrophobic anisotropic microparticles. RSC Adv 2015;5:46981–8. doi:10.1039/C5RA05690J.

[6] Zhao Y, Gu H, Xie Z, Shum HC, Wang B, Gu Z. Bioinspired multifunctional janus particles for droplet manipulation. J Am Chem Soc 2013;135:54–7. doi:10.1021/ja310389w.

[7] Khan IU, Serra CA, Anton N, Li X, Akasov R, Messaddeq N, et al. Microfluidic conceived drug loaded Janus particles in side-by-side capillaries device. Int J Pharm 2014;473:239–49. doi:10.1016/j.ijpharm.2014.06.035.

[8] Yang Y, Wei J, Li X, Wu L, Chang Z, Serra CA. A side-by-side capillaries-based microfluidic system for synthesizing size- and morphology-controlled magnetic anisotropy janus beads. Adv Powder Technol 2015;26:156–62. doi:10.1016/j.apt.2014.08.018.

[9] Lan J, Chen J, Li N, Ji X, Yu M, He Z. Microfluidic generation of magnetic-fluorescent Janus microparticles for biomolecular detection. Talanta 2016;151:126–31. doi:10.1016/j.talanta.2016.01.024.

[10] Hasinovic H, Friberg SE, Kovach I, Koetz J. Destabilization of a dual emulsion to form a Janus emulsion. Colloid Polym Sci 2014;292:2319–24. doi:10.1007/s00396-014-3263-3.

[11] Hasinovic H, Friberg SE, Rong G. A one-step process to a Janus emulsion. J Colloid Interface Sci 2011;354:424–6. doi:10.1016/j.jcis.2010.10.004.

[12] Yoon J, Lee KJ, Lahann J. Multifunctional polymer particles with distinct compartments. J Mater Chem 2011;21:8502–10. doi:10.1039/c1jm10673b.

[13] Hasinovic H, Friberg SE. One-step inversion process to a Janus emulsion with two mutually insoluble oils. Langmuir 2011;27:6584–8. doi:10.1021/la105118h.

[14] Guzowski J, Korczyk PM, Jakiela S, Garstecki P. The structure and stability of multiple micro-droplets. Soft Matter 2012;8:7269–78. doi:10.1039/c2sm25838b.

[15] Friberg SE, Kovach I, Koetz J. Equilibrium topology and partial inversion of janus drops: A numerical analysis. ChemPhysChem 2013;14:3772–6. doi:10.1002/cphc.201300635.

[16] Ge L, Shao W, Lu S, Guo R. Droplet topology control of Janus emulsion prepared in one-

step high energy mixing. Soft Matter 2014;10:4498–505. doi:10.1039/c4sm00456f.

[17] Ge L, Lu S, Guo R. Janus emulsions formed with a polymerizable monomer, silicone oil, and Tween 80 aqueous solution. J Colloid Interface Sci 2014;423:108–12. doi:10.1016/j.jcis.2014.02.023.

[18] Zarzar LD, Sresht V, Sletten EM, Kalow JA, Blankschtein D, Swager TM. Dynamically reconfigurable complex emulsions via tunable interfacial tensions. Nature 2015;518:520–4. doi:10.1038/nature14168.

[19] Ge L, Friberg SE, Guo R. Recent studies of Janus emulsions prepared by one-step vibrational mixing. Curr Opin Colloid Interface Sci 2016;25:58–66. doi:10.1016/j.cocis.2016.05.001.

[20] Hasinovic H, Friberg SE, Kovach I, Koetz J. Janus Emulsion Drops:Equilibrium Calculations. J Dispers Sci Technol 2013;34:1683–9. doi:10.1080/01932691.2013.763728.

[21] Ahn MM, Im DJ, Yoo BS, Kang IS. Characterization of electrode alignment for optimal droplet charging and actuation in droplet-based microfluidic system. Electrophoresis 2015;36:2086–93. doi:10.1002/elps.201500141.

[22] Joensson HN, Zhang C, Uhlén M, Andersson-Svahn H. A homogeneous assay for protein analysis in droplets by fluorescence polarization. Electrophoresis 2012;33:436–9. doi:10.1002/elps.201100350.

[23] Schoeman RM, Kemna EWM, Wolbers F, van den Berg A. High-throughput deterministic single-cell encapsulation and droplet pairing, fusion, and shrinkage in a single microfluidic device. Electrophoresis 2014;35:385–92. doi:10.1002/elps.201300179.

[24] Nisisako T, Torii T. Formation of biphasic janus droplets in a microfabricated channel for the synthesis of shape-controlled polymer microparticles. Adv Mater 2007;19:1489–93. doi:10.1002/adma.200700272.

[25] Nisisako T, Hatsuzawa T. A microfluidic cross-flowing emulsion generator for producing biphasic droplets and anisotropically shaped polymer particles. Microfluid Nanofluid 2010;9:427–37. doi:10.1007/s10404-009-0559-6.

[26] Maeda K, Onoe H, Takinoue M, Takeuchi S. Controlled synthesis of 3D multi-compartmental particles with centrifuge-based microdroplet formation from a multi-barrelled capillary. Adv Mater 2012;24:1340–6. doi:10.1002/adma.201102560.

[27] Hirama H, Odera T, Torii T, Moriguchi H. A lithography-free procedure for fabricating three-dimensional microchannels using hydrogel molds. Biomed Microdev 2012;14:689–97. doi:10.1007/s10544-012-9649-4.

[28] Zhang M, Zhao H, Xu J, Luo G. Controlled coalescence of two immiscible droplets for Janus emulsions in a microfluidic device. RSC Adv 2015;5:32768–74. doi:10.1039/C5RA01718A.

[29] Nie Z, Xu S, Seo M, Lewis PC, Kumacheva E. Polymer particles with various shapes and morphologies produced in continuous microfluidic reactors. J Am Chem Soc 2005;127:8058–63. doi:10.1021/ja042494w.

[30] Utada A, Lorenceau E, Link D, Kaplan P. Monodisperse double emulsions generated from a microcapillary device. Science 2005;308:537–41.

[31] Nisisako T, Okushima S, Torii T. Controlled formulation of monodisperse double emulsions in a multiple-phase microfluidic system. Soft Matter 2005;1:23. doi:10.1039/b501972a.

[32] Hayward RC, Utada AS, Dan N, Weitz DA. Dewetting instability during the formation of polymersomes from block-copolymer-stabilized double emulsions. Langmuir 2006;22:4457–61. doi:10.1021/la060094b.

[33] Pannacci N, Bruus H, Bartolo D, Etchart I, Lockhart T, Hennequin Y, et al. Equilibrium and Nonequilibrium States in Microfluidic Double Emulsions. Phys Rev Lett 2008;101:164502. doi:10.1103/PhysRevLett.101.164502.

[34] Shum HC, Zhao YJ, Kim SH, Weitz DA. Multicompartment polymersomes from double emulsions. Angew Chemie 2011;123:1686–9. doi:10.1002/ange.201006023.

[35] Bayley H, Cronin B, Heron A, Holden M a., Hwang WL, Syeda R, et al. Droplet interface bilayers. Mol Biosyst 2008;4:1191–208. doi:10.1039/b808893d.

[36] Deshpande S, Caspi Y, Meijering AE, Dekker C. Octanol-assisted liposome assembly on chip. Nat Commun 2016;7:10447. doi:10.1038/ncomms10447.

[37] Choi CH, Weitz DA, Lee CS. One step formation of controllable complex emulsions: From functional particles to simultaneous encapsulation of hydrophilic and hydrophobic agents into desired position. Adv Mater 2013;25:2536–41. doi:10.1002/adma.201204657.

[38] Jeong J, Gross A, Wei WS, Tu F, Lee D, Collings PJ, et al. Liquid crystal Janus emulsion droplets: preparation, tumbling, and swimming. Soft Matter 2015;11:6747–54. doi:10.1039/C5SM01053E.

[39] Zhang Q, Xu M, Liu X, Zhao W, Zong C, Yu Y, et al. Fabrication of Janus droplets by evaporation driven liquid–liquid phase separation. Chem Commun 2016;52:5015–8. doi:10.1039/C6CC00249H.

[40] Nisisako T, Hatsuzawa T. Microfluidic fabrication of oil-filled polymeric microcapsules with independently controllable size and shell thickness via Janus to core-shell evolution of biphasic droplets. Sensors Actuators, B Chem 2016;223:209–16. doi:10.1016/j.snb.2015.09.085.

[41] Nisisako T, Ando T, Hatsuzawa T. High-volume production of single and compound emulsions in a microfluidic parallelization arrangement coupled with coaxial annular world-to-chip interfaces. Lab Chip 2012;12:3426. doi:10.1039/c2lc40245a.

[42] Muluneh M, Issadore D. Hybrid soft-lithography/laser machined microchips for the parallel generation of droplets. Lab Chip 2013;13:4750–4. doi:10.1039/c3lc50979f.

[43] Conchouso D, Castro D, Khan SA, Foulds IG. Three-dimensional parallelization of microfluidic droplet generators for a litre per hour volume production of single emulsions. Lab Chip 2014;14:3011–20. doi:10.1039/c4lc00379a.

[44] Femmer T, Jans A, Eswein R, Anwar N, Moeller M, Wessling M, et al. High-Throughput Generation of Emulsions and Microgels in Parallelized Microfluidic Drop-Makers Prepared by Rapid Prototyping. ACS Appl Mater Interfaces 2015;7:12635–8. doi:10.1021/acsami.5b03969.

[45] Jeong HH, Yelleswarapu VR, Yadavali S, Issadore D, Lee D. Kilo-scale droplet generation

in three-dimensional monolithic elastomer device (3D MED). Lab Chip 2015;15:4387–92. doi:10.1039/C5LC01025J.

[46] Nisisako T. Recent advances in microfluidic production of Janus droplets and particles. Curr Opin Colloid Interface Sci 2016;25:1–12. doi:10.1016/j.cocis.2016.05.003.

[47] Li M, Li D. Redistribution of charged aluminum nanoparticles on oil droplets in water in response to applied electrical field. J Nanopart Res 2016;18:120. doi:10.1007/s11051-016-3390-5.

[48] Zhakin AI. Electrohydrodynamics of charged surfaces. Phys Uspekhi 2013;56:141–63. doi:10.3367/UFNe.0183.201302c.0153.

[49] Saville DA. ELECTROHYDRODYNAMICS:The Taylor-Melcher Leaky Dielectric Model. Annu Rev Fluid Mech 1997;29:27–64. doi:10.1146/annurev.fluid.29.1.27.

[50] McConnell LC, Miksis MJ, Vlahovska PM. Vesicle electrohydrodynamics in DC electric fields. IMA J Appl Math (Institute Math Its Appl 2013;78:797–817. doi:10.1093/imamat/hxt023.

[51] Melcher JR, Taylor GI. Electrohydrodynamics - A review of the role of interfacial shear stresses. n.d. doi:10.1146/annurev.fl.01.010169.000551.

[52] Ouriemi M, Vlahovska PM. Electrohydrodynamic Deformation and Rotation of a Particle-Coated Drop. Langmuir 2015;31:6298–305. doi:10.1021/acs.langmuir.5b00774.

[53] Amah E, Shah K, Fischer I, Singh P. Electrohydrodynamic manipulation of particles adsorbed on the surface of a drop. Soft Matter 2016;12:1663–73. doi:10.1039/C5SM02195B.

[54] Rozynek Z, Dommersnes P, Mikkelsen A., Michels L, Fossum JO. Electrohydrodynamic controlled assembly and fracturing of thin colloidal particle films confined at drop interfaces. Eur Phys J Spec Top 2014;223:1859–67. doi:10.1140/epjst/e2014-02231-x.

[55] Rozynek Z, Mikkelsen A, Dommersnes P, Fossum JO. Electroformation of Janus and patchy capsules. Nat Commun 2014;5:1–6. doi:10.1038/ncomms4945.

[56] Bormashenko E, Bormashenko Y, Pogreb R, Gendelman O. Janus Droplets: Liquid Marbles Coated with Dielectric/Semiconductor Particles. Langmuir 2011;27:7–10. doi:10.1021/la103653p.

[57] Xu J, Ma A, Liu T, Lu C, Wang D, Xu H. Janus-like Pickering emulsions and their controllable coalescence. Chem Commun 2013;49:10871–3. doi:10.1039/c3cc46738d.

[58] Subramaniam AB, Abkarian M, Stone HA. Controlled assembly of jammed colloidal shells on fluid droplets. Nat Mater 2005;4:553–6. doi:10.1038/nmat1412.

[59] Chen L, Choo J, Yan B. The microfabricated electrokinetic pump: a potential promising drug delivery technique. Expert Opin Drug Deliv 2007;4:119–29. doi:10.1517/17425247.4.2.119.

[60] Chung AJ, Kim D, Erickson D. Electrokinetic microfluidic devices for rapid, low power drug delivery in autonomous microsystems. Lab Chip 2008;8:330–8. doi:10.1039/b713325a.

[61] Song Y, Li M, Pan X, Wang Q, Li D. Size-based cell sorting with a resistive pulse sensor and an electromagnetic pump in a microfluidic chip. Electrophoresis 2015;36:398–404.

doi:10.1002/elps.201400292.

[62] Bhagat AAS, Bow H, Hou HW, Tan SJ, Han J, Lim CT. Microfluidics for cell separation. Med Biol Eng Comput 2010;48:999–1014. doi:10.1007/s11517-010-0611-4.

[63] Wong PK, Wang T, Deval JH, Ho C. Electrokinetics in microdevices for biotechnology applications 2004;9:1–11.

[64] Song Y, Wang C, Li M, Pan X, Li D. Focusing particles by induced charge electrokinetic flow in a microchannel. Electrophoresis 2016;37:666–75. doi:10.1002/elps.201500361.

[65] Wuzhang J, Song Y, Sun R, Pan X, Li D. Electrophoretic mobility of oil droplets in electrolyte and surfactant solutions. Electrophoresis 2015.

[66] Kang Y, Li D. Electrokinetic motion of particles and cells in microchannels. Microfluid Nanofluid 2009;6:431–60. doi:10.1007/s10404-009-0408-7.

[67] Li D. Electrokinetics in Microfluidics. London: Academic Press; 2004.

[68] Li M, Li D. Redistribution of mobile surface charges of an oil droplet in water in applied electric field. Adv Colloid Interface Sci 2016;236:142–51. doi:10.1016/j.cis.2016.08.006.

[69] Ohshima H. A simple expression for Henry's function for the retardation effect in electrophoresis of spherical colloidal particles. J Colloid Interface Sci 1994;168:269–71.

[70] Keh H, Chen S. Electrophoresis of a Colloidal Sphere Parallel To a Dielectric Plane. J Fluid Mech 1988;194:377–90. doi:10.1017/S0022112088003039.

[71] Xuan X, Ye C, Li D. Near-wall electrophoretic motion of spherical particles in cylindrical capillaries. J Colloid Interface Sci 2005;289:286–90. doi:10.1016/j.jcis.2005.03.045.

[72] Ye C, Xuan X, Li D. Eccentric electrophoretic motion of a sphere in circular cylindrical microchannels. Microfluid Nanofluid 2005;1:234–41. doi:10.1007/s10404-004-0016-5.

[73] Unni HN, Keh HJ, Yang C. Analysis of electrokinetic transport of a spherical particle in a microchannel. Electrophoresis 2007;28:658–64. doi:10.1002/elps.200600576.

[74] Keh HJ, Wan YW. Diffusiophoresis of a colloidal sphere in nonelectrolyte gradients perpendicular to two plane walls. Chem Eng Sci 2008;63:1612–25. doi:10.1016/j.ces.2007.11.017.

[75] Keh HJ, Anderson JL. Boundary effects on electrophoretic motion of colloidal cylinders. J Fluid Mech 1985;153:417. doi:10.1017/S002211208500132X.

[76] Ye C, Sinton D, Erickson D, Li D. Electrophoretic motion of a circular cylindrical particle in a circular cylindrical microchannel. Langmuir 2002;18:9095–101. doi:10.1021/la026070w.

[77] Liu H, Bau HH, Hu HH. Electrophoresis of concentrically and eccentrically positioned cylindrical particles in a long tube. Langmuir 2004;20:2628–39. doi:10.1021/la035849i.

[78] Ai Y, Joo SW, Jiang Y, Xuan X, Qian S. Transient electrophoretic motion of a charged particle through a converging-diverging microchannel: Effect of direct current-dielectrophoretic force. Electrophoresis 2009;30:2499–506. doi:10.1002/elps.200800792.

[79] Jones TB, Washizu M. Multipolar dielectrophoretic and electrorotation theory. J Electrostat 1996;37:121–34. doi: 10.1016/0304-3886(96)00006-X.

[80] Wang X, Wang XB, Gascoyne PRC. General expressions for dielectrophoretic force and

electrorotational torque derived using the Maxwell stress tensor method. J Electrostat 1997;39:277–95. doi: 10.1016/S0304-3886(97)00126-5.

[81] Barbulovic-Nad I, Xuan X, Lee JSH, Li D. DC-dielectrophoretic separation of microparticles using an oil droplet obstacle. Lab Chip 2006;6:274–9. doi: 10.1039/B513183A.

[82] Lapizco-Encinas BH, Simmons BA, Cummings EB, Fintschenko Y. Insulator-based dielectrophoresis for the selective concentration and separation of live bacteria in water. Electrophoresis 2004;25:1695–704. doi:10.1002/elps.200405899.

[83] Kang Y, Li D, Kalams SA, Eid JE. DC-Dielectrophoretic separation of biological cells by size. Biomed Microdev 2008;10:243–9. doi:10.1007/s10544-007-9130-y.

[84] Çetin B, Li D. Dielectrophoresis in microfluidics technology. Electrophoresis 2011;32:2410–27. doi: 10.1002/elps.201100167.

[85] Anderson JL. Effect of nonuniform zeta potential on particle movement in electric fields. J Colloid Interface Sci 1985;105:45–54. doi:10.1016/0021-9797(85)90345-5.

[86] Fair MC, Anderson JL. Electrophoresis of nonuniformly charged ellipsoidal particles. J Colloid Interface Sci 1989;127:388–400. doi:10.1016/0021-9797(89)90045-3.

[87] Hsieh TH, Keh HJ. Boundary effects on electrophoresis of a colloidal cylinder with a nonuniform zeta potential distribution. J Colloid Interface Sci 2007;315:343–54. doi:10.1016/j.jcis.2007.06.066.

[88] Keh HJ, Hsieh TH. Electrophoresis of a colloidal sphere in a spherical cavity with arbitrary zeta potential distributions and arbitrary double-layer thickness. Langmuir 2008;24:390–8. doi:10.1021/la702399u.

[89] Hsu JP, Huang HT, Yeh LH, Tseng S. Electrophoresis of a particle at an arbitrary surface potential and double layer thickness: Importance of nonuniformly charged conditions. Langmuir 2012;28:2997–3004. doi:10.1021/la204468t.

[90] Qian S, Joo SW, Hou W, Zhao X. Nonuniform Surface Charge Distribution in a Nanotube. Society 2008:5332–40.

[91] Boymelgreen AM, Miloh T. Induced-charge electrophoresis of uncharged dielectric spherical Janus particles. Electrophoresis 2012;33:870–9. doi:10.1002/elps.201100446.

[92] Boymelgreen AM, Miloh T. A theoretical study of induced-charge dipolophoresis of ideally polarizable asymmetrically slipping Janus particles. Phys Fluids 2011;23. doi:10.1063/1.3609804.

[93] Gangwal S, Cayre OJ, Bazant MZ, Velev OD. Induced-charge electrophoresis of metallodielectric particles. Phys Rev Lett 2008;100:58302. doi:10.1103/PhysRevLett.100.058302.

[94] Squires TM, Bazant MZ. Breaking symmetries in induced-charge electro-osmosis and electrophoresis. J Fluid Mech 2006;560:65–101. doi:10.1017/S0022112006000371.

[95] Daghighi Y, Gao Y, Li D. 3D numerical study of induced-charge electrokinetic motion of heterogeneous particle in a microchannel. Electrochim Acta 2011;56:4254–62. doi:10.1016/j.electacta.2011.01.083.

[96] Daghighi Y, Li D. Micro-valve using induced-charge electrokinetic motion of Janus particle.

Lab Chip 2011;11:2929–40. doi:10.1039/c1lc20229d.

[97] Daghighi Y, Sinn I, Kopelman R, Li D. Experimental validation of induced-charge electrokinetic motion of electrically conducting particles. Electrochim Acta 2013;87:270–6. doi:10.1016/j.electacta.2012.09.021.

[98] Zhao Y, Shum HC, Chen H, Adams LLA, Gu Z, Weitz DA. Microfluidic generation of multifunctional quantum dot barcode particles. J Am Chem Soc 2011;133:8790–3. doi:10.1021/ja200729w.

[99] Seiffert S, Romanowsky MB, Weitz DA. Janus microgels produced from functional precursor polymers. Langmuir 2010;26:14842–7. doi:10.1021/la101868w.

[100] Hong L, Cacciuto A, Luijten E, Granick S. Clusters of amphiphilic colloidal spheres. Langmuir 2008;24:621–5. doi:10.1021/la7030818.

[101] Jiang S, Chen Q, Tripathy M, Luijten E, Schweizer KS, Granick S. Janus particle synthesis and assembly. Adv Mater 2010;22:1060–71. doi:10.1002/adma.200904094.

[102] Yi GR, Pine DJ, Sacanna S. Recent progress on patchy colloids and their self-assembly. J Phys Condens Matter 2013;25:193101. doi:10.1088/0953-8984/25/19/193101.

[103] Synytska A, Khanum R, Ionov L, Cherif C, Bellmann C. Water-repellent textile via decorating fibers with amphiphilic janus Particles. ACS Appl Mater Interfaces 2011;3:1216–20. doi:10.1021/am200033u.

[104] Kim SH, Lee SY, Yang SM. Janus microspheres for a highly flexible and impregnable waterrepelling interface. Angew Chem Int Ed 2010;49:2535–8. doi:10.1002/anie.201000108.

[105] Yánez-Sedeño P, Campuzano S, Pingarrón JM. Janus particles for (bio)sensing. Appl Mater Today 2017;9:276–88. doi:10.1016/j.apmt.2017.08.004.

[106] Yoshida K, Tanaka S, Hagihara Y, Tomonari S, Esashi M. Normally closed electrostatic microvalve with pressure balance mechanism for portable fuel cell application. Sensors Actuators, A Phys 2010;157:290–8. doi:10.1016/j.sna.2009.11.030.

[107] Yin SN, Wang CF, Yu ZY, Wang J, Liu SS, Chen S. Versatile bifunctional magnetic-fluorescent responsive Janus supraballs towards the flexible bead display. Adv Mater 2011;23:2915–9. doi:10.1002/adma.201100203.

[108] Li Z, Yang T, Lin C, Li Q, Liu S, Xu F, et al. Sonochemical Synthesis of Hydrophilic Drug Loaded Multifunctional Bovine Serum Albumin Nanocapsules. ACS Appl Mater Interfaces 2015;7:19390–7. doi:10.1021/acsami.5b05558.

[109] Wu Y, Lin X, Wu Z, Möhwald H, He Q. Self-propelled polymer multilayer janus capsules for effective drug delivery and light-triggered release. ACS Appl Mater Interfaces 2014;6:10476–81. doi:10.1021/am502458h.

[110] He W, Frueh J, Wu Z, He Q. How Leucocyte Cell Membrane Modified Janus Microcapsules are Phagocytosed by Cancer Cells. ACS Appl Mater Interfaces 2016;8:4407–15. doi:10.1021/acsami.5b10885.

[111] Lu AX, Liu Y, Oh H, Gargava A, Kendall E, Nie Z, et al. Catalytic Propulsion and Magnetic Steering of Soft, Patchy Microcapsules: Ability to Pick-Up and Drop-Off Microscale Cargo. ACS Appl Mater Interfaces 2016;8:15676–83. doi:10.1021/acsami.6b01245.

[112] Chera L, Palcevskis E, Berzins M, Lipe A, Jansone I. Dispersion of nanosized ceramic powders in aqueous suspensions. J Phys Conf Ser 2007;93:12010. doi:10.1088/1742-6596/93/1/012010.

[113] Reincke F, Hickey SG, Kegel WK, Vanmaekelbergh D. Spontaneous Assembly of a Monolayer of Charged Gold Nanocrystals at the Water/Oil Interface. Angew Chemie - Int Ed 2004;43:458–62. doi:10.1002/anie.200352339.

[114] Li YJ, Huang WJ, Sun SG. A universal approach for the self-assembly of hydrophilic nanoparticles into ordered monolayer films at a toluene/water interface. Angew Chemie - Int Ed 2006;45:2537–9. doi:10.1002/anie.200504595.

[115] Nakajima Y, Sato T. Calculation of electrostatic force between two charged dielectric spheres by the re-expansion method. J Electrostat 1999;45:213–26. doi:10.1016/S0304-3886(98)00051-5.

[116] Ye C, Li D. Electrophoretic motion of a sphere in a microchannel under the gravitational field. J Colloid Interface Sci 2002;251:331–8. doi:10.1006/jcis.2002.8438.

[117] Bichoutskaia E, Boatwright AL, Khachatourian A, Stace AJ. Electrostatic analysis of the interactions between charged particles of dielectric materials. J Chem Phys 2010;133:24105. doi:10.1063/1.3457157.

[118] Stenhammar J, Linse P, Wennerström H, Karlström G. An exact calculation of the van der Waals interaction between two spheres of classical dipolar fluid. J Phys Chem B 2010;114:13372–80. doi:10.1021/jp105754t.

[119] Gu Y. The electrical double-layer interaction between a spherical particle and a cylinder. J Colloid Interface Sci 2000;231:199–203. doi:10.1006/jcis.2000.7110.

[120] Li M, Li D. Electrokinetic motion of an electrically induced Janus droplet in microchannels. Microfluid Nanofluid 2017;21:16. doi:10.1007/s10404-016-1838-7.

[121] Lee JSH, Li D. Electroosmotic flow at a liquid-air interface. Microfluid Nanofluid 2006;2:361–5. doi:10.1007/s10404-006-0084-9.

[122] Movahed S, Khani S, Wen JZ, Li D. Electroosmotic flow in a water column surrounded by an immiscible liquid. J Colloid Interface Sci 2012;372:207–11. doi:10.1016/j.jcis.2012.01.044.

[123] Gao Y, Wong TN, Yang C, Ooi KT. Transient two-liquid electroosmotic flow with electric charges at the interface. Colloids Surfaces A Physicochem Eng Asp 2005;266:117–28. doi:10.1016/j.colsurfa.2005.05.068.

[124] Lee JSH, Barbulovic-Nad I, Wu Z, Xuan X, Li D. Electrokinetic flow in a free surface-guided microchannel. J Appl Phys 2006;99:54905. doi:10.1063/1.2177428.

[125] Wu Z, Gao Y, Li D. Electrophoretic motion of ideally polarizable particles in a microchannel. Electrophoresis 2009;30:773–81. doi:10.1002/elps.200800381.

[126] Kolch W, Neusüß C, Pelzing M, Mischak H. Capillary electrophoresis–mass spectrometry as a powerful tool in clinical diagnosis and biomarker discovery. Mass Spectrom Rev 2005;24:959–77.

[127] Ozkan M, Pisanic T, Scheel J, Barlow C, Esener S, Bhatia SN. Electro-optical platform for the manipulation of live cells. Langmuir 2003;19:1532–8. doi:10.1021/la0261848.

[128] Huang LR, Tegenfeld JO, Kraeft JJ, Sturm JC, Austin RH, Cox EC. A DNA prism for high-speed continuous fractionation of large DNA molecules. Nat Biotechnol 2002;20:1048–51. doi:10.1038/nbt733.

[129] Fu J, Schoch RB, Stevens AL, Tannenbaum SR, Han J. A patterned anisotropic nanofluidic sieving structure for continuous-flow separation of DNA and proteins. Nat Nanotechnol 2007;2:121–8. doi:10.1038/nnano.2006.206.

[130] Barchini R, Saville DA. Electrokinetic properties of surfactant-stabilized oil droplets. Langmuir 1996;12:1442–5.

[131] Probstein RF. Physicochemical hydrodynamics: an introduction. 2nd ed. New York: John Wiley & Sons; 2005.

[132] Booth F. The Cataphoresis of Spherical Fluid Droplets in Electrolytes. J Chem Phys 1951;19:1331–6. doi:10.1063/1.1747478.

[133] Kelsall GH, Tang S, Yurdakult S, Smith AL. Electrophoretic behaviour of bubbles in aqueous electrolytes. J Chem Soc, Faraday Trans 1996;92:3887–93. doi: 10.1039/FT9969203887.

[134] Baygents JC, Saville DA. Electrophoresis of drops and bubbles. J Chem Soc Faraday Trans 1991;87:1883. doi:10.1039/ft9918701883.

[135] Ohshima H. Electrophoretic mobility of a liquid drop in a salt-free medium. J Colloid Interface Sci 2003;263:333–6. doi:10.1016/S0021-9797(03)00289-3.

[136] Marinova K, Alargova R, Denkov N. Charging of oil-water interfaces due to spontaneous adsorption of hydroxyl ions. Langmuir 1996;12:2045–51. doi:10.1021/la950928i.

[137] Nespolo SA, Bevan MA, Chan DYC, Grieser F, Stevens GW. Hydrodynamic and electrokinetic properties of decane droplets in aqueous sodium dodecyl sulfate solutions. Langmuir 2001;17:7210–8. doi:10.1021/la0103968.

[138] Gu Y, Li D. The zeta-Potential of Silicone Oil Droplets Dispersed in Aqueous Solutions. J Colloid Interface Sci 1998;206:346–9. doi:10.1006/jcis.1998.5612.

[139] Gu Y, Li D. Electric charge on small silicone oil droplets dispersed in ionic surfactant solutions. Colloids Surfaces A Physicochem Eng Asp 1998;139:213–25. doi:10.1016/S0927-7757(98)00283-0.

[140] Wang C, Li M, Song Y, Pan X, Li D. Electrokinetic motion of a spherical micro particle at an oil−water interface in microchannel. Electrophoresis 2017;39:807–15. doi:10.1002/elps.201700289.

[141] Lee JH, Hwang KS, Jang SP, Lee BH, Kim JH, Choi SUS, et al. Effective viscosities and thermal conductivities of aqueous nanofluids containing low volume concentrations of Al2O3 nanoparticles. Int J Heat Mass Transf 2008;51:2651–6. doi:10.1016/j.ijheatmasstransfer.2007.10.026.

[142] Shirai T, Watanabe H, Fuji M, Takahashi M. Structural Properties and Surface Characteristics on Aluminum Oxide Powders. Annu Rep Adv Ceram Res Cent Nagoya Inst Technol 2009;9:23–31. doi:

[143] Nguyen VS, Rouxel D, Hadji R, Vincent B, Fort Y. Effect of ultrasonication and dispersion stability on the cluster size of alumina nanoscale particles in aqueous solutions. Ultrason

Sonochem 2011;18:382–8. doi:10.1016/j.ultsonch.2010.07.003.

[144] Basheva ES, Gurkov TD, Christov NC, Campbell B. Interactions in oil/water/oil films stabilized by β-lactoglobulin; role of the surface charge. Colloids Surfaces A Physicochem Eng Asp 2006;282–283:99–108. doi:10.1016/j.colsurfa.2006.01.023.

[145] Wu Z, Li D. Induced-charge electrophoretic motion of ideally polarizable particles. Electrochim Acta 2009;54:3960–7. doi:10.1016/j.electacta.2009.02.016.

[146] Huang CH, Lee E. Electrophoretic motion of a liquid droplet in a cylindrical pore. J Phys Chem C 2012;116:15058–67. doi:10.1021/jp301388a.

[147] Davison SM, Sharp K V. Boundary effects on the electrophoretic motion of cylindrical particles: Concentrically and eccentrically-positioned particles in a capillary. J Colloid Interface Sci 2006;303:288–97. doi:10.1016/j.jcis.2006.07.063.

[148] Lee GB, Lin CH, Lee KH, Lin YF. On the surface modification of microchannels for microcapillary electrophoresis chips. Electrophoresis 2005;26:4616–24. doi:10.1002/elps.200500382.

[149] Chun MS, Shim MS, Choi NW. Fabrication and validation of a multi-channel type microfluidic chip for electrokinetic streaming potential devices. Lab Chip 2006;6:302–9. doi:10.1039/b514327f.

[150] De Geest BG, Urbanski JP, Thorsen T, Demeester J, De Smedt SC. Synthesis of monodisperse biodegradable microgels in microfluidic devices. Langmuir 2005;21:10275–9. doi:10.1021/la051527y.

[151] Yang WW, Lu YC, Xiang ZY, Luo GS. Monodispersed microcapsules enclosing ionic liquid of 1-butyl-3-methylimidazolium hexafluorophosphate. React Funct Polym 2007;67:81–6. doi:10.1016/j.reactfunctpolym.2006.10.005.

[152] Henkel T, Bermig T, Kielpinski M, Grodrian a., Metze J, Köhler JM. Chip modules for generation and manipulation of fluid segments for micro serial flow processes. Chem Eng J 2004;101:439–45. doi:10.1016/j.cej.2004.01.021.

[153] Ju J, Zeng C, Zhang L, Xu N. Continuous synthesis of zeolite NaA in a microchannel reactor. Chem Eng J 2006;116:115–21. doi:10.1016/j.cej.2005.11.006.

[154] Ahmed B, Barrow D, Wirth T. Enhancement of reaction rates by segmented fluid flow in capillary scale reactors. Adv Synth Catal 2006;348:1043–8. doi:10.1002/adsc.200505480.

[155] Sakai S, Hashimoto I, Kawakami K. Usefulness of flow focusing technology for producing subsieve-size cell enclosing capsules: Application for agarose capsules production. Biochem Eng J 2006;30:218–21. doi:10.1016/j.bej.2006.04.003.

[156] Clausell-Tormos J, Lieber D, Baret JC, El-Harrak A, Miller OJ, Frenz L, et al. Droplet-based microfluidic platforms for the encapsulation and screening of mammalian cells and multicellular organisms. Chem Biol 2008;15:427–37. doi:10.1016/j.chembiol.2008.04.004.

[157] Kato A, Shindo E, Sakaue T, Tsuji A, Yoshikawa K. Conformational transition of giant DNA in a confined space surrounded by a phospholipid membrane. Biophys J 2009;97:1678–86. doi:10.1016/j.bpj.2009.06.041.

[158] Dittrich PS, Jahnz M, Schwille P. A new embedded process for compartmentalized cell-free protein expression and on-line detection in microfluidic devices. ChemBioChem

2005;6:811–4. doi:10.1002/cbic.200400321.

[159] Funakoshi K, Suzuki H, Takeuchi S. Lipid bilayer formation by contacting monolayers in a microfluidic device for membrane protein analysis. Anal Chem 2006;78:8169–74. doi:10.1021/ac0613479.

[160] Chen Q, Whitmer JK, Jiang S, Bae SC, Luijten E, Granick S. Supracolloidal reaction kinetics of Janus spheres. Science 2011;331:199–202. doi:10.1126/science.1197451.

[161] Hu SH, Gao X. Nanocomposites with spatially separated functionalities for combined imaging and magnetolytic therapy. J Am Chem Soc 2010;132:7234–7. doi:10.1021/ja102489q.

[162] Zhao CX. Multiphase flow microfluidics for the production of single or multiple emulsions for drug delivery. Adv Drug Deliv Rev 2013;65:1420–46. doi:10.1016/j.addr.2013.05.009.

[163] Hung SH, Lin YH, Lee G Bin. A microfluidic platform for manipulation and separation of oil-in-water emulsion droplets using optically induced dielectrophoresis. J Micromech Microeng 2010:45026. doi:10.1088/0960-1317/20/4/045026.

[164] Oh KW, Ahn CH. A review of microvalves. J Micromech Microeng 2006;16:R13–39. doi:10.1088/0960-1317/16/5/R01.

[165] Basu AS. Droplet morphometry and velocimetry (DMV): a video processing software for time-resolved, label-free tracking of droplet parameters. Lab Chip 2013;13:1892–901. doi:10.1039/c3lc50074h.

[166] Baroud CN, Delville JP, Gallaire F, Wunenburger R. Thermocapillary valve for droplet production and sorting. Phys Rev E 2007;75:46302. doi:10.1103/PhysRevE.75.046302.

[167] Basu AS, Gianchandani YB. Virtual microfluidic traps, filters, channels and pumps using Marangoni flows. J Micromech Microeng 2008;18:115031. doi:10.1088/0960-1317/18/11/115031.

[168] Abate AR, Agresti JJ, Weitz DA. Microfluidic sorting with high-speed single-layer membrane valves. Appl Phys Lett 2010;96:203509. doi:10.1063/1.3431281.

[169] Cao Z, Chen F, Bao N, He H, Xu P, Jana S, et al. Droplet sorting based on the number of encapsulated particles using a solenoid valve. Lab Chip 2013;13:171–8. doi:10.1039/C2LC40950J.

[170] Franke T, Abate AR, Weitz DA, Wixforth A. Surface acoustic wave (SAW) directed droplet flow in microfluidics for PDMS devices. Lab Chip 2009;9:2625–7. doi:10.1039/b906819h.

[171] Franke T, Braunmuller S, Schmid L, Wixforth A, Weitz DA. Surface acoustic wave actuated cell sorting (SAWACS). Lab Chip 2010;10:789–94. doi:10.1039/B915522H.

[172] Manneberg O, Melker Hagsäter S, Svennebring J, Hertz HM, Kutter JP, Bruus H, et al. Spatial confinement of ultrasonic force fields in microfluidic channels. Ultrasonics 2009;49:112–9. doi:10.1016/j.ultras.2008.06.012.

[173] Ahn K, Kerbage C, Hunt TP, Westervelt RM, Link DR, Weitz DA. Dielectrophoretic manipulation of drops for high-speed microfluidic sorting devices. Appl Phys Lett 2006;88:24104. doi:10.1063/1.2164911.

[174] Zhang F, Li D. Separation of dielectric Janus particles based on polarizability-dependent induced-charge electroosmotic flow. J Colloid Interface Sci 2015;448:297–305.

doi:10.1016/j.jcis.2015.02.006.

[175] Young EWK, Li D. Dielectrophoretic force on a sphere near a planar boundary. Langmuir 2005;21:12037–46. doi:10.1021/la0518546.

[176] Yariv E. Dielectrophoretic sphere–wall repulsion due to a uniform electric field. Soft Matter 2016;12:6277–84. doi:10.1039/C6SM00462H.

[177] Yariv E. "Force-free" electrophoresis? Phys Fluids 2006;18:31702. doi:10.1063/1.2185690.

[178] Zhao H, Bau HH. On the effect of induced electro-osmosis on a cylindrical particle next to a surface. Langmuir 2007;23:4053–63. doi:10.1021/la063224p.

[179] Kang S. Dielectrophoretic motions of a single particle in the vicinity of a planar wall under a direct-current electric field. J Electrostat 2015;76:159–70. doi:10.1016/j.elstat.2015.05.007.

[180] Liang L, Qian S, Xuan X. Three-dimensional electrokinetic particle focusing in a rectangular microchannel. J Colloid Interface Sci 2010;350:377–9. doi:10.1016/j.jcis.2010.06.067.

[181] Liang L, Ai Y, Zhu J, Qian S, Xuan X. Wall-induced lateral migration in particle electrophoresis through a rectangular microchannel. J Colloid Interface Sci 2010;347:142–6. doi:10.1016/j.jcis.2010.03.039.

[182] Kazoe Y, Yoda M. Experimental study of the effect of external electric fields on interfacial dynamics of colloidal particles. Langmuir 2011;27:11481–8. doi:10.1021/la202056b.

[183] Liang Q, Zhao C, Yang C. Enhancement of electrophoretic mobility of microparticles near a solid wall-Experimental verification. Electrophoresis 2015;36:731–6. doi:10.1002/elps.201400405.

[184] Lu X, Hsu JP, Xuan X. Exploiting the wall-induced non-inertial lift in electrokinetic flow for a continuous particle separation by size. Langmuir 2015;31:620–7. doi:10.1021/la5045464.

[185] Thomas C, Lu X, Todd A, Raval Y, Tzeng TR, Song Y, et al. Charge-based separation of particles and cells with similar sizes via the wall-induced electrical lift. Electrophoresis 2017;38:320–6. doi:10.1002/elps.201600284.

[186] Li M, Li D. Fabrication and electrokinetic motion of electrically anisotropic Janus droplets in microchannels. Electrophoresis 2017;38:287–95. doi:10.1002/elps.201600310.

[187] Gravesen P, Branebjerg J, Jensen OS. Microfluidics-a review. J Micromech Microeng 1993;3:168–82. doi:10.1088/0960-1317/3/4/002.

[188] Whitesides GM. The origins and the future of microfluidics. Nature 2006;442:368–73. doi:10.1038/nature05058.

[189] Reyes DR, Iossifidis D, Auroux PA, Manz A. Micro total analysis systems. 1. Introduction, theory, and technology. Anal Chem 2002;74:2623–36. doi:10.1021/ac0202435.

[190] Auroux PA, Iossifidis D, Reyes DR, Manz A. Micro total analysis systems. 2. Analytical standard operations and applications. Anal Chem 2002;74:2637–52. doi:10.1021/ac020239t.

[191] Haeberle S, Zengerle R. Microfluidic platforms for lab-on-a-chip applications. Lab Chip 2007;7:1094–110. doi:10.1039/b706364b.

[192] Au AK, Lai H, Utela BR, Folch A. Microvalves and micropumps for BioMEMS. Micromachines 2011;2:179–220. doi:10.3390/mi2020179.

[193] Ogden S, Klintberg L, Thornell G, Hjort K, Bodén R. Review on miniaturized paraffin phase change actuators, valves, and pumps. Microfluid Nanofluid 2014;17:53–71. doi:10.1007/s10404-013-1289-3.

[194] Terry SC, Herman JH, Angell JB. A gas chromatographic air analyzer fabricated on a silicon wafer. IEEE Trans Electron Devices 1979;26:1880–6. doi:10.1109/T-ED.1979.19791.

[195] Fu C, Rummler Z, Schomburg W. Magnetically driven micro ball valves fabricated by multilayer adhesive film bonding. J Micromech Microeng 2003;13:S96. doi:10.1088/0960-1317/13/4/316.

[196] Chen CY, Chen CH, Tu TY, Lin CM, Wo AM. Electrical isolation and characteristics of permanent magnet-actuated valves for PDMS microfluidics. Lab Chip 2011;11:733–7. doi:10.1039/C0LC00415D.

[197] Kirby BJ, Shepodd TJ, Hasselbrink EF. Voltage-addressable on/off microvalves for high-pressure microchip separations. J Chromatogr A 2002;979:147–54. doi:10.1016/S0021-9673(02)01453-X.

[198] Oh KW, Han A, Bhansali S, Ahn CH. A low-temperature bonding technique using spin-on fluorocarbon polymers to assemble microsystems. J Micromech Microeng 2002;12:187–91. doi:10.1088/0960-1317/12/2/313.

[199] Han J, Yeom J, Mensing G, Flachsbart B, Shannon MA. Characteristics of electrostatic gas micro-pump with integrated polyimide passive valves. J Micromech Microeng 2012;22:95007. doi:10.1088/0960-1317/22/9/095007.

[200] Reynaerts D, Peirs J, Van Brussel H. An implantable drug-delivery system based on shape memory alloy micro-actuation. Sensors Actuators A Phys 1997;61:455–62. doi:10.1016/S0924-4247(97)80305-6.

[201] Ruzzu A, Bade K, Fahrenberg J, Maas D. Positioning system for catheter tips based on an active microvalve system. J Micromech Microeng 1998;8:161–4. doi:10.1088/0960-1317/8/2/030.

[202] Baechi D, Buser R. Suspension handling system. Sensors Actuators, B Chem 2000;63:195–200. doi:10.1016/S0925-4005(00)00357-9.

[203] Liu Y, Kohl M, Okutsu K, Miyazaki S. A TiNiPd thin film microvalve for high temperature applications. Mater Sci Eng A 2004;378:205–9. doi:10.1016/j.msea.2003.10.369.

[204] Vyawahare S, Sitaula S, Martin S, Adalian D, Scherer A. Electronic control of elastomeric microfluidic circuits with shape memory actuators. Lab Chip 2008;8:1530–5. doi:10.1039/b804515a.

[205] Augustine S, Gu P, Zheng X, Nishida T, Fan ZH. Low-power electrically controlled thermoelastic microvalves integrated in thermoplastic microfluidic devices. Microfluid Nanofluid 2015;19:1385–94. doi:10.1007/s10404-015-1653-6.

[206] Unger MA, Chou HP, Thorsen T, Scherer A, Quake SR. Monolithic Microfabricated Valves and Pumps by Multilayer Soft Lithography. Science 2000;288:113–6. doi:10.1126/science.288.5463.113.

[207] Park W, Han S, Kwon S. Fabrication of membrane-type microvalves in rectangular microfluidic channels via seal photopolymerization. Lab Chip 2010;10:2814–7. doi:10.1039/c005173j.

[208] Didar TF, Li K, Tabrizian M, Veres T. High throughput multilayer microfluidic particle separation platform using embedded thermoplastic-based micropumping. Lab Chip 2013;13:2615–22. doi:10.1039/c3lc50181g.

[209] Jang LW, Razu ME, Jensen EC, Jiao H, Kim J. A fully automated microfluidic micellar electrokinetic chromatography analyzer for organic compound detection. Lab Chip 2016;16:3558–64. doi:10.1039/C6LC00790B.

[210] Gui L, Liu J. Ice valve for a mini/micro flow channel. J Micromech Microeng 2004;14:242–6. doi:10.1088/0960-1317/14/2/011.

[211] Suzuki A, Tanaka T. Phase transition in polymer gels induced by visible light. Nature 1990;346:345–7. doi:10.1038/346345a0.

[212] Tanaka T, Nishio I, Sun S-T, Ueno-Nishio S. Collapse of gels in an electric field. Science 1982;218:467–9. doi:10.1126/science.218.4571.467.

[213] Lin S, Wang W, Ju XJ, Xie R, Chu LY. A simple strategy for in situ fabrication of a smart hydrogel microvalve within microchannels for thermostatic control. Lab Chip 2014;14:2626–34. doi:10.1039/c4lc00039k.

[214] Park I, Li Z, Li X, Pisano AP, Williams RS. Towards the silicon nanowire-based sensor for intracellular biochemical detection. Biosens Bioelectron 2007;22:2065–70. doi:10.1016/j.bios.2006.09.017.

[215] Baek SK, Yoon YK, Jeon HS, Seo S, Park JH. A wireless sequentially actuated microvalve system. J Micromech Microeng 2013;23:45006. doi:10.1088/0960-1317/23/4/045006.

[216] Park JM, Cho YK, Lee BS, Lee JG, Ko C. Multifunctional microvalves control by optical illumination on nanoheaters and its application in centrifugal microfluidic devices. Lab Chip 2007;7:557–64. doi:10.1039/b616112j.

[217] Kaigala G V., Hoang VN, Backhouse CJ. Electrically controlled microvalves to integrate microchip polymerase chain reaction and capillary electrophoresis. Lab Chip 2008;8:1071–8. doi:10.1039/b802853b.

[218] Hitzbleck M, Avrain L, Smekens V, Lovchik RD, Mertens P, Delamarche E. Capillary soft valves for microfluidics. Lab Chip 2012;12:1972–8. doi:10.1039/c2lc00015f.

[219] Mohammed MI, Abraham E, Desmulliez MPY. Rapid laser prototyping of valves for microfluidic autonomous systems. J Micromech Microeng 2013;23:35034. doi:10.1088/0960-1317/23/3/035034.

[220] Sochol RD, Lu A, Lei J, Iwai K, Lee LP, Lin L. Microfluidic bead-based diodes with targeted circular microchannels for low Reynolds number applications. Lab Chip 2014;14:1585–94. doi:10.1039/c3lc51069g.

[221] Biswas GC, Watanabe T, Carlen ET, Yokokawa M, Suzuki H. Switchable hydrophobic valve for controlled microfluidic processing. ChemPhysChem 2016;17:817–21. doi:10.1002/cphc.201501015.

[222] Yamada M, Seki M. Nanoliter-sized liquid dispenser array for multiple biochemical

analysis in microfluidic devices. Anal Chem 2004;76:895–9. doi:10.1021/ac0350007.

[223] Andersson H, van der Wijngaart W, Griss P, Niklaus F, Stemme G. Hydrophobic valves of plasma deposited octafluorocyclobutane in DRIE channels. Sensors Actuators B Chem 2001;75:136–41. doi:10.1016/S0925-4005(00)00675-4.

[224] Jiang H, Weng X, Chon CH, Wu X, Li D. A microfluidic chip for blood plasma separation using electro-osmotic. J Micromech Microeng 2011;21:85019. doi:10.1088/0960-1317/21/8/085019.

[225] Ren CL, Li D. Electrokinetic sample transport in a microchannel with spatial electrical conductivity gradients. J Colloid Interface Sci 2006;294:482–91. doi:10.1016/j.jcis.2005.07.051.

[226] Hu G, Gao Y, Sherman PM, Li D. A microfluidic chip for heterogeneous immunoassay using electrokinetical control. Microfluid Nanofluid 2005;1:346–55. doi:10.1007/s10404-005-0040-0.

[227] Gao Y, Lin FYH, Hu G, Sherman PM, Li D. Development of a novel electrokinetically driven microfluidic immunoassay for the detection of Helicobacter pylori. Anal Chim Acta 2005;543:109–16. doi:10.1016/j.aca.2005.04.032.

[228] Ren CL, Li D. Effects of spatial gradients of electrical conductivity on chip-based sample injection processes. Anal Chim Acta 2004;518:59–68. doi:10.1016/j.aca.2004.05.018.

[229] Sinton D, Ren L, Xuan X, Li D. Effects of liquid conductivity differences on multi-component sample injection , pumping and stacking in microfluidic chips. Lab Chip 2003;3:173–9. doi:10.1039/b304614a.

[230] Sinton D, Ren L, Li D. A dynamic loading method for controlling on-chip microfluidic sample injection. J Colloid Interface Sci 2003;266:448–56. doi:10.1016/S0021-9797(03)00630-1.

[231] Weng X, Jiang H, Li D. Electrokinetically-controlled RNA-DNA hybridization assay for foodborne pathogens. Microchim Acta 2012;178:381–7. doi:10.1007/s00604-012-0853-y.

[232] Zhang F, Daghighi Y, Li D. Control of flow rate and concentration in microchannel branches by induced-charge electrokinetic flow. J Colloid Interface Sci 2011;364:588–93. doi:10.1016/j.jcis.2011.08.070.

[233] Kim SH, Jeon SJ, Jeong WC, Park HS, Yang SM. Optofluidic synthesis of electroresponsive photonic janus balls with isotropic structural colors. Adv Mater 2008;20:4129–34. doi:10.1002/adma.200801167.

[234] Maggi C, Simmchen J, Saglimbeni F, Katuri J, Dipalo M, De Angelis F, et al. Self-assembly of micromachining systems powered by Janus micromotors. Small 2016;12:446–51. doi:10.1002/smll.201502391.

[235] Brown A, Poon W. Ionic effects in self-propelled Pt-coated Janus swimmers. Soft Matter 2014;10:4016–27. doi:10.1039/c4sm00340c.

[236] Gao W, Feng X, Pei A, Gu Y, Li J, Wang J. Seawater-driven magnesium based Janus micromotors for environmental remediation. Nanoscale 2013;5:4696–700. doi:10.1039/c3nr01458d.

[237] Yoshida M, Roh KH, Mandal S, Bhaskar S, Lim D, Nandivada H, et al. Structurally

controlled bio-hybrid materials based on unidirectional association of anisotropic microparticles with human endothelial cells. Adv Mater 2009;21:4920–5. doi:10.1002/adma.200901971.

[238] Yang S, Guo F, Kiraly B, Mao X, Lu M, Leong KW, et al. Microfluidic synthesis of multifunctional Janus particles for biomedical applications. Lab Chip 2012;12:2097–102. doi:10.1039/c2lc90046g.

[239] Yi Y, Sanchez L, Gao Y, Yu Y. Janus particles for biological imaging and sensing. Analyst 2016;141:3526–39. doi:10.1039/C6AN00325G.

[240] Gao W, Wang J. Synthetic micro/nanomotors in drug delivery. Nanoscale 2014;6:10486–94. doi:10.1039/C4NR03124E.

[241] Li W, Dong H, Tang G, Ma T, Cao X. Controllable microfluidic fabrication of Janus and microcapsule particles for drug delivery applications. RSC Adv 2015;5:23181–8. doi:10.1039/C4RA17153E.

[242] Patra D, Sengupta S, Duan W, Zhang H, Pavlick R, Sen A. Intelligent, self-powered, drug delivery systems. Nanoscale 2013;5:1273–83. doi:10.1039/C2NR32600K.

[243] Wang T, Chen H, Liu K, Wang S, Xue P, Yu Y, et al. Janus Si micropillar arrays with thermal-responsive anisotropic wettability for manipulation of microfluid motions. ACS Appl Mater Interfaces 2014;7:376–82. doi:10.1021/am5063647.

[244] Seemann R, Brinkmann M, Pfohl T, Herminghaus S. Droplet based microfluidics. Reports Prog Phys 2012;75:16601. doi:10.1088/0034-4885/75/1/016601.

[245] Mazutis L, Gilbert J, Ung WL, Weitz DA, Griffiths AD, Heyman JA. Single-cell analysis and sorting using droplet-based microfluidics. Nat Protoc 2013;8:870–91. doi:10.1038/nprot.2013.046.

[246] Zhu Y, Fang Q. Analytical detection techniques for droplet microfluidics-A review. Anal Chim Acta 2013;787:24–35. doi:10.1016/j.aca.2013.04.064.

[247] Teh SY, Lin R, Hung LH, Lee AP. Droplet microfluidics. Lab Chip 2008;8:198. doi:10.1039/b715524g.

[248] Wang Z, Zhe J. Recent advances in particle and droplet manipulation for lab-on-a-chip devices based on surface acoustic waves. Lab Chip 2011;11:1280. doi:10.1039/c0lc00527d.

[249] Lagus TP, Edd JF. A review of the theory, methods and recent applications of high-throughput single-cell droplet microfluidics. J Phys D Appl Phys 2013;46:114005. doi:10.1088/0022-3727/46/11/114005.

[250] Toyota T, Maru N, Hanczyc MM, Ikegami T, Sugawara T. Self-Propelled Oil Droplets Consuming “Fuel” Surfactant. J Am Chem Soc 2009;131:5012–3. doi:10.1021/ja806689p.

[251] Ban T, Tani K, Nakata H, Okano Y. Self-propelled droplets for extracting rare-earth metal ions. Soft Matter 2014;10:6316–20. doi:10.1039/C4SM01001A.

[252] Nagai K, Sumino Y, Kitahata H, Yoshikawa K. Mode selection in the spontaneous motion of an alcohol droplet. Phys Rev E 2005;71:65301. doi:10.1103/PhysRevE.71.065301.

[253] Pimienta V, Brost M, Kovalchuk N, Bresch S, Steinbock O. Complex shapes and dynamics of dissolving drops of dichloromethane. Angew Chemie - Int Ed 2011;50:10728–31. doi:10.1002/anie.201104261.

[254] Molin D, Mauri R, Tricoli V. Experimental evidence of the motion of a single out-of-equilibrium drop. Langmuir 2007;23:7459–61. doi:10.1021/la700826z.

[255] Ban T, Yamada T, Aoyama A, Takagi Y, Okano Y. Composition-dependent shape changes of self-propelled droplets in a phase-separating system. Soft Matter 2012;8:3908. doi:10.1039/c2sm07176b.

[256] Gutierrez JMP, Hinkley T, Taylor JW, Yanev K, Cronin L. Evolution of oil droplets in a chemorobotic platform. Nat Commun 2014;5:5571. doi:10.1038/ncomms6571.

[257] Cazabat AM, Heslot F, Troian SM, Carles P. Fingering instability of thin spreading films driven by temperature gradients. Nature 1990;346:824–6. doi:10.1038/346824a0.

[258] Diguet A, Guillermic RM, Magome N, Saint-Jalmes A, Chen Y, Yoshikawa K, et al. Photomanipulation of a droplet by the chromocapillary effect. Angew Chemie - Int Ed 2009;48:9281–4. doi:10.1002/anie.200904868.

[259] Ichimura K, Oh SK, Nakagawa M. Light-driven motion of liquids on a photoresponsive surface. Science 2000;288:1624–6. doi:10.1126/science.288.5471.1624.

[260] Florea L, Wagner K, Wagner P, Wallace GG, Benito-Lopez F, Officer DL, et al. Photo-chemopropulsion-light-stimulated movement of microdroplets. Adv Mater 2014;26:7339–45. doi:10.1002/adma.201403007.

[261] Lin YY, Welch ERF, Fair RB. Low voltage picoliter droplet manipulation utilizing electrowetting-on- dielectric platforms. Sensors Actuators, B 2012;173:338–45. doi:10.1016/j.snb.2012.07.022.

[262] Cooney CG, Chen CY, Emerling MR, Nadim A, Sterling JD. Electrowetting droplet microfluidics on a single planar surface. Microfluid Nanofluid 2006;2:435–46. doi:10.1007/s10404-006-0085-8.

[263] Čejková J, Novák M, Štěpánek F, Hanczyc MM. Dynamics of Chemotactic Droplets in Salt Concentration Gradients. Langmuir 2014;30:11937–44. doi:10.1021/la502624f.

[264] Ban T, Nakata H. Metal-Ion-Dependent Motion of Self-Propelled Droplets Due to the Marangoni Effect. J Phys Chem B 2015;119:7100–5. doi:10.1021/acs.jpcb.5b02522.

[265] Jurado-Sánchez B, Pacheco M, Maria-Hormigos R, Escarpa A. Perspectives on Janus micromotors: Materials and applications. Appl Mater Today 2017;9:407–18. doi:10.1016/j.apmt.2017.09.005.

[266] Liu L, Bai T, Chi Q, Wang Z, Xu S, Liu Q, et al. How to make a fast, efficient bubble-driven micromotor: A mechanical view. Micromachines 2017;8:267. doi:10.3390/mi8090267.

[267] Wu Z, Lin X, Si T, He Q. Recent Progress on Bioinspired Self-Propelled Micro/Nanomotors via Controlled Molecular Self-Assembly. Small 2016;12:3080–93. doi:10.1002/smll.201503969.

[268] Dong R, Hu Y, Wu Y, Gao W, Ren B, Wang Q, et al. Visible-light-driven BiOI-based janus micromotor in pure water. J Am Chem Soc 2017;139:1722–5. doi:10.1021/jacs.6b09863.

[269] Dong R, Zhang Q, Gao W, Pei A, Ren B. Highly efficient light-driven TiO2-Au Janus Micromotors. ACS Nano 2016;10:839–44. doi:10.1021/acsnano.5b05940.

[270] Mou F, Chen C, Zhong Q, Yin Y, Ma H, Guan J. Autonomous motion and temperature-

controlled drug delivery of Mg/Pt-poly(n -isopropylacrylamide) janus micromotors driven by simulated body fluid and blood plasma. ACS Appl Mater Interfaces 2014;6:9897–903. doi:10.1021/am502729y.

[271] Simoncelli S, Summer J, Nedev S, Kühler P, Feldmann J. Combined Optical and Chemical Control of a Microsized Photofueled Janus Particle. Small 2016;12:2854–8. doi:10.1002/smll.201503712.

[272] Gao W, D'Agostino M, Garcia-Gradilla V, Orozco J, Wang J. Multi-fuel driven janus micromotors. Small 2013;9:467–71. doi:10.1002/smll.201201864.

[273] Aveyard R, Binks BP, Clint JH. Emulsions stabilised solely by colloidal particles. Adv Colloid Interface Sci 2003;100–102:503–46. doi:10.1016/S0001-8686(02)00069-6.

[274] Binks BP. Particles as surfactants—similarities and differences. Curr Opin Colloid Interface Sci 2002;7:21–41. doi:10.1016/S1359-0294(02)00008-0.

[275] Wang B, Wang M, Zhang H, Sobal NS, Tong W, Gao C, et al. Stepwise interfacial self-assembly of nanoparticles via specific DNA pairing. Phys Chem Chem Phys 2007;9:6313. doi:10.1039/b705094a.

[276] Gibbs JG, Zhao YP. Autonomously motile catalytic nanomotors by bubble propulsion. Appl Phys Lett 2009;94:163104. doi:10.1063/1.3122346.

[277] Yuet KP, Hwang DK, Haghgooie R, Doyle PS. Multifunctional superparamagnetic janus particles. Langmuir 2010;26:4281–7. doi:10.1021/la903348s.

[278] Gao W, Pei A, Wang J. Water-driven micromotors. ACS Nano 2012;6:8432–8. doi:10.1021/nn303309z.

[279] Porciúncula CB, Marcilio NR, Tessaro IC, Gerchmann M. Production of hydrogen in the reaction between aluminum and water in the presence of NaOH and KOH. Brazilian J Chem Eng 2012;29:337–48. doi:10.1590/S0104-66322012000200014.

[280] Wang CC, Chou YC, Yen CY. Hydrogen generation from aluminum and aluminum alloys powder. Procedia Eng 2012;36:105–13. doi:10.1016/j.proeng.2012.03.017.

[281] Wang H, Zhao G, Pumera M. Crucial role of surfactants in bubble-propelled microengines. J Phys Chem C 2014;118:5268–74. doi:10.1021/jp410003e.

[282] Nidhi K, Indrajeet S, Khushboo M, Gauri K, Sen DJ. Hydrotropy: A promising tool for solubility enhancement: A review. Int J Drug Dev Res 2011;3:26–33. doi:10.1002/jps.

[283] Li Y, Hewitt D, Lentz YK, Ji JA, Zhang TY, Zhang K. Characterization and stability study of polysorbate 20 in therapeutic monoclonal antibody formulation by multidimensional ultrahigh-performance liquid chromatography-charged aerosol detection-mass spectrometry. Anal Chem 2014;86:5150–7. doi:10.1021/ac5009628.

[284] McShan AC, Kei P, Ji JA, Kim DC, Wang YJ. Hydrolysis of polysorbate 20 and 80 by a range of carboxylester hydrolases. PDA J Pharm Sci Technol 2016;70:332–45. doi: 10.5731/pdajpst.2015.005942.

[285] Gray AL, Hsu JT. Novel sulfonic acid-modified starburst dendrimer used as a pseudostationary phase in electrokinetic chromatography. J Chromatogr A 1998;824:119–24. doi:10.1016/S0021-9673(98)00623-2.

[286] Ramos-Tejada MM, Dura JDG, Ontiveros-Ortega A, Espinosa-Jimenez M, Perea-Carpio R,

Chibowski E. Investigation of alumina/(+)-catechin system properties. Part II: ζ-potential and surface free energy changes of alumina. Colloids and Surfaces 2002;24:309–20. doi:doi.org/10.1016/S0927-7765(01)00285-5.

Publications

(1) **Li, M.**; Li, D. Redistribution of Mobile Surface Charges of an Oil Droplet in Water in Applied Electric Field. *Adv. Colloid Interface Sci.* **2016**, *236*, 142–151.

(2) **Li, M.**; Li, D. Redistribution of Charged Aluminum Nanoparticles on Oil Droplets in Water in Response to Applied Electrical Field. *J. Nanopart. Res.* **2016**, *18* (5), 120.

(3) Song, Y.; Wang, C.; **Li, M.**; Pan, X.; Li, D. Focusing Particles by Induced Charge Electrokinetic Flow in a Microchannel. *Electrophoresis* **2016**, *37* (4), 666–675.

(4) **Li, M.**; Li, D. Vortices around Janus Droplets under Externally Applied Electrical Field. *Microfluid. Nanofluid.* **2016**, *20* (5), 79.

(5) Wang, C.; **Li, M.**; Song, Y.; Pan, X.; Li, D. Electrokinetic Motion of a Spherical Micro Particle at an Oil−water Interface in Microchannel. *Electrophoresis* **2017**, *39*, 807–815.

(6) **Li, M.**; Li, D. Separation of Janus Droplets and Oil Droplets in Microchannels by Wall-Induced Dielectrophoresis. *J. Chromatogr. A* **2017**, *1501*, 151–160.

(7) **Li, M.**; Li, D. Electrokinetic Motion of an Electrically Induced Janus Droplet in Microchannels. *Microfluid. Nanofluid.* **2017**, *21* (2), 16.

(8) **Li, M.**; Li, D. Fabrication and Electrokinetic Motion of Electrically Anisotropic Janus Droplets in Microchannels. *Electrophoresis* **2017**, *38*, 287–295.

(9) **Li, M.**; Li, D. Self-Propulsion of Aluminum Particle-Coated Janus Droplet in Alkaline Solution. *J. Colloid Interface Sci.* **2018**, *532*, 657–665.

(10) **Li, M.**; Li, D. Janus Droplets and Droplets with Multiple Heterogeneous Surface Strips Generated with Nanoparticles under Applied Electric Field. *J. Phys. Chem. C* **2018**, *122* (15), 8461–8472.

(11) **Li, M.**; Li, D. Microvalve Using Electrokinetic Motion of Electrically Induced Janus Droplet. *Anal. Chim. Acta* **2018**, *1021*, 85–94.

Appendix A

Details of the Numerical Investigation

In Chapter 4, the electroosmotic flow field around EIJDs was studied both experimentally and numerically. In the numerical part, a 2D model was set up to simulate the flow fields inside and outside of a sessile EIJD under electric field. In the model the EDL+SC model was applied to simulate the motion of the oil-water interface under externally applied electric field. The EDL+SC model considers the force balance at the interface. The forces acting at the oil-water interface includes: the shear force on the water side, the shear force on the oil side and the electrostatic force. The meshes in the main computation domain are set to be triangular, while the rectangular meshes were employed in vicinity of the oil-water interface for the calculation of shear forces, as shown in Figure A-1. The dimensions of the rectangular meshes should be much smaller than the EDL thickness for simulating the EOF inside EDL; hence, the shear force acting on the interface can be calculated accurately.

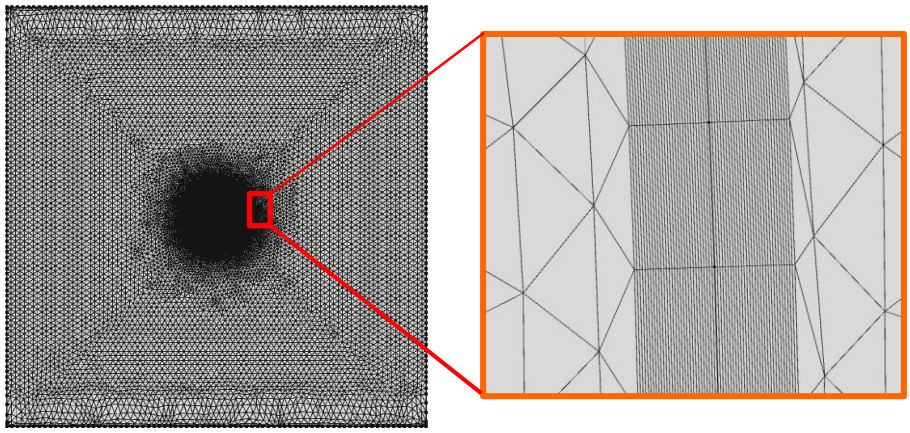

Figure A-1. Mesh structure used to model the main domain and the oil-water interface.

The mesh sensitivity analysis was conducted by detecting the effect of the total number of meshes on the EOF velocity at a certain point. The point located in the water phase near the oil-water interface was chosen. The variation of the calculated EOF velocity in terms of the total number of meshes is shown in Figure A-2. It can be seen clearly from this figure that the calculated EOF velocity remain stable when the total number of meshes reaches 80,000. In Chapter 4, the total number of meshes used in this simulation is 131,034, and the simulation result is insensitive to the mesh number. While calculating, the COMSOL built-in solver of MUMPS was implied. This solver compute finite element problems with Newton iteration method.

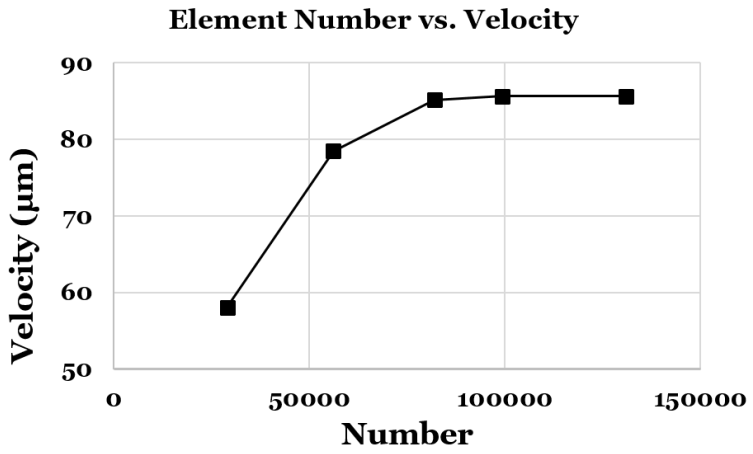

Figure A-2. Effect of the total number of meshes on the calculated EOF velocity.

Appendix B

Comparison of the Simulation Results of the Electrokinetic Velocities of EIJDs Obtained from Different Models

Apart from the EDL+SC model, some other models were also presented in some papers to evalute the fluid flow at the oil-water interface, for example, the EDL model. In this model, the following boundary conditions are given to the liquid-liquid interface:

$$\vec{u}_w = \vec{u}_o \tag{A-1}$$

$$\eta_w \frac{\partial \vec{u}_w}{\partial \vec{n}} = \eta_o \frac{\partial \vec{u}_o}{\partial \vec{n}} \tag{A-2}$$

Comparison between the EDL model and the EDL+SC model indicates that both EDL and EDL+SC models consider the continuity of shear stress at the liquid-liquid interface. However, the EDL model neglects the electrostatic force acting on the surface charges at the interface ($\sigma_s \vec{E}_o$). The EOF at the charged liquid-liquid interface has been analyzed with the two models, and the simulated results indicate that under the same condition, the EDL model always overestimates the velocity of the interface. While using the EDL model to calculate the electrokinetic motion of the Janus droplet, the velocity of the interface and the strength of the vortex inside of the droplet are stronger than normal, which causes the overestimate of the electrophoretic motion of the Janus droplet and the underestimate of the electrokinetic motion of it in a microchannel. In conclusion, with the EDL model, the calculated electrokinetic velocity of the Janus droplet is smaller than normal.

Figure A-1 shows the comparisons between different models for the electrokinetic velocity of Janus droplet with d = 45μm, η_o = 0.07 Pa·s and θ = 83.5°. It's clearly shown in this figure that the electrokinetic velocity calculated with the EDL model is smaller than the experimental result especially under high electrical field. This meets our estimation shown above. Figure 44 also indicates that under the experimental condition, the difference between the calculated electrokinetic velocity of Janus droplet with EDL+SC model and that of solid Janus particle is very small, and both of the two models can be used to evaluate the electrokinetic velocity of Janus droplets. This phenomena can be understand like this:

(1) As shown in Figure A-1, for the Janus droplet with θ = 90° (circular points), when η_r > 50, U_d^* almost reaches to a constant, and the Janus droplet performs as a solid particle. In the experiment, the Janus droplet with η_r = 70 and θ = 83.5° was used. The viscosity effect on its electrokinetic motion is limited; therefore, the Janus droplet can be approximated to Janus particle.

(2) For small Janus droplet (d = 45μm) moving in a mcirochannel under weak electric field (ranging from 50V/cm to 100V/cm), the capillary number is very low that the surface tension at the interface is great larger than the viscous force. Under low capillary number condition, the effect of the viscous force is negligible, that the droplet can be regarded as solid particle.

In conclusion, the EDL+SC model is suitable for evaluating the electrokinetic velocity of Janus droplet. For small Janus droplet with high visocisity and nanoparticle coverage area, the Janus droplet performs as solid particle that the solid Janus particle model can be used to evaluate the electrokinetic motion of it.

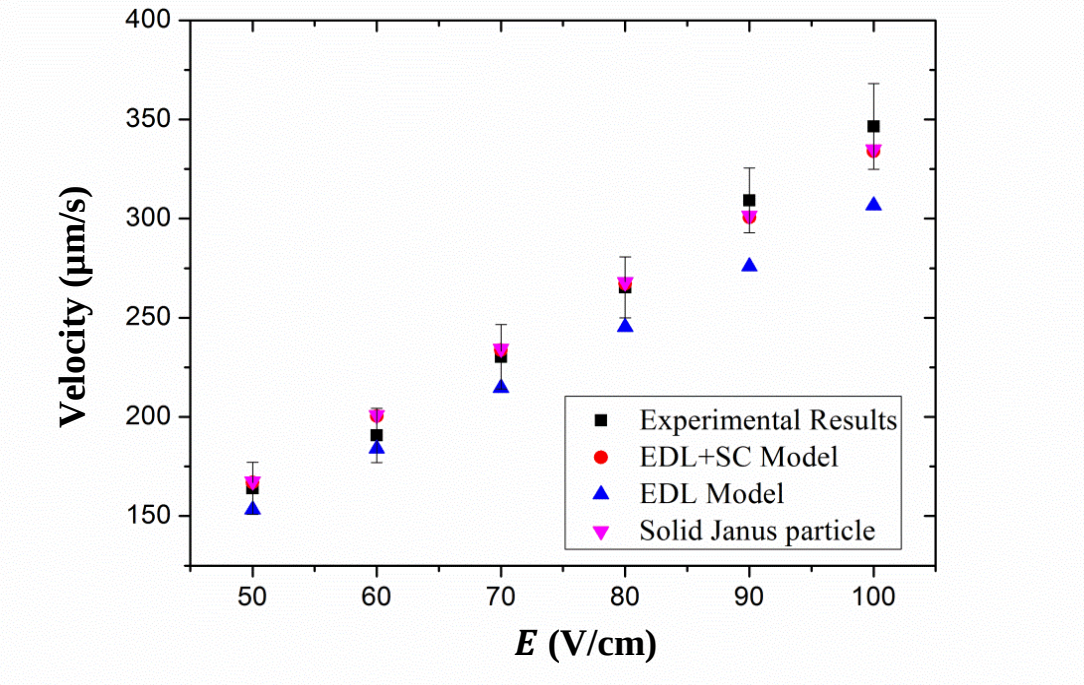

Figure A-1. Comparisons between the experimental results and the simulated results under three different models for the electrokinetic velocity of Janus droplet and particle with d *= 45μm,* θ *= 83.5°. The rectangular points represent the experimental measured electrokinetic velocity of Janus droplet. The circular points, triangular points represent the simulated electrokinetic velocities of Janus droplets for EDL+SC model and EDL model, respectively. The inverted triangular points represent the simulated electrokinetic velocities of solid Janus particle. The viscosity of the oil phase of the Janus droplet is* η_o *= 0.07 Pa·s.*

Appendix C

Electric Field in the Main Channel of the Wall-induced DEP Separation Microfluidic Chip

In chapter 7, to separate the target droplet from others, the voltages applied to the two outlets were verified to control the proportion of the liquid moving from the main channel into each of the outlet channels. When the voltages change, the electric field strength inside each outlet branch varies accordingly. To investigate the electric field distribution in the main channel, numerical simulation was conducted with the software of COMSOL. The numerical results are shown in Figure A-2. As shown in this figure, the electric field lines are always uniformly distributed inside of the main channel regardless of the variation of the voltages applied to the outlets. Therefore, the wall-induced DEP theory shown in chapter 7 is also applicable to estimate the lateral migration of droplet in the separation process.

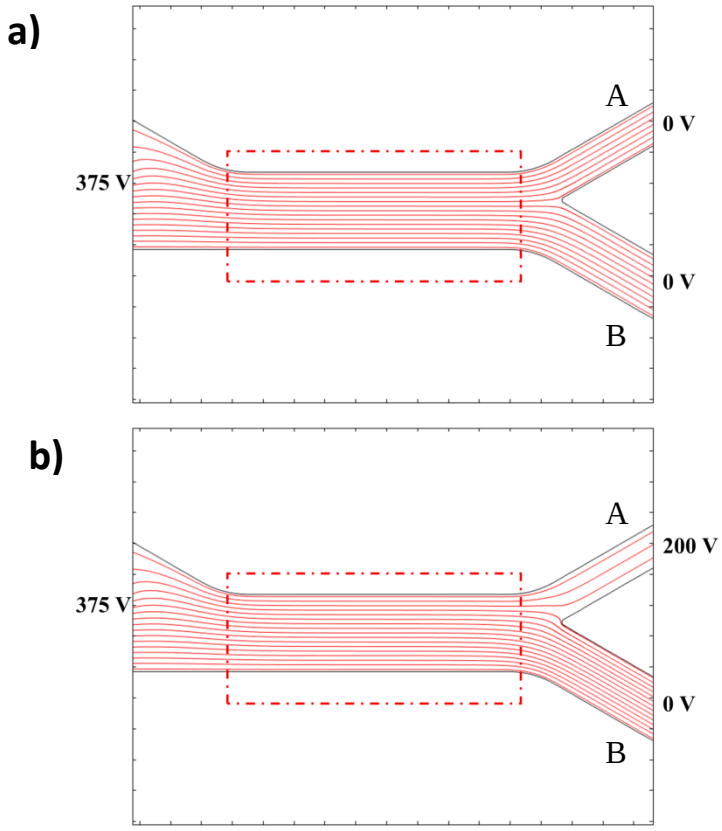

Figure A-2. Electric field in the main channel of the wall-induced DEP separation microfluidic chip. (a) $\phi_{oA} = \phi_{oB} = 0$ V; (b) $\phi_{oA} = 200$ V, $\phi_{oB} = 0$ V.

Appendix D

EOF Fields around Droplets with Heterogeneous Strips

The numerical simulation results of the EOF fields around sessile droplets with heterogeneous strips in a microchannel are shown in Figure A-3. The droplets in Figure A-3(a)-(c) are covered with three strips which are A-B-A from left to right, and the droplet in Figure A-3(d) is covered with four strips of B-A-B-A by turns. The effects of the zeta potential and the coverage of the strips on the vortices can be obtained by comparing these figures.

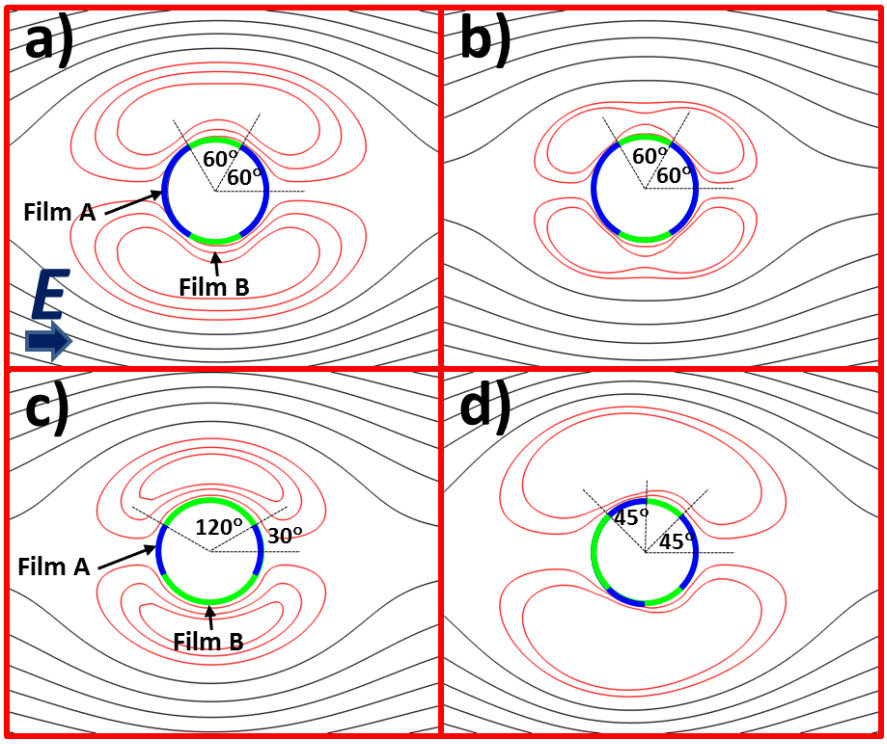

Figure A-3. Numerical simulation results of the EOF fields around droplets with heterogeneous strip. (a) Droplet with A-B-A three strips, $\zeta_w = -60\ mV$, $\zeta_{nanoA} = 40\ mV$ *and* $\zeta_{nanoB} = 20\ mV$; *(b) droplet with A-B-A three strips,* $\zeta_w = -60\ mV$, $\zeta_{nanoA} = 30\ mV$ *and* $\zeta_{nanoB} = 10\ mV$; *(c) droplet with A-B-A three strips,* $\zeta_w = -60\ mV$, $\zeta_{nanoA} = 40\ mV$ *and* $\zeta_{nanoB} = 20\ mV$; *(d) droplet with B-A-B-A four strips,* $\zeta_w = -60\ mV$, $\zeta_{nanoA} = 40\ mV$ *and* $\zeta_{nanoB} = 20\ mV$.

Appendix E

EOF Fields around Sessile Janus Droplets in a Microchannel*

In chapter 4, the EOF fields around sessile Janus droplets in a infinitely large container were studied. Figure A-4 shows the EOF fields around sessile Janus droplets in a microchannel. The experimental results of the EOF fields in the vicinity of sessile oil-Al_2O_3 Janus droplet and sessile MgO-Al_2O_3 Janus droplet in different pH solutions are presented in Figure A-4(a)-(d). The EOF fields around the sessile oil-Al_2O_3 Janus droplet in pH 7 and 9 buffer solutions are shown in Figure A-4(c) and (d). In pH 7 and pH 9 buffer solutions, the oil-water interface carries negative charges and the Al_2O_3 nanoparticle film carries positive charges. Under rightward electrical field, EOFs with opposite directions (from left to right on left hemisphere, and from right to left on right hemisphere) are induced on the Janus droplet. As the zeta potential of the microchannel wall is also negative in these buffer solutions, with the combined effects of the bulk liquid motion and the EOF around the Janus droplet, two vortices are formed on the right hemisphere of the Janus droplets. In comparison with these two figures, with the increase of pH value of the buffer solution from 7 to 9, the zeta potentials of both microchannel wall and Al_2O_3 nanoparticle film shift towards negative direction, which leads to the increase of the absolute value of zeta potential of the channel wall and the decrease of that of the nanoparticle film; hence, smaller size of the vortices. However, when the pH value of the buffer solution is reduced to 2, the electrical property of the Janus droplet and the microchannel wall change and all surfaces are positively charged. Correspondingly, the bulk liquid EOF and the EOFs around both sides of the Janus droplets are in the same direction (from right to left) and no vortex shows up (Figure A-4(a)). In Figure A-4(d), the EOF field around MgO-Al_2O_3 Janus droplet immersed in pH 9 buffer solution is presented. As the zeta potentials of both MgO nanoparticle film and Al_2O_3 nanoparticle film are positive while that of the

* A similar version of this section was submitted or published as:

Li, M.; Li, D. Janus Droplets and Droplets with Multiple Heterogeneous Surface Strips Generated with Nanoparticles under Applied Electric Field. *J. Phys. Chem.* **2018**, 122, 8461-8472. https://pubs.acs.org/doi/abs/10.1021/acs.jpcc.8b01920

microchannel wall is negative, the EOF of the bulk liquid is in the opposite direction to the EOF around the droplet, which leads to two vortices along the surface of the droplet.

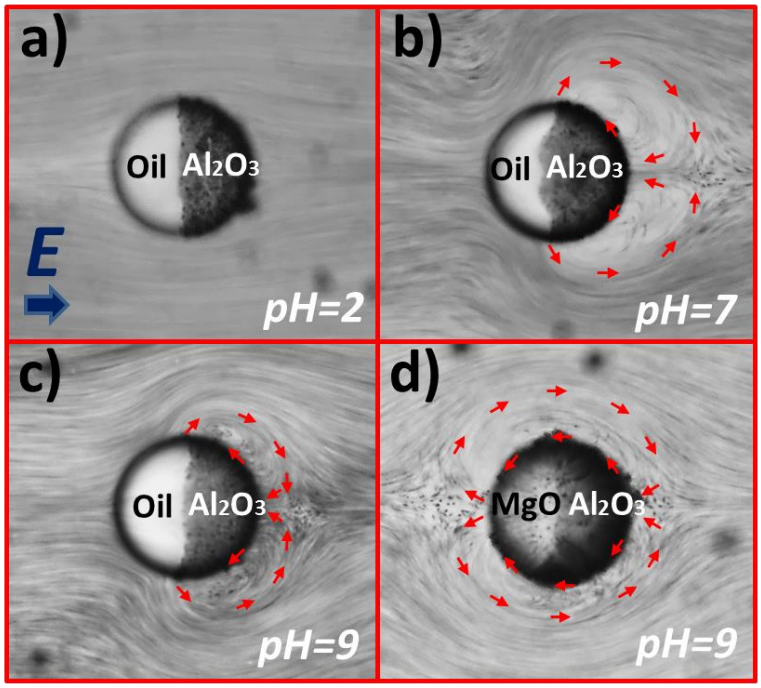

Figure A-4. EOF fields around sessile Janus droplets in a microchannel. (a) Oil-Al_2O_3 Janus droplet immersed in pH 2 buffer solution; (b) oil-Al_2O_3 Janus droplet in pH 7 buffer solution; (c) oil-Al_2O_3 Janus droplet in pH 9 buffer solution; (d) MgO-Al_2O_3 Janus droplet in pH 9 buffer solution. 1 µm polystyrene particles are employed as tracing particles. DC electric field of 150 V/cm is applied from left to right.

Appendix F

Electrokinetic Motion of Droplets with Different Nanoparticle Films*

The electrokinetic motion of droplets covered with different nanoparticle films in a microchannel is due to the combined effects of the electrophoresis (EP) of the droplets and the electroosmosis of the bulk liquid in the microchannel. As both EOF of the bulk liquid and EP of the droplets are linearly proportional to the electrical field, the electrokinetic velocity of these droplets in a straight microchannel has linear relationship with the applied electrical field.

As an example, the electrokinetic motion of an oil-Al_2O_3 Janus droplet under the electric field of 100 V/cm is shown in Figure A-5(a). The images are captured from a video. As indicated in these time-lapse images, the Janus droplet moves uniformly in a straight microchannel. Due to its dipolar property, when moving in the microchannel, the Janus droplet always aligns to the electrical field with the negatively charged hemisphere facing the cathode of the externally applied electrical field. For the droplets of similar size moving in a straight microchannel, the EOF of the bulk liquid is identical, the difference of electrokinetic velocities between these droplets results from different EP. The EP of the droplet is caused by the interaction between the electric field and the surface charges of the droplets. Generally, the stronger net surface charge or higher net zeta potential of the droplets will result in a stronger electrophoretic motion of the droplets.

The electrokinetic velocities of oil-MgO Janus droplets, oil-Al_2O_3 Janus droplets, MgO-Al_2O_3 Janus droplets and droplets fully covered by Al_2O_3 nanoparticle film in a microchannel with the cross section of 250 μm × 80 μm (Width × Height) under different strengths of electrical fields are measured and shown in Figure A-5(b). To make comparison, the size of the droplets is controlled to be approximately 45 μm. It can be seen from this figure that, for the same droplet, the electrokinetic velocity increases with the electrical field linearly. Furthermore, under the same electrical field, the measured electrokinetic velocity increases in the sequence of oil-MgO Janus

* A similar version of this section was submitted or published as:
Li, M.; Li, D. Janus Droplets and Droplets with Multiple Heterogeneous Surface Strips Generated with Nanoparticles under Applied Electric Field. *J. Phys. Chem.* **2018**, 122, 8461-8472. https://pubs.acs.org/doi/abs/10.1021/acs.jpcc.8b01920

droplets, oil-Al_2O_3 Janus droplets, MgO-Al_2O_3 Janus droplets and droplets fully covered by Al_2O_3 nanoparticle film. In pH 7 buffer solution, the zeta potentials of oil droplet, MgO nanoparticle film and Al_2O_3 nanoparticle film have the relationship of $\zeta_{ow} < 0 < \zeta_{nanoMgO} < \zeta_{nanoAl_2O_3}$. Therefore, the oil-MgO Janus droplet with a zeta potential of ζ_{ow} on the left hemisphere and a zeta potential of $\zeta_{nanoMgO}$ on the right hemisphere moves slower than the oil-Al_2O_3 Janus droplet with the zeta potentials of ζ_{ow} (left hemisphere) and $\zeta_{nanoAl_2O_3}$ (right hemisphere), because of the difference of surface charges. The EK velocity of the droplet fully covered with Al_2O_3 nanoparticles is the largest. Based on the different EK velocities of these droplets, they can be separated in a microchannel.

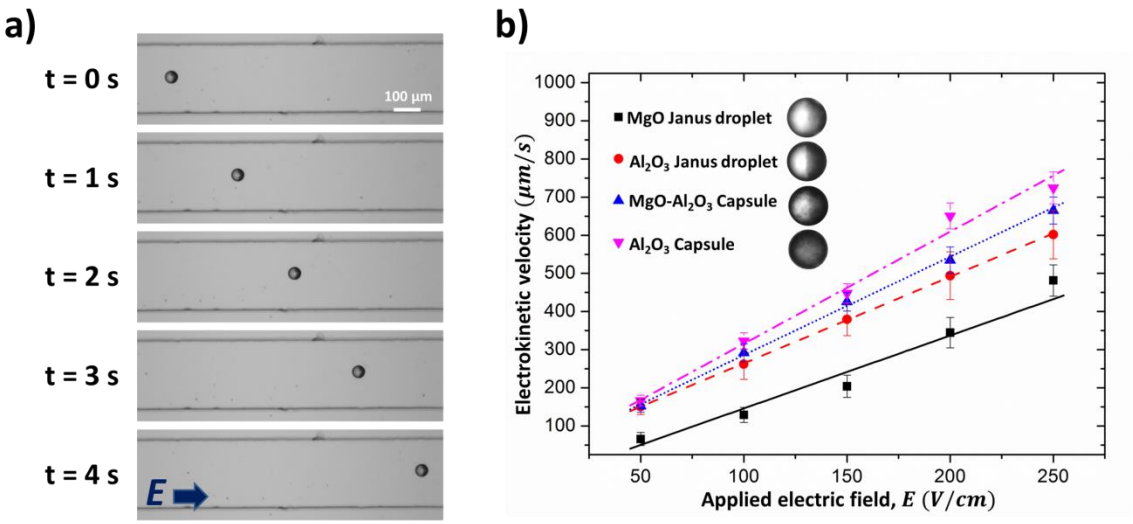

Figure A-5. (a) Time-lapse sequences of the electrokinetic motion of an oil-Al_2O_3 Janus droplet in a microchannel under the electric field of 100 V/cm. The diameter of the Janus droplet is 45 μm and the width of the microchannel is 250 μm. (b) Electrokinetic velocities of oil-MgO Janus droplets, oil-Al_2O_3 Janus droplets, MgO-Al_2O_3 Janus droplets and droplets fully covered with Al_2O_3 film in a microchannel as a function of applied DC electrical field. The cross section of the microchannel is 250 μm × 80 μm (Width × Height). The diameters of the droplets are approximately 45 μm. The buffer solution is deionized water.

Appendix G

Flow Focusing with Positively Charged Capsules*

If a pair of oil droplets fully covered by positively charged nanoparticle films is anchored in a negatively charged microchannel, under electrical field, EOF of the bulk liquid in the microchannel is in the opposite direction to the EOF around the droplets. Hence, vortices form in the vicinity of the droplets, as shown in Figure A-6(a). The two vortices around the droplets act as virtual columns to reduce the flow passage in the microchannel. Consequently, the liquid is forced to flow through a narrower virtual channel between the two vortices. Such an effect is referred to as the flow focusing. To demonstrate the focusing performance of this strategy, a Y-shape microchannel consisting of two inlet branches and one main channel is used. As shown in Figure A-6(b), two oil droplets fully covered with Al_2O_3 nanoparticles are anchored in the main channel by two pillars. 1 μm polystyrene particles are employed in the experiments to visualize the flow focusing effect. Under the electric field of 100 V/cm, the tracing particles are transported to move through the microchannel by EOF. When flowing through the space between the two droplets, the particles are forced to move through the narrow passageway with a width of approximately 17 μm due to the effect of the two vortices. As indicated in Figure A-6(b), the blank regions without the presence of the tracing particles are the vortices regions (labelled with red dash lines). For the droplets with constant size, the location and size of the vortices are fixed, regardless of the strength of the electric field; thus, the focusing effect remains constant. In order to achieve a narrower focused flow width, two larger droplets covered with a positively charged nanoparticle film should be employed in the microchannel to generate bigger vortices. In comparison with the traditional method that designing a tapered channel for flow focusing, the positively charged droplets flow-focusing method has the advantage of easy adjustment of flow focusing effect. As described above, an enhanced focusing can be achieved by replacing small droplets with larger ones regardless of changing the structure of the microchannel. However, for the traditional focusing method, it's essential to re-design the

* A similar version of this section was submitted or published as:

Li, M.; Li, D. Janus Droplets and Droplets with Multiple Heterogeneous Surface Strips Generated with Nanoparticles under Applied Electric Field. *J. Phys. Chem.* **2018**, 122, 8461-8472. https://pubs.acs.org/doi/abs/10.1021/acs.jpcc.8b01920

microchannel and conduct microfabrication again to adjust the focusing effect. It should be noted that, apart from particles, this focusing method can also be employed to bio samples by replacing the deionized water with the buffer solutions used for bio experiments.

Flow focusing is particularly useful in microfluidic flow cytometry where cells and particles are required to move in a single line to pass through a sensor. The generation of vortices in a laminar-flow microfluidic device is a challenge, and however, has extensive applications, for example, cell trapping, generating concentration gradient, mixing, separation and pumping. Therefore, apart from flow focusing, the nanoparticle film covered droplets fabricated in this paper also have potential in the above mentioned fields.

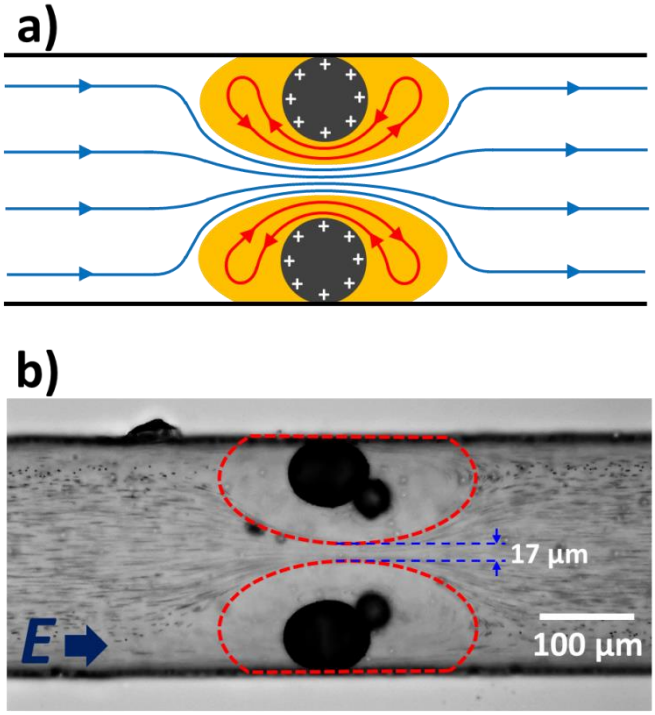

Figure A-6. Flow focusing with a pair of droplets fully covered with Al_2O_3 nanoparticles in a microchannel. (a) Schematic diagram of the EOF field in a microchannel with the presence of two positively charged droplets. (b) Experimental observation of particle focusing occurring between two oil droplets fully covered with Al_2O_3 nanoparticles under the electric field of 100 V/cm. The diameters of the two droplets are approximately 80 µm and the cross section of the microchannel is 250 µm × 80 µm (Width × Height). The buffer solution is deionized water.

Appendix H

Electric Field Distribution in Microvalve

To study the effect of the size of microchamber on the strength of electrical field, a 3D model was built up with commercial simulation software COMSOL and the electric field distribution in the microvalve was studied. The results are shown in Figure A-7. To show the electrical field distribution in the microchamber clearly, the maximum color range was set to be 50 V/cm; therefore, the regions labelled with red color represents the local electrical field is equal to or larger than 50 V/cm. By comparing Figure A-7(a) and (b), it's clearly shown that, with the reduction of the size of the microchamber, the distance between the two entrances decreases and the strength of the electrical field between the two entrances in the microchamber increases. Furthermore, as shown in the figure, although high voltage is applied to the microchannel, the strength of the electrical field is very weak in the microchamber due to the large size difference between the microchamber and the branches (around 10 V/cm in the middle of the microchamber). Therefore, by embedding plane electrodes under branches next to the entrances, the electrical field is applied directly to the microchamber without consuming in the branches. Hence, the electrical field applied to the microchamber can be increased easily, and the switching speed of the microvalve increases.

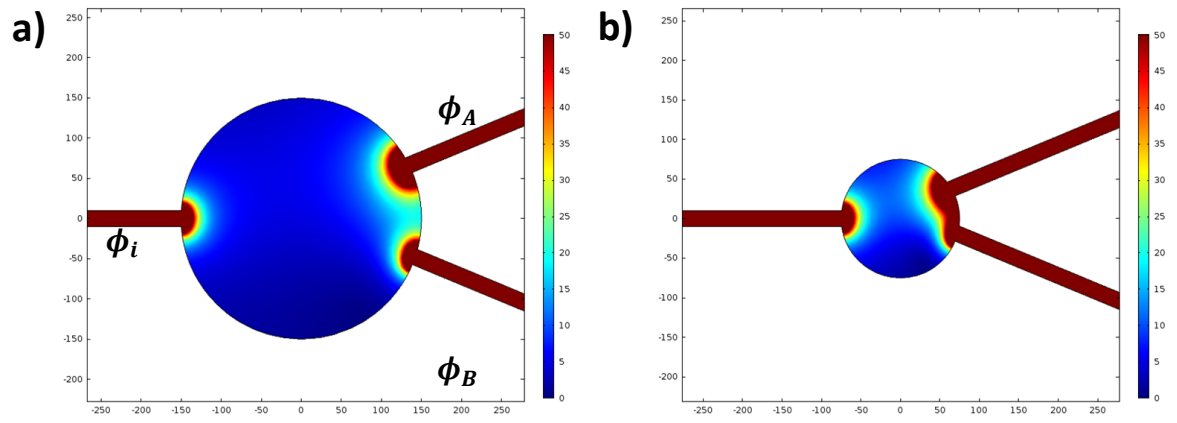

Figure A-7. Electric field distributions in microvalves with different sizes. (a) The diameter of the microchamber is 300 µm; (b) The diameter of the microchamber is 150 µm. The applied voltages are $\phi_i = 375\ V$, $\phi_A = 0\ V$ *and* $\phi_B = 375\ V$.